Asteroseismology: Data Analysis Methods and Interpretation for Space and Ground-based Facilities

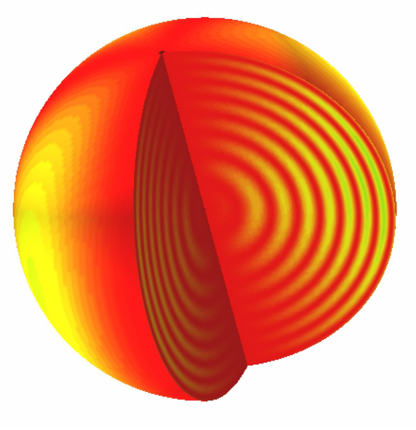

Tiago L. Campante

Faculdade de Ciências e Centro de Astrofísica da Universidade do Porto
Institut for Fysik og Astronomi, Aarhus Universitet, Danmark

A thesis submitted for the degree of

Doutor em Astronomia (3^o Ciclo da Universidade do Porto)

November 2011

Cover figure taken from `http://science.au.dk/`.

Abstract

This dissertation has been submitted to the *Faculdade de Ciências da Universidade do Porto* in partial fulfillment of the requirements for the PhD degree in Astronomy. The scientific results presented herein follow from the research activity performed under the supervision of Dr. Mário João Monteiro at the *Centro de Astrofísica da Universidade do Porto* and Dr. Hans Kjeldsen at the *Institut for Fysik og Astronomi, Aarhus Universitet.*

The dissertation is mainly composed of three chapters and a list of appendices. Chapter 1 serves as an unpretentious and rather general introduction to the field of asteroseismology of solar-like stars. It starts with an historical account of the field of asteroseismology followed by a general review of the basic physics and properties of stellar pulsations. Emphasis is then naturally placed on the stochastic excitation of stellar oscillations and on the potential of asteroseismic inference. The chapter closes with a discussion about observational techniques and the observational status of the field. Given my exclusive role as a data analyst, I have devoted Chapter 2 to the subject of data analysis in asteroseismology. This is an extensive subject, therefore I have opted for presenting a compilation of relevant data analysis methods and techniques employed contemporarily in asteroseismology of solar-like stars, and of which I have made recurrent use. Special attention has been drawn to the subject of statistical inference both from the competing Bayesian and frequentist perspectives, a matter that I consider to be currently in vogue. The chapter ends with a description of the implementation of a pipeline for mode parameter analysis of *Kepler* data. In the course of these two first chapters, reference is made to a series of published articles that have greatly benefited from my contribution and are, for that reason, collected in Appendices A to E. Chapter 3 then goes on to present a series of additional published results to which my contribution has been significant, although in a somewhat less determinant way. The compendium of scientific results presented in this dissertation is, to my mind, representative of my research activity and technical expertise.

The dawn of a new and prosperous era for the field of asteroseismology coincided with the development of space-based missions using the technique of ultra-high-precision photometry. The advent of the French-led *CoRoT* and NASA *Kepler* space missions had finally provided the possibility of carrying out long and almost uninterrupted observations of a multitude of targets, being at the same time capable of detecting faint solar-like oscillations in main-sequence stars. The main goal of my research activity has been the development of innovative data analysis methods and subsequent interpretation of the results in the context of space-based asteroseismology. That being said, the development of two pipelines for the analysis of *Kepler* asteroseismic data, together with the development of a Bayesian peak-bagging tool based on Markov chain Monte Carlo techniques, constitute some of the main outcomes of my research work.

An active membership of the *Kepler* Asteroseismic Science Consortium (KASC) has allowed me not only to exchange technical skills and relevant knowledge with other members of the consortium, but also to take part in – and even lead – a series of workpackages covering a diversity of scientific aims, ranging from the comprehensive analysis of single objects to ensemble and differential asteroseismology. In this regard, I would highlight the analysis of multi-month time-series data on four evolved Sun-like stars, the very first results from ensemble asteroseismology based on a large cohort of solar-type field stars, and the observational confirmation of the presence of solar-like oscillations in a δ Sct star.

Despite having focused my efforts on *Kepler*-related investigations, I have still managed to sporadically contribute to the analysis of targets observed by *CoRoT* (e.g., establishing a definite mode identification for the F-type star HD 49933, or characterizing the exoplanet-host solar-like star HD 52265 using both spectroscopic and seismic data) or during ground-based campaigns (e.g., a multi-site campaign dedicated to Procyon, or an asteroseismic and interferometric study of the solar twin 18 Scorpii), thus widening the scope of my research.

Sumário

Esta dissertação foi submetida à Faculdade de Ciências da Universidade do Porto no cumprimento parcial dos requisitos necessários à obtenção do grau de Doutor. Os resultados científicos aqui apresentados decorrem da actividade de investigação realizada sob a orientação do Dr. Mário João Monteiro do Centro de Astrofísica da Universidade do Porto e do Dr. Hans Kjeldsen do *Institut for Fysik og Astronomi, Aarhus Universitet.*

A dissertação é composta principalmente de três capítulos e de uma lista de anexos. O primeiro capítulo serve de introdução despretensiosa e bastante geral ao campo da asterossismologia de estrelas do tipo solar. Começa com um relato histórico do campo da asterossismologia seguido de uma revisão da física básica e propriedades das pulsações estelares. É então dado natural ênfase à excitação estocástica de oscilações estelares e ao potencial da inferência asterossísmica. O capítulo termina com uma discussão sobre técnicas de observação e sobre o estado actual do campo em termos observacionais. Dado o meu papel exclusivo como analista de dados, consagrei o segundo capítulo ao tema da análise de dados em asterossismologia. Este é um tema extenso e, por esse motivo, optei por apresentar uma compilação de métodos e técnicas de análise de dados relevantes, utilizados contemporaneamente na asterossismologia de estrelas do tipo solar, e dos quais fiz uso recorrente. Foi dada especial atenção ao tema da inferência estatística tanto de uma perspectiva Bayesiana como de uma perspectiva frequentista, um assunto que considero estar actualmente em voga. O capítulo termina com a descrição da implementação de um *pipeline* usado na análise dos parâmetros de modos de oscilação presentes em dados do satélite *Kepler.* Ao longo destes dois primeiros capítulos, é feita referência a uma série de artigos publicados que beneficiaram de modo determinante da minha contribuição e que, por essa razão, aparecem compilados na lista de anexos. O terceiro capítulo passa então a apresentar uma série adicional de resultados publicados, para a obtenção dos quais a minha contribuição foi significativa, embora de forma não tão determinante. O compêndio de resultados científicos apresentados

nesta dissertação é, a meu ver, representativo da minha actividade de investigação e conhecimento técnico.

O alvorecer de uma nova e próspera era para o campo da asterossismologia coincidiu com o desenvolvimento de missões espaciais empregando a técnica de fotometria de muito alta precisão. O advento da missão espacial francesa *CoRoT* e do satélite *Kepler* da NASA, tornou finalmente possível a realização de observações demoradas e quase ininterruptas de um sem-número de estrelas, sendo ao mesmo tempo essas missões capazes de detectar ténues oscilações do tipo solar em estrelas da sequência principal. O objectivo principal da minha actividade de investigação consistiu no desenvolvimento de métodos inovadores de análise de dados e subsequente interpretação dos resultados no âmbito da asterossismologia espacial. Dito isto, o desenvolvimento de dois *pipelines* usados na análise de dados provenientes do satélite *Kepler*, juntamente com o desenvolvimento de uma ferramenta Bayesiana a usar na análise de espectros de potência, constituem alguns dos principais resultados do meu trabalho de investigação.

Uma participação activa no âmbito do KASC (*Kepler* Asteroseismic Science Consortium) permitiu-me não só a partilha de competências técnicas e conhecimentos relevantes com os demais membros do consórcio, mas também integrar, e até mesmo liderar, uma série de grupos de trabalho abrangendo uma diversidade de fins científicos, desde a análise detalhada de objectos individuais à prática estatística da asterossismologia com base em grupos numerosos de estrelas. A este respeito, gostaria de destacar a análise das séries temporais, com a duração de vários meses, de quatro estrelas evoluídas do tipo solar, os primeiros resultados provenientes da prática estatística da asterossismologia com base num grande número de estrelas de campo do tipo solar, e a confirmação observacional da presença de oscilações do tipo solar numa estrela δ Sct.

Apesar de ter centrado os meus esforços em investigações relacionadas com o *Kepler*, pude ainda contribuir esporadicamente para a análise de estrelas observadas pela missão espacial *CoRoT* (por exemplo, estabelecendo de modo definitivo a identificação dos modos de oscilação da estrela HD 49933, de tipo espectral F, ou ao caracterizar a estrela de tipo solar HD 52265, que também alberga um exoplaneta, através do uso de dados sísmicos e espectroscópicos) ou durante campanhas de observação feitas a partir do solo (por exemplo, um campanha envolvendo vários telescópios dedicada a Procyon, ou um estudo sísmico e interferométrico de 18 Scorpii, uma estrela muito semelhante ao nosso Sol), tendo assim alargado o âmbito da minha actividade de investigação.

To Isabel, my parents, and my sister.

Acknowledgements

First of all, I wish to thank both my supervisors, Mário João Monteiro and Hans Kjeldsen, for their invaluable advice and unconditional support throughout the past three years or so.

I am grateful to my colleagues at CAUP, namely, Isa Brandão, Margarida Cunha and Michaël Bazot. I wish to thank all my former colleagues at Aarhus University, namely, Gülnur Doğan, Jørgen Christensen-Dalsgaard, Christoffer Karoff, Torben Arentoft, Frank Grundahl, Rasmus Handberg and Søren Frandsen. A word of appreciation goes also to the people with whom I had the privilege of maintaining close collaborations, namely, Tim Bedding, Bill Chaplin, Thierry Appourchaux, Rafa García, Savita Mathur, Vichi Antoci and Othman Benomar.

I should also acknowledge the *Fundação para a Ciência e a Tecnologia* for the financial support provided in the course of my research work.

Porto, 30 October 2011

Contents

List of Publications

Refereed papers

- Benomar, O., Baudin, F., Campante, T. L., et al. 2009, A&A, 507, L13
  URL: `http://adsabs.harvard.edu/abs/2009A%26A...507L..13B`
- Bedding, T. R., Kjeldsen, H., Campante, T. L., et al. 2010, ApJ, 713, 935
  URL: `http://adsabs.harvard.edu/abs/2010ApJ...713..935B`
- Chaplin, W. J., Appourchaux, T., Elsworth, Y., et al. 2010, ApJ, 713, L169
  URL: `http://adsabs.harvard.edu/abs/2010ApJ...713L.169C`
- Bedding, T. R., Huber, D., Stello, D., et al. 2010, ApJ, 713, L176
  URL: `http://adsabs.harvard.edu/abs/2010ApJ...713L.176B`
- Campante, T. L., Karoff, C., Chaplin, W. J., et al. 2010, MNRAS, 408, 542
  URL: `http://adsabs.harvard.edu/abs/2010MNRAS.408..542C`
- de Meulenaer, P., Carrier, F., Miglio, A., et al. 2010, A&A, 523, A54
  URL: `http://adsabs.harvard.edu/abs/2010A%26A...523A..54D`
- Metcalfe, T. S., Monteiro, M. J. P. F. G., Thompson, M. J., et al. 2010, ApJ, 723, 1583
  URL: `http://adsabs.harvard.edu/abs/2010ApJ...723.1583M`
- Bazot, M., Ireland, M. J., Huber, D., et al. 2011, A&A, 526, L4
  URL: `http://adsabs.harvard.edu/abs/2011A%26A...526L...4B`
- Handberg, R. & Campante, T. L. 2011, A&A, 527, A56
  URL: `http://adsabs.harvard.edu/abs/2011A%26A...527A..56H`

LIST OF PUBLICATIONS

- Chaplin, W. J., Kjeldsen, H., Christensen-Dalsgaard, J., et al. 2011, Science, 332, 213
  URL: `http://adsabs.harvard.edu/abs/2011Sci...332..213C`
- Chaplin, W. J., Kjeldsen, H., Bedding, T. R., et al. 2011, ApJ, 732, 54
  URL: `http://adsabs.harvard.edu/abs/2011ApJ...732...54C`
- Chaplin, W. J., Bedding, T. R., Bonanno, A., et al. 2011, ApJ, 732, L5
  URL: `http://adsabs.harvard.edu/abs/2011ApJ...732L...5C`
- Ballot, J., Gizon, L., Samadi, R., et al. 2011, A&A, 530, A97
  URL: `http://adsabs.harvard.edu/abs/2011A%26A...530A..97B`
- Mathur, S., Handberg, R., Campante, T. L., et al. 2011, ApJ, 733, 95
  URL: `http://adsabs.harvard.edu/abs/2011ApJ...733...95M`
- Silva Aguirre, V., Chaplin, W. J., Ballot, J., et al. 2011, ApJ, 740, L2
  URL: `http://adsabs.harvard.edu/abs/2011ApJ...740L...2S`
- Campante, T. L., Handberg, R., Mathur, S., et al. 2011, A&A, 534, A6
  URL: `http://adsabs.harvard.edu/abs/2011A%26A...534A...6C`
- Verner, G. A., Chaplin, W. J., Basu, S., et al. 2011, ApJ, 738, L28
  URL: `http://adsabs.harvard.edu/abs/2011ApJ...738L..28V`
- Verner, G. A., Elsworth, Y., Chaplin, W. J., et al. 2011, MNRAS, 415, 3539
  URL: `http://adsabs.harvard.edu/abs/2011MNRAS.415.3539V`
- Antoci, V., Handler, G., Campante, T. L., et al. 2011, Nature, 477, 570
  URL: `http://adsabs.harvard.edu/abs/2011Natur.477..570A`
- White, T. R., Bedding, T. R., Stello, D., et al. 2011, ApJ, 742, L3
  URL: `http://adsabs.harvard.edu/abs/2011ApJ...742L...3W`
- Huber, D., Bedding, T. R., Stello, D., et al. 2011, ApJ, 743, 143
  URL: `http://adsabs.harvard.edu/abs/2011ApJ...743..143H`
- Creevey, O. L., Doğan, G., Frasca, A., et al. 2012, A&A, 537, A111
  URL: `http://adsabs.harvard.edu/abs/2012A%26A...537A.111C`

- Appourchaux, T., Benomar, O., Gruberbauer, M., et al. 2012, A&A, 537, A134
  URL: `http://adsabs.harvard.edu/abs/2012A%26A...537A.134A`

- Howell, S. B., Rowe, J. F., Bryson, S. T., et al. 2011, ApJ, 746, 123
  URL: `http://adsabs.harvard.edu/abs/2012ApJ...746..123H`

Peer-reviewed conference proceedings

- Doğan, G., Bonanno, A., Bedding, T. R., et al. 2010, Astronomische Nachrichten, 331, 949
  URL: `http://adsabs.harvard.edu/abs/2010AN....331..949D`

- Karoff, C., Chaplin, W. J., Appourchaux, T., et al. 2010, Astronomische Nachrichten, 331, 972
  URL: `http://adsabs.harvard.edu/abs/2010AN....331..972K`

Preprints

- Mathur, S., Metcalfe, T. S., Woitaszek, M., et al. 2012, ApJ, in press [arXiv:1202.2844v1]
  URL: `http://arxiv.org/abs/1202.2844`

- García, R. A., Ceillier, T., Campante, T. L., et al. 2011, Astronomical Society of the Pacific, in press [arXiv:1109.6488v1]
  URL: `http://arxiv.org/abs/1109.6488`

- Mathur, S., Campante, T. L., Handberg, R., et al. 2011, Astronomical Society of the Pacific, in press [arXiv:1110.0135v1]
  URL: `http://arxiv.org/abs/1110.0135`

Conference proceedings without referee

- Campante, T. L., Grigahcène, A., Suárez, J. C., et al. 2010, Astronomische Nachrichten, in press [arXiv:1003.4427v1]
  URL: `http://arxiv.org/abs/1003.4427`

LIST OF PUBLICATIONS

- Karoff, C., Campante, T. L., & Chaplin, W. J. 2010, Astronomische Nachrichten, in press [arXiv:1003.4167v1]
  URL: `http://arxiv.org/abs/1003.4167`

List of Figures

List of Tables

Chapter 1

Asteroseismology of solar-like stars

This chapter introduces the field of asteroseismology of solar-like stars by presenting and discussing a series of key concepts that are essential for a complete understanding of the remaining of this dissertation. Following a brief historical account of the field of asteroseismology, an overview of the origin and nature of stellar pulsations is presented to the reader. The basic properties of oscillation modes are discussed next, before particular attention is paid to the process of stochastic excitation of oscillations and to the potential of asteroseismic inference. The chapter ends with summaries of the main observational techniques used in the field and of its observational status.

The current chapter is by no means intended as a thorough review of the field. To serve that purpose I would strongly recommend the book by Aerts et al. (2010), J. Christensen-Dalsgaard's *Lecture Notes on Stellar Oscillations*[1], and the reviews by Christensen-Dalsgaard (2004), Cunha et al. (2007) and Bedding (2011), on which the following discussion is somewhat based.

1.1 A brief encounter with history

The longest known case of a pulsating star is that of *o* Ceti (Mira), the discovery of its variability being attributed to a Lutheran pastor and amateur astronomer named David Fabricius in 1596 (e.g., Hoffleit 1997). The star was then practically forgotten

---

[1] `http://users-phys.au.dk/jcd/oscilnotes/`

until Johann Fokkens Holwarda rediscovered it in 1638 and found that its magnitude varied periodically with a period of eleven months. By the time of the second centennial of its discovery, 1796, eleven variables had been discovered, four of them of the Mira type. However, firm establishment that such variability is in many cases due to intrinsic stellar pulsations came only in the twentieth century. In this regard Shapley (1914) wrote: "The main conclusion is that the Cepheid and cluster variables are not binary systems, and that the explanation of their light-changes can much more likely be found in a consideration of internal or surface pulsations of isolated stellar bodies."

Early studies of pulsating stars were obviously restricted to large-amplitude pulsators such as the Cepheids and the long-period variables. The simple pulsatory behavior of these stars was interpreted in terms of pulsations in the fundamental radial mode, characterized by expansion of the star followed by its contraction, while preserving spherical symmetry. The discovery of the period-luminosity relation for the Cepheids by Henrietta Swan Leavitt (Leavitt 1908; Leavitt & Pickering 1912) supplied the foundation for the measurement of extragalactic distances. The decades that followed saw emphasis being placed on understanding the mechanism driving the pulsations, which would first be arrived at independently by Cox & Whitney (1958) and Zhevakin (1963). The latter reference provides a review of the early developments of such studies.

The first detections of the oscillatory motion in the atmosphere of the Sun (as local modes), with periods of approximately five minutes, were made in the early 1960s by Leighton et al. (1962), paving the way for the development of helioseismology, by then an entire new field of research. The first detection and identification of these oscillations as global modes is attributed to Claverie et al. (1979). Helioseismology has ever since proved to be extremely successful in probing the physics and dynamics of the solar interior. The vast amount of data on solar oscillations made available in the last two decades led to a considerably accurate determination of the solar sound speed, detailed testing of the equation of state and inference of the solar internal rotation (e.g., Christensen-Dalsgaard 2002; Basu & Antia 2008; Chaplin & Basu 2008; Howe 2009, and references therein).

The Sun is, however, a single star at a specific evolutionary stage, and it is further structurally simple if compared with certain other stars. A logical consequence was therefore the advent of asteroseismology, whereby one would expect to be able to probe the interiors of stars other than the Sun through the use of their intrinsic oscillations. The limited spatial resolution with which we can observe distant stars poses, however, a serious obstacle. Moreover, the very small number of oscillation frequencies observed for most of the pulsating stars renders them unsuitable for the pursuit of asteroseismic studies. Nonetheless, the field thrived and we are today able to proudly answer Sir Arthur Eddington's famous lament (Eddington 1926): "What appliance can pierce through the outer layers of a star and test the conditions within?"

The definite detection of solar-like oscillations in stars other than the Sun had long been an illusory goal due to their very small amplitudes, particularly for main-sequence stars. However, the development of very stable techniques for radial-velocity observations, promoted by the hunt for extrasolar planets, produced a major breakthrough in the field by the turn of the millennium and led to the detection of solar-like oscillations in several stars (e.g., Bedding & Kjeldsen 2003). That was only the beginning of an exciting and successful journey.

1.2 Overview of the origin and nature of stellar pulsations

In order to conduct an asteroseismic study and to fully explore the diagnostic potential of the observed oscillations, one has to understand first their origin and physical nature. A relevant timescale in understanding the properties of oscillations is the dynamical timescale:

$$t_{\rm dyn} = \left(\frac{R^3}{GM}\right)^{1/2} \propto (G\,\overline{\rho})^{-1/2} \ , \tag{1.1}$$

where R and M are the surface radius and mass of the star, respectively, G is the gravitational constant, and $\overline{\rho}$ is the mean stellar density. The periods of the oscillations generally scale as $t_{\rm dyn}$. More specifically, $t_{\rm dyn}$ expresses the time the star needs to go back into hydrostatic equilibrium whenever some dynamical process disrupts the balance between pressure and gravitational force. Pressure modes (see below) may be the cause of such a disturbance and so their oscillation periods should not exceed $t_{\rm dyn}$. It is remarkable how the measurement of a period of oscillation immediately provides us with an estimate of an intrinsic property of the star, namely, its mean density.

Many stars, including the Sun, pulsate in more complex ways than the Cepheids do, being ubiquitous for more than one mode of oscillation to be excited simultaneously.

These modes may include radial overtones, in addition to the fundamental radial mode, as well as non-radial modes, whose motion does not preserve spherical symmetry.

The physical nature of the oscillations concerns the restoring force at play: modes are of the nature of either standing acoustic waves (p modes) with pressure acting as the restoring force or internal gravity waves (g modes; these are exclusively non-radial modes) with buoyancy acting as the restoring force. There is a clear separation between these two classes of modes in unevolved stars. This, however, may not be the case in evolved stars. Due to strong internal gradients in the chemical composition or large gravitational acceleration in a compact core, modes of mixed p- and g-mode character may occur in evolved stars. In addition, the Sun also displays surface gravity waves of large horizontal wave number (f modes).

When talking about their origin, one means the mechanism responsible for driving the oscillations. Oscillations can be either intrinsically unstable or intrinsically stable. In the former case, oscillations result from the amplification of small disturbances by means of a heat-engine mechanism converting thermal into mechanical energy in a specific region of the star, usually a radial layer. This region is heated up during the compressional phase of the pulsation cycle while being cooled off during expansion. An amplitude-limiting mechanism then sets in at some point, determining the final amplitude of the growing disturbance. Such a region inside the star is typically associated with opacity (κ) features and the resulting driving mechanism is thus known as the κ mechanism. The κ mechanism is responsible for the oscillatory behavior in Cepheids, RR Lyrae stars, δ Sct stars, β Cep stars, and in most of the pulsating classes displayed in Fig. 1.1. A particularly important area depicted in that figure is the Cepheid (or classical) instability strip, where pulsating class members are believed to have their oscillations driven by an opacity mechanism associated with the second helium-ionization zone. In order to cause overall excitation of the oscillations, the region associated with the driving has to be placed at an appropriate depth inside the star, thus providing an explanation for the specific location of the resulting instability belt in the H-R diagram. This type of oscillations are generally known as classical oscillations.

On the other hand, intrinsically stable oscillations, such as the solar five-minute oscillations, are stochastically excited by the vigorous near-surface convection. This type of oscillations, having first been detected in the Sun, are referred to as solar-like oscillations. Solar-like oscillations are predicted for all stars cool enough to harbor an outer convective envelope, and are thus found among main-sequence core, and post-main-sequence shell, hydrogen-burning stars, residing on the cool side of the Cepheid instability strip. Besides main-sequence stars with masses up to about $1.5\mathrm{M}_\odot$, solar-like oscillations are also expected to occur from the end of the main sequence up to the giant and asymptotic giant branches. The resulting mode amplitudes are considerably smaller than those generally found in classical pulsators. However, the stochastic process is characterized by varying slowly with frequency and hence modes tend to be excited to comparable amplitudes within a substantial frequency range. This happens in contrast to the distribution of mode amplitudes of classical pulsators which is highly irregular over the range of unstable modes.

1.3 Basic properties of oscillation modes

1.3.1 Describing the oscillations

Small-amplitude oscillations of a spherically symmetric star depend on co-latitude θ and longitude ϕ in terms of a spherical harmonic $Y_l^m(\theta, \phi)$. Use is made of spherical polar coordinates, (r, θ, ϕ), where r is the distance to the center of the star. The degree l specifies the number of nodal surface lines, i.e., the complexity of the mode, better understood by defining the surface horizontal wave number, $k_\mathrm{h}^{(\mathrm{surf})}$:

$$k_\mathrm{h}^{(\mathrm{surf})} = \frac{\sqrt{l(l+1)}}{R} \, . \tag{1.2}$$

Radial modes have $l = 0$, whereas for non-radial modes $l > 0$. The azimuthal order is represented by m, with $|m|$ specifying how many of the nodal surface lines are lines of longitude. Values of m range from $-l$ to l, and thus there are $2l + 1$ modes for each multiplet of degree l. Figure 1.2 illustrates the appearance of the $l = 3$ octupole modes on a stellar surface. Modes are additionally characterized by the radial order n, which is related to the number of radial nodes.

As an example of an eigenfunction, I introduce the radial component of displacement which may be expressed as

$$\xi_r(r, \theta, \phi; t) = \Re\left\{a(r)\, Y_l^m(\theta, \phi)\, \exp(-\mathrm{i}\, 2\pi\nu t)\right\} \, , \tag{1.3}$$

where $a(r)$ is an amplitude function, and ν is the (cyclic) frequency of oscillation. For a spherically symmetric star the frequency of oscillation depends only on n and l, i.e.,

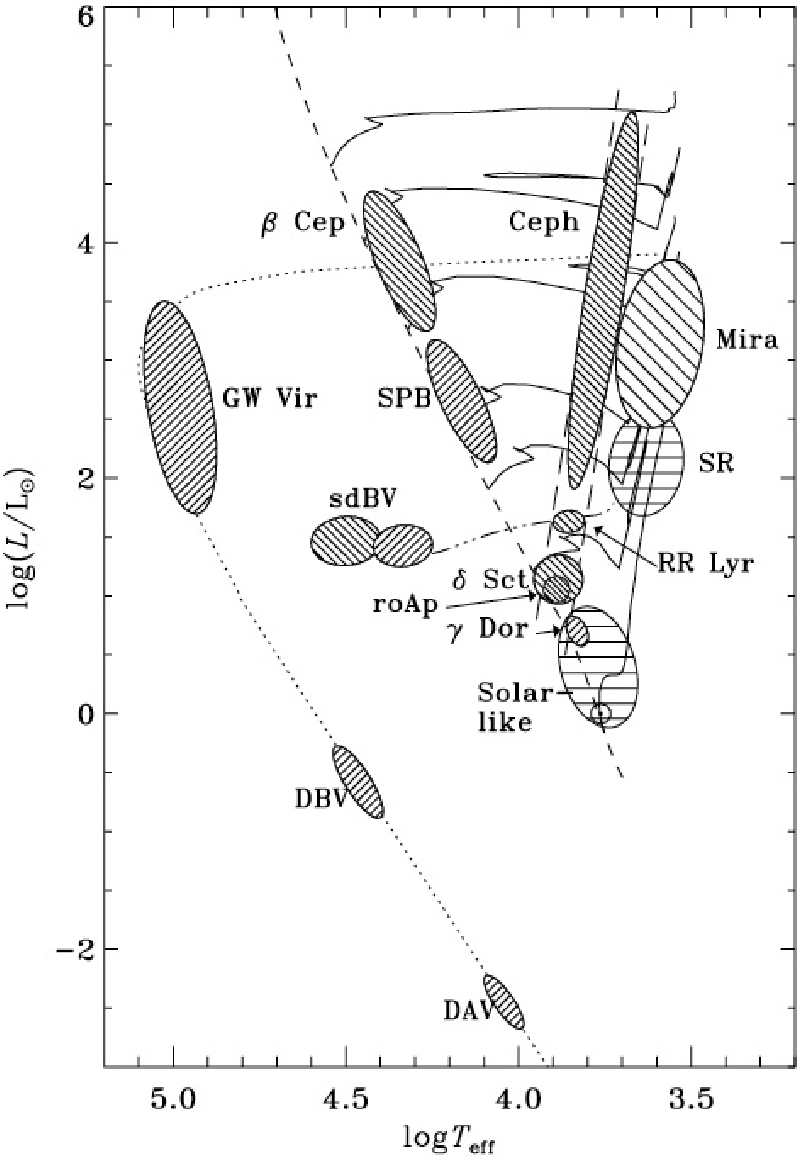

Figure 1.1: Pulsating stars across the Hertzsprung-Russell diagram - Several classes of pulsating stars, for which asteroseismology is possible, have been located. T_{eff} and L are the effective temperature and stellar luminosity, respectively. The dashed line indicates the zero-age main sequence (ZAMS), the solid curves represent selected evolutionary tracks (for 1, 2, 3, 4, 7, 12, and 20 $\mathrm{M}_{\odot}$), the triple-dot-dashed line indicates the horizontal branch and the dotted curve follows the white-dwarf cooling track. The parallel long-dashed lines enclose the Cepheid instability strip. From Bedding et al. (2007a).

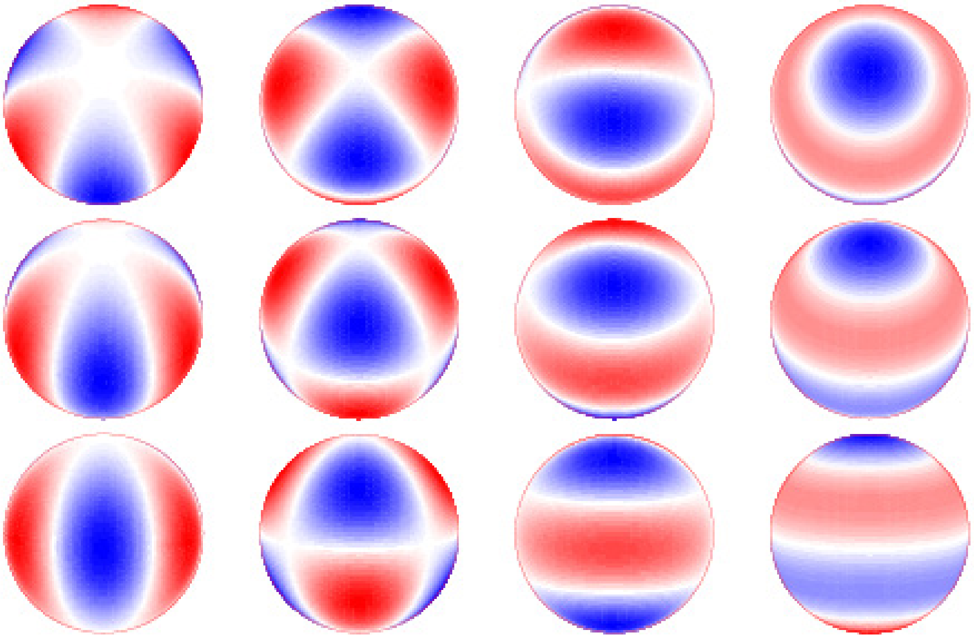

Figure 1.2: Freeze-frame of the radial component of the $l = 3$ octupole modes - Rows display the same modes although with different inclination angles of the polar axis with respect to the line of sight: 30° (top row), 60° (middle row), and 90° (bottom row). White bands represent the nodal surface lines. Red and blue sections represent portions of the stellar surface that are moving in and out, respectively. The rightmost column displays the axisymmetric (i.e., with $m = 0$) mode ($l = 3, m = 0$). From right to left, the middle columns display the tesseral (i.e., with $0 < |m| < l$) modes ($l = 3, m = \pm 1$) and ($l = 3, m = \pm 2$). The leftmost column displays the sectoral (i.e., with $|m| = l$) mode ($l = 3, m = \pm 3$). Figure courtesy of Conny Aerts.

$\nu = \nu_{nl}$. The spherical harmonic $Y_l^m(\theta, \phi)$ is expressed as

$$Y_l^m(\theta, \phi) = (-1)^m \, c_{lm} \, P_l^m(\cos\theta) \, \exp(\mathrm{i}\, m\phi) \, , \tag{1.4}$$

where P_l^m is an associated Legendre function given by

$$P_l^m(\cos\theta) = \frac{1}{2^l l!} \, (1 - \cos^2\theta)^{m/2} \, \frac{\mathrm{d}^{l+m}}{\mathrm{d}\cos^{l+m}\theta} (\cos^2\theta - 1)^l \, , \tag{1.5}$$

and the normalization constant c_{lm} is determined by

$$c_{lm}^2 = \frac{(2l+1)(l-m)!}{4\pi(l+m)!} \, , \tag{1.6}$$

such that the integral of $|Y_l^m|^2$ over the unit sphere is unity.

1.3.2 Spatial filtering

Unlike the case of the Sun, for which modes of very high degree l can be observed, we have not yet reached the stage where we can resolve stellar surfaces using either velocity or intensity observations. In the stellar case our observations actually result from weighted averages of the pulsation amplitude over the stellar disk. Consequently, modes of moderate and high degree l, and hence of increasing complexity, tend to average out in what is known as partial cancellation or spatial filtering. Particularly for solar-like oscillations, whose intrinsic amplitudes are rather low, this means that only modes of the lowest degree, i.e., with $l \leq 3$, are expected to be observed. Furthermore, in the case of velocity observations, the projection of the velocity onto the line of sight introduces an extra factor of $\cos\theta$ in the weighting function. This effectively gives more sensitivity to the center of the disk relative to the limb, ultimately resulting in a slightly larger response to modes of $l=3$ than for intensity observations.

The preceding considerations can be supported by very simple calculations. Assuming the case of surface-integrated intensity of an axisymmetric mode over the stellar disk, while neglecting the effects of limb darkening and rotation, the spatial response function $S_l^{(\mathrm{I})}$ is then given by

$$S_l^{(\mathrm{I})} = 2\sqrt{2l+1} \int_0^{\pi/2} P_l^0(\cos\theta) \cos\theta \sin\theta \, \mathrm{d}\theta \,. \tag{1.7}$$

A similar calculation can be carried out for the case of velocity observations and assuming that the velocity field is predominantly in the radial direction, giving

$$S_l^{(\mathrm{V})} = 2\sqrt{2l+1} \int_0^{\pi/2} P_l^0(\cos\theta) \cos^2\theta \sin\theta \, \mathrm{d}\theta \,. \tag{1.8}$$

The spatial response functions $S_l^{(\mathrm{I})}$ and $S_l^{(\mathrm{V})}$ are plotted in Fig. 1.3 as a function of l.

Kjeldsen et al. (2008a) provide spatial responses to modes with degree l relative to those with $l=0$ for a set of intensity and velocity observations (see their table 1). Radial modes make a sensible reference since they are not split by rotation, as will be seen in Sect. 1.3.5. Those ratios were computed using the results of Christensen-Dalsgaard (1989) and Bedding et al. (1996). Particularly useful is the latter work, where the authors provide approximate expressions for computing the spatial response functions taking into account the effect of limb darkening. Those expressions are, however, only valid in the case of a slow rotator. Recently, Salabert et al. (2011) provided precise

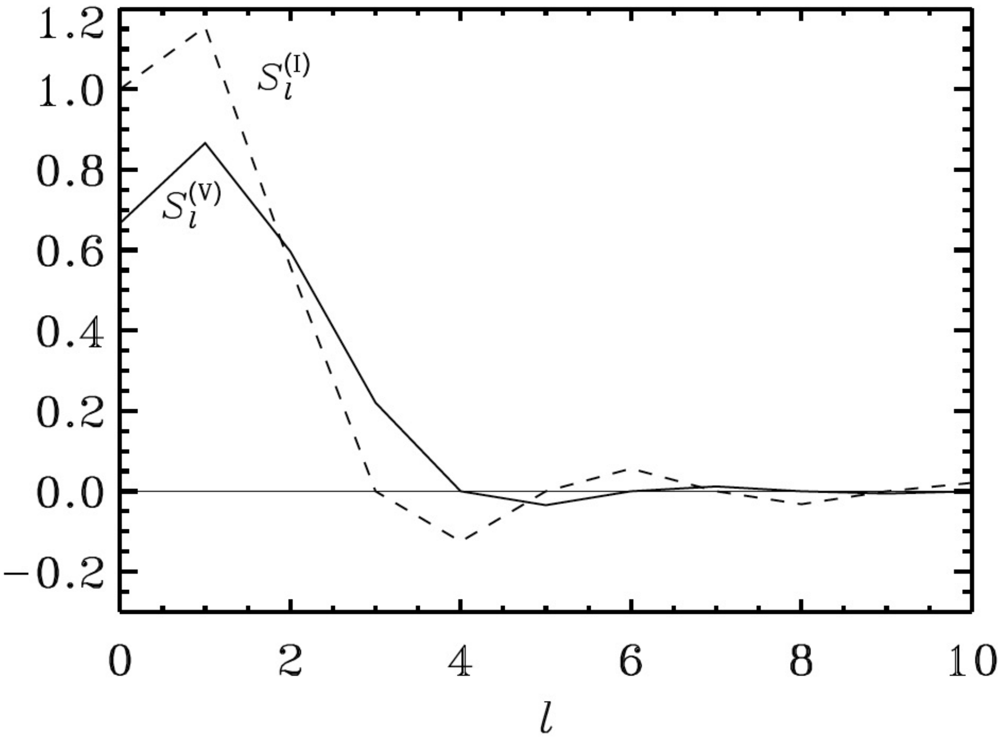

Figure 1.3: Spatial response functions - $S_l^{(\mathrm{I})}$ and $S_l^{(\mathrm{V})}$ for surface-integrated intensity and velocity, respectively, are plotted as a function of l. Negative values of either quantity mean that the oscillations will appear to have reversed phases. Figure courtesy of J. Christensen-Dalsgaard.

estimates of mode visibilities for radial-velocity and photometric observations of the Sun-as-a-star (i.e., whole-disk observations of the Sun), further comparing them to theoretical predictions.

Table 1.1 displays the relative spatial response functions S_l/S_0, computed according to Bedding et al. (1996), for a number of present and upcoming instruments/missions used to measure solar-like oscillations. Those performing intensity measurements are the red channel of the VIRGO/SPM instrument (Fröhlich et al. 1995, 1997) on board the *SOHO* spacecraft, as well as the *CoRoT* (Baglin et al. 2006) and NASA *Kepler* (Borucki et al. 2010; Koch et al. 2010) space missions. On the other hand, radial-velocity measurements are performed by the HARPS spectrograph (Mayor et al. 2003) and are the purpose of the forthcoming SONG network (Grundahl et al. 2009a,b).

Table 1.1: Relative spatial response functions S_l/S_0 - These are given for a number of present and upcoming instruments/missions.

	Intensity			Velocity	
	VIRGO/SPM (862 nm)	*CoRoT* (660 nm)	*Kepler* (641 nm)	HARPS (535 nm)	SONG (550 nm)
S_0/S_0	1.00	1.00	1.00	1.00	1.00
S_1/S_0	1.20	1.22	1.22	1.35	1.35
S_2/S_0	0.67	0.70	0.71	1.02	1.01
S_3/S_0	0.10	0.14	0.14	0.48	0.47
S_4/S_0	−0.10	−0.09	−0.08	0.09	0.09

1.3.3 Understanding the behavior of mode eigenfunctions

The diagnostic potential of the oscillation frequencies can be better understood through asymptotic analyses of the oscillation equations. This sort of approach approximates these equations to such an extent that they can be discussed analytically. The fact that a reasonable number of classes of pulsating stars display high-order acoustic or gravity modes justifies employing an asymptotic analysis.

An approximate asymptotic description of the oscillation equations has been derived by D. O. Gough (Deubner & Gough 1984; Gough 1986, 1993), on the basis of an earlier work by Lamb (1932):

$$\frac{\mathrm{d}^2X}{\mathrm{d}r^2} + K(r)X = 0\,, \tag{1.9}$$

where

$$K(r) = \frac{\omega^2}{c^2}\left[1 - \frac{\omega_\mathrm{c}^2}{\omega^2} - \frac{S_l^2}{\omega^2}\left(1 - \frac{N^2}{\omega^2}\right)\right]\,, \tag{1.10}$$

and

$$X = c^2\rho^{1/2}\,\mathrm{div}\,\delta\mathbf{r}\,. \tag{1.11}$$

The adiabatic sound speed, c, is given by $c^2 = \Gamma_1\,p/\rho$, p being pressure, and $\Gamma_1 = (\partial\ln p/\partial\ln\rho)_\mathrm{ad}$ being the adiabatic exponent relating pressure and density; $\delta\mathbf{r}$ is the displacement vector in the last equation. The behavior of the eigenfunction of a mode is determined by three characteristic (angular) frequencies varying throughout the star: the acoustic (S_l), the buoyancy (N), and the acoustic cut-off (ω_c) frequencies (cf. Eq. 1.10). Figure 1.4 displays the three characteristic frequencies as a function of fractional radius for a set of selected stellar models.

The acoustic (or Lamb) frequency[1] S_l is determined by

$$S_l^2 = \frac{l(l+1)\,c^2}{r^2}\,, \tag{1.12}$$

being interpreted as the frequency of a sound wave traveling horizontally with local wave number $k_\mathrm{h} = \sqrt{l(l+1)}/r$.

The buoyancy (or Brunt-Väisälä) frequency N is determined by

$$\begin{aligned} N^2 &= g\left(\frac{1}{\Gamma_1}\frac{\mathrm{d}\ln p}{\mathrm{d}r} - \frac{\mathrm{d}\ln\rho}{\mathrm{d}r}\right) \\ &\approx \frac{g^2\rho}{p}\left(\nabla_\mathrm{ad} - \nabla + \nabla_\mu\right)\,, \end{aligned} \tag{1.13}$$

where g is the local gravitational acceleration. To obtain the second equality, the gas has been regarded as a fully-ionized ideal gas and the effects of degeneracy and radiation pressure, as well as of Coulomb interactions, have been neglected. This constitutes a fairly good approximation in much of the interior of the majority of stars. The resulting simple equation of state, $p = \rho\, k_\mathrm{B}T/\mu m_\mathrm{u}$, where k_B is Boltzmann's constant, μ is the mean molecular weight, and m_u is the atomic mass unit, then leads to

$$c = \sqrt{\frac{\Gamma_1\, k_\mathrm{B}T}{\mu\, m_\mathrm{u}}}\,, \tag{1.14}$$

with the sound speed depending on the temperature and chemical composition of the gas. Moreover,

$$\nabla = \frac{\mathrm{d}\ln T}{\mathrm{d}\ln p}\,, \quad \nabla_\mathrm{ad} = \left(\frac{\partial \ln T}{\partial \ln p}\right)_\mathrm{ad}\,, \quad \nabla_\mu = \frac{\mathrm{d}\ln\mu}{\mathrm{d}\ln p}\,. \tag{1.15}$$

For $N^2 > 0$, N can be interpreted as the frequency of a gas element of reduced horizontal extent which oscillates due to buoyancy. Conversely, regions for which $N^2 < 0$ satisfy the Ledoux criterion of convective instability, i.e.,

$$\nabla > \nabla_\mathrm{ad} + \nabla_\mu\,. \tag{1.16}$$

Gravity waves cannot, therefore, propagate in convective regions.

The acoustic cut-off frequency ω_c is determined by

$$\omega_\mathrm{c}^2 = \frac{c^2}{4H_\rho^2}\left(1 - 2\frac{\mathrm{d}H_\rho}{\mathrm{d}r}\right)\,, \tag{1.17}$$

---

[1] Note that both the Lamb frequency and the spatial response function are represented by S_l. However, with attention to context, this should not result in confusion.

where $H_\rho = -(\mathrm{d}\ln\rho/\mathrm{d}r)^{-1}$ is the density scale height. In an isothermal atmosphere, H_ρ is constant, and thus $\omega_\mathrm{c} = c/(2H_\rho)$. In the solar atmosphere, $H_\rho \approx 120\mathrm{km}$, corresponding to a (cyclic) cut-off frequency of about 5mHz, or a period of 3 minutes. A useful relation, describing the behavior of the acoustic cut-off frequency (in units of $\omega_\mathrm{dyn} = 2\pi/t_\mathrm{dyn}$) as a function of the stellar parameters, is given by

$$\frac{\omega_\mathrm{c}}{\omega_\mathrm{dyn}} \propto \left(\frac{M}{\mathrm{M}_\odot}\right)^{1/2} \left(\frac{L}{\mathrm{L}_\odot}\right)^{-1/4} \left(\frac{T_\mathrm{eff}}{\mathrm{T}_{\mathrm{eff},\odot}}\right)^{1/2} . \tag{1.18}$$

The eigenfunction of a mode oscillates as a function of r in regions satisfying $K(r) > 0$, where it is said to be propagating. Conversely, in regions satisfying $K(r) < 0$, the eigenfunction behaves exponentially, and it is said to be evanescent. Finally, the location of the turning points of the eigenfunction are determined by $K(r) = 0$. Typically, the eigenfunction has large amplitude in just one, dominant, propagating region, with the solution decaying exponentially away from it. This region, where the mode is said to be trapped, will then determine the eigenfrequency according to suitable phase relations at its boundaries.

Let us start off with the superficial layers. Here, typically $\omega \gg S_l$ and the behavior of the eigenfunction is thus controlled by ω_c; the role of ω_c is, nonetheless, minor in the remaining of the star, where the properties of the eigenfunction are effectively controlled by S_l and N. Modes with frequency below the atmospheric value of ω_c or, equivalently, with wavelength exceeding the density scale height, decay exponentially in the atmosphere, being reflected back and hence ending up trapped inside the star.

In unevolved stars (e.g., the Sun) the buoyancy frequency N remains at relatively low values throughout the star, in which case the behavior of a high-frequency mode is mostly controlled by S_l. The eigenfunction of such a mode will be trapped between the near-surface reflection determined by $\omega = \omega_\mathrm{c}$ and an inner turning point located where $S_l(r_\mathrm{t}) = \omega$, or

$$\frac{c^2(r_\mathrm{t})}{r_\mathrm{t}^2} = \frac{\omega^2}{l(l+1)} , \tag{1.19}$$

with r_t being determined by l and ω. These are p modes, and so are the solar five-minute oscillations. For p modes, typically $\omega \gg N$, and K may thus be approximated by

$$K(r) \approx \frac{1}{c^2}(\omega^2 - S_l^2) . \tag{1.20}$$

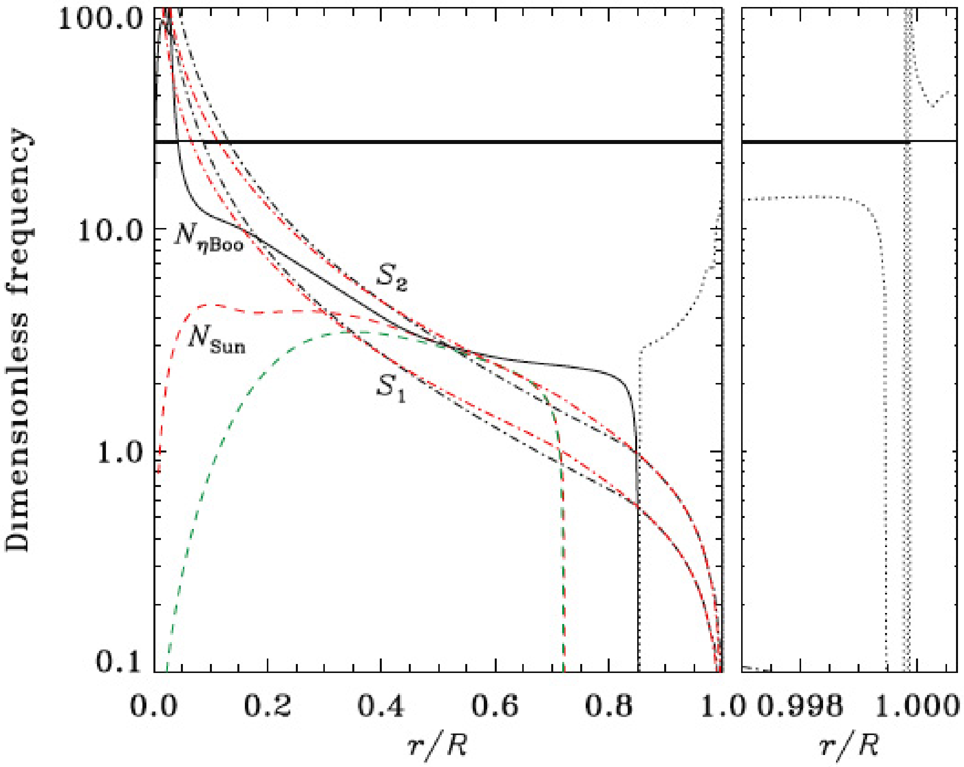

Figure 1.4: Dimensionless characteristic frequencies - The characteristic frequencies are given, in units of ω_{dyn} and as a function of the fractional stellar radius, for a 1-$\mathrm{M}_{\odot}$ ZAMS model, a model of the present Sun and a model of η Boo (a 1.63-$\mathrm{M}_{\odot}$ subgiant in the shell hydrogen-burning phase). Dot-dashed lines represent S_l, for $l = 1$ and $l = 2$, in the solar model (red) and the model of η Boo (black), being barely indistinguishable. The buoyancy frequency N is represented – except for the atmosphere – by a dashed line in the ZAMS model (green) and the solar model (red), and by a solid line in the model of η Boo. The dotted line represents ω_{c} in the model of η Boo from the base of the convective envelope outward. The horizontal line represents the frequency of a stochastically-excited $l = 1$ mode in the model of η Boo, being thicker in regions where the mode propagates (see discussion in the text). From Cunha et al. (2007).

In this approximation, the dynamics of the p modes is therefore solely determined by the variation of the sound speed with r. From Eq. (1.19) it turns out that, for low-degree modes, r_{t} is small, meaning that those modes will sample most of the stellar interior. Radial p modes, in particular, travel all the way to the center of the star. Figure 1.5 illustrates the propagation of acoustic waves in a so-called ray plot.

Let us continue looking at the case of an unevolved star. Low-frequency modes

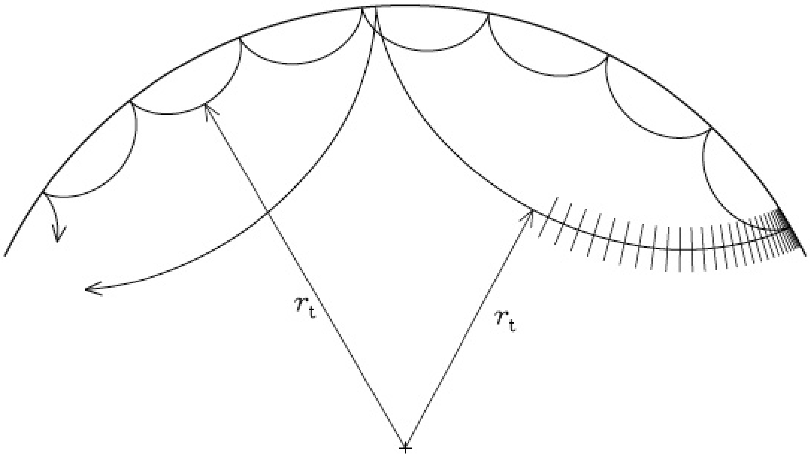

Figure 1.5: Acoustic-ray propagation in a cross-section of the solar interior - A mode with $l = 30$ and $\nu = 3$ mHz penetrates deeper into the Sun than a mode with $l = 100$ and $\nu = 3$ mHz. The lines perpendicular to the ray path of the $l = 30$ mode represent wave fronts. As the acoustic wave propagates into the star, the deeper wave fronts experience a higher sound speed. As a consequence, the ray path is bent away from the radial direction. At the inner turning point waves travel horizontally and undergo total internal refraction. At the surface, the acoustic waves are reflected due to a sudden decrease in density. Figure courtesy of J. Christensen-Dalsgaard.

satisfy $\omega \ll S_l$ throughout most of the stellar radius. Under these circumstances the eingenfunction of a mode oscillates in a region approximately determined by $\omega < N$, and thus to great extent independent of the degree l. These are g modes, having one turning point very near the center of the star and a second one just below the base of the convection zone. For g modes in general $\omega^2 \ll S_l^2$, and K may then be approximated by

$$K(r) \approx \frac{1}{\omega^2}(N^2 - \omega^2)\,\frac{l(l+1)}{r^2}\,. \tag{1.21}$$

It is now obvious that the dynamics is controlled by the variation of N with r.

However, it is evident from Eq. (1.13) and Fig. 1.4 that N may attain very large values in the core of an evolved star. This comes as a result of an increase of the local gravitational acceleration g due to the contraction of the core. Furthermore, strong gradients in the hydrogen abundance may enhance that effect by causing ∇_μ to become a large positive number. Consequently, even at high frequencies close to the atmospheric value of $\omega_{\rm c}$, relevant for stochastic excitation, K may have a positive value both in the envelope where $\omega > S_l, N$ (p-mode behavior), and in the deep interior where $\omega < S_l, N$ (g-mode behavior). This interchangeable physical nature is illustrated in Fig. 1.4 for a stochastically-excited $l = 1$ mixed mode in the model of η Boo. A more detailed discussion on these so-called mixed modes will be presented in Sect. 1.5.3.

1.3.4 p modes and g modes in the Sun

At this stage it is instructive to have a quick look at the eigenfrequencies computed for a model of the present Sun. These are displayed in Fig. 1.6 as a function of degree l. Two distinct, although slightly overlapping, families of modes are obvious, viz., p and g modes. The frequencies of p modes are seen to increase with radial order n and degree l. The frequencies of g modes – also increasing with l – are now seen to decrease with overtone (i.e., with the number of radial nodes $|n|$), while increasing with n[1]. Since buoyancy demands gas motions that are primarily horizontal, there are no radial (i.e., $l = 0$) g modes.

A third family of modes, labeled with $n = 0$, although similar in behavior to the p modes, are in fact physically distinct. They are surface gravity waves and are known as f modes.

1.3.5 The effect of rotation

The dependence of the oscillations on the azimuthal order m has been so far neglected. From Eqs. (1.3) and (1.4) it can be seen that, for $m \neq 0$, the exponentials in both equations combine to give $\exp[-{\rm i}\,(2\pi\nu t - m\phi)]$. The extra phase in this time-dependent term means that modes with $m \neq 0$ are in fact traveling waves; modes formed by waves moving with the rotation of the star are called prograde modes (positive m), while those formed by waves traveling against the rotation of the star are called retrograde modes (negative m).

---

[1] Here, I adopt the convention that n is negative for g modes, with $|n|$ corresponding to the number of radial nodes in the eigenfunction. On the other hand, p modes are assigned positive values of n corresponding to the number of radial nodes.

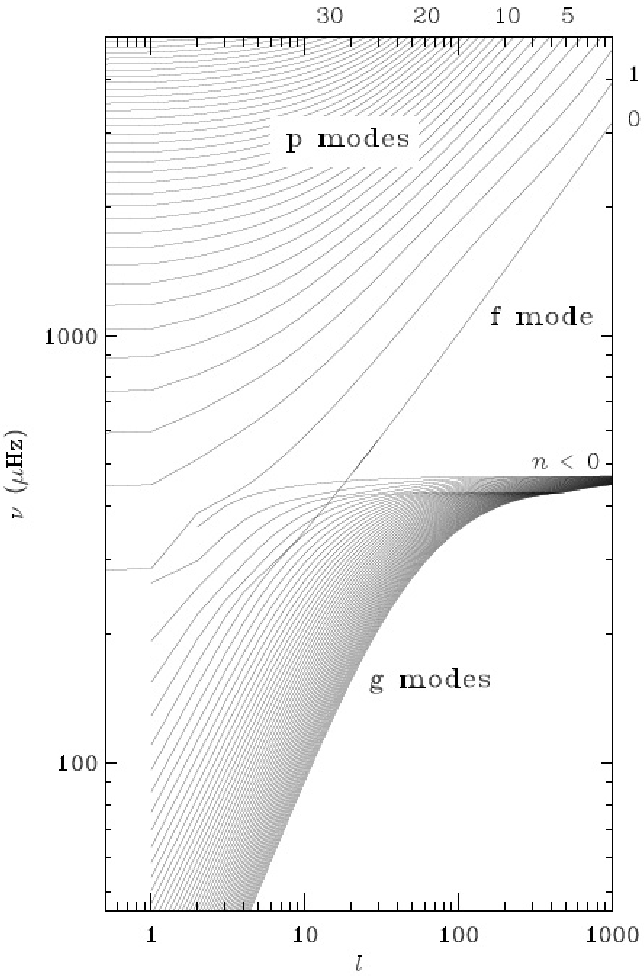

Figure 1.6: Computed eigenfrequencies for a model of the present Sun - Although only integral l have physical meaning, continuous lines are shown for clarity. Selected values of the radial order n are indicated for the p modes. Close inspection tells us that the solar five-minute oscillations are indeed standing acoustic waves, generally of high radial order. Figure courtesy of J. Christensen-Dalsgaard.

As already stated, there are $2l+1$ modes for each multiplet of degree l. Moreover, in the case of a spherically symmetric star, their frequencies will be the same. However, this frequency degeneracy is lifted by departures from spherical symmetry, of which the most notorious physical cause is rotation. Rotation introduces a dependence of the mode frequencies on m, with prograde (retrograde) modes having frequencies slightly higher (lower) than the axisymmetric mode in the observer's frame of reference. For the radial modes one simply cannot see this rotational signature.

When the angular velocity of the star, Ω, is small, as it is expected for most solar-like pulsators, the effect of rotation can be treated following a perturbative analysis. In the case of rigid-body rotation (i.e., $\Omega = \Omega(r)$), the frequency ω_{nlm} of a mode, as observed in an inertial frame, can be expressed to a first order of approximation as (Ledoux 1951):

$$\omega_{nlm} = \omega_{nl0} + m\langle\Omega\rangle_{nl}\,(1 - C_{nl})\,, \tag{1.22}$$

where $\langle\Omega\rangle_{nl}$ is an average of Ω over the stellar interior that depends on the properties of the eigenfunction in the non-rotating star. The kinematic splitting $m\langle\Omega\rangle_{nl}$ is corrected for the effect of the Coriolis force through the dimensionless Ledoux constant, C_{nl}. For high-order acoustic modes $C_{nl} \ll 1$, and the rotational splitting is thus dominated by advection and given by the average angular velocity. With access only to low-degree acoustic modes, limited information can be achieved on the profile of rotation throughout the star. In that instance one would, however, still expect to obtain a measure of the average internal angular velocity. Finally, for high-order g modes $C_{nl} \simeq 1/[l(l+1)]$.

To a second order of approximation, centrifugal effects that disrupt the equilibrium structure of the star are taken into account through an additional frequency perturbation that is independent of the sign of m. This perturbation scales as the ratio of the centrifugal to the gravitational forces at the stellar surface. Although negligible in the Sun, these effects may be significant for faster solar-like rotators. Ballot (2010) alerts to the need of considering second-order effects and, based on the work of Saio (1981), presents an alternative description to that given in Eq. (1.22). Rotation is not the only physical cause behind a departure from spherical symmetry. Other agents, such as large-scale magnetic fields, may introduce additional corrections to the oscillation frequencies.

A way of measuring the inclination angle, i, between the direction of the rotation axis of a solar-like pulsator and the line of sight, is provided by asteroseismology. A knowledge of i is not only important for obtaining improved stellar parameters, but also for determining the true masses of extrasolar planets that have been detected from periodic Doppler shifts seen in the spectra of their host stars. Assuming energy equipartition between multiplet components with different azimuthal order, the dependence of mode power on m is given by (Gizon & Solanki 2003):

$$\mathscr{E}_{lm}(i) = \frac{(l-|m|)!}{(l+|m|)!}\left[P_l^{|m|}(\cos i)\right]^2 . \tag{1.23}$$

Handberg & Campante (2011) present explicit expressions for the computation of $\mathscr{E}_{lm}(i)$ with l ranging from 0 to 4. Sensitivity to multiplet components with different m is essentially a geometrical effect, mainly linked to the limb-darkening function. However, for velocity observations, the rotational shift of the spectral lines across the stellar disk may induce a departure from the description adopted above (Brookes et al. 1978; Christensen-Dalsgaard 1989; Broomhall et al. 2009). I will mention this point again in Sect. 2.2.3.1.

According to Eq. (1.23), when the rotation axis points toward the observer (i.e., $i = 0°$), only the axisymmetric mode is visible and no inference can thus be made of the rotation. In the case of the Sun, on the other hand, whose rotation axis is approximately in the plane of the sky (i.e., $i \approx 90°$), whole-disk observations are essentially sensible only to modes with even $|l-m|$. Figure 1.7 displays the limit power spectra (for a definition see Sect. 1.4.1) of dipole and quadrupole multiplets as a function of the inclination i.

1.4 Stochastic excitation of oscillations

Intrinsically stable oscillations, such as the ones present in stars on the cool side of the Cepheid instability strip, of which the Sun is an example, are thought to be stochastically excited by the vigorous near-surface convection (e.g., Goldreich & Keeley 1977). In these stars, the turbulent convective motion near the surface reaches speeds close to the speed of sound, and consequently acts as an efficient source of acoustic radiation that will excite the normal modes of the star. Houdek (2006) provides a recent review of the process of stochastic excitation in solar-like pulsators.

1.4.1 Power spectrum of a solar-like oscillator

Understanding the characteristics of the power spectrum of a solar-like oscillator is fundamental in order to extract information on the physics of the modes. Batchelor (1953) treated the general problem of the stochastic driving of a damped oscillator.

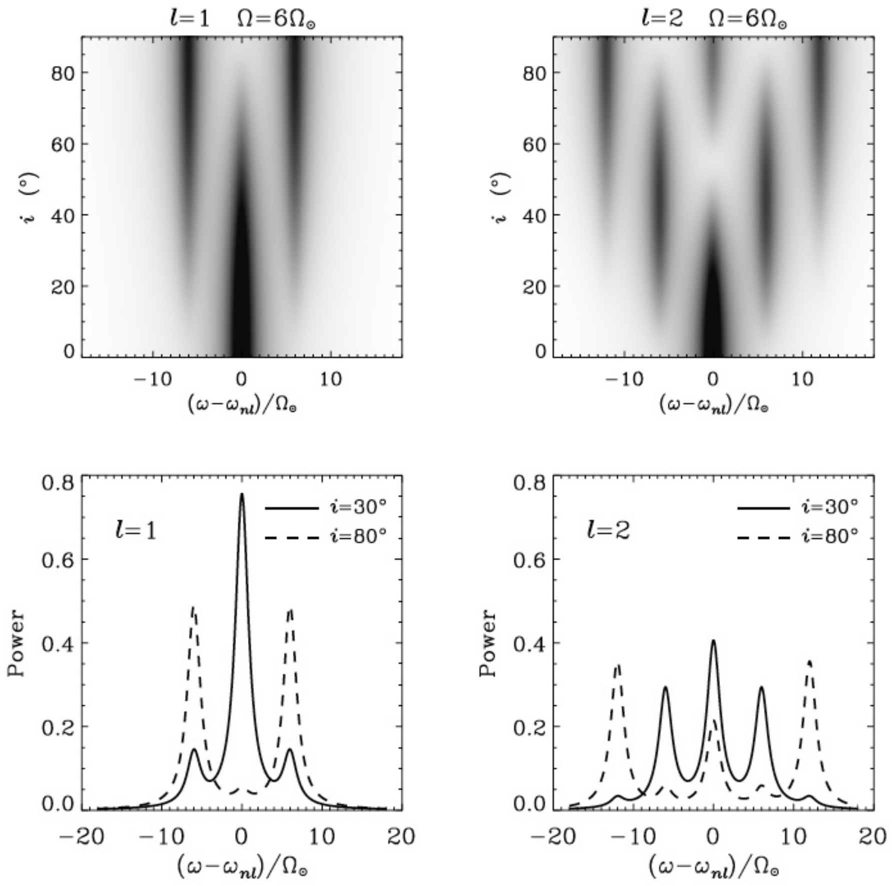

Figure 1.7: Power spectra of dipole and quadrupole multiplets as a function of the inclination i - Limit power spectra, with no background noise added, are displayed in the left-hand panels for a dipole (i.e., $l=1$) multiplet and in the right-hand panels for a quadrupole (i.e., $l=2$) multiplet. Mode linewidths were assigned solar values ($\Gamma_\odot \approx 1\,\mu$Hz; for a definition see Sect. 1.4.3) and the angular velocity is six times solar (where $\Omega_\odot/2\pi \approx 0.5\,\mu$Hz). From Gizon & Solanki (2003).

Such a system can be described by

$$\frac{\mathrm{d}^2}{\mathrm{d}t^2}y(t) + 2\eta\,\frac{\mathrm{d}}{\mathrm{d}t}y(t) + \omega_0^2\,y(t) = f(t)\,, \tag{1.24}$$

where $y(t)$ is the amplitude of the oscillator, η is the linear damping rate, ω_0 is the frequency of the undamped oscillator, and $f(t)$ is a random forcing function. By introducing the Fourier transforms of y and f as

$$Y(\omega) = \int y(t)\,\mathrm{e}^{\mathrm{i}\,\omega t}\mathrm{d}t\,, \quad F(\omega) = \int f(t)\,\mathrm{e}^{\mathrm{i}\,\omega t}\mathrm{d}t\,, \tag{1.25}$$

the Fourier transform of Eq. (1.24) is then expressed as

$$-\,\omega^2\,Y(\omega) - \mathrm{i}\,2\eta\omega\,Y(\omega) + \omega_0^2\,Y(\omega) = F(\omega). \tag{1.26}$$

When a finite realization of the process described by $y(t)$ is observed for a given period of time, long enough so as to fully resolve the resonance, an estimate of the power spectrum (see Fig. 1.8) is then given by

$$P(\omega) = |Y(\omega)|^2 = \frac{|F(\omega)|^2}{(\omega_0^2-\omega^2)^2 + 4\,\eta^2\omega^2}\,. \tag{1.27}$$

The power spectrum of the random forcing function, $|F(\omega)|^2$, is uncorrelated at (angular) frequency separations of $2\pi/T_{\mathrm{obs}}$, with T_{obs} being the total observational span. Furthermore, at a fixed frequency, the spectra of different realizations take values that obey a χ^2 distribution with 2 degrees of freedom[1] (or χ^2_2). Woodard (1984) showed that solar oscillation data are consistent with this distribution.

In the limit of taking the ensemble average of an infinite number of realizations, and further considering that the damping rate is generally very small compared to the frequency of oscillation, one obtains near the resonance (i.e., for $|\omega-\omega_0| \ll \omega_0$) the following expression for the expectation value of the power spectrum (also called limit spectrum; see Fig. 1.8):

$$\langle P(\omega)\rangle \simeq \frac{1}{4\,\omega_0^2}\frac{\langle P_f(\omega)\rangle}{(\omega-\omega_0)^2+\eta^2}\,. \tag{1.28}$$

The average power spectrum of the random forcing function, $\langle P_f(\omega)\rangle$, is expected to be a slowly-varying function of frequency. The result will thus be a Lorentzian profile, characterized by the central frequency ω_0 and a width determined by the linear damping rate η.

However, the fact that the dominant contributions to the driving of the oscillations are restricted to a region of small radial extent, will lead to asymmetries in the mode profiles (e.g., Duvall et al. 1993; Abrams & Kumar 1996). These asymmetries are determined by the relative location of the region responsible for the driving with respect to the resonant cavity. The detection of these asymmetries in the case of the Sun made it possible to estimate the location of the dominant source of mode excitation (e.g., Chaplin & Appourchaux 1999). Moreover, the sign of the asymmetry depends

---

[1] The statistics of the power spectrum of a pure noise signal is derived in Sect. 2.1.5.

upon the observable, an aspect that is related to the different correlation, found in velocity and intensity measurements, between the background stellar noise and the convective excitation of the oscillations (e.g., Nigam et al. 1998). A simple expression for describing an asymmetrical mode profile is given by Nigam & Kosovichev (1998). In principle, similar detections are possible for other stars through the analysis of long and continuous observations with overall high signal-to-noise ratio (SNR).

Very often, one implicitly assumes that the background stellar noise and the convective excitation of the oscillations are statistically uncorrelated stationary processes. In that case, the overall power spectrum is simply given by the sum of the separate power spectra. This is usually a fairly good approximation for solar-like oscillations, meaning that we end up neglecting any asymmetries in the mode profiles. If, however, one assumes that the processes are correlated but that their correlation is stationary, then we should take into account profile asymmetry. Such correlations have been studied by Severino et al. (2001) in the helioseismic context.

1.4.2 Mode excitation

I start by introducing two useful global properties of a mode, namely, its normalized inertia E and its mode mass M_{mode}:

$$E = \frac{M_{\mathrm{mode}}}{M} \equiv \frac{\int_V \rho |\delta \mathbf{r}|^2 \, \mathrm{d}V}{M |\delta \mathbf{r}|^2_{\mathrm{ph}}} \,, \tag{1.29}$$

where the integration is over the volume V of the star, and $|\delta \mathbf{r}|^2_{\mathrm{ph}}$ is the squared norm of the displacement vector at the photosphere. Based on the definition of mode inertia, one would thus expect modes trapped in the deep stellar interior to have large values of E. Mode inertia relates the photospheric rms velocity, V_{rms}, to the kinetic energy of the mode, $\mathcal{E}_{\mathrm{kin}}$, through:

$$\mathcal{E}_{\mathrm{kin}} = \frac{1}{2} M_{\mathrm{mode}} V^2_{\mathrm{rms}} = \frac{1}{2} M E V^2_{\mathrm{rms}} \,. \tag{1.30}$$

Based on a detailed description of the stochastic mechanism of mode excitation, Chaplin et al. (2005) obtained the following result for the expected mode amplitude[1]:

$$V^2_{\mathrm{rms}} = \frac{1}{\eta E} \frac{\tilde{\mathcal{P}}}{E} \approx \frac{\mathcal{F}(\omega)}{E} \,, \tag{1.31}$$

---

[1] This expression predicts the theoretical mode amplitude. In order to predict the observed quantity, one should multiply this expression by a factor $K_{\theta,\phi}$ accounting for the spatial filter of real observations.

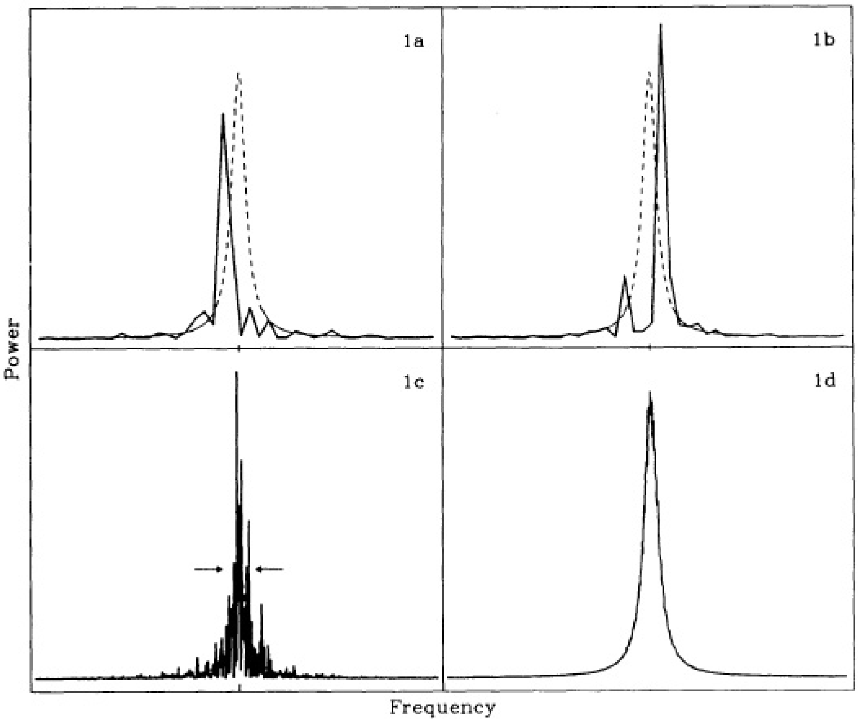

Figure 1.8: Power spectrum of a solar-like oscillator - Panels (a) and (b) display two realizations of the same limit spectrum (shown as a dotted curve). Both power spectra appear as an erratic function concealing the subjacent Lorentzian profile. Panel (c) displays a realization of the same limit spectrum, although with a resolution twenty times higher. Increasing the total observational span, and hence the resolution, did nothing to reduce the erratic behavior of the power spectrum. This panel is scaled differently to the remaining panels, with arrows marking the maximum value of the limit spectrum. Panel (d) displays the ensemble average of a large number of realizations with the same resolution as in (c). From Anderson et al. (1990).

where $\tilde{\mathcal{P}}$ is a measure of the acoustic energy input. Both terms $\tilde{\mathcal{P}}$ and ηE depend on the properties of the eigenfunction in the near-surface region of the star and are thus predominantly functions of frequency, which justifies the second equality in the last equation. It follows from Eq. (1.31) that, for a given frequency, mode amplitude essentially scales as $E^{-1/2}$; also, mode energy (cf. Eq. 1.30) is predominantly a function of frequency.

The stochastic process gives rise to the excitation of all modes in a substantial range of frequencies, with an amplitude modulation that reflects the slow frequency dependence of the energy input and damping rate. The properties of the mode eigenfunctions in the near-surface region of vigorous convection also play an important role in determining the frequency dependence of the mode amplitudes. Low-frequency modes tend to be evanescent near the surface, hence leading to inefficient excitation and small mode amplitudes. High-frequency modes, on the other hand, see their amplitudes reduced due to a decrease of the convective energy at the timescale of the oscillations, combined with an increase in the damping rate. The driving is ultimately most efficient for those modes whose periods match the relevant timescales of near-surface convection, from 5 to 10 minutes in the solar case. The frequency of maximum amplitude, $\nu_{\rm max}$, is supposed to scale with the acoustic cut-off frequency (Brown et al. 1991; Kjeldsen & Bedding 1995; Bedding & Kjeldsen 2003; Chaplin et al. 2008b; Belkacem et al. 2011), which when determined for an isothermal stellar atmosphere gives a scaling relation in terms of mass, radius, and effective temperature of (cf. Eqs. 1.1 and 1.18)

$$\nu_{\rm max} \propto M\,R^{-2}\,T_{\rm eff}^{-1/2}\,. \tag{1.32}$$

The overall result is a characteristic amplitude distribution with frequency (very often modulated by a bell-shaped envelope), which constitutes a signature of the presence of solar-like oscillations (see Fig. 1.9). Our ability to theoretically predict the amplitudes of stochastically-excited modes, combined with a complete set of observed modes over a broad frequency range, substantially simplify the process of mode identification and hence the comparison with stellar models, ultimately exponentiating the asteroseismic diagnostic potential of solar-like oscillations. This comes in great contrast to heat-engine excitation, for which the mechanism determining the final amplitudes of the modes is not well understood.

Christensen-Dalsgaard & Frandsen (1983) provided rough estimates of the oscillation amplitudes in main-sequence stars and cool giants from model calculations. Based on those results, Kjeldsen & Bedding (1995) found that mode amplitudes given in terms of surface velocities scale approximately as

$$V_{\rm rms} \propto \left(\frac{L}{M}\right)^{s}\,, \tag{1.33}$$

with $s = 1$. They further argued that the oscillation amplitudes, $A_{\rm rms}$, observed in photometry at a wavelength λ, are related to the velocity amplitudes according to

$$A_{\rm rms} = ({\rm d}L/L)_\lambda \propto \frac{V_{\rm rms}}{\lambda\,T_{\rm eff}^{r}}\,, \tag{1.34}$$

or, in terms of bolometric amplitudes,

$$A_{\rm rms}^{\rm bol} \propto \frac{V_{\rm rms}}{T_{\rm eff}^{r-1}}\,. \tag{1.35}$$

The exponent s has since been revised both theoretically (Houdek et al. 1999; Houdek 2006; Samadi et al. 2007), as well as observationally using red-giant stars (Gilliland 2008; Dziembowski & Soszyński 2010; Mosser et al. 2010; Stello et al. 2010), main-sequence stars (Verner et al. 2011b), and an ensemble of main-sequence and red-giant stars (Baudin et al. 2011). As a result, its value is now seen to reside roughly within the range from 0.7 to 1.5. The value of r is chosen to be either $r = 1.5$ (assuming adiabatic oscillations) or $r = 2$ (following a fit to observational data in Kjeldsen & Bedding 1995).

Accordingly, amplitudes are predicted to increase with increasing luminosity along the main sequence and relatively large amplitudes are expected for red giants. Such predictions are now being increasingly tested against observations. Reasonable agreement is apparently found between predicted and observed amplitudes for stars cooler or as hot as the Sun, while for hotter stars predictions considerably exceed the observed values. As an example of the type of discrepancy just mentioned, early *CoRoT* results, based on the analysis of the light curves of three main-sequence F stars fairly hotter than the Sun, showed that the oscillation amplitudes of those solar-like pulsators are about 25% below the theoretical predictions (Michel et al. 2008).

Recently, Kjeldsen & Bedding (2011) argued that amplitudes of oscillations in velocity should scale in proportion to velocity fluctuations due to granulation, since the physical motion of convective cells is what drives the oscillations. Therefore, they proposed a revised scaling relation for the velocities:

$$V_{\rm rms} \propto \frac{L\,\tau^{0.5}}{M^{1.5}\,T_{\rm eff}^{2.25}}\,, \tag{1.36}$$

where τ is the e-folding mode lifetime. Compared to Eq. (1.33), this revised scaling relation now incorporates a strong temperature dependence and also a weak dependence on mode lifetime. Stars with shorter mode lifetimes will show lower amplitudes, all other parameters remaining unaltered. Note that simple scaling relations exist in the literature for τ (Chaplin et al. 2009; Baudin et al. 2011; Appourchaux et al. 2012). A revised scaling relation for (narrowband) intensity amplitudes is then given by

$$A_{\rm rms} \propto \frac{L\,\tau^{0.5}}{\lambda\,M^{1.5}\,T_{\rm eff}^{2.25+r}}\,, \tag{1.37}$$

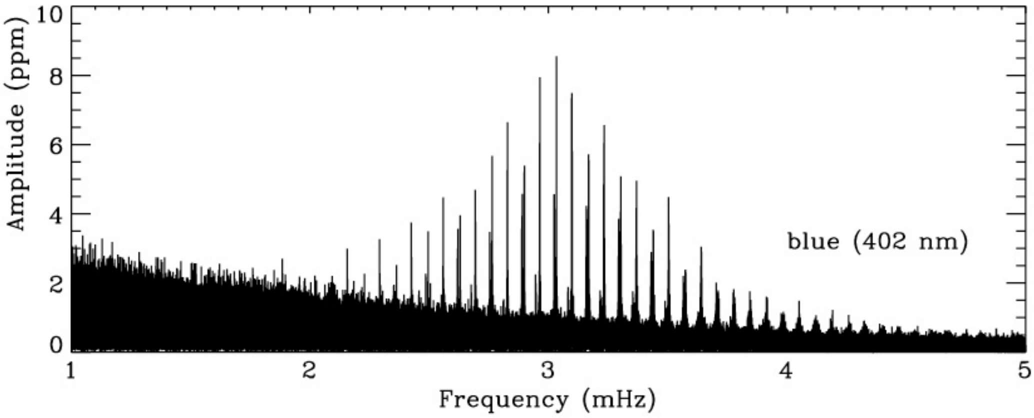

Figure 1.9: p-mode amplitude spectrum of the Sun - The spectrum is based on whole-disk observations of the solar irradiance using the blue channel of the VIRGO/SPM instrument on board the *SOHO* spacecraft. The observations have been smoothed and rescaled to show the spectrum corresponding to 30 days. Adapted from Bedding & Kjeldsen (2003).

or, in terms of bolometric amplitudes,

$$A_{\mathrm{rms}}^{\mathrm{bol}} \propto \frac{L\,\tau^{0.5}}{M^{1.5}\,T_{\mathrm{eff}}^{1.25+r}}\,. \tag{1.38}$$

This revised scaling relation can now be extensively tested with observations from *CoRoT* and *Kepler* (e.g., Campante et al. 2011).

1.4.3 Mode height and mode linewidth

It is not the integrated power V_{rms}^2 (or A_{rms}^2) that is observed directly in the power spectrum, but instead the power spectral density. If the total observational span is long enough in order to resolve a mode peak in the power spectrum (i.e., $T_{\mathrm{obs}} \gg 2\tau$, where the mode lifetime is given by $\tau = 1/\eta$), then the mode height (or maximum power spectral density) is given by (Chaplin et al. 2003, 2005):

$$H \approx \frac{2\,V_{\mathrm{rms}}^2}{\eta} = \frac{2\,V_{\mathrm{rms}}^2}{\pi\Gamma}\,, \tag{1.39}$$

where $\Gamma = (\pi\tau)^{-1}$ is the full width at half maximum of the mode peak, being commonly called the mode linewidth[1]. In this regime, H is independent of E, since both V_{rms}^2 and

---

[1] The dominant modes in the Sun have linewidths of 1–2 μHz and hence lifetimes of 2–4 days (e.g., Chaplin et al. 1997b).

η scale as E^{-1} at fixed frequency. Conversely, when $T_{\rm obs} \ll 2\tau$ the mode peak is not resolved, and power is essentially confined in one bin of the power spectrum, meaning that

$$H \sim V_{\rm rms}^2 T_{\rm obs}\,, \tag{1.40}$$

and H is thus proportional to E^{-1}. A proper description of H, covering these two extreme regimes as well as the intermediate regime, is given by (Fletcher et al. 2006; Chaplin et al. 2008b)

$$H = \frac{2\,V_{\rm rms}^2 T_{\rm obs}}{\pi\Gamma\,T_{\rm obs}+2}\,. \tag{1.41}$$

1.4.4 Statistical properties of the oscillators

Let us bear in mind Eq. (1.24) describing a damped linear oscillator forced by a random function. Since a very large number of convective elements is responsible for exciting the oscillations, it is reasonable to assume that $f(t)$ is a white-noise process with a Gaussian distribution. Furthermore, the energy of an oscillator in stochastic equilibrium can be interpreted in terms of the distance from the starting point of a two-dimensional random walk with a variable step size in the phase plane. The forcing function $f(t)$ being random means that each step is independent of the previous one. Once a large number of steps has been taken, the displacement $y(t)$ and velocity $\mathrm{d}y(t)/\mathrm{d}t$ will both be normally distributed. Therefore, the total energy of the oscillator, given by the sum of its kinetic energy, $[\mathrm{d}y(t)/\mathrm{d}t]^2$, and potential energy, $\omega_0^2\,y^2(t)$, follows by definition a χ_2^2 distribution, i.e., a Boltzmann distribution:

$$p(\mathcal{E}) = \frac{1}{\langle\mathcal{E}\rangle}\exp\left(-\frac{\mathcal{E}}{\langle\mathcal{E}\rangle}\right)\,, \tag{1.42}$$

where $\langle\mathcal{E}\rangle$ is the mean energy. This relation will only hold if the mode energy can be measured over time intervals much smaller than the damping time (Kumar et al. 1988). The observed solar oscillations amply satisfy this relation (e.g., Chaplin et al. 1997a).

In order to obtain the amplitude distribution, one takes into account that $p(\mathcal{E})\mathrm{d}\mathcal{E} = p(A)\mathrm{d}A$, and that the energy $\mathcal{E}$ is proportional to the square of the amplitude, A^2. As a result, the amplitude distribution turns out to be a Rayleigh-type distribution:

$$p(A) = \frac{2A}{\langle A^2\rangle}\exp\left(-\frac{A^2}{\langle A^2\rangle}\right)\,, \tag{1.43}$$

where $\langle A^2 \rangle$ is the mean-square amplitude. Interestingly, the mean $\langle A \rangle$ and standard deviation $\sigma(A)$ of this distribution obey the following relation:

$$\sigma(A) = \left(\frac{4}{\pi} - 1 \right)^{1/2} \langle A \rangle \approx 0.52 \, \langle A \rangle \, , \tag{1.44}$$

which holds true as long as the oscillator is in stochastic equilibrium.

Therefore, one expects stars whose oscillations are stochastically excited to verify $\sigma(A) \approx 0.52\langle A \rangle$. Christensen-Dalsgaard et al. (2001) noticed that observed amplitudes of semi-regular variables on the asymptotic giant branch approximately followed this relation. They argued that such variability might be due to stochastically-excited oscillations with mode lifetimes ranging from years to decades, a result later confirmed observationally by Bedding (2003). This result, first obtained from amateur astronomer data from the American Association of Variable Star Observers (AAVSO), was later also confirmed by Kiss & Bedding (2003) using data from the OGLE-II microlensing project. Furthermore, the regime $\sigma(A) < 0.52\langle A \rangle$ is expected to hold for oscillations excited by thermal overstability. Most of the oscillations excited by the κ mechanism, such as in subdwarf B stars (Pereira & Lopes 2005), are expected to be found in this regime. Finally, the regime $\sigma(A) > 0.52\langle A \rangle$ corresponds to stochastic oscillations that are not in stochastic equilibrium, a type of oscillatory behavior yet to be observed.

Based on the ratio $\sigma(A)/\langle A \rangle$, a simple diagnostic method has been established by Pereira & Lopes (2005) that probes the excitation mechanism of stellar pulsations through the analysis of the temporal variation of the amplitude of oscillation modes (see Fig. 1.10). Numerical simulations and the application to the γ Dor star HD 22702 served as a test to this method (Pereira et al. 2007). The same method has also been applied by Campante et al. (2010a) to the *CoRoT* hybrid γ Dor/δ Sct star HD 49434 in order to investigate the mechanism responsible for the excitation of the observed intermediate-order g modes (see Sect. 3.2.3).

Recent detection claims, based on *CoRoT* observations, of solar-like oscillations in the massive star V1449 Aql (Belkacem et al. 2009), previously known to be a β Cep pulsator, constituted the first plausible evidence of simultaneous classical and solar-like oscillations, thus providing additional modeling constraints if we bear in mind that these modes probe different layers of the star. *Kepler* observations of similar stars, however, have so far failed to confirm stochastically-excited oscillations (Balona et al. 2011). This is clearly a domain that may benefit from the application of the aforementioned

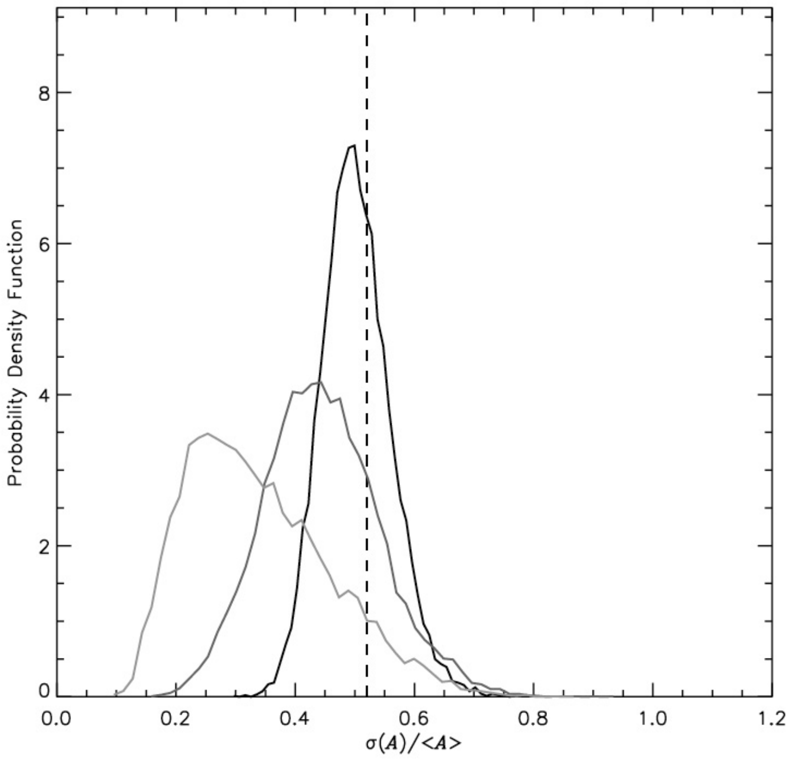

Figure 1.10: Probing the excitation mechanism of stellar pulsations - Probability density function of the statistic $\sigma(A)/\langle A\rangle$ computed by means of Monte Carlo simulations. From left to right, the curves correspond to samples of 40, 200 and 1000 amplitude measurements of a stochastic mode. These measurements come from contiguous time series considerably shorter than the damping time of the mode. The vertical dashed line corresponds to $\sigma(A)/\langle A\rangle = 0.52$. As the number of measurements increases, the distribution gradually acquires a Gaussian profile with the location of its peak converging to 0.52. Moreover, the width of the distribution is substantially reduced.

diagnostic method. This has certainly been the case of the very first detection of solar-like oscillations in a δ Sct star by Antoci et al. (2011), where its application proved decisive to set the claims on firm ground. Notice that solar-like oscillations in δ Sct stars had already been predicted by theory (Houdek et al. 1999; Samadi et al. 2002). The scientific relevance and implications of this groundbreaking work together with my substantial contribution to its completion, to be specific, in testing the stochastic origin of the oscillatory signal, led me to place the resulting article as a supplement in Appendix A.

1.4.5 Near-surface effects on computed oscillation frequencies

The effects of near-surface convection on the computation of oscillation frequencies are a very delicate matter. Computation of oscillation frequencies of stellar models usually assumes adiabaticity, a valid approximation in much of the stellar interior, viz., in regions where the thermal timescale is considerably longer than the period of the oscillations. This is certainly not the case in the near-surface region. Moreover, the dynamical effects of convection are usually neglected. This improper modeling of the near-surface layers gives rise to an offset between observed and computed oscillation frequencies. Grigahcène et al. (2011) address the problem of frequency precision in non-adiabatic models using a time-dependent treatment of convection.

Near-surface effects are essentially independent of l for low-degree modes. Moreover, these effects are predominantly functions of frequency, rapidly increasing with $\omega/\omega_{\rm c}$ (e.g., Christensen-Dalsgaard & Gough 1980), and thus of vital importance if we are to correctly interpret the high-order acoustic modes. Kjeldsen et al. (2008b) devised an empirical correction for the near-surface offset in the form of a power law:

$$\delta^{(\rm surf)}\nu = a\,(\nu/\nu_0)^b\,, \tag{1.45}$$

where ν_0 is a suitably chosen reference frequency, and the amplitude a and exponent b are obtained from a fit to solar frequencies of radial modes. They extended this correction to the stellar case with reasonable success by adopting the solar value of the exponent b and using the frequencies of a reference stellar model. Nevertheless, this correction is calibrated with respect to the Sun and thus needs to be thoroughly tested to assess its validity when applied to other solar-like oscillators. Brandão et al. (2011) show that, after applying this correction to the case of β Hyi, the observed modes are well reproduced, including those that have mixed-mode character. On the other hand, application of this same correction to the case of Procyon has led to mixed success (Doğan et al. 2010). One hopes that *Kepler* observations of a broad sample of solar-like pulsators will yield insight into the dependence of these effects on stellar parameters.

In order to account for the minor dependence of the near-surface effects on mode inertia, we may want to rewrite Eq. (1.45) as

$$\delta^{(\rm surf)}\nu_{nl} = Q_{nl}^{-1}a\,(\nu_{nl}/\nu_0)^b\,, \tag{1.46}$$

where the inertia ratio Q_{nl} is given by

$$Q_{nl} = \frac{E_{nl}}{\overline{E}_0(\nu_{nl})} \,, \tag{1.47}$$

that is to say, the ratio of mode inertia to the interpolated inertia of radial modes. The power-law correction is based on a fit to the radial modes and, relative to these, the effect on the non-radial modes is reduced by a factor proportional to the mode inertia. Q_{nl} also accounts for the presence of mixed modes, for which the near-surface effect is smaller due to the higher inertia ratio Q_{nl}.

1.5 Asteroseismic inference

1.5.1 Asymptotic signatures

1.5.1.1 Asymptotic relation for p modes

The observed modes of solar-like oscillations are typically high-order acoustic modes. If interaction with a g mode can be neglected, linear, adiabatic, high-order acoustic modes, in a spherically symmetric star, satisfy an asymptotic relation for the frequencies (Vandakurov 1967; Tassoul 1980):

$$\nu_{nl} \simeq \left(n + \frac{l}{2} + \epsilon\right) \Delta\nu_0 - \left\{ \frac{l(l+1)}{4\pi^2 \, \Delta\nu_0} \left[\frac{c(R)}{R} - \int_0^R \frac{\mathrm{d}c}{\mathrm{d}r} \frac{\mathrm{d}r}{r} \right] - \delta \right\} \frac{{\Delta\nu_0}^2}{\nu_{nl}} \,, \tag{1.48}$$

where

$$\Delta\nu_0 = \left(2 \int_0^R \frac{\mathrm{d}r}{c} \right)^{-1} \tag{1.49}$$

is the inverse of the sound-travel time across the stellar diameter; additionally, the term $\epsilon = \epsilon(\nu)$ is determined by the reflection properties of the surface layers, as is the small correction term δ.

To leading order, Eq. (1.48) predicts that modes should occur in groups corresponding to degree of the same parity (i.e., either even or odd degree) such that $n + l/2$ are the same, and being further uniformly spaced with a separation given by $\Delta\nu_0$. This degeneracy is lifted by considering the second-order term in Eq. (1.48). The spectrum is then characterized both by the large frequency separation

$$\Delta\nu_{nl} = \nu_{n+1\,l} - \nu_{nl} \approx \Delta\nu_0 \,, \tag{1.50}$$

a quantity depending both on frequency and on mode degree l, and by the small frequency separation

$$\delta\nu_{nl} = \nu_{nl} - \nu_{n-1\,l+2} \approx -(4l+6)\frac{\Delta\nu_0}{4\pi^2\,\nu_{nl}}\int_0^R \frac{\mathrm{d}c}{\mathrm{d}r}\frac{\mathrm{d}r}{r}\,, \tag{1.51}$$

also a frequency- and degree-dependent quantity (I have here neglected the term in the surface sound speed appearing in Eq. 1.48). It should be noted that the small frequency separation may become a negative quantity during stellar evolution. This apparent violation of Eq. (1.51) is associated with the presence of a convective helium-rich core (Soriano & Vauclair 2008).

Both the large and the small frequency separations are shown in Fig. 1.11 in the case of the acoustic amplitude spectrum of the Sun. The quasi-regularity of the spectrum of high-order p modes, along with the characteristic amplitude distribution with frequency discussed in Sect. 1.4.2, constitute the main signatures of the presence of solar-like oscillations. The large and small frequency separations are extremely valuable diagnostic tools for asteroseismic studies of solar-like oscillators. In fact, these two quantities can be measured with considerable precision, even in the case of low-SNR observations where a determination of individual oscillation frequencies is hindered.

Moreover, it may be also convenient to consider small separations that take into account modes with adjacent degree:

$$\delta^{(1)}\nu_{nl} = \nu_{nl} - \frac{1}{2}(\nu_{n-1\,l+1} + \nu_{n\,l+1}) \approx -(2l+2)\frac{\Delta\nu_0}{4\pi^2\,\nu_{nl}}\int_0^R \frac{\mathrm{d}c}{\mathrm{d}r}\frac{\mathrm{d}r}{r}\,, \tag{1.52}$$

viz., the amount by which modes with degree l are offset from the midpoint between the $l+1$ modes on either side.

A recurrent way of visualizing the asymptotic properties of the acoustic spectrum is to build an échelle diagram (e.g., Grec et al. 1983), for which one starts by expressing the frequencies as

$$\nu_{nl} = \nu_0 + k\langle\Delta\nu\rangle + \tilde{\nu}_{nl}\,, \tag{1.53}$$

where ν_0 is a reference frequency, $\langle\Delta\nu\rangle$ is a suitable average of the large frequency separation $\Delta\nu_{nl}$, and k is an integer such that $\tilde{\nu}_{nl}$ takes a value between 0 and $\langle\Delta\nu\rangle$. Finally, the diagram is built by plotting $\tilde{\nu}_{nl}$ on the abscissa and $\nu_0 + k\langle\Delta\nu\rangle$ on the ordinate, the graphical equivalent to slicing the spectrum into segments of length $\langle\Delta\nu\rangle$ and stacking them one on top of the other. Figure 1.12 displays a scaled échelle diagram

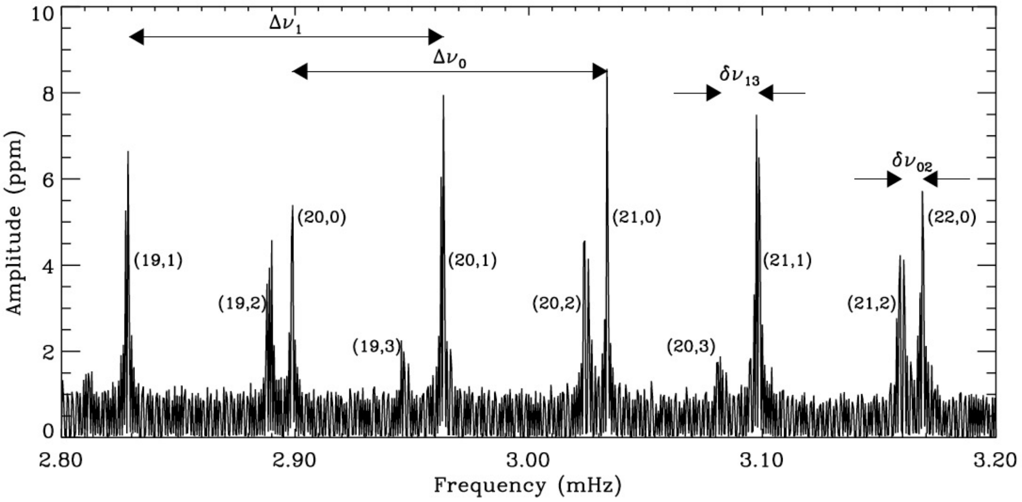

Figure 1.11: Close-up of the p-mode amplitude spectrum of the Sun - This is a close-up of the p-mode spectrum displayed in Fig. 1.9. Mode peaks are tagged with the corresponding (n, l) values, which were determined by comparison with theoretical models. The large and small frequency separations are indicated with a slightly different nomenclature than the one used in the text, which should, however, still be clear. From Bedding & Kjeldsen (2003).

(Bedding & Kjeldsen 2010) where the p-mode frequencies of three main-sequence stars are simultaneously plotted. If the frequencies of these stars were to strictly obey the asymptotic relation in Eq. (1.48), then they would exhibit essentially vertical ridges in the échelle diagram. However, departures from regularity are clearly present: variations in the large separation with frequency are seen to introduce a curvature in the ridges, while variations in the small separation with frequency appear as a convergence or divergence of the relevant ridges.

The small frequency separation is mostly sensitive to conditions in the stellar core, where the eigenfunctions of modes of similar frequency but of different degree mainly differ. As stellar evolution takes its course, hydrogen is burned into helium in the core leading to an increase of the mean molecular weight. Bearing in mind Eq. (1.14) for the sound speed in an ideal gas, and taking into consideration that the central temperature will not vary significantly during the phase of hydrogen burning, the sound speed in the core will thus decrease as the star becomes more evolved, such decrease being more intense at the center and becoming more pronounced with increasing age. Therefore,

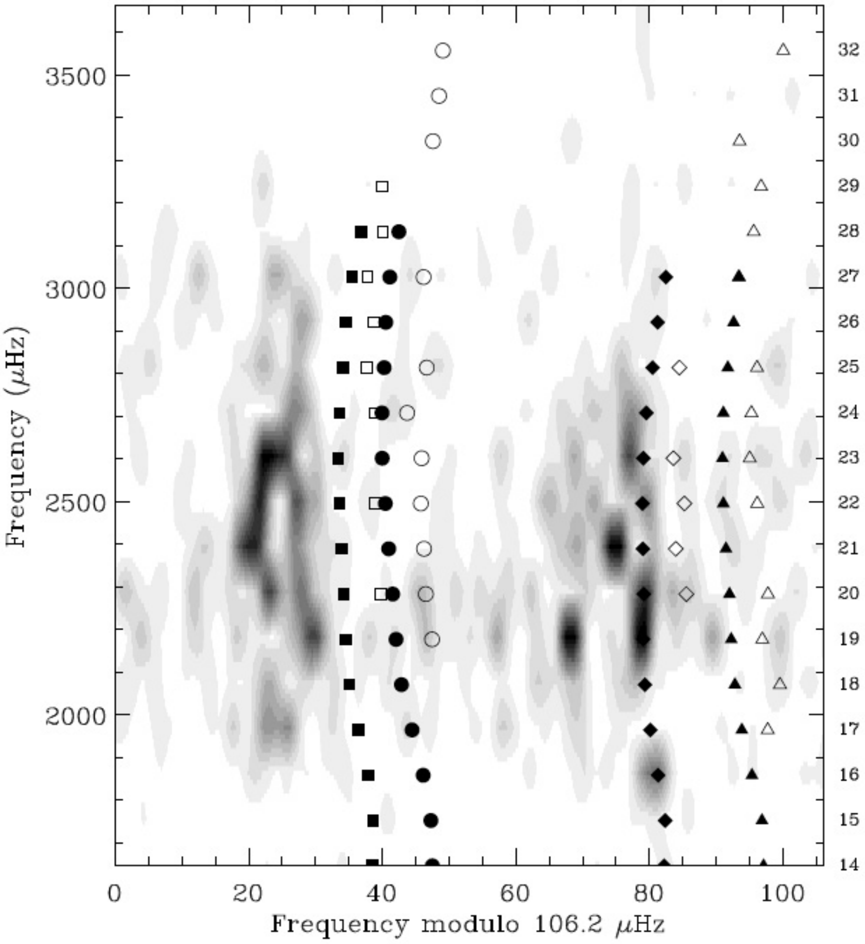

Figure 1.12: Scaled échelle diagram - Three main-sequence stars are simultaneously compared: the power spectrum of α Cen A is given in grayscale, filled symbols represent scaled solar frequencies, and open symbols represent scaled frequencies for α Cen B. Scaling factors for the frequencies were computed based on a homology relation (cf. Eq. 1.54) and fine-tuned so as to match the slopes of the ridges for the three stars (making them vertical), which means matching $\Delta\nu_0$. Symbol shapes indicate mode degree: $l=0$ (circles), $l=1$ (triangles), $l=2$ (squares), and $l=3$ (diamonds). From Bedding & Kjeldsen (2010).

the resulting positive sound-speed gradient $\mathrm{d}c/\mathrm{d}r$ in the core causes a gradual reduction of $\delta\nu_{nl}$ and $\delta^{(1)}\nu_{nl}$ with increasing stellar age (cf. Eqs. 1.51 and 1.52, respectively). In conclusion, the small frequency separation can be seen as a diagnostic tool of the evolutionary stage of a (main-sequence) star.

On the other hand, the large frequency separation provides a more global measure of the properties of a star, essentially scaling as $t_{\rm dyn}^{-1}$ (cf. Eq. 1.1):

$$\Delta\nu_0 \propto \left(\frac{M}{R^3}\right)^{1/2} \propto \sqrt{\bar{\rho}}\,. \tag{1.54}$$

Besides providing a measure of the mean stellar density, it may be taken as a measure of stellar mass for stars residing on the main sequence. Based on theoretical models, White et al. (2011b) suggested that the scaling relation of $\Delta\nu_0$ with density may be improved by including a function of $T_{\rm eff}$.

The preceding considerations suggest presenting the large and small frequency separations in a two-dimensional diagram, which can be thought of as an asteroseismic H-R diagram, known as the C-D diagram (e.g., Christensen-Dalsgaard 1984, 1988). An example of such a diagram is displayed in Fig. 1.13. Assuming that the remaining stellar parameters (e.g., the chemical composition) are known, the location of a star in this diagram would then determine its mass and age. Monteiro et al. (2002) present an interesting analysis of the uncertainties associated with the use of this diagram due to the sensitivity to several model parameters.

For subgiants as well as for red giants, however, the small separation is approximately a fixed fraction of the large separation, regardless of mass or evolutionary state (Bedding et al. 2010a; White et al. 2011a). As a consequence, the distribution of evolved stars in the C-D diagram becomes highly degenerate as evolutionary stellar tracks converge. Based on models extending from the zero-age main sequence to the tip of the red-giant branch, White et al. (2011b) revived the diagnostic potential of an alternative asteroseismic diagram relating ϵ (cf. Eq. 1.48) to the large separation (see Fig. 1.14 for an example). They found that evolutionary tracks in this so-called ϵ diagram (originally introduced by Christensen-Dalsgaard 1984) are more sensitive to the mass and age of evolved stars than in the C-D diagram. They have also shown that ϵ is mostly determined by $T_{\rm eff}$ and that it could thus be useful for addressing the problem of mode identification in F stars (see also Sect. 2.2.3.2), as previously suggested by Bedding & Kjeldsen (2010).

Finally, the small frequency separation still retains a residual sensitivity to the properties of the stellar envelope. Roxburgh & Vorontsov (2003) showed that ratios such as

$$r_{02} = \frac{\nu_{n0} - \nu_{n-1\,2}}{\nu_{n1} - \nu_{n-1\,1}}\,, \tag{1.55}$$

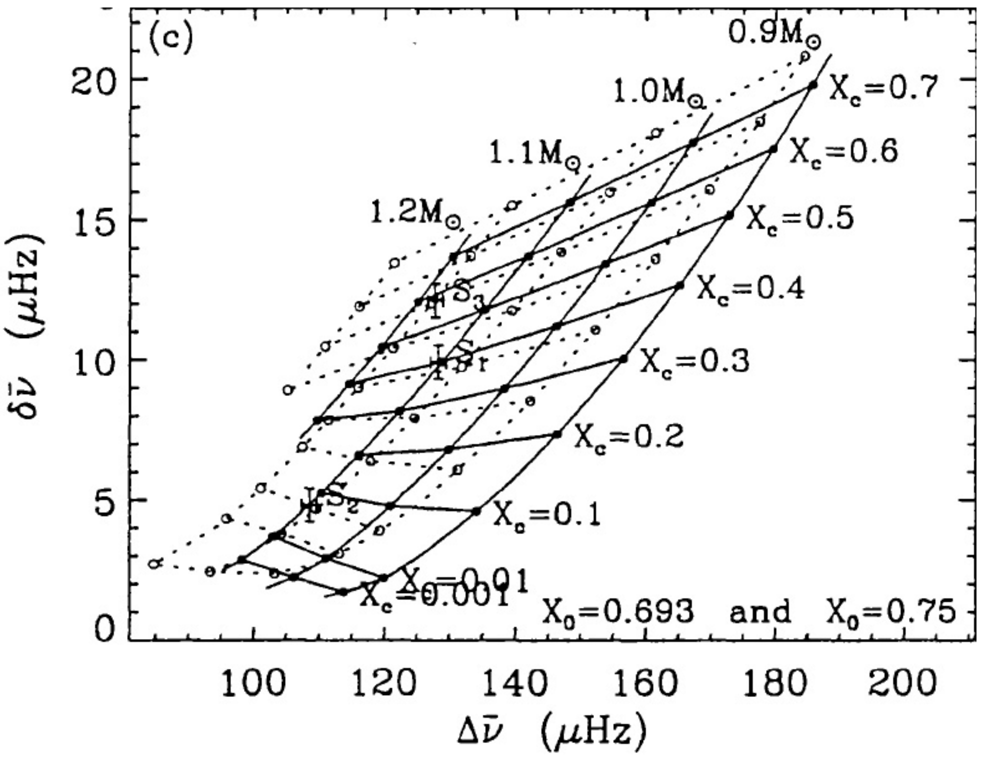

Figure 1.13: Example of a C-D diagram - Evolutionary sequences of stars with 0.9, 1.0, 1.1, and 1.2 $\mathrm{M}_{\odot}$ are displayed, together with curves of constant central hydrogen abundance, X_{c}. Stellar age increases as one moves downward along an evolutionary sequence of given mass. Sequences corresponding to models with an initial hydrogen abundance $X_0 = 0.75$ appear as solid curves, whereas sequences corresponding to models with $X_0 = 0.693$ are displayed as dotted curves. Adapted from Monteiro et al. (2002).

and

$$r_{10} = \frac{-\frac{1}{8}(\nu_{n-1\,1} - 4\nu_{n0} + 6\nu_{n1} - 4\nu_{n+1\,0} + \nu_{n+1\,1})}{\nu_{n+1\,0} - \nu_{n0}} \,, \tag{1.56}$$

between small and large frequency separations, are largely independent of the surface layers and provide a reliable measure of the core properties.

1.5.1.2 Asymptotic relation for g modes

High-order, low-degree g modes obey the following first-order asymptotic expression for the periods (Vandakurov 1967; Smeyers 1968; Tassoul 1980):

$$\Pi_{nl} = \frac{1}{\nu_{nl}} \simeq \frac{\Pi_0}{\sqrt{l(l+1)}} \left(n + \epsilon_{\mathrm{g}}\right) \,, \tag{1.57}$$

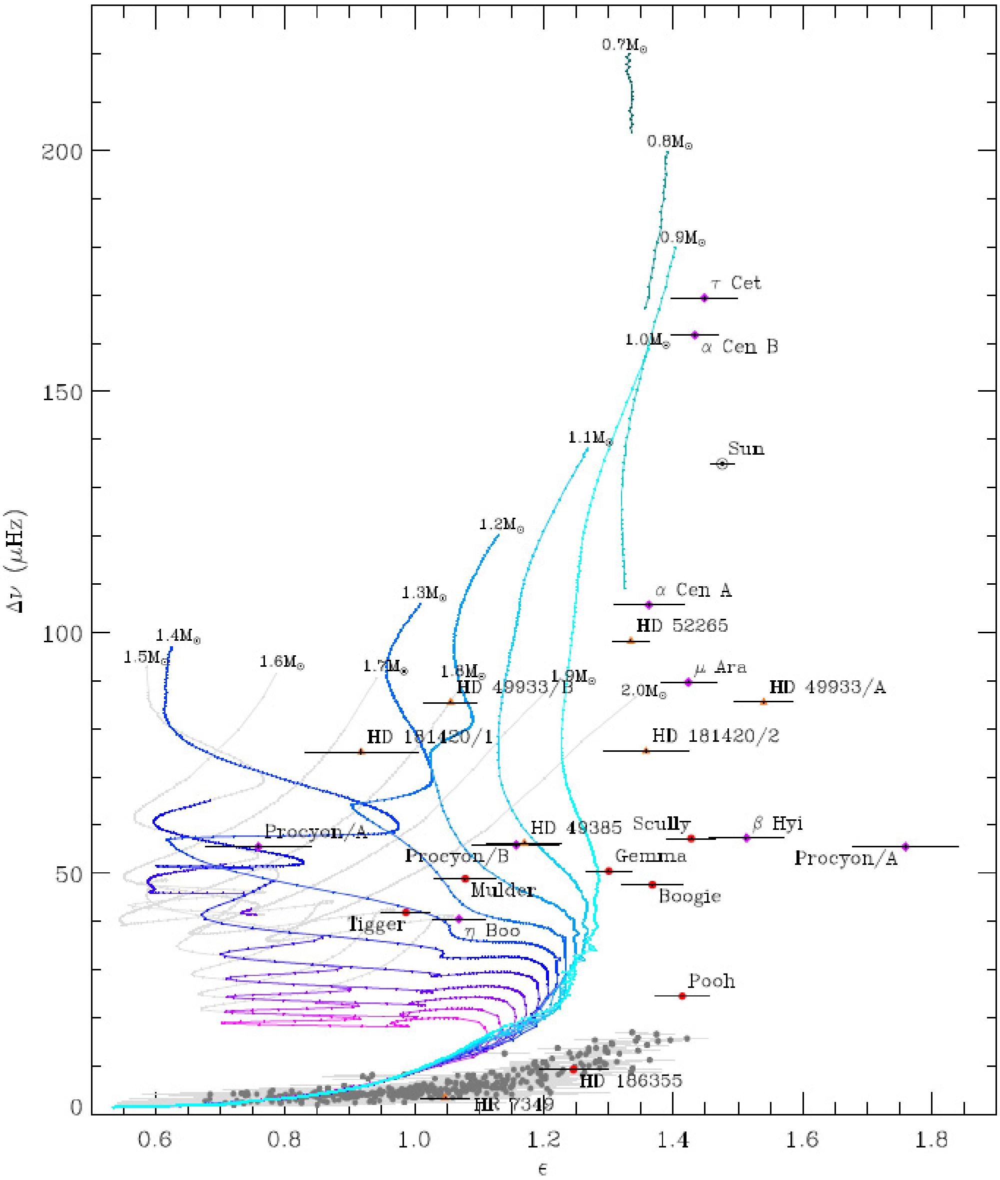

Figure 1.14: Example of an ε diagram - ε diagram with model tracks for near-solar metallicity ($Z_0 = 0.017$). Tracks increase in mass from 0.7 to 2.0 M$_\odot$ (green to magenta lines) in steps of 0.1 M$_\odot$. The sections of the evolutionary tracks in which the models are hotter than the approximate cool edge of the classical instability strip are shown in gray. Stars shown, as labeled, were observed by either *CoRoT* (orange triangles), *Kepler* (red circles) or from the ground (purple diamonds). Gray circles are *Kepler* red giants (Huber et al. 2010). The Sun is marked by its usual symbol. From White et al. (2011b).

where

$$\Pi_0 = 2\pi^2 \left(\int \frac{N}{r} \mathrm{d}r \right)^{-1} ; \tag{1.58}$$

the phase term ϵ_g depends on the details of the boundaries of the g-mode trapping region and the integral is computed over that same region. The periods are now nearly uniformly spaced, and not the frequencies, as was the case for p modes (cf. Eq. 1.48). Furthermore, the period spacings depend on degree l. Departures from the simple asymptotic relation given in Eq. (1.57) are used as a means of diagnosing the stratification inside stars (e.g., inside white dwarfs), since the magnitude of these departures is very sensitive to strong abundance gradients and their effect on the buoyancy frequency.

1.5.2 Effects of sharp features

Oscillation frequencies contain a greater deal of information besides what is suggested by the simple asymptotic description. In fact, sharp features (i.e., features varying more rapidly than the scale of the eigenfunction) in the internal structure of a star are known to give rise to oscillatory signals in observable seismic parameters (e.g., Monteiro et al. 2000; Ballot et al. 2004; Basu et al. 2004; Verner et al. 2006; Houdek & Gough 2007). This oscillatory behavior is a function of frequency and arises from the varying phase of the oscillation at the location of the sharp feature, ultimately causing departures from the asymptotic description. In particular, these oscillatory signals can be found in the frequencies themselves, in the large frequency separation, and in higher-order differences. The second difference, defined as

$$\Delta_2\nu_{nl} = \nu_{n-1\,l} - 2\,\nu_{nl} + \nu_{n+1\,l} \,, \tag{1.59}$$

is the most widely exploited parameter. Other diagnostics from which to extract such signatures are frequency differences that make use of the $l=0$ and $l=1$ modes (Roxburgh 2009b).

The modulation of the seismic parameters with frequency may be written in the form

$$A(\omega)\,\cos[2(\omega\,\tau_\mathrm{d} + \phi)] \,, \tag{1.60}$$

where $A(\omega)$ is an amplitude, τ_d is the acoustic depth of the feature, and ϕ is a surface phase. The frequency dependence of the amplitude $A(\omega)$ is determined by the physical properties of the feature. The acoustic depth τ_{d} is defined as

$$\tau_{\mathrm{d}} = \int_{r_{\mathrm{d}}}^{R} \frac{\mathrm{d}r}{c} \,, \tag{1.61}$$

where r_{d} is the acoustic radius of the feature.

These sharp features are associated with abrupt variations of the sound speed and thus are also called acoustic glitches. The two main sources behind an abrupt variation of the sound speed are the border of a convection zone and the ionization of a dominant element. The former source is related to the sharp transition of the temperature gradient from being radiative to becoming adiabatic, which causes a discontinuity in the second derivative of the sound speed. Moreover, convective overshoot may produce a discontinuity in the temperature gradient with a consequent discontinuity in the first derivative of the sound speed, ultimately leading to a stronger oscillatory signal. Determination of the lower boundary of a convective envelope is a very important matter, since this region is believed to play a key role in stellar dynamos. The latter source is related to a rapid variation of the adiabatic exponent Γ_1 (and hence of the local sound speed) associated with the ionization of an abundant element, e.g., arising from the second ionization of helium. Extraction of the helium signature allows tight constraints to be placed on the helium abundance in stellar envelopes, otherwise not possible when dealing with such cool stars (since ionization temperatures are too high to yield usable photospheric lines for spectroscopy in these stars).

The effects of sharp features are detectable from the analysis of the frequencies of low-degree modes. Therefore, one expects to be able to conduct such analyses in the stellar case once frequency precision is high enough. Monteiro et al. (2000) conducted a seismic study that aimed at determining the characteristics of the convective envelopes of low-mass stars, namely, measuring the acoustic depth of the base of the convection zone and constraining the properties of an overshoot layer at the base of such an envelope. Using frequencies of low-degree modes (up to $l = 2$) they concluded that the signal in the frequencies (see Fig. 1.15) could be measured if the precision in frequency determination was 0.1 μHz or better. Ballot et al. (2004) conducted a detailed investigation on the seismic extraction of the convective extent in solar-like stars, again using low-degree data. Their analysis was mainly based on the use of the second difference $\Delta_2\nu_{nl}$, after having asserted that this seismic parameter constitutes the best compromise between enhancing the oscillatory signal while keeping the errors acceptably low.

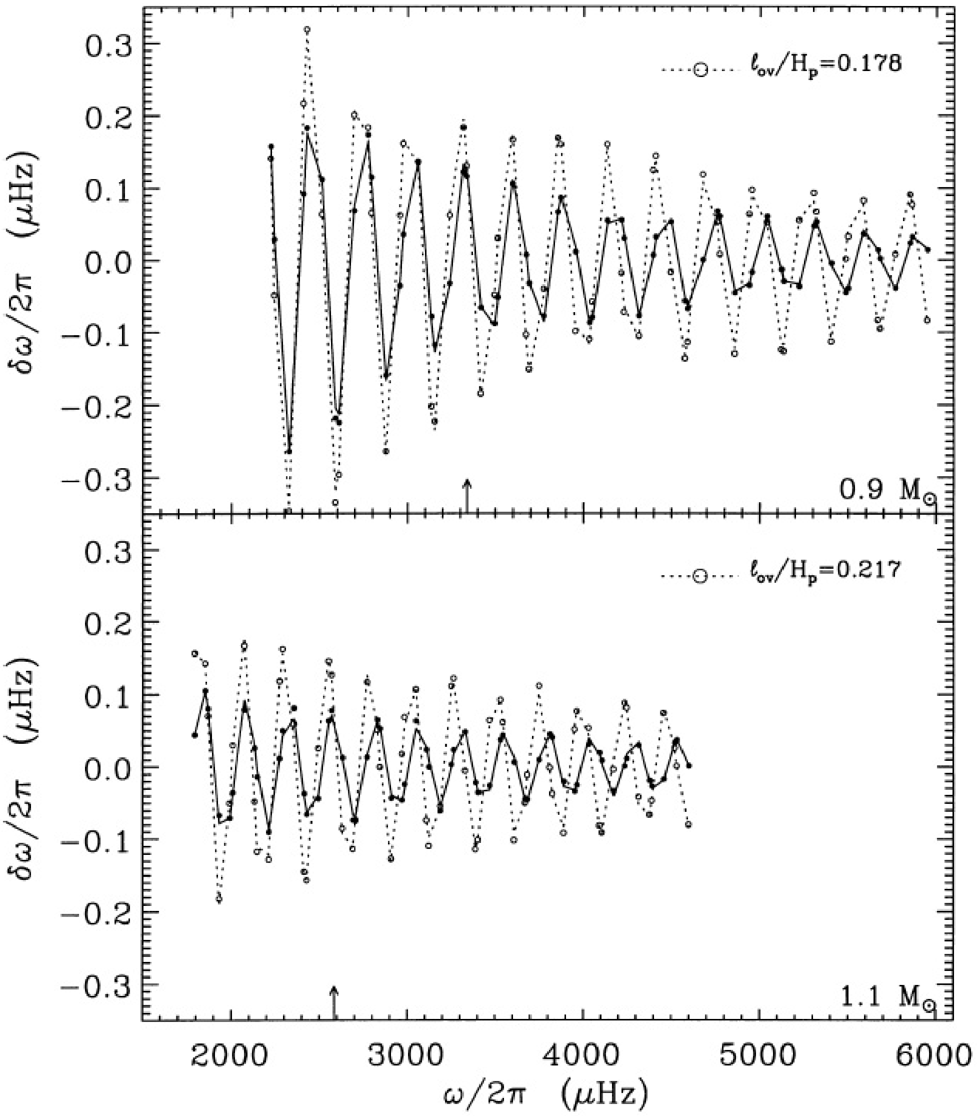

Figure 1.15: Oscillatory signal from the base of the convection zone - These signals are present in the frequencies of zero-age main-sequence models of a 0.9-$M_\odot$ (top panel) and a 1.1-$M_\odot$ (bottom panel) stars. Model frequencies are represented by circles: open circles correspond to models incorporating overshoot and filled circles correspond to models without overshoot. Dotted lines indicate the fit to the former groups of points, whereas solid lines indicate the fit to the latter groups of points. The size of the overshoot layer, $\ell_{\rm ov}$, is indicated in both panels in units of the pressure scale height, H_p. It can be clearly seen that the amplitude of the signal reflects the presence or not of convective overshoot. From Monteiro et al. (2000).

They concluded that an observational span of at least 150 days is necessary if we are to reliably extract the signature of the base of the convection zone for a large sample of solar-like stars. Very recently, Miglio et al. (2010) found evidence of the seismic signature of a sharp transition in the internal structure of the *CoRoT* red-giant star HR 7349. Through comparison with stellar models they were led to conclude that this feature is associated with the helium second-ionization region. In another very recent work, Mazumdar & Michel (2010) claim to have determined the acoustic depth of both the base of the convection zone and the helium second-ionization region of HD 49933 with a precision of 10% by means of the second difference.

Finally, the sharp transition associated with the edge of a convective core – found in solar-type stars that are slightly more massive than the Sun – also produces an effect on the oscillation frequencies (e.g., Cunha & Metcalfe 2007). In the case of a main-sequence solar-like oscillator harboring a convective core, its edge will be situated near the inner turning point of low-degree p modes and, as a result, the signal will no longer be periodic. Measurement of the frequency dependence of suitable frequency separations of low-degree modes provides a diagnostic tool of both the presence and size of a convective core (e.g., Cunha & Brandão 2011; Silva Aguirre et al. 2011a). Determining the sizes of convective cores and the overshoot of the corresponding convective motions can provide an accurate calibration of the ages of such stars (e.g., Mazumdar et al. 2006).

1.5.3 Mixed modes

I ended Sect. 1.3.3 by mentioning that modes with mixed p- and g-mode character may occur in evolved stars. This comes as a result of the large magnitude attained by the buoyancy frequency in the stellar core, which reaches frequency values relevant for stochastic excitation. Hereafter, an illustration of the signatures of mixed modes is provided, based on a model[1] of the subgiant η Boo having a mass of 1.7 $\mathrm{M}_\odot$ and a heavy-element abundance of $Z = 0.04$ (di Mauro et al. 2003; Christensen-Dalsgaard & Houdek 2010). Interestingly, η Boo is the first star other than the Sun for which definite frequencies of solar-like oscillations have been identified (Kjeldsen et al. 1995);

---

[1] This is not the same model as considered in Fig. 1.4. The general properties of the characteristic frequencies of both models are, however, very similar.

these would be later confirmed by Kjeldsen et al. (2003) and Carrier et al. (2005) (see Sect. 1.6.2 for a more detailed account).

In the course of its evolution along the subgiant branch, the star expands at roughly constant luminosity and consequently its effective temperature drops. In addition, as a result of this expansion, the eigenfrequencies tend to decrease (cf. Eq. 1.1). On the other hand, the increasing central condensation leads to an increase of the buoyancy frequency in the deep interior, which in turn tends to augment the frequencies of the g modes. Panel (a) of Fig. 1.16 displays the evolution with age or, equivalently, decreasing effective temperature, of the frequencies of selected radial ($l=0$) and dipole ($l=1$) modes of the model of η Boo being considered. The frequencies of the purely acoustic $l=0$ modes are seen to decrease monotonically in accordance with Eq. (1.1). Also, the frequencies of the predominantly acoustic $l=1$ modes – with their values roughly halfway between those of the radial modes on either side – follow the same general behavior. However, also evident, is a branch of increasing frequency that corresponds to a $l=1$ mode whose predominant character is that of a g mode. Where this mode meets a predominantly acoustic mode, their frequencies undergo what is called an avoided crossing (Osaki 1975; Aizenman et al. 1977), i.e., closely approaching without actually crossing. At the point of closest approach these modes have a mixed character, with considerable amplitudes both in the g- and p-mode trapping regions. The important role of mixed modes as diagnostic tools resides here, namely, in the fact that their sensitivity to the properties of stellar cores is greatly enhanced when compared to purely acoustic modes.

The changing nature of the modes can also be traced by means of the behavior of their normalized inertia E (cf. Eq. 1.29), as depicted in panel (b) of Fig. 1.16 for a couple of $l=1$ modes undergoing an avoided crossing. When their character is predominantly acoustic their inertia is similar to that of a neighboring (purely acoustic) radial mode. As they approach the g-mode branch, however, their inertia modestly rises above what would be expected for a purely acoustic mode. The two modes are seen to exchange nature during the avoided crossing. Furthermore, at the point of closest approach (near the vertical line) the two modes have essentially the same inertia.

Inspection of Fig. 1.4 tells us that the evanescent region is narrower for $l=1$ modes than for $l=2$ modes. Consequently, discrimination between g- and p-mode behavior is effectively blended for the dipole modes, as suggested by the gradual nature of the

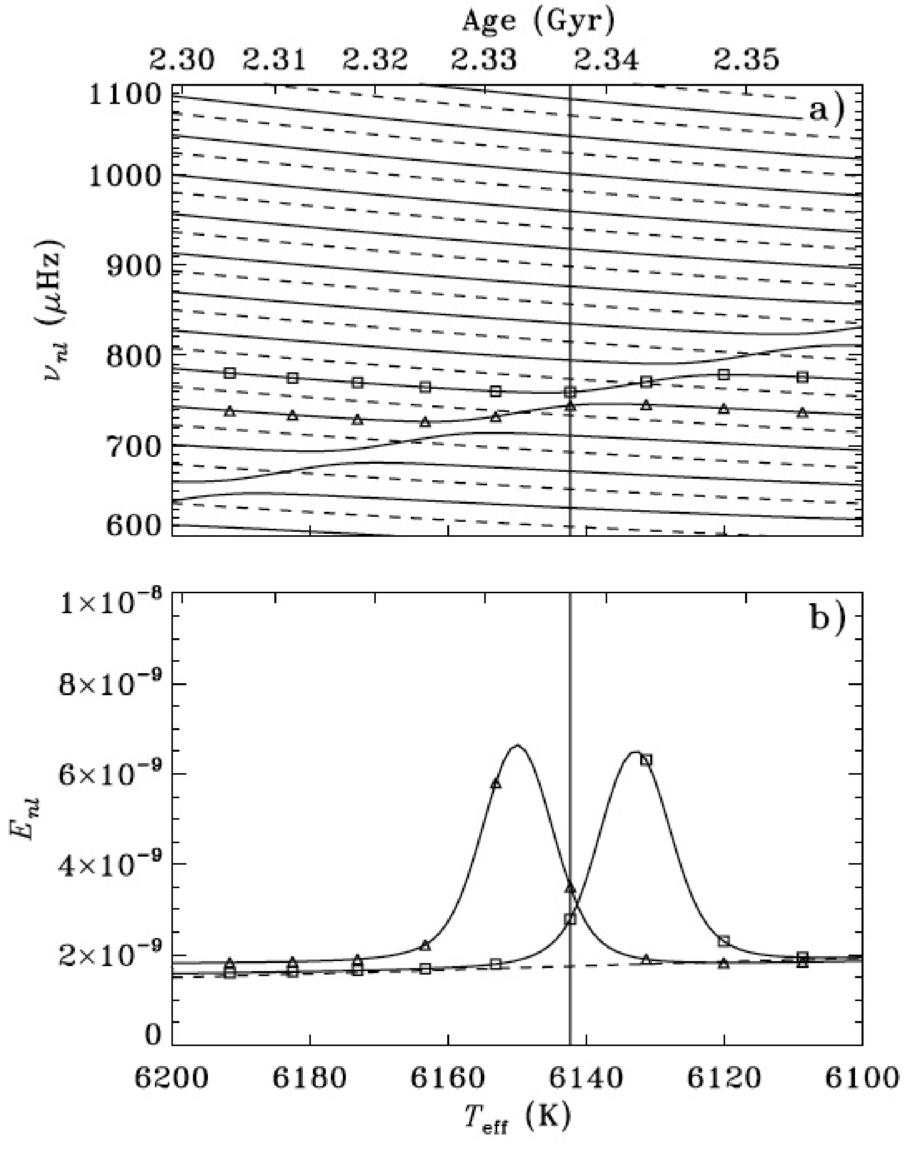

Figure 1.16: Evolution of mode properties in a model of η Boo - Panel (a) displays the evolution of the frequencies of selected radial (dashed curves) and dipole (solid curves) modes. Panel (b) depicts the evolution of the normalized inertia for a couple of $l=1$ modes (solid curves) marked by triangles and squares in panel (a). The normalized inertia of a neighboring radial mode is also depicted (dashed curve), seen to vary slowly with age. The vertical line indicates the location of the specific model being considered and whose oscillation frequencies are displayed in Fig. 1.17. From Christensen-Dalsgaard & Houdek (2010).

avoided crossings in panel (a) of Fig. 1.16. On the other hand, for modes with $l > 1$, the evanescent region is broader. This gives rise to a better discrimination between the two types of behavior by reducing the coupling between the g- and p-mode regions, as well as to a decrease in the likelihood of finding a mode in a mixed state. Also, this is accompanied by a plummeting increase of the mode inertia while approaching a g-mode branch, which can become higher by several orders of magnitude than for a purely acoustic mode.

An issue not yet addressed is whether or not such mixed modes are expected to be excited to observable amplitudes. It follows from Eq. (1.31) that, for a given frequency, the amplitudes of stochastically-excited modes will scale inversely to the mode inertia, more specifically, as $E^{-1/2}$. Based on this and the above considerations, one may predict that $l = 1$ mixed modes are likely to be excited to observable amplitudes, whereas this is less likely to happen for mixed modes of higher degree.

The échelle diagram in Fig. 1.17 shows computed and observed frequencies for η Boo. The jagged appearance of the $l = 1$ ridge – an obvious departure from the asymptotic description – is a trademark of the presence of an avoided crossing and hence of the evolved nature of a star. This is also known as mode bumping, meaning that mode frequencies are shifted from their regular spacing. These same features have also been seen in the cases of ground-based observations of β Hyi (Bedding et al. 2007b) and possibly Procyon (Bedding et al. 2010b), as well as in the cases of the *CoRoT* target HD 49385 (Deheuvels et al. 2010) and of a few *Kepler* targets (e.g., Metcalfe et al. 2010; Campante et al. 2011; Mathur et al. 2011). The diagnostic potential of mixed modes is also being recognized by the red-giant community: detected g-mode period spacings in red giants (Beck et al. 2011) are used to discriminate between hydrogen- and helium-burning red-giant stars (Bedding et al. 2011; Mosser et al. 2011a).

Bedding (2011) suggested a new asteroseismic diagram – inspired by the C-D diagram – in which the frequencies of the avoided crossings (i.e., the frequencies of the pure g modes in the core cavity) for a number of stars are plotted against the large separation of the p modes (e.g., Campante et al. 2011). This so-called p-g diagram could prove to be an instructive way to display results of many stars and to allow for a first comparison with theoretical models. Much of the diagnostic potential of mixed modes can be captured in this way, since their overall pattern is determined by the

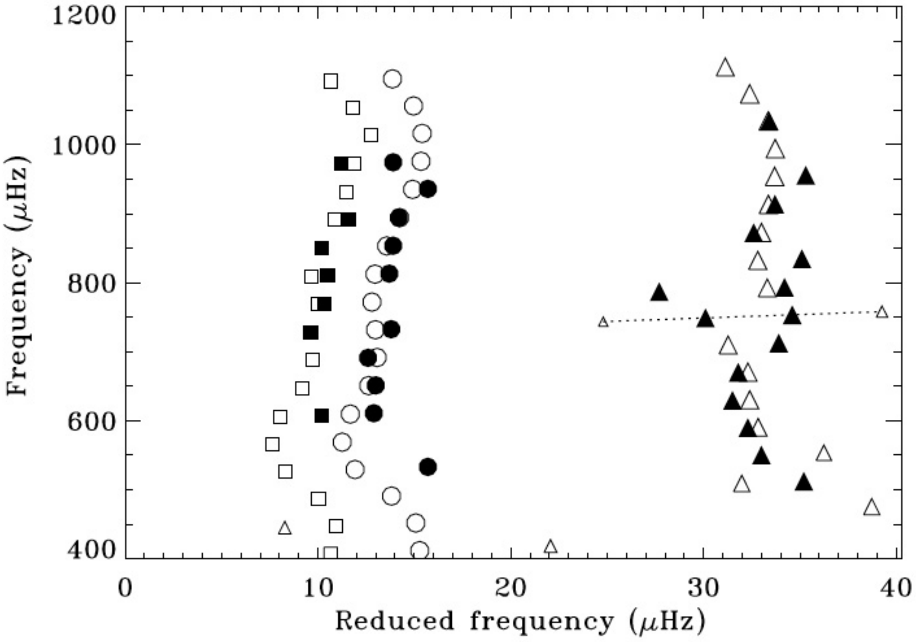

Figure 1.17: Échelle diagram showing computed and observed oscillation frequencies for η Boo - Symbol shapes indicate mode degree: $l=0$ (circles), $l=1$ (triangles), and $l=2$ (squares). Open symbols represent computed frequencies corresponding to the model being considered in the current discussion and that has been indicated with a vertical line in Fig. 1.16. Filled symbols represent a combined set of observed frequencies based on the works of Kjeldsen et al. (2003) and Carrier et al. (2005). Symbol size reflects the amplitude of a mode relative to that of a (purely acoustic) radial mode of the same frequency. The dotted line connects the two modes undergoing an avoided crossing as depicted in panel (b) of Fig. 1.16. Also visible, although only for the computed frequencies, is a second avoided crossing at the low-frequency end. From Christensen-Dalsgaard & Houdek (2010).

mode bumping at each avoided crossing, which in turn is determined by the g modes trapped in the core.

In his *Lecture Notes on Stellar Oscillations*, J. Christensen-Dalsgaard proposed a simple analogy based on coupled oscillators to describe an avoided crossing between two modes. Very recently, Deheuvels & Michel (2010) presented an extension of that analogy to the case of more than two modes, having shown that the presence of an avoided crossing will induce a characteristic distortion of the ridge of degree l, an effect that is most prominent for $l=1$ modes. Based on the behavior of the eigenfrequencies, they concluded that HD 49385 should be in the post-main-sequence phase.

1.6 Observational aspects

1.6.1 Techniques

There are two main observational techniques used in asteroseismology: (i) photometric observations of variability in the stellar flux resulting from the intrinsic pulsation of the star and (ii) spectroscopic observations of velocity variations due to the motion of elements on the stellar surface. It should be noted that intensity and velocity (or Doppler) observations sample the same properties of the pulsations, although not in exactly the same way. In fact, we have already seen in Sect. 1.3.2 that the response of velocity observations to modes of moderate degree is larger compared to intensity observations. Such difference in response can in principle be used in the process of mode identification, a particularly complicated issue in the case of classical pulsators.

Velocity shifts of spectral lines are measured using high-dispersion spectrographs with stable reference sources, mounted on ground-based telescope facilities. The oscillation amplitudes in solar-like pulsators are nonetheless extremely small, particularly for main-sequence stars (see Fig. 1.18): e.g., for the Sun the velocity amplitude per mode is typically less than $15\,\mathrm{cm\,s^{-1}}$, while the corresponding amplitude in broadband intensity is around 4 ppm. However, the last decade or so has seen a rampant increase in the achievable precision of radial-velocity measurements promoted by the detection of extrasolar planets. Presently, radial-velocity determination has reached a precision of only a few tens of $\mathrm{cm\,s^{-1}}$ per exposure. It should be noted that this method is strongly biased toward low-effective temperature and slowly-rotating stars, since velocity observations require the analysis of many narrow spectral lines, as well as toward subgiant and giant stars, as a result of their larger intrinsic amplitudes.

Most of the pre-*CoRoT* detections have indeed come from high-precision radial-velocity measurements using spectrographs such as: CORALIE at the 1.2-m Euler telescope at ESO La Silla in Chile, HARPS at the ESO La Silla 3.6-m telescope, UCLES at the 3.9-m AAT in Australia, UVES at the 8.2-m UT2 of the VLT at ESO Paranal in Chile, SARG at the 3.6-m TNG in La Palma, etc. Besides weather instabilities, a serious limitation when it comes to ground-based asteroseismic observations of solar-like pulsators is the lack of dedicated facilities, either in the format of a network of telescopes at low and/or intermediate latitudes or as an asteroseismic telescope in Antarctica. This considerably undermines both the duration and continuity of the

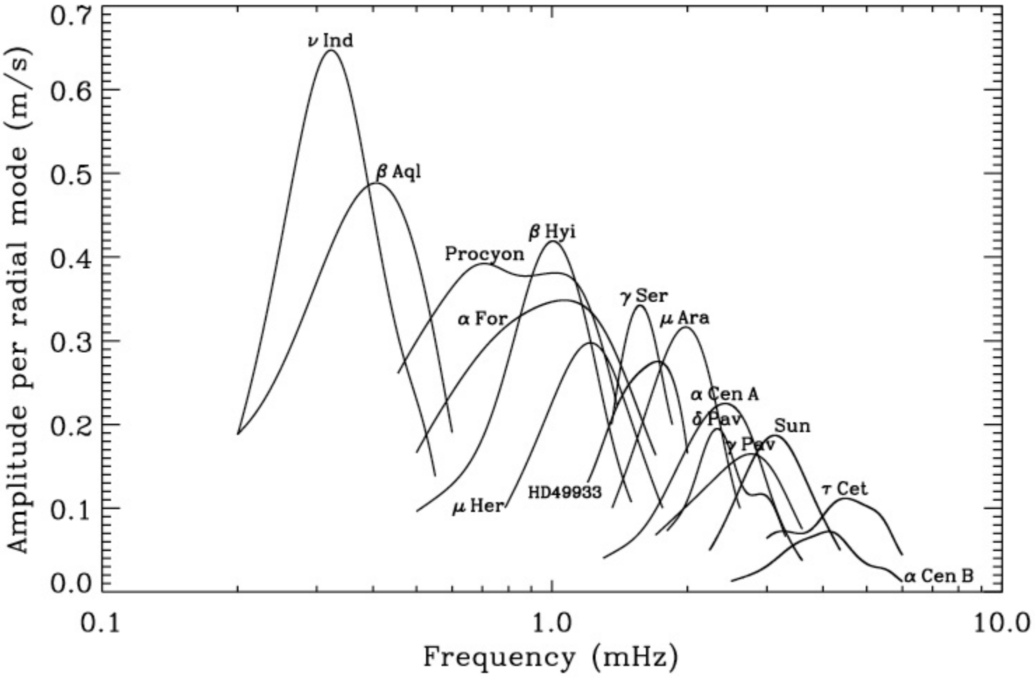

Figure 1.18: Amplitudes of solar-like oscillations in a variety of stars - Amplitudes have been normalized so as to correspond to the amplitude per radial mode. The location of $\nu_{\rm max}$ occurs at lower frequencies for more evolved stars, while the velocity amplitude generally increases with increasing L/M. In order to allow for a direct comparison, the solar data were obtained by observing the blue sky with a technique corresponding to the stellar observations. From Arentoft et al. (2008).

available observations due to diurnal interruptions and the annual motion of the Earth. In an attempt to augment the duty cycle of ground-based observations, several successful double-site campaigns have been coordinated that used the instruments in Chile and at the AAT (e.g., Butler et al. 2004; Kjeldsen et al. 2005). These coordination efforts culminated in the realization of a multi-site campaign to measure oscillations in the F5IV star Procyon, which has been the most extensive campaign so far organized on any solar-like pulsator (Arentoft et al. 2008). Furthermore, a dedicated network of 1-m telescopes equipped with iodine-stabilized spectrographs is the goal of the SONG project (Grundahl et al. 2009a,b), while the SIAMOIS project (Mosser et al. 2008) has plans to install an instrument performing spectrometric observations at the Concordia station at Dome C in Antarctica.

On the other hand, performing intensity measurements presents two significant advantages: the instrumentation is rather simple and the flux is measured within bands of medium to low spectral resolution. Nevertheless, the intrinsic stellar background signal arising from non-oscillatory fluctuations associated with granulation, activity, etc., is substantially higher for photometric measurements than for spectroscopic measurements, meaning that velocity observations have higher SNR at low frequencies (e.g., Harvey 1988). The fact that photometric measurements are primarily sensitive to temperature variations – caused by the compression and expansion of the stellar atmosphere during the oscillation cycle – explains their higher sensitivity to granulation (the sloping background seen in Fig. 1.9 is actually due to granulation). Figure 1.19 compares the solar spectra as measured in velocity with GOLF (Gabriel et al. 1995) and in intensity using the green channel of the VIRGO/SPM, both instruments being on board the *SOHO* spacecraft.

When envisaging the study of classical pulsators, characterized by the relatively high amplitudes of their oscillations, the use of ground-based photometry is ubiquitous, owing to the fact that most small and medium-sized telescopes have the necessary instrumentation to carry out absolute or relative photometry in a variety of photometric systems. However, scintillation from the Earth's atmosphere strongly limits the achievable precision of ground-based photometry. Until now, all ground-based attempts to detect solar-like oscillations in stars near the main sequence through intensity measurements have failed. The most ambitious enterprise consisted of a multi-site campaign – using differential photometry and employing most of the world's then-largest telescopes – on the open cluster M67 that failed, however, to detect any oscillations (Gilliland et al. 1993). In some cases upper limits for oscillation amplitudes were well below the theoretical predictions, which are now known to have been overestimated. It should be noted that the observed stars in M67 consisted of turn-off stars somewhat hotter than the Sun. Lately, two ground-based photometric campaigns have attempted to detect solar-like oscillations in red-giant cluster members (Frandsen et al. 2007; Stello et al. 2007). Having been the only successful of the two campaigns, Stello et al. (2007) were able to make the first test of relevant scaling relations with an homogeneous ensemble of stars and to detect excess power consistent with the expected signal from stellar oscillations.

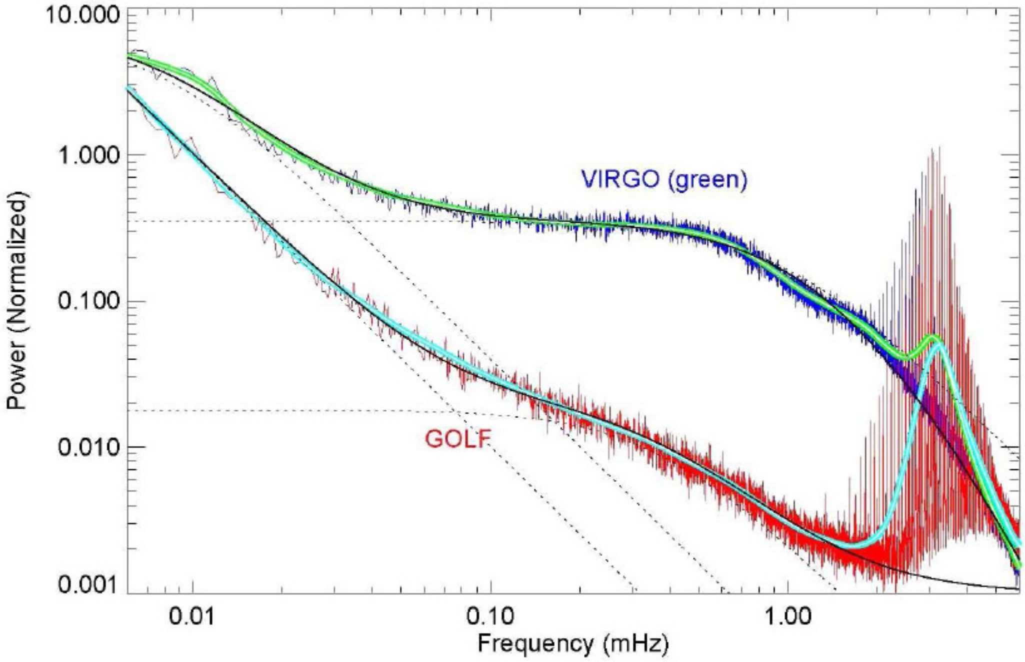

Figure 1.19: Comparison of solar spectra computed from velocity and intensity observations - Velocity observations were performed with GOLF, while intensity observations are from the green channel of the VIRGO/SPM. Both instruments are on board the *SOHO* spacecraft. The stellar background signal has contributions both from activity and from granulation. A simple Harvey-like profile (cf. Eq. 2.74) has been used to describe the background signal with dashed curves representing the different components of such profile. The smoothed spectra are shown as solid thick curves. From Grundahl et al. (2007).

The development of space-based asteroseismology using the technique of ultra-high-precision photometry has been a major breakthrough. It finally provided the possibility of carrying out long and almost uninterrupted observations of the same targets. Moreover, using moderate apertures, space photometry is capable of detecting oscillations whose amplitudes are about 1 ppm. Non-dedicated instruments, such as the three Fine Guidance Sensors on the *Hubble Space Telescope* (e.g., Zwintz et al. 1999; Gilliland et al. 2011), the 52-mm star camera on the *WIRE* satellite (e.g., Buzasi 2002; Bruntt et al. 2005) and the SMEI experiment on board the *Coriolis* satellite (e.g., Tarrant et al. 2007, 2008), have been used to acquire high-precision photometric data for asteroseismic studies.

The Canadian microsat *MOST* (e.g., Walker et al. 2003), the first dedicated asteroseismology mission to be launched successfully (in June 2003), is able to measure intensity variations of relatively bright stars by producing light curves with time spans of the order of a few weeks. It is not expected, however, to reach the low-noise levels required for the detection of solar-like oscillations in main-sequence stars. The French-led *CoRoT* mission, launched in December 2006, produced a major leap in the domain of space-based asteroseismology. Photometric variations of a few hundred asteroseismic targets are being monitored in the course of the mission, although the number of observed solar-like pulsators residing on or near the main sequence is quite reduced (just over ten). A major strength of this mission resides in the possibility of conducting nearly continuous observations, extending over five months, of the same field of view. A further advance is provided by the asteroseismic program of the *Kepler* mission, launched in March 2009, whereby thousands of stars have been monitored during a survey phase, after which there is the possibility of conducting long-term follow-ups of a selection of those stars. *Kepler* will lead to a revolution in the field of solar-like oscillations, since the number of known solar-like pulsators is expected to increase by several orders of magnitude.

If selected for funding following its present design study, the ESA *PLATO* mission[1] (Catala 2009) will provide very extensive and high-quality asteroseismic data as an integral part of its goal to study extrasolar planetary systems. A more distant milestone should be reached when imaging of stellar surfaces will be made possible. The Stellar Imager is a planned space-based interferometer, designed to enable 0.1-milliarcsecond spectral imaging of stellar surfaces and capable of probing flows and structures in stellar interiors through asteroseismology (Christensen-Dalsgaard et al. 2011).

1.6.2 The observational status

The information conveyed by solar-like oscillations can be used to determine fundamental stellar properties such as mass, radius, and age. Furthermore, the internal stellar structure can be constrained to unprecedented levels provided that individual mode parameters are measured. We thus believe that asteroseismology will produce significant improvements on the theories related to stellar structure and evolution, on

---

[1] Unfortunately, shortly before the submission of this dissertation, the news came that ESA had not selected *PLATO* in the context of its Cosmic Vision program.

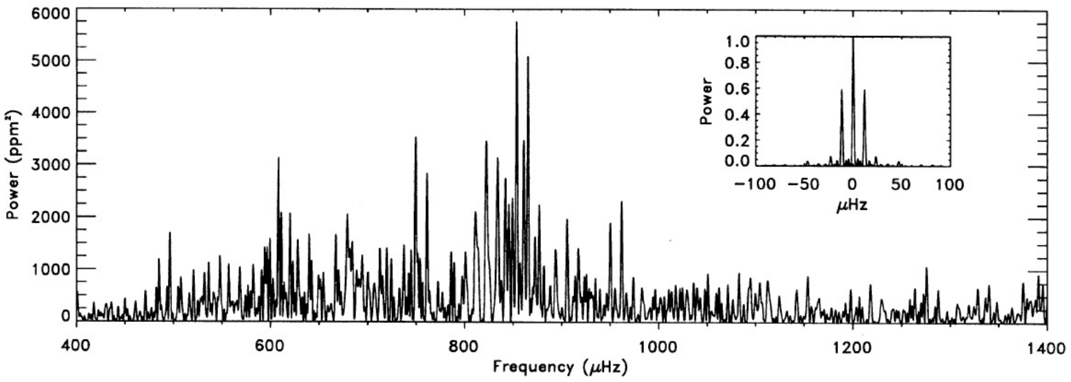

Figure 1.20: Power spectrum of η Boo from equivalent-width measurements - There is a clear hump of excess power centered at about 850 μHz due to solar-like oscillations. The inset depicts the power spectrum of the window function (see Sect. 2.1.1 for a definition). The observations were made over six nights using the 2.5-m Nordic Optical Telescope (single-site observations). Owing to the daily gaps in the data, strong sidelobes appear in the spectral window at splittings of ±1 cycle/day or, equivalently, ±11.57 μHz. These sidelobes greatly complicate the determination of individual frequencies. From Kjeldsen et al. (1995).

topics as diverse as energy generation and transport, rotation and stellar cycles. The interdisciplinary aspect of the field should not be neglected, the best example of which is probably its potential use to characterize exoplanet-host stars, thus providing key information for understanding the formation and evolution of planetary systems, as well as for constraining the location of habitable zones based on a knowledge of the stellar magnetic activity.

The search for solar-like oscillations in stars other than the Sun has started some thirty years ago. The first hint of a hump of excess power with a frequency dependence similar to the one observed in the solar case was obtained by Brown et al. (1991) from radial-velocity observations of Procyon (α CMi). The first plausible detection of individual oscillation frequencies and a large frequency separation is, however, attributed to Kjeldsen et al. (1995), who observed the G0IV star η Boo by employing a novel technique that involved measuring fluctuations in the equivalent widths of the temperature-sensitive Balmer lines using low-resolution spectroscopy (see Fig. 1.20 for a power spectrum of the observations). Subsequently, Brown et al. (1997) were unable to confirm the presence of oscillations in η Boo using radial-velocity measurements, which would be later confirmed by further equivalent-width and radial-velocity measurements by Kjeldsen et al. (2003), as well as by independent radial-velocity measurements carried out by Carrier et al. (2005). Space-based observations of this star, conducted with the *MOST* satellite, led to considerable controversy after claims that a series of low-overtone p modes had been identified (Guenther et al. 2005). The fact that the orbital frequency of the spacecraft is nearly a multiple of the large separation means that caution is needed in the interpretation of those low-frequency peaks.

Coming back to the case of Procyon, it is interesting to note that not until 1999 were solar-like oscillations definitely confirmed in this star (Martić et al. 1999). Being the eighth brightest star in the night sky, Procyon has indeed been a long-time favorite for the search of oscillations, with several independent radial-velocity studies, mostly single-site, reporting an excess in the power spectrum. Controversy arised when photometric observations obtained with *MOST* failed to detect oscillations (Matthews et al. 2004), leading Bedding et al. (2005) shortly thereafter to argue that such non-detection was consistent with the ground-based data. All these efforts culminated in the realization of an extensive multi-site campaign carried out in January 2007, whereby high-precision velocity observations over more than three weeks were obtained with eleven telescopes at eight observatories. The analysis of these observations has been presented in Arentoft et al. (2008) and Bedding et al. (2010b). Given my extensive contribution to the latter paper, I have decided to place it as a supplement in Appendix B. In the latest work dedicated to Procyon, Huber et al. (2011a) compared a new and more accurate 2007 set of *MOST* data with the simultaneous data acquired during the multi-site campaign, concluding that the *MOST* power spectrum shows clear evidence of individual oscillation frequencies and thus refuting the renewed non-detection claims made by Walker (2008).

The year 2001 came and oscillations were found in the G2IV star β Hyi and in the G2V star α Cen A. The following year would also bring the first firm establishment of solar-like oscillations in a giant star (ξ Hya; Frandsen et al. 2002), based on a continuous 1-month monitoring with CORALIE.

Bedding et al. (2001) and Carrier et al. (2001) confirmed the presence of solar-like oscillations in β Hyi, but were unable to identify individual mode frequencies. Subsequently, Bedding et al. (2007b) observed this star during more than a week with HARPS and UCLES, being able to identify 28 oscillation modes that included some mixed modes of degree $l=1$. Frequently regarded as an older Sun, β Hyi is for that reason a particularly interesting object of study.

During the last decade, the visual binary system α Cen has been a preferred asteroseismic target due to its proximity and to the similarity of its components to the Sun. The unambiguous detection of solar-like oscillations in α Cen A by Bouchy & Carrier (2001, 2002), based on 13 nights of single-site observations with CORALIE, is hailed as a milestone in the field, confirming the earlier claimed detection made by Schou & Buzasi (2001) with the *WIRE* satellite. Simultaneously with the CORALIE observations, a double-site campaign was being devoted to this star employing UVES and UCLES (Butler et al. 2004; Bedding et al. 2004). In the meantime, a re-analysis of the *WIRE* data (Fletcher et al. 2006) and ground-based spectroscopy with HARPS (Bazot et al. 2007) have been conducted. Very recently, de Meulenaer et al. (2010) combined and analysed the radial-velocity time series obtained in May 2001 with CORALIE, UVES, and UCLES (see Sect. 3.1.2).

These early discoveries paved the way for the detection of solar-like oscillations in a number of stars. A thorough, although pre-*CoRoT*, observational review is provided by Bedding & Kjeldsen (2008), referring not only to main-sequence and subgiant stars, but also to G and K giants, semi-regular variables, and red supergiants. Although ground-based spectroscopic campaigns seem to be loosing momentum as we move deep into the era of space asteroseismology, it should be noted that they provide the ultimate precision for asteroseismic investigations, at least for bright and/or nearby stars. Not to mention the ability to cover the whole sky and to target stars whose parallaxes and other parameters are accurately known. While waiting for the advent of projects such as SONG and SIAMOIS, it is still rewarding to explore the use of existing facilities for short (1–2 weeks) ground-based campaigns devoted to carefully selected solar-like pulsators. A striking example was the first application of asteroseismology (8 nights of observations with HARPS) to an exoplanet-host star (μ Ara; Bouchy et al. 2005; Bazot et al. 2005). Another remarkable example is the recent work of Bazot et al. (2011), who have employed asteroseismology (12 nights with HARPS) and long-baseline interferometry (with the PAVO beam-combiner at the CHARA array) in order to derive the radius and mass of the solar twin 18 Sco (see Sect. 3.1.1).

Asteroseismology has definitely entered a new and golden era with the advent of the *CoRoT* and *Kepler* space missions. Together, they are up to date responsible for the detection of solar-like oscillations in several hundred main-sequence and subgiant stars, as well as in several thousand stars residing on the red-giant branch. These numbers are indeed stratospheric. An overview of the most important results obtained so far with both these space missions is provided by García (2011).

The *CoRoT* satellite has been the first asteroseismic mission to be able to perform ultra-high-precision, wide-field photometry for extended and continuous periods of time (up to 150 days) on the same targets. Launched into an inertial polar orbit at an altitude of 897 km, it carries a 4-CCD array fed by a 27-cm telescope and is able to measure stellar brightnesses to μmag precision (Baglin et al. 2006). The mission comprises two main scientific programs – asteroseismology and the detection of exoplanets by the transit method – simultaneously working on adjacent fields in the sky.

In the asteroseismic context, *CoRoT* has been successful in providing observations that allowed a seismic analysis of a few late-type main-sequence and post-main-sequence stars displaying solar-like oscillations (Appourchaux et al. 2008; Michel et al. 2008; Barban et al. 2009; Benomar et al. 2009b; García et al. 2009; Mosser et al. 2009; Deheuvels et al. 2010; Mathur et al. 2010a). These have been joined by a study of the exoplanet-host star HD 52265 (see Sect. 3.2.2; Ballot et al. 2011). The availability of long time-series data on solar-type stars presents good prospects for probing stellar cycles with asteroseismology (e.g., Chaplin et al. 2007; Metcalfe et al. 2007; Karoff et al. 2009; Chaplin 2011). García et al. (2010) recently uncovered the first evidence of global changes in the oscillation frequencies and mode amplitudes associated with a stellar activity cycle in another solar-type star, to be specific, the *CoRoT* target HD 49933 (see Fig. 1.21). The results on HD 49933 (with a period of the stellar cycle probably between 1 and 2 years) seem to be consistent with the paradigm that stars divide into two distinct sequences in terms of activity (the active sequence and the inactive sequence), with stars along each sequence displaying a similar number of rotational periods per activity cycle (e.g., Böhm-Vitense 2007), meaning that solar-type stars with short rotational periods – HD 49933 has a surface rotational period of about 3.4 days – tend to have short activity cycles.

Notable success came from the asteroseismic study of several hundreds of red giants observed in the exoplanet channel of *CoRoT*. These data made it possible to establish new seismic scaling relations (e.g., Hekker et al. 2009; Mosser et al. 2010), to unambiguously detect for the first time non-radial modes in red giants (De Ridder et al.

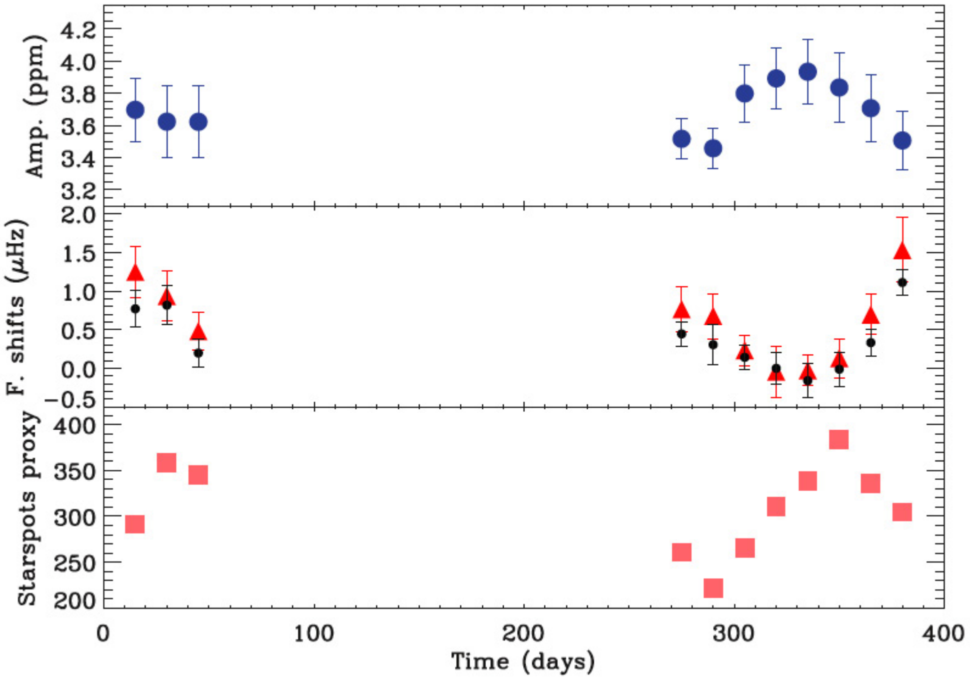

Figure 1.21: Evidence of a magnetic activity cycle in the Sun-like star HD 49933 - Temporal evolution of the mode amplitudes (top panel), the frequency shifts using two different methods (middle panel), and a starspot proxy (bottom panel). The seismic indicators (top and middle panels) are anticorrelated in time – as observed for the Sun – and reveal a modulation in the second epoch that suggests a period of at least 120 days related to the internal magnetic activity. Moreover, the starspot signature confirms the existence of an activity cycle, which seems to be temporally shifted compared with the seismic indicators. From García et al. (2010).

2009; Carrier et al. 2010) and to directly estimate stellar masses and radii from scaling relations (Kallinger et al. 2010b). The studies are being extended to make inference on the red-giant population – dominated by red-clump stars in the *CoRoT* ensemble – and by that means to test population-synthesis models of the evolution of the Galaxy (Miglio et al. 2009). The establishment of a universal red-giant oscillation pattern (Mosser et al. 2011b) and the analysis of mixed modes in these stars to determine their evolutionary status (Mosser et al. 2011a) constitute the latest developments.

The NASA *Kepler* mission was designed with the intent of detecting – using the transit photometry method – Earth-like planets in and near the habitable zones of late-type main-sequence stars (Borucki et al. 2010; Koch et al. 2010). The satellite,

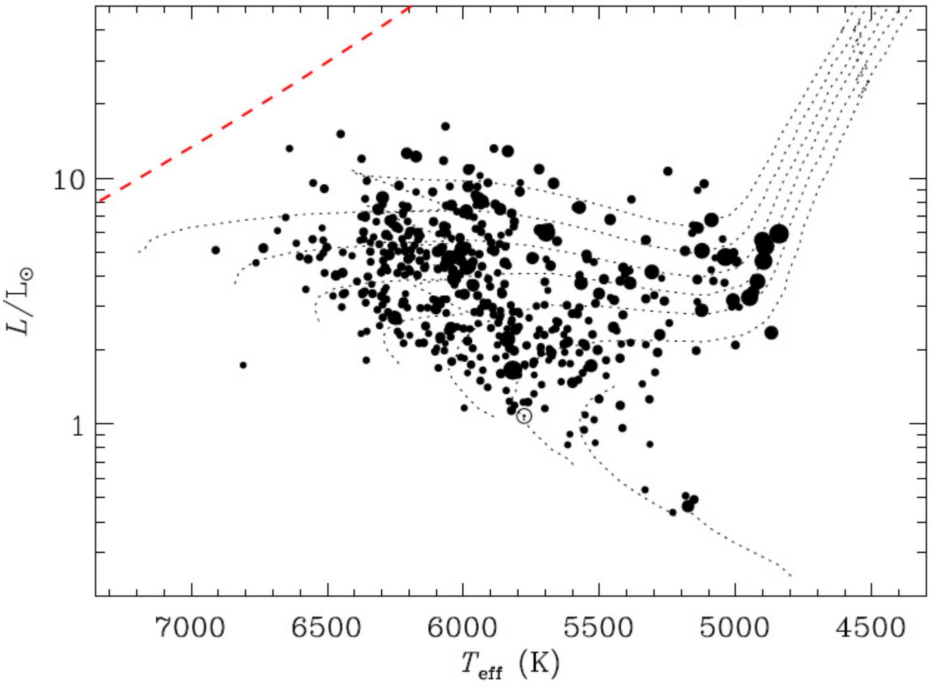

Figure 1.22: H-R diagram of solar-type stars displaying solar-like oscillations from seven months of *Kepler* survey data - Symbol size is proportional to the SNR in the acoustic spectrum. The location of the Sun is indicated with the usual solar symbol. Dotted curves represent evolutionary tracks for solar composition, computed for masses ranging from 0.7 to 1.5 $M_\odot$. The dashed red line marks the location of the red edge of the Cepheid instability strip. Adapted from Chaplin et al. (2011b).

which operates in an Earth-trailing heliocentric orbit, consists of a 95-cm aperture photometer with a CCD array capable of producing photometric observations with a precision of a few ppm during a period of 4–6 years. The high-quality data provided by *Kepler* are also well suited for conducting asteroseismic studies of stars as part of the *Kepler* Asteroseismic Investigation (KAI; Gilliland et al. 2010a). Photometry of the vast majority of these stars is conducted in long-cadence mode (29.4 minutes; see Jenkins et al. 2010), whereas a revolving selection of up to 512 stars are monitored in short-cadence mode (58.85 seconds; see Gilliland et al. 2010b).

Short-cadence data are necessary in order to investigate solar-like oscillations in main-sequence and subgiant stars, whose dominant periods are of the order of several minutes (e.g., Chaplin et al. 2010; Metcalfe et al. 2010). Christensen-Dalsgaard et al.

(2010) reported the first application of asteroseismology to known exoplanet-host stars in the *Kepler* field. During the first seven months of *Kepler* science operations, an asteroseismic survey of solar-type stars – each star being observed for one month at a time in short-cadence mode – made it possible to detect solar-like oscillations in about 500 targets (see Fig. 1.22). This constitutes an increase of one order of magnitude in the number of such stars with confirmed oscillations (Chaplin et al. 2011b). This large, homogeneous data sample opens the possibility of, for the first time, conducting ensemble asteroseismology on a population of solar-type field stars (see Sect. 3.3.2). A statistical survey of trends in relevant seismic parameters will allow tests of basic scaling relations, comparisons with trends predicted from models, and lead to crucial insights on the detailed modeling of stars (e.g., Chaplin et al. 2011a,c; Huber et al. 2011b; Verner et al. 2011b; White et al. 2011a). Performing what might be called differential (or comparative) seismology is also made possible by picking from a large ensemble pairs, small groups, or sequences of stars sharing common stellar properties such as mass, composition, or surface gravity (e.g., Silva Aguirre et al. 2011b). This allows eliminating any dependence of the results on the common property, or properties. Since the start of the mission, a selection of survey stars have been continuously monitored in short-cadence mode to test and validate the time-series photometry, five of which show evidence of solar-like oscillations. The analysis of two of these solar-like oscillators, namely, KIC 10273246 and KIC 10920273, is presented in Campante et al. (2011). This article can be found as a supplement in Appendix C. Two other such oscillators, namely, KIC 11395018 and KIC 11234888, are analysed in a companion paper (see Sect. 3.3.3; Mathur et al. 2011).

Studies of large samples of long-cadence G and K giants, extending in luminosity from the red clump down to the bottom of the giant branch, have shown clear evidence of the presence of $l = 3$ modes (Bedding et al. 2010a), while confirming theoretical scaling laws (Huber et al. 2010; Hekker et al. 2011b) and allowing the computation of asteroseismic fundamental parameters (Kallinger et al. 2010a). Photometric data of red giants in the open cluster NGC 6819 allowed a first clear detection of solar-like oscillations in cluster stars to be made, and provided additional tests for cluster membership based on the analysis of the asteroseismic parameters (Stello et al. 2010). Other seismic studies of red giants in open clusters ensued (e.g., Basu et al. 2011; Hekker et al. 2011a).

Chapter 2

Data analysis in asteroseismology

This chapter is intended as a practical guide into some of the main data analysis methods and techniques employed contemporarily in asteroseismology of solar-like stars, and of which I have made recurrent use. The goal has been, since the very beginning, to produce a text that could prove useful to initiate graduate students, by providing them with a solid background in data analysis in asteroseismology, a mere starting point from which they can follow their own paths. From my own personal experience, I must say that this sort of manuals are indeed hard to come across with and increasingly so for the initiate student. The interested reader may also want to consult Hans Kjeldsen's notes on *Time Series Analysis in Astrophysics*[1] and the very useful crash course in data analysis presented in Appourchaux (2011).

The way matters are presented in this chapter does not deviate much from the structure adopted in the latter work. The subjects of digital signal processing and spectral analysis are treated first. These concern the acquisition of continuous physical signals to be subsequently digitally analysed. Notice that the instrumentation, although being itself an integrant part of the data analysis process, is beyond the scope of this dissertation and is thus not explicitly discussed here. The subjects of hypothesis testing and parameter estimation are discussed next both from the competing Bayesian and frequentist points of view. Finally, the implementation of a pipeline for mode parameter analysis of *Kepler* data is described.

---

[1] `http://owww.phys.au.dk/~hans/tidsserie/`

2.1 Digital signal processing and spectral analysis

2.1.1 Nyquist sampling theorem and aliasing

Let us assume that $s(\tau)$ is the time-averaged value of some continuous signal $x(t)$ around $t = \tau$:

$$s(\tau) = \frac{\int_{-\infty}^{+\infty} w(t-\tau)x(t)\,\mathrm{d}t}{\int_{-\infty}^{+\infty} w(t-\tau)\,\mathrm{d}t}\;, \tag{2.1}$$

where $w(t)$ is a suitable weighting function. Ideally, $w(t) = \delta(t)$ (the impulse or Dirac delta function) and, in that particular case, the result of sampling a continuous signal at uniform intervals separated by Δt is represented by the product of the signal and a set of impulse functions regularly spaced in time. Bearing in mind that the Fourier transform of such a set of impulse functions is another set of impulse functions with separation $1/\Delta t$ in the frequency domain, one can use the convolution theorem to show that the transform of a properly sampled band-limited signal $x(t)$ is periodic, with each of its periods being equal to (within a constant) the transform of the continuous signal:

$$x(t) \sum_{n=-\infty}^{+\infty} \delta\,(t - n\,\Delta t) \Longleftrightarrow X(\nu) * \frac{1}{\Delta t} \sum_{n=-\infty}^{+\infty} \delta\left(\nu - \frac{n}{\Delta t}\right)\;, \tag{2.2}$$

where $X(\nu)$ is the Fourier transform of $x(t)$, the symbol "$\Longleftrightarrow$" indicates a Fourier pair, and the symbol "$*$" denotes convolution. Therefore, information is not lost about the original continuous signal $x(t)$, which can be identically reconstructed by filtering a single undistorted period out of the transform in Eq. (2.2) and then taking its inverse Fourier transform. In practice, however, the original signal can only be approximately recovered since we observe for a finite amount of time.

At this point, I find it appropriate to introduce a very important concept, to be specific, that of the spectral window. For that purpose use is made of Eq. (2.2). In this idealized example, the window function (i.e., the observational window) is given by $\sum_{n=-\infty}^{+\infty} \delta\,(t - n\,\Delta t)$. The spectral window is simply the Fourier transform of the window function and is thus given by $\frac{1}{\Delta t}\sum_{n=-\infty}^{+\infty} \delta\left(\nu - \frac{n}{\Delta t}\right)$ in the current example. It is important to retain that the Fourier transform of a windowed signal is given by the convolution of the spectral window with the transform of the continuous and uninterrupted version of the signal (see Eq. 2.10 below for the case of finite and discrete sampling).

But what is meant by a properly sampled signal, as mentioned above? The answer to this question is given by the Nyquist sampling theorem (also known as the Nyquist-Shannon sampling theorem; Nyquist 1928; Shannon 1949): It states that if the Fourier transform of a continuous signal $x(t)$ is band-limited[1], i.e., is zero for all $|\nu| \geq \nu_{\rm lim}$, then $x(t)$ can be uniquely reconstructed from a knowledge of its sampled values at uniform intervals of $\Delta t \leq 1/(2\,\nu_{\rm lim})$ (see Fig. 2.1). For a given uniform sampling interval Δt, the Nyquist frequency is defined as $\nu_{\rm Nyq} = 1/(2\Delta t)$. In case the continuous signal being sampled contains frequency components above the Nyquist frequency, these will give rise to an effect known as aliasing, whereby the original spectrum will be distorted due to spectral leaking. The signal is then said to be undersampled and can no longer be uniquely recovered (see Fig. 2.2). The Nyquist frequency can be thought of as the highest useful frequency to search for in the spectrum, although some authors will argue that, based on astrophysical arguments, one can also accept frequencies above $\nu_{\rm Nyq}$.

Going back to Eq. (2.1), a more realistic choice of $w(t)$ would be that of a rectangular pulse of width $\Delta t_{\rm int} \leq \Delta t$, thus mimicking the effect of integration of the detector, normally a CCD. This results in multiplication of the transform of the continuous signal by $\mathrm{sinc}(\nu\,\Delta t_{\rm int})$:

$$\left[x(t) * \frac{1}{\Delta t_{\rm int}}\,\Pi\left(\frac{t-\Delta t_{\rm int}/2}{\Delta t_{\rm int}}\right)\right] \sum_{n=-\infty}^{+\infty} \delta\,(t - n\,\Delta t) \Longleftrightarrow$$
$$\Longleftrightarrow \left[X(\nu)\,\mathrm{sinc}(\nu\,\Delta t_{\rm int})\,\mathrm{e}^{\mathrm{i}\,\pi\nu\Delta t_{\rm int}}\right] * \frac{1}{\Delta t} \sum_{n=-\infty}^{+\infty} \delta\left(\nu - \frac{n}{\Delta t}\right)\,, \tag{2.3}$$

where $\Pi\left(\frac{t-\Delta t_{\rm int}/2}{\Delta t_{\rm int}}\right)$ is a boxcar function of width $\Delta t_{\rm int}$ centered at $\Delta t_{\rm int}/2$. Therefore, integration reduces the amplitude of the high-frequency noise in the time series, an effect that is maximal for a fill cycle of 100%, i.e., for $\Delta t_{\rm int} = \Delta t$. In truth, the asteroseismic signal is not band-limited, meaning that the highest frequencies will not be properly sampled, ultimately resulting in an undersampled signal. In the solar case, the power of the background signal at high frequencies shows a drop-off proportional to ν^{-2}, or possibly even more accentuated (e.g., Karoff 2012). Therefore, it is critical to make sure that the fill cycle is as high as possible, thereby helping to reduce the aliasing

---

[1] Conversely, if $x(t)$ is time-limited, i.e., is zero for all $|t| \geq T/2$, then $x(t)$ can be uniquely reconstructed from samples of its transform, $X(\nu)$, at frequency intervals of $1/T$.

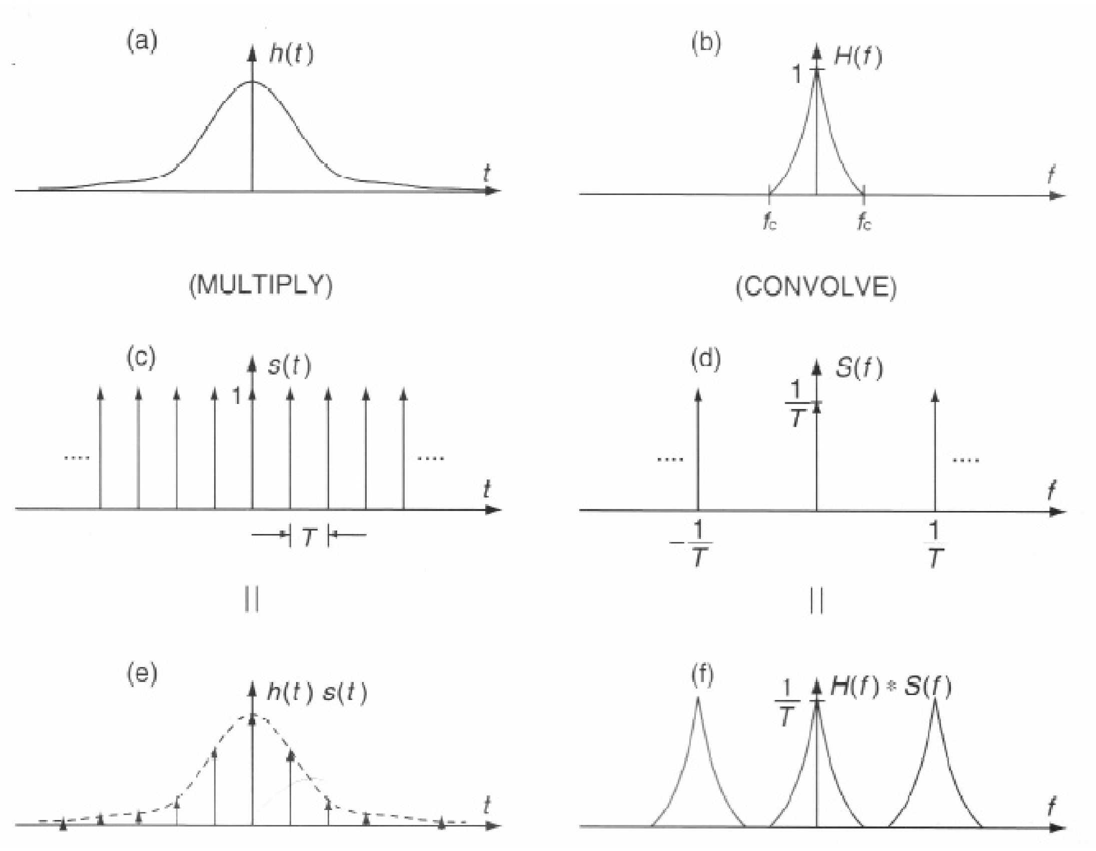

Figure 2.1: Illustration of the Nyquist sampling theorem (proper sampling) - Panels (a) and (b) respectively represent a continuous waveform, $h(t)$, and its band-limited Fourier transform, $H(f)$. Panels (c) and (d) respectively represent the window function, $s(t)$, and the spectral window, $S(f)$. Panels (e) and (f) respectively represent the sampled waveform, $h(t)s(t)$, and its Fourier transform, $H(f) * S(f)$. From Gregory (2005).

effects. The VIRGO/SPM instrument on board *SOHO*, for example, has a fill cycle of about 94% (Fröhlich et al. 1997).

When the available data are not uniformly sampled there is, strictly speaking, no Nyquist frequency, even though equivalent frequencies have been suggested in the literature (e.g., Bretthorst 2000). Choosing an adequate value depends on the magnitude of the departure from uniformity of the sampling intervals. If large, it has been shown that $\nu_{\rm Nyq}$ could in fact be controlled by the greatest common divisor of the sampling intervals; if small, $\nu_{\rm Nyq}$ can be estimated using either the mean or the median sampling interval.

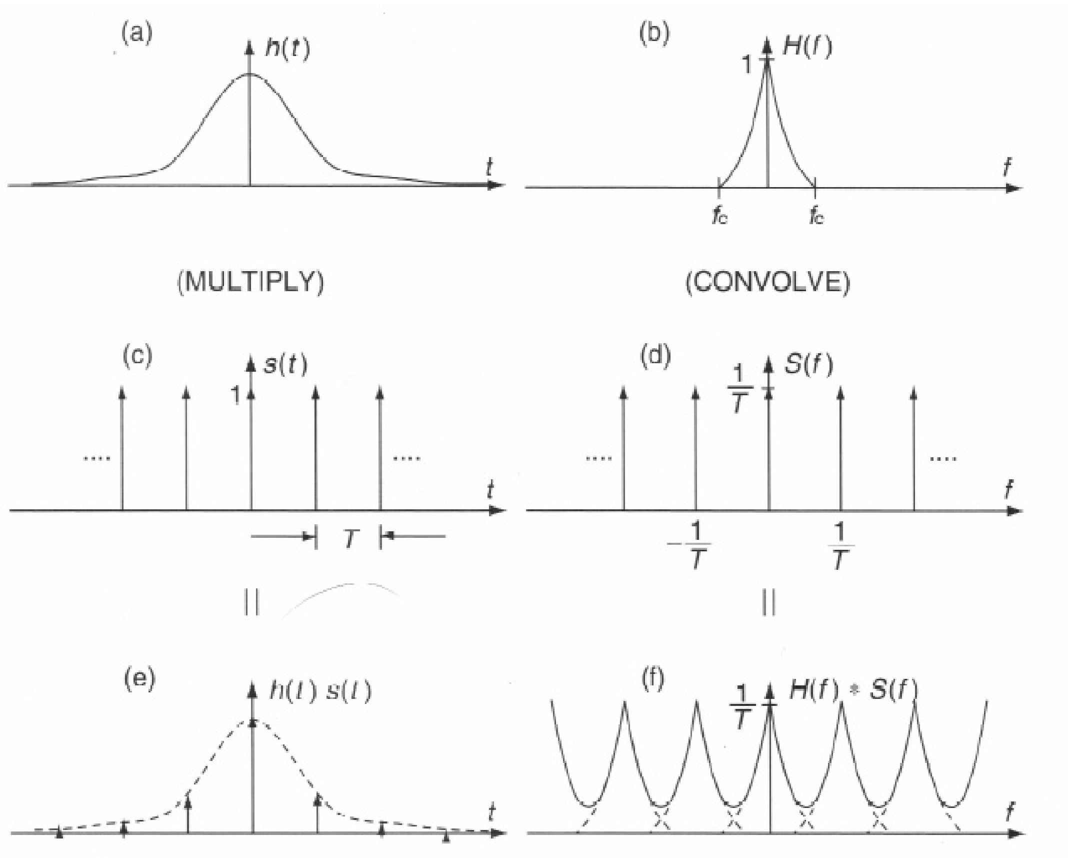

Figure 2.2: Illustration of the Nyquist sampling theorem (undersampling) - Similar to Fig. 2.1 but for the case of an undersampled signal. From Gregory (2005).

Regular gaps in the time series due to diurnal interruptions and, for data sets spanning more than one year, caused by the annual motion of the Earth, are usually present in asteroseismic observations carried out from the ground. These regular gaps also give rise to frequency aliasing. The former kind of so-called daily aliases, appearing at splittings of ±1 cycle/day (or, equivalently, $\pm 11.57\,\mu$Hz) and their non-zero multiples (see Fig. 1.20), are particularly problematic when observing solar-like oscillations since frequency separations of that same magnitude are common. A similar occurrence concerns the *CoRoT* satellite. The extra noise associated with data collected by *CoRoT* while passing across the South Atlantic anomaly (e.g., Auvergne et al. 2009) gives rise to strong harmonics of the satellite's orbital frequency (see Fig. 2.3).

The effect on the spectral window caused by the presence of regular gaps in the

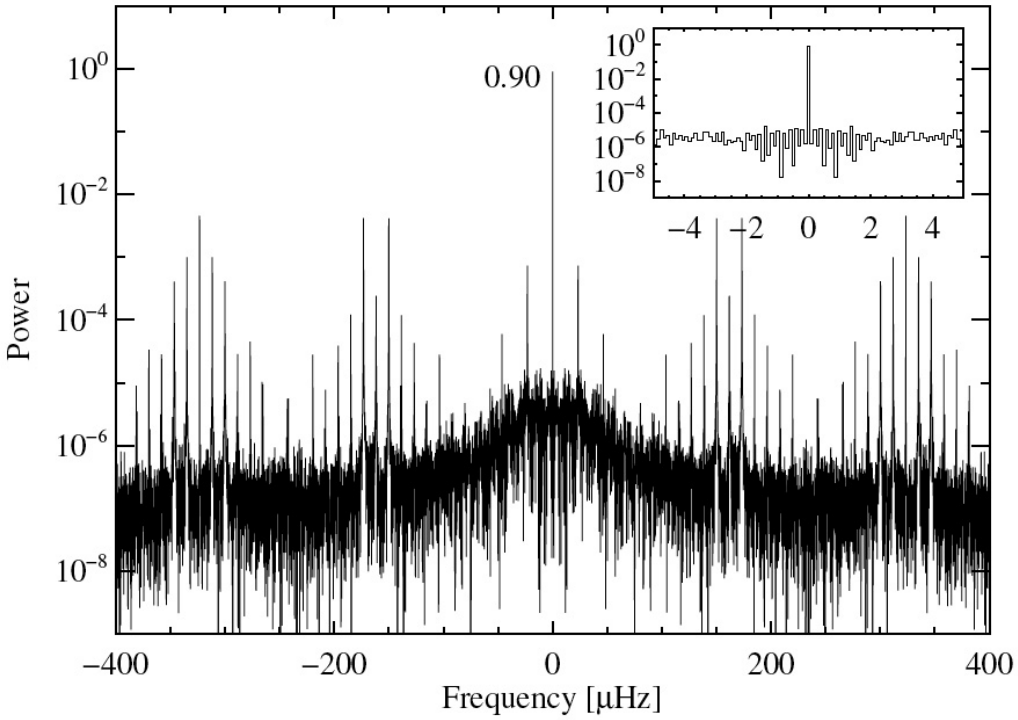

Figure 2.3: Power spectral window for *CoRoT* observations of HD 52265 - A forest of peaks corresponding to the orbital frequency (161.7 μHz), its harmonics, and also daily aliases are clearly visible on a logarithmic scale. The inset provides a close-up around zero frequency. The power spectral window has been normalized so that the ordinate at zero frequency takes the value of the fractional duty cycle. From Ballot et al. (2011).

time series can be understood by means of a simple idealized example. Let us start by constructing a window function that is the result of the convolution of a boxcar function of width T_0 with a set of impulse functions with separation $T > T_0$. Such a window function then simply consists of a series of boxcar functions of width T_0 whose midpoints are separated at uniform intervals of T. Taking $T = 1$ day and $T_0 = 1/3$ day, for example, could very well correspond to the window function obtained from a single-site ground-based campaign where one observes during 8 hours every night. Let us compute the corresponding spectral window:

$$\frac{1}{T_0}\,\Pi\!\left(\frac{t}{T_0}\right) * \sum_{n=-\infty}^{+\infty} \delta\,(t - n\,T) \Longleftrightarrow \mathrm{sinc}(\nu T_0)\,\frac{1}{T}\sum_{n=-\infty}^{+\infty} \delta\left(\nu - \frac{n}{T}\right) . \qquad (2.4)$$

The spectral window thus results from the product of a sinc function and a bed of nails. As T_0 increases (i.e., increasing duty cycle) the central lobe of the sinc function becomes narrower with an accompanying reduction of the aliases at $\pm 1/T$. In the limit when $T_0 \rightarrow T$, i.e., the data recording is continuous and its length infinite, the spectral window is an impulse function and the aliases consequently vanish.

2.1.2 Temporal filtering

A problem commonly encountered while analysing asteroseismic time series is the presence of low-frequency drifts which can be either of instrumental origin or else intrinsic to the star. These low-frequency drifts introduce a background in the Fourier domain that will ultimately lead to a decrease of the SNR of the oscillation modes in the power spectrum. In order to prevent this from happening, high-pass filters are widely used, ideally reducing the effect of the drifts while preserving the relevant signals.

Let us start by shedding some light on the process of smoothing of a time series, which can usually be interpreted as an application of a low-pass filter. Smoothing consists in convolving a signal $x(t)$ with a weighting function $w(t)$ (possibly complex) in the time domain:

$$x_{\text{low}}(t) = x(t) * w(t) \Longleftrightarrow X_{\text{low}}(\nu) = X(\nu)\, W(\nu)\,, \tag{2.5}$$

where $X(\nu)$ and $W(\nu)$ are the transforms of $x(t)$ and $w(t)$, respectively. Conversely, a high-pass filter can be implemented by simply computing $x_{\text{high}}(t) = x(t) - x_{\text{low}}(t)$:

$$x_{\text{high}}(t) \Longleftrightarrow X_{\text{high}}(\nu) = X(\nu)\,[1 - W(\nu)]\ . \tag{2.6}$$

Typical examples of the weighting function $w(t)$ are a boxcar function, a triangular function (equivalent to the convolution of two boxcar functions), and a bell-shaped function (equivalent to the convolution of four boxcar functions or two triangular functions). The transform of the simple boxcar function is the sinc function and thus leads to an excessive ringing (or Gibbs-like) effect in the Fourier domain. Multiple-boxcar smoothing is therefore advisable as a means to suppress this ringing effect. It is up to the data analyst, however, to carefully take into consideration the trade-off between ringing artifacts and frequency-domain sharpness.

A commonly used high-pass filter in helioseismology is the backwards-difference filter (e.g., García & Ballot 2008):

$$x_{\mathrm{bd}}(t) = x(t) - x(t-t_0) = x(t) - [x(t) * \delta(t-t_0)] \ , \tag{2.7}$$

where a time shift t_0 has been considered, while becoming apparent that $w(t) = \delta(t-t_0)$ in Eq. (2.5). Using Eq. (2.6), one can then determine the transfer function of the backwards-difference filter:

$$|1 - W(\nu)|^2 = \left[2 \sin \left(\frac{\pi}{2} \frac{\nu}{\nu_{\mathrm{c}}} \right) \right]^2 , \tag{2.8}$$

where the cut-off frequency, $\nu_{\mathrm{c}} = 1/(2\,t_0)$, has been introduced.

2.1.3 Discrete Fourier Transform

Attention is now drawn to the computation of an estimate of the Fourier transform of a function based on a finite number of samples. Suppose there are N evenly spaced available samples $x(t_n) = x(n\Delta t)$ at intervals of Δt, with $n = 0, 1, 2, \ldots, N-1$. Then according to the Nyquist sampling theorem (see Sect. 2.1.1), useful frequency information is only obtainable for $|\nu| \leq \nu_{\mathrm{Nyq}} = 1/(2\Delta t)$. The Discrete Fourier Transform (DFT) is defined as:

$$X_{\mathrm{DFT}}(\nu_p) = \sum_{n=0}^{N-1} x(t_n)\, \mathrm{e}^{\mathrm{i}\, 2\pi\nu_p t_n} \quad \text{for } \nu_p = p/(N\Delta t)\,,\ p = 0, 1, 2, \ldots, N-1\,. \tag{2.9}$$

The transform $X_{\mathrm{DFT}}(\nu)$ has periodicity $1/\Delta t$ or twice the Nyquist frequency. Then $p = 0$ corresponds to the DFT at zero frequency and $p = N/2$ to the value at $\pm\nu_{\mathrm{Nyq}}$. Values of p between $N/2+1$ and $N-1$ correspond to values of the DFT for negative frequencies from $-(N/2-1)/(N\Delta t)$ to $-1/(N\Delta t)$.

For deterministic processes (not necessarily periodic), the observed Fourier transform, $X_{\mathrm{DFT}}(\nu)$, results from the convolution of the true Fourier transform $X(\nu)$ with a spectral window $W_{\mathrm{DFT}}(\nu)$ (e.g., Deeming 1975):

$$X_{\mathrm{DFT}}(\nu) = X(\nu) * W_{\mathrm{DFT}}(\nu) \equiv \int_{-\infty}^{+\infty} X(\nu - \nu')\, W_{\mathrm{DFT}}(\nu')\, \mathrm{d}\nu' \,, \tag{2.10}$$

where the Fourier pair composed of the window function and spectral window is given by

$$\sum_{n=0}^{N-1} \delta(t - t_n) \Longleftrightarrow W_{\mathrm{DFT}}(\nu) = \sum_{n=0}^{N-1} \mathrm{e}^{\mathrm{i}\, 2\pi\nu t_n} \,. \tag{2.11}$$

Cooley & Tukey (1965) introduced the Fast Fourier Transform (FFT), an efficient method of implementing the DFT that removes certain redundancies in the computation and speeds up the calculation (the speed enhancement is approximately given by $N \log_2 N/N^2$).

2.1.4 Power spectral density estimation

As astrophysicists we are constantly being faced with the problem of having to analyse waveforms that are in fact random processes. Observations are affected by noise associated with the observed physical phenomenon and the instrumentation. Therefore, it is necessary to develop suitable statistical approaches to spectral estimation.

Here, I present two common approaches to the estimation of the power spectral density of a random process denoted by $x(t)$. But first, a definition of the power spectral density (PSD) needs to be given:

$$P(\nu) = \lim_{T\to\infty} \frac{1}{T} \left| \int_{-T/2}^{T/2} x(t)\, \mathrm{e}^{\mathrm{i}\,2\pi\nu t}\, \mathrm{d}t \right|^2 , \tag{2.12}$$

where T is the length of the data set.

A widely employed approach to the estimation of the PSD is to use the periodogram, also known as the Schuster periodogram and originally introduced in the field of meteorology (Schuster 1905):

$$\hat{P}_{\mathrm{p}}(\nu) = \frac{1}{T} \left| \int_{-T/2}^{T/2} x(t)\, \mathrm{e}^{\mathrm{i}\,2\pi\nu t}\, \mathrm{d}t \right|^2 . \tag{2.13}$$

In practice this usually involves the computation of a FFT.

Before presenting the second approach to spectral estimation, the Wiener-Khintchine theorem (Wiener 1930; Khintchine 1934) is introduced, according to which the power spectral density, $P(\nu)$, and the autocorrelation function, $\phi(\tau)$, are a Fourier pair:

$$\phi(\tau) = \int_{-\infty}^{+\infty} P(\nu)\, \mathrm{e}^{-\mathrm{i}\,2\pi\nu\tau}\, \mathrm{d}\nu \Longleftrightarrow P(\nu) = \int_{-\infty}^{+\infty} \phi(\tau)\, \mathrm{e}^{\mathrm{i}\,2\pi\nu\tau}\, \mathrm{d}\tau\, , \tag{2.14}$$

where

$$\phi(\tau) = \lim_{T\to\infty} \frac{1}{T} \int_{-T/2}^{T/2} x(t)x(t+\tau)\, \mathrm{d}t\, . \tag{2.15}$$

If we further assume that $x(t)$ is a stationary and ergodic process, one then has

$$\phi(\tau) = \mathrm{E}\left[x(t)x(t+\tau)\right] . \tag{2.16}$$

The Wiener-Khintchine theorem is absolutely crucial to the understanding of the spectral analysis of random processes. It straightforwardly explains, for instance, why white noise, whose autocorrelation function is the Dirac delta function, has constant power spectral density.

Since the random process $x(t)$ is observed over a finite time interval, an estimator of $\phi(\tau)$ has to be searched for:

$$\hat{\phi}(\tau) = \frac{1}{T-|\tau|} \int_{0}^{T-|\tau|} x(t)x(t+|\tau|)\,\mathrm{d}t\,, \;\; |\tau| < T\,. \tag{2.17}$$

A second approach to the estimation of the PSD is the so-called correlation or lagged-product estimator (commonly referred to as the Blackman-Tukey procedure; Blackman & Tukey 1958a,b), which can be simply arrived at by employing the Wiener-Khintchine theorem (cf. Eq. 2.14):

$$\hat{P}_{\mathrm{c}}(\nu) = \int_{-\infty}^{+\infty} w(\tau)\hat{\phi}(\tau)\,\mathrm{e}^{\mathrm{i}\,2\pi\nu\tau}\,\mathrm{d}\tau\,, \tag{2.18}$$

where the window function $w(\tau)$ is unit for $|\tau|<T$ and zero elsewhere.

Finally, it can be shown (Jenkins & Watts 1968; Deeming 1975) that the mean (expectation) value of both the periodogram (cf. Eq. 2.13) and the correlation (cf. Eq. 2.18) estimators is given by the convolution of the true power spectral density $P(\nu)$ with the power spectral window, i.e.,

$$\mathrm{E}\left[\hat{P}_{\mathrm{p}}(\nu)\right] = \mathrm{E}\left[\hat{P}_{\mathrm{c}}(\nu)\right] = P(\nu) * W(\nu)\,, \tag{2.19}$$

meaning that the mean value of the estimator will be biased unless, of course, the data recording has infinite duration, in which case $W(\nu)$ is the Dirac delta function. This relationship is essentially the same as that for deterministic processes presented in Eq. (2.10).

2.1.4.1 The discrete case

The discrete form of the PSD is now presented based on the use of Parseval's theorem (Parseval des Chênes 1806). This theorem can be seen as an alternative formulation of the energy conservation principle, stating that the energy in a signal $x(t)$ computed in the time domain equals the energy as computed in the frequency domain:

$$\int_{-\infty}^{+\infty} x^2(t)\,\mathrm{d}t = \int_{-\infty}^{+\infty} |X(\nu)|^2\,\mathrm{d}\nu\,, \tag{2.20}$$

where $X(\nu)$ is the Fourier transform of $x(t)$. One immediately notices that $|X(\nu)|^2$ is an energy spectral density. Recovering the same terminology that has been employed in Sect. 2.1.3, the discrete form of Parseval's theorem is introduced as:

$$\sum_{n=0}^{N-1} x^2(t_n)\,\Delta t = \sum_{p=0}^{N-1} |\Delta t\, X_{\mathrm{DFT}}(\nu_p)|^2 \;\Delta\nu\,, \tag{2.21}$$

where $\Delta\nu = 1/(N\Delta t)$. By analogy with the continuous case, it is obvious that $|\Delta t\, X_{\mathrm{DFT}}(\nu_p)|^2$ is a discrete energy spectral density.

From Eq. (2.21) it can be easily shown that the average signal power, i.e., the ratio of signal energy to its duration, is given by its mean-square amplitude:

$$\begin{aligned} \frac{1}{N\Delta t}\sum_{n=0}^{N-1} x^2(t_n)\,\Delta t &= \frac{1}{N}\sum_{n=0}^{N-1} x^2(t_n) \\ &= \sum_{p=0}^{N-1} \frac{|X_{\mathrm{DFT}}(\nu_p)|^2\;\Delta t}{N}\,\Delta\nu\,, \end{aligned} \tag{2.22}$$

where $|X_{\mathrm{DFT}}(\nu_p)|^2\,\Delta t/N$ can be identified with the two-sided discrete PSD in units of power per unit of bandwidth[1]. It should be noticed that this result can also be derived from Eqs. (2.14) and (2.16) by setting $\tau = 0$:

$$\phi(0) = \int_{-\infty}^{+\infty} P(\nu)\,\mathrm{d}\nu = \mathrm{E}\left[x^2(t)\right]\,. \tag{2.23}$$

Finally, I introduce the one-sided discrete PSD, $P(\nu_q)$, defined only for nonnegative frequencies (with $q = 0, 1, \ldots, N/2$):

$$\begin{aligned} P(\nu_0) &= \frac{\Delta t}{N}\,|X_{\mathrm{DFT}}(\nu_0)|^2\,, \\ P(\nu_q) &= \frac{\Delta t}{N}\left[|X_{\mathrm{DFT}}(\nu_p)|^2 + |X_{\mathrm{DFT}}(\nu_{N-p})|^2\right]\,,\ \ p = 1, 2, \ldots, N/2-1\,, \\ P(\nu_{N/2}) &= \frac{\Delta t}{N}\left|X_{\mathrm{DFT}}(\nu_{N/2})\right|^2\,, \end{aligned} \tag{2.24}$$

where $\nu_{N/2} = 1/(2\Delta t)$, viz., the Nyquist frequency. Furthermore, it follows from Eq. (2.22) that $P(\nu_q)$ is normalized according to

$$\sum_{q=0}^{N/2} P(\nu_q)\,\Delta\nu = \frac{1}{N}\sum_{n=0}^{N-1} x^2(t_n)\,. \tag{2.25}$$

---

[1] To convert to units of power per bin one simply has to multiply by $\Delta\nu$.

2.1.5 Statistics of the power spectrum

In the following I consider the statistics of the power spectrum of a pure noise signal. Let $x(t)$ represent a random process from which a finite number of samples denoted by $x(t_n)$ have been drawn. These samples are assumed to be independent and identically distributed[1] (i.i.d.), with $\mathrm{E}\left[x(t_n)\right]=0$ and $\mathrm{E}\left[x^2(t_n)\right]=\sigma_0^2$ for all n (i.e., the random process is further assumed to be stationary). The DFT of the set $x(t_n)$ (cf. Eq. 2.9) may be decomposed into its real and imaginary parts as:

$$\begin{aligned} X_{\mathrm{DFT}}(\nu_p) &= X_{\mathrm{DFT}}^{\mathrm{Re}}(\nu_p) + \mathrm{i}\, X_{\mathrm{DFT}}^{\mathrm{Im}}(\nu_p) \\ &= \sum_{n=0}^{N-1} x(t_n)\cos(2\pi\nu_p t_n) + \mathrm{i}\sum_{n=0}^{N-1} x(t_n)\sin(2\pi\nu_p t_n)\,. \end{aligned} \tag{2.26}$$

It then follows from the Central Limit theorem that for a large number of samples (i.e., for large N) both $X_{\mathrm{DFT}}^{\mathrm{Re}}(\nu_p)$ and $X_{\mathrm{DFT}}^{\mathrm{Im}}(\nu_p)$ are normally distributed. Finally, given the fact that $X_{\mathrm{DFT}}^{\mathrm{Re}}(\nu_p)$ and $X_{\mathrm{DFT}}^{\mathrm{Im}}(\nu_p)$ are independent and have the same normal distribution, the power spectrum, $|X_{\mathrm{DFT}}(\nu_p)|^2$, of a pure noise signal then has by definition a χ^2 distribution with 2 degrees of freedom.

Bearing in mind that

$$\forall p:\ \mathrm{E}\left[\left(X_{\mathrm{DFT}}^{\mathrm{Re}}(\nu_p)\right)^2\right] = \mathrm{E}\left[\left(X_{\mathrm{DFT}}^{\mathrm{Im}}(\nu_p)\right)^2\right] = \frac{N}{2}\sigma_0^2\,, \tag{2.27}$$

and adopting $|X_{\mathrm{DFT}}(\nu_p)|^2\,\Delta t/N$ as our normalization of the power spectrum, yields a constant power spectral density for the noise given by $\sigma_0^2\Delta t$. Consequently, at a fixed frequency bin, the probability density, $p(z)$, that the observed power spectrum takes a particular value z, is given by

$$p(z) = \frac{1}{\sigma_0^2\Delta t}\exp\left(-\frac{z}{\sigma_0^2\Delta t}\right)\,, \tag{2.28}$$

having mean $\langle z\rangle = \sigma_0^2\Delta t$ and variance $\sigma_z^2 \equiv \langle z^2\rangle - \langle z\rangle^2 = \left(\sigma_0^2\Delta t\right)^2$. The probability density function of an exponential distribution with unit mean and unit variance is displayed in the right-hand panel of Fig. 2.5.

Equation (2.28) enables one to derive the probability that the power in one bin is greater than m times the mean level of the continuum, $\langle z\rangle$:

$$F(m) = \mathrm{e}^{-m}\,. \tag{2.29}$$

---

[1] This would be the case for white Gaussian noise, although here I consider the more general case of an unknown distribution.

For a frequency band containing M bins, the probability that at least one bin has a normalized power greater than m is then (e.g., Chaplin et al. 2002):

$$F_M(m) = 1 - (1 - \mathrm{e}^{-m})^M \,, \tag{2.30}$$

which approximates to $F_M(m) = M\mathrm{e}^{-m}$ for $\mathrm{e}^{-m} \ll 1$. Based on Monte Carlo simulations, Gabriel et al. (2002) found that, to account for the modified statistics resulting from oversampling[1] the spectrum, the number of original bins M in the frequency interval being considered should be multiplied by a factor ζ, which is a function of the oversampling factor (see their table 1):

$$F_M(m) = 1 - (1 - \mathrm{e}^{-m})^{M\zeta} \,. \tag{2.31}$$

Surprisingly, as N tends to infinity by sampling a longer stretch of data, the variance (σ_z^2) in the power spectrum remains unchanged. The information resulting from the introduction of additional sampled points goes instead into producing estimates at a greater number of discrete frequencies ν_p. This rather frustrating property can be seen in Fig. 1.8 by comparing panel (c) with panels (a) and (b). There are, however, ways of reducing the variance in the power spectrum. A very simple technique consists in partitioning the original time series into k segments of equal length, computing their separate power spectra and finally averaging them. Despite the spectral resolution of the average spectrum being k times lower than that of the original spectrum, its variance has now decreased by the same factor k. It should be noted that the statistics of the average power spectrum now follows a χ^2 distribution with $2k$ degrees of freedom (Appourchaux 2003). The effect of reducing the variance in the power spectrum can be seen in panel (d) of Fig. 1.8. There, the fact that the random excitation arises from a system in statistical equilibrium means that averaging the power spectrum over a large number of realizations will reduce the erratic behavior while preserving the spectral feature.

Although stationarity is generally satisfied by the random processes under consideration, the same is not true about the property of their samples being i.i.d., since these processes may in fact have a memory. Nonetheless, it has been shown (Peligrad & Wu

---

[1] This is achieved by zero-padding the time series, i.e., adding zeros onto the end of the series. Zero-padding is frequently used to accurately determine the amplitudes of intrinsically narrow spectral features.

2010) that even in that event both components of the Fourier transform are normally distributed with zero mean and the same frequency-dependent variance.

A very interesting observational property of stochastically-excited modes can now be tackled. Let us recall Eqs. (1.39) and (1.40), respectively describing the mode height H of a resolved and an unresolved peak in the power spectrum. We define the noise-to-signal ratio, β, of a given mode as:

$$\beta \equiv B/H = \begin{cases} (\pi\sigma_0^2\Gamma\Delta t)/(2V_{\mathrm{rms}}^2) & \text{for } T \gg 2\tau\,; \\ \sim (\sigma_0^2\Delta t)/(V_{\mathrm{rms}}^2 T) & \text{for } T \ll 2\tau\,. \end{cases} \tag{2.32}$$

Here, $B = \langle z \rangle = \sigma_0^2\Delta t$, represents the mean noise level. Therefore, given fixed noise and mode characteristics, and a chosen observational cadence, the noise-to-signal ratio cannot be improved with time once a mode is resolved, i.e., for $T \gg 2\tau$ (Chaplin et al. 2003).

2.1.6 Generalized Lomb-Scargle periodogram

In astrophysics it is very common to deal with unevenly sampled time series. In that event, an existing frequentist statistic known as the Lomb-Scargle periodogram (Lomb 1976; Scargle 1982, 1989) is widely used as a replacement for the Schuster periodogram, the latter being only suitable in the case of uniform sampling. In the following I introduce the generalized Lomb-Scargle periodogram (Bretthorst 2001b), which reduces to the Lomb-Scargle periodogram for a real stationary sinusoid.

Let us assume the general case of quadrature data sampling, i.e., involving the measurement of the real and imaginary parts of a complex signal. I let $x_{\mathrm{Re}}(t_i)$ denote the set of N_{Re} real data samples taken at times t_i and $x_{\mathrm{Im}}(t'_j)$ denote the set of N_{Im} imaginary data samples taken at times t'_j (total of $N = N_{\mathrm{Re}} + N_{\mathrm{Im}}$ data samples). The sampling is allowed to be non-uniform and it is not required that the t_i and t'_j are simultaneous. Furthermore, the adopted model for both signals is that of a non-stationary single sinusoid, and so one has:

$$x_{\mathrm{Re}}(t_i) = A\cos(2\pi\nu\, t_i - \theta)Z(t_i) + B\sin(2\pi\nu\, t_i - \theta)Z(t_i) + \mathrm{error} \tag{2.33}$$

and

$$x_{\mathrm{Im}}(t'_j) = B\cos(2\pi\nu\, t'_j - \theta)Z(t'_j) - A\sin(2\pi\nu\, t'_j - \theta)Z(t'_j) + \mathrm{error}\,, \tag{2.34}$$

where "error" denotes the misfit between the data and the model, and $Z(t)$ describes an arbitrary amplitude modulation (e.g., exponential decay) whose time dependence and parameters (if any) are fully specified. $Z(t)$ can be thought of as a weighting or apodizing function. The condition that the overall complex model be orthogonal leads to the following definition of the angle θ[1]:

$$\theta = \frac{1}{2}\tan^{-1}\left[\frac{\sum_{i=1}^{N_{\mathrm{Re}}}\sin(4\pi\nu\, t_i)Z^2(t_i) - \sum_{j=1}^{N_{\mathrm{Im}}}\sin(4\pi\nu\, t'_j)Z^2(t'_j)}{\sum_{i=1}^{N_{\mathrm{Re}}}\cos(4\pi\nu\, t_i)Z^2(t_i) - \sum_{j=1}^{N_{\mathrm{Im}}}\cos(4\pi\nu\, t'_j)Z^2(t'_j)}\right]. \tag{2.35}$$

Finally, having adopted the same nomenclature as used by Bretthorst (2001b), the generalized Lomb-Scargle periodogram is given by

$$\overline{h^2} = \frac{R^2(\nu)}{C(\nu)} + \frac{I^2(\nu)}{S(\nu)}\,, \tag{2.36}$$

where

$$\begin{aligned} R(\nu) \;&\equiv\; \sum_{i=1}^{N_{\mathrm{Re}}} x_{\mathrm{Re}}(t_i)\cos(2\pi\nu\, t_i - \theta)\, Z(t_i) \\ &-\; \sum_{j=1}^{N_{\mathrm{Im}}} x_{\mathrm{Im}}(t'_j)\sin(2\pi\nu\, t'_j - \theta)\, Z(t'_j)\,, \end{aligned} \tag{2.37}$$

$$\begin{aligned} I(\nu) \;&\equiv\; \sum_{i=1}^{N_{\mathrm{Re}}} x_{\mathrm{Re}}(t_i)\sin(2\pi\nu\, t_i - \theta)\, Z(t_i) \\ &+\; \sum_{j=1}^{N_{\mathrm{Im}}} x_{\mathrm{Im}}(t'_j)\cos(2\pi\nu\, t'_j - \theta)\, Z(t'_j)\,, \end{aligned} \tag{2.38}$$

$$C(\nu) \;\equiv\; \sum_{i=1}^{N_{\mathrm{Re}}}\cos^2(2\pi\nu\, t_i - \theta)\, Z^2(t_i) + \sum_{j=1}^{N_{\mathrm{Im}}}\sin^2(2\pi\nu\, t'_j - \theta)\, Z^2(t'_j)\,, \tag{2.39}$$

$$S(\nu) \;\equiv\; \sum_{i=1}^{N_{\mathrm{Re}}}\sin^2(2\pi\nu\, t_i - \theta)\, Z^2(t_i) + \sum_{j=1}^{N_{\mathrm{Im}}}\cos^2(2\pi\nu\, t'_j - \theta)\, Z^2(t'_j)\,. \tag{2.40}$$

In the case of a real stationary sinusoidal signal (i.e., $N_{\mathrm{Im}} = 0$ and constant $Z(t)$, respectively), Eqs. (2.37) to (2.40) greatly simplify and the generalized Lomb-Scargle periodogram (cf. Eq. 2.36) reduces to the Lomb-Scargle periodogram. Furthermore, for uniformly sampled quadrature data and a stationary sinusoid it reduces to the Schuster

---

[1] For simultaneous sampling this condition is automatically satisfied and θ is defined to be zero.

periodogram. The term generalized Lomb-Scargle has also been used in the literature by Zechmeister & Kürster (2009) to denote the generalization to a full sine-wave fit, including an offset and statistical weights based on the measurement errors. The two approaches are indeed similar and I invite the interested reader to consult both works and references therein.

I still would like to make a few remarks on the Lomb-Scargle periodogram. The Lomb-Scargle periodogram is actually equivalent to a Least-Squares spectrum (e.g., Horne & Baliunas 1986), viz., the solution obtained by linear least-squares fitting to the model

$$\sum_{i=1}^{N} \left[x(t_i) - a\cos(2\pi\nu\, t_i) - b\sin(2\pi\nu\, t_i)\right]^2 \ . \tag{2.41}$$

For each test frequency ν, solutions are then obtained for the unknowns a and b that are given by $R(\nu)/C(\nu)$ and $I(\nu)/S(\nu)$, respectively, after setting $N_{\mathrm{Im}}=0$ and $Z(t)=1$. In addition, the Lomb-Scargle periodogram has the attractive property of retaining the χ_2^2 statistics (Scargle 1982). Fast computation of the periodogram is achieved using the algorithm presented in Press & Rybicki (1989), whose trick is to carry out extirpolation[1] of the data onto a regular mesh and subsequently employ the FFT, thus obtaining an accurate approximation of the periodogram.

2.1.7 Gapped time series and bin correlations in the Fourier spectrum

The presence of gaps in the time series introduces frequency correlations in complex Fourier space through convolution of the observable with the spectral window (Gabriel 1994). These correlations should be taken into account, especially when performing a fit to the power spectrum (see Sect. 2.2.3). To that end, Stahn & Gizon (2008) describe and implement a rather general method to retrieve maximum likelihood estimates of the oscillation parameters which accounts for the proper statistics of the spectrum. Here, however, I will merely summarize an important result derived in Appourchaux (2011) that proves to be very useful for computing bin correlations in complex Fourier space.

---

[1] Extirpolation is the process by which a function value at an arbitrary point is replaced by several function values on a regular mesh.

Let us assume that a random process denoted by $x(t)$ is observed through a window function $w(t)$. Then the Fourier transform of the windowed signal is given by

$$\tilde{X}(\nu) = \int_{-\infty}^{+\infty} x(t)w(t)\,\mathrm{e}^{\mathrm{i}\,2\pi\nu t}\mathrm{d}t = X(\nu) * W(\nu)\,, \tag{2.42}$$

where $X(\nu)$ and $W(\nu)$ are the transforms of $x(t)$ and $w(t)$, respectively. In his work, Appourchaux (2011) elegantly arrives at the following useful expression for the mean correlation between any two frequency bins in complex Fourier space:

$$\mathrm{E}\left[\tilde{X}(\nu_1)\tilde{X}^*(\nu_2)\right] = 2\int_{-\infty}^{+\infty} \mathrm{E}\left[X_{\mathrm{Re}}^2(\nu)\right] W(\nu_1-\nu)W(\nu-\nu_2)\,\mathrm{d}\nu\,, \tag{2.43}$$

where $X_{\mathrm{Re}}(\nu) \equiv \Re\{X(\nu)\}$ and the superscript asterisk denotes the complex conjugate. An alternative way to express this correlation, not provided in the aforementioned work, is to use Eq. (2.42) to write:

$$\mathrm{E}\left[\tilde{X}(\nu_1)\tilde{X}^*(\nu_2)\right] = \int\int \mathrm{E}\left[x(t)x(t')\right] \mathrm{e}^{\mathrm{i}\,2\pi(\nu_1 \mathrm{t}-\nu_2 \mathrm{t}')}w(t)w(t')\,\mathrm{d}t\,\mathrm{d}t'\,. \tag{2.44}$$

Further assuming that the process is stationary and ergodic, use of Eq. (2.16) then leads to the following alternative formulation:

$$\mathrm{E}\left[\tilde{X}(\nu_1)\tilde{X}^*(\nu_2)\right] = \int\int \phi(\tau)\mathrm{e}^{\mathrm{i}\,2\pi(\nu_1\tau+(\nu_1-\nu_2)\mathrm{t}')}w(\tau+t')w(t')\,\mathrm{d}\tau\,\mathrm{d}t'\,, \tag{2.45}$$

where $\tau = t - t'$.

Let us investigate what happens in the case of a continuous and infinite window function, for which we know the spectral window to be the impulse function $\delta(\nu)$. In this case one has:

$$\mathrm{E}\left[\tilde{X}(\nu_1)\tilde{X}^*(\nu_2)\right] = 2\,\mathrm{E}\left[X_{\mathrm{Re}}^2(\nu_1)\right]\delta(\nu_1-\nu_2)\,, \tag{2.46}$$

where use was made of Eq. (2.43). From Eq. (2.46) it becomes apparent that a given bin is uncorrelated with any other bin in the spectrum.

Furthermore, for slowly varying power spectra, i.e., for which the variations of $\mathrm{E}\left[X_{\mathrm{Re}}^2(\nu)\right]$ are slow with respect to $W(\nu)$, Eq. (2.43) may be rewritten as

$$\begin{aligned}\mathrm{E}\left[\tilde{X}(\nu_1)\tilde{X}^*(\nu_2)\right] &\approx 2\,\mathrm{E}\left[X_{\mathrm{Re}}^2(\nu_1)\right]\int_{-\infty}^{+\infty} W(\nu_1-\nu)W(\nu-\nu_2)\,\mathrm{d}\nu \\ &= 2\,\mathrm{E}\left[X_{\mathrm{Re}}^2(\nu_1)\right]\int_{-\infty}^{+\infty} w^2(t)\mathrm{e}^{\mathrm{i}\,2\pi(\nu_1-\nu_2)t}\,\mathrm{d}\nu \\ &= 2\,\mathrm{E}\left[X_{\mathrm{Re}}^2(\nu_1)\right]W_{\mathrm{sq}}(\nu_1-\nu_2)\,, \end{aligned} \tag{2.47}$$

where the integral, denoted by $W_{\mathrm{sq}}(\nu_1 - \nu_2)$, is simply the Fourier transform of the square of the window function. When observing white noise, $\mathrm{E}\left[X^2_{\mathrm{Re}}(\nu)\right]$ is constant and will be denoted by σ^2. The equality in Eq. (2.47) then holds exactly.

Let us see what happens when the window function is rectangular with width T and centered at $t=0$:

$$\mathrm{E}\left[\tilde{X}(\nu_1)\tilde{X}^*(\nu_2)\right] = 2\sigma^2\,\frac{\sin\left(\pi T(\nu_1 - \nu_2)\right)}{\pi(\nu_1 - \nu_2)}\,. \tag{2.48}$$

Frequency bins are thus uncorrelated at frequency separations that are non-zero multiples of $1/T$, the so-called Rayleigh resolution. And if one would instead opt for apodizing (i.e., weighting) the data, such that the square of the window function becomes a triangular (Barlett) window while keeping T as the length of the observation? The answer can be easily computed:

$$\mathrm{E}\left[\tilde{X}(\nu_1)\tilde{X}^*(\nu_2)\right] = 2\sigma^2\,\left[\frac{\sin\left(\pi T(\nu_1 - \nu_2)/2\right)}{\pi(\nu_1 - \nu_2)}\right]^2\,. \tag{2.49}$$

This would in fact reduce the spectral leakage at high frequencies while increasing it at the low-frequency end. Frequency bins are now uncorrelated at frequency separations that are non-zero multiples of $2/T$.

These simple calculations exemplify how the introduction of weights on the data may induce modifications to bin correlations in Fourier space. Weights are commonly used when analysing ground-based observations of stellar oscillations as a way of taking into account the significant variations in data quality during a typical observing campaign, especially when two or more telescopes are involved. This has certainly been the case in the analysis of the time series of velocity observations obtained for Procyon over 25 days using 11 telescopes at eight observatories (Bedding et al. 2010b). In that work use was made of two alternative weighting schemes, namely, noise-optimized weights and sidelobe-optimized weights (see also Arentoft et al. 2009). Proper account was taken of the weighting by using Eq. (2.47) to determine the effective frequency resolution prior to the computation of the power spectrum.

2.1.8 Bayesian insight into the periodogram

The Schuster periodogram was originally introduced, rather intuitively, in order to detect a periodicity and estimate its frequency. Jaynes (1987), however, demonstrated that the periodogram follows naturally from Bayesian probability theory[1]. Considering the analysis of a time series known to contain a single sine wave with frequency ν_0, which is additionally contaminated with additive independent Gaussian noise with variance σ^2, Jaynes (1987) showed that the posterior probability of the frequency of the periodic sinusoidal signal is approximately given by

$$p(\nu|D,I) \propto \exp\left\{\frac{\hat{P}_{\mathrm{p}}(\nu)}{\sigma^2}\right\} , \tag{2.50}$$

where D and I respectively represent the observed data and the prior information, and $\hat{P}_{\mathrm{p}}(\nu)$ is the Schuster periodogram (cf. Eq. 2.13). The periodogram is defined here as the squared magnitude of the FFT times the reciprocal of the number N of samples drawn. If the noise variance is not a known quantity, then the resulting posterior probability may instead be expressed in the form of a Student's t distribution and is given approximately by (Bretthorst 1988)

$$p(\nu|D,I) \propto \left[1 - \frac{2\,\hat{P}_{\mathrm{p}}(\nu)}{N\overline{x^2}}\right]^{\frac{2-N}{2}} , \tag{2.51}$$

where $\overline{x^2}$ is the mean-square amplitude of the data values. Equations (2.50) and (2.51) do not require the data to be uniformly sampled provided that several specific conditions are met.

By computing the first and second moments of the distribution in Eq. (2.50), Jaynes (1987) also showed that $\langle\nu\rangle = \nu_0$ and that, for a sine wave of amplitude A, the rms error on the determination of the frequency is given by

$$\begin{aligned} \sigma_\nu &= \frac{\sqrt{6}}{\pi}\frac{\sigma}{A}\frac{1}{T\sqrt{N}} \\ &= \frac{\sqrt{6}}{\pi}\frac{\sigma}{A}\frac{\sqrt{\Delta t}}{T^{3/2}} , \end{aligned} \tag{2.52}$$

where T is the length of the observation and the second equality assumes the data to be uniformly sampled at intervals of Δt (a formula also given in Cuypers 1987; Koen 1999; Montgomery & O'Donoghue 1999). Frequency precision is therefore determined by the SNR in the time domain, the length of the observation, and the number of data points. Notice that, for high SNR, frequency precision can greatly surpass the Rayleigh resolution.

---

[1] The topic of Bayesian inference will be dealt with throughout Sect. 2.2.

Bretthorst (2000, 2001a,b) generalized this Bayesian approach to the periodogram to a broader range of single-frequency estimation problems (single sinusoid with arbitrary decay as well as periodic but nonsinusoidal functions) and sampling conditions. An exact Bayesian expression for $p(\nu|D,I)$ was derived that involves a nonlinear processing of the generalized Lomb-Scargle periodogram analogous to the nonlinear processing of the Schuster periodogram in Eq. (2.51):

$$p(\nu|D,I) \propto \frac{1}{\sqrt{C(\nu)S(\nu)}} \left[N\overline{x^2} - \overline{h^2} \right]^{\frac{2-N}{2}} . \tag{2.53}$$

Here, I have recovered the terminology introduced in Sect. 2.1.6, where $\overline{h^2}$ represents the generalized Lomb-Scargle periodogram, and the mean-square amplitude of the data values is defined as

$$\overline{x^2} = \frac{1}{N} \left[\sum_{i=1}^{N_{\mathrm{Re}}} x_{\mathrm{Re}}^2(t_i) + \sum_{j=1}^{N_{\mathrm{Im}}} x_{\mathrm{Im}}^2(t'_j) \right] . \tag{2.54}$$

The latter formalism is not applicable to stochastic oscillators due to the multiplicative nature of the associated noise. In fact, separation between the deterministic signal and the noise is not possible in the time domain for stochastically-excited oscillators, but only in the frequency domain. This same formalism is, however, certainly relevant to the case of classical pulsators, whose oscillations are periodic but not necessarily sinusoidal.

2.1.9 Multisine estimation

Fourier-based methods are well suited to the analysis of sinusoidal oscillations. Even though approaches such as the Lomb-Scargle periodogram (Lomb 1976; Scargle 1982, 1989) and the date-compensated DFT (Ferraz-Mello 1981) take into account sampling irregularities in the time series, they are only statistically valid in the case of a single sinusoid present in the data (Foster 1996). If, on the other hand, multiple sinusoids are present then these are required to be well separated in frequency (Bretthorst 1988), which is not always the case. So how does one proceed when searching for multiple sinusoids in the data?

Multisine estimation is usually performed by employing sequential methods. These methods iteratively remove sinusoidal components from the data while taking into account the effect of the window function in a rather straightforward way. Such components are identified as the maxima of the Fourier spectrum of the residuals after a prewhitening step, i.e., after the contributions of previous estimated frequencies have been removed. This approach is commonly known in the literature as Iterative Sine-Wave Fitting (ISWF). However, due to the presence of noise peaks and sampling artifacts in the Fourier spectrum, these maxima may not correspond to genuine frequencies, thus leading to fatal error propagation. Several refinements of the basic ISWF procedure have been posteriorly developed that aim at improving its efficiency, most notoriously the CLEAN algorithm (Roberts et al. 1987), originally introduced in radio astronomy (Högbom 1974). The CLEAN algorithm as described by Roberts et al. (1987) introduces a clean gain whereby only a fraction of the sinusoidal component is removed at each iteration, in an attempt to prevent the propagation of errors resulting from false detections. Furthermore, since the number of oscillation modes present in the data is unknown a priori, a stopping rule is needed that associates a confidence level to the amplitude of each extracted sinusoidal component (e.g., Breger et al. 1993; Reegen 2004). Although these methods are better suited to the analysis of classical pulsators, they have been successfully employed in the analysis of a number of ground-based observations of solar-like stars (e.g., Bedding et al. 2004; Kjeldsen et al. 2005; Bedding et al. 2007b), always under the assumption that the characteristic mode lifetime is (much) longer than the length of the time series (i.e., that the modes are unresolved). These methods have also been extensively tested on solar-like artificial data (White et al. 2010).

Several other methods exist for multisine estimation. One such method, based on the framework of sparse representations, is suggestively named SparSpec (Bourguignon et al. 2007). SparSpec addresses multisine estimation by reconstructing a high-dimensional vector of spectral amplitudes corresponding to a discrete frequency grid. A sparse representation of the spectrum is desired, i.e., one with the fewest non-zero spectral amplitudes, which can be accomplished by minimizing a convex criterion. In a second article (in preparation) devoted to the solar twin 18 Sco, we compare several different approaches to frequency estimation, including CLEAN, SparSpec, and also Lorentzian-profile fitting techniques (see Sect. 2.2.3 for more on the last-mentioned techniques).

2.1.10 Wavelet analysis

I cannot come up with a better way of finishing the current section than to present a tool performing time-frequency analysis, namely, the wavelet transform. The following discussion is based on the work by Torrence & Compo (1998), who supply a useful guide to wavelet analysis containing examples of its application in the field of geophysics and a link to open-source software. In short, a wavelet-based analysis decomposes a time series into time-frequency space allowing one to determine both the dominant modes of oscillation and their temporal variability. For us, asteroseismologists, I perceive at least two novel domains of application for this sort of tool: (i) in assessing whether or not a given set of modes are stochastically excited (e.g., Belkacem et al. 2009; Antoci et al. 2011) and (ii) in determining the stellar rotational period from the modulation of a light curve caused by photospheric spots (e.g., Mathur et al. 2010a; Ballot et al. 2011; García et al. 2011a).

As a preamble, I should mention the windowed Fourier transform, by which the Fourier transform of a given time series is performed on a running segment of length T. This analysis tool is widely used for time-frequency localization, although in a rather inaccurate and inefficient way, since it imposes a scale T on the analysis. When analysing a signal possibly containing non-stationary power over a wide range of frequencies, one should opt instead for a method of time-frequency localization that is independent of scale, the wavelet transform being such an approach.

Let us start by considering a time series that has been uniformly sampled at intervals of Δt, i.e., $x(t_n) = x(n\Delta t)$, with $n = 0, 1, 2, \ldots, N-1$. We also consider a wavelet function, $\psi_0(\eta)$, which depends on the nondimensional time parameter η, having zero mean and being localized both in time and in frequency space. A common example of such a wavelet function is the Morlet wavelet, assumed hereafter, and which consists of a plane wave modulated by a Gaussian. Finally, the continuous wavelet transform of the set $x(t_n)$ is defined as the convolution of $x(t_n)$ with a scaled and translated version of $\psi_0(\eta)$ that has further been normalized (and so the subscript in ψ_0 is dropped):

$$W_n(s) = \sum_{n'=0}^{N-1} x(t_{n'})\, \psi^* \left[\frac{(n'-n)\Delta t}{s} \right] . \tag{2.55}$$

Therefore, by varying the wavelet scale[1] s and translating along the time index n, one

---

[1] Notice that, for the Morlet wavelet, the equivalent Fourier period is given by $1.03s$.

may generate a diffuse two-dimensional time-frequency image of the signal amplitude. Computation of the wavelet transform is, however, notably faster if done in Fourier space:

$$W_n(s) = \sum_{p=0}^{N-1} \hat{x}_p \, \hat{\psi}^*(s\,\omega_p)\, \mathrm{e}^{\mathrm{i}\,\omega_p n \Delta t}\,, \tag{2.56}$$

where $\hat{x}_p$ is the DFT of $x(t_n)$ and $\hat{\psi}(s\,\omega)$ is the Fourier transform of $\psi(t/s)$. The angular frequency ω_p is in turn defined as

$$\omega_p = \begin{cases} \frac{2\pi p}{N\Delta t} & \text{for } 0 \leq p \leq N/2\,; \\ -\frac{2\pi p}{N\Delta t} & \text{for } N/2 < p \leq N-1\,. \end{cases} \tag{2.57}$$

Moreover, a properly normalized wavelet transform satisfies, for each scale s, the following equality (cf. Eq. 2.56):

$$\sum_{p=0}^{N-1} |\hat{\psi}(s\,\omega_p)|^2 = N\,. \tag{2.58}$$

The wavelet transform is, therefore, weighted solely by the amplitude of the Fourier coefficients $\hat{x}_p$ and not by the wavelet function itself.

The wavelet power spectrum is then simply given by $|W_n(s)|^2$ (see Fig. 2.4 for an example). In order to compare wavelet power spectra arising from different time series, one is obviously interested in finding a common normalization factor. This can be easily done. From Eqs. (2.56) and (2.58), the expectation value of $|W_n(s)|^2$ is N times that of $|\hat{x}_p|^2$. Assuming a white-noise process, the expectation value of $|\hat{x}_p|^2$ is given by[1] σ_0^2/N, with σ_0^2 representing the variance in the time series. Finally, the expectation value of $|W_n(s)|^2$ is given by σ_0^2, and normalization of the wavelet power spectrum by $1/\sigma_0^2$ will then provide a measure of the power relative to white noise.

We should not forget that we will always be dealing with finite-length time series and, since the inverse Fourier transform in Eq. (2.56) assumes the data are cyclic[2], this means that the wavelet power spectrum will be subject to errors at both ends of the time interval. A way of reducing these edge effects consists in padding the time series with enough zeros. This will, of course, introduce discontinuities at both endpoints

---

[1] In the present discussion, a normalization factor of $1/N$ is applied to the definition of the DFT in Eq. (2.9).

[2] Note that sampling in the frequency domain results in a periodic version of the signal in the time domain.

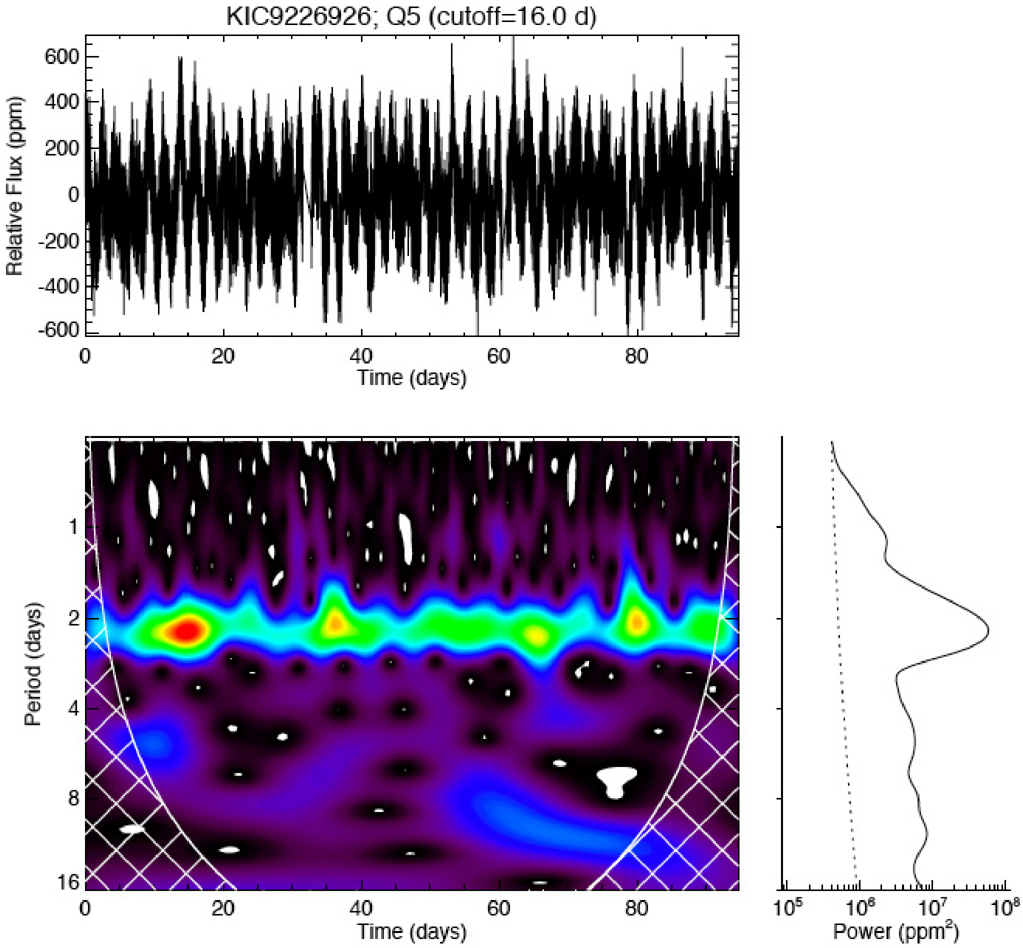

Figure 2.4: Wavelet power spectrum of KIC 9226926 from three months of *Kepler* photometry - The top panel displays the light curve of KIC 9226926 obtained during Quarter 5 (Q5) after being corrected for instrumental perturbations according to García et al. (2011b). The light curve has further been high-pass filtered with a cutoff of 16 days. The corresponding wavelet spectrum is shown on the bottom left-hand panel for periods ranging from 0.5 to 16 days. A signature of the stellar rotational period (first harmonic) can be immediately recognized at a period of approximately 2.2 days, being nearly stationary over the entire observational span. The cone of influence (see discussion in the text) is represented by the hatched area. The bottom right-hand panel depicts the so-called global wavelet spectrum (solid line), i.e., the time-averaged wavelet spectrum. The dotted line represents the 99% confidence level assuming a red-noise background.

and, as we move to larger scales, the amplitude decrease near the edges will, as a result of the larger number of included zeros, be more conspicuous. Hence we define the so-called cone of influence, viz., the region of the wavelet power spectrum where edge effects are significant, underneath which any reading is dubious. The cone of influence is determined by the e-folding time of the autocorrelation of wavelet power at each scale, given by $\sqrt{2}s$ for the Morlet wavelet.

Significance levels can be easily computed for wavelet power spectra based on hypothesis testing (these are, however, not displayed in Fig. 2.4). As a first step one needs to choose an appropriate mean background for the local wavelet power spectrum, defined as a vertical slice through the bottom left-hand panel of Fig. 2.4. This theoretical background spectrum is usually chosen as being either a white- (constant spectral density) or a red-noise (spectral density inversely proportional to frequency squared) spectrum. Moreover, it can be shown that the wavelet power spectrum, $|W_n(s)|^2$, is distributed as χ_2^2. Finally, in order to compute the, say, 95% confidence level for $|W_n(s)|^2/\sigma_0^2$, one simply has to multiply the theoretical background spectrum by the 95th percentile for $\frac{1}{2}\,\chi_2^2$ at each scale (the $\frac{1}{2}$ factor accounts for the degrees of freedom in χ_2^2).

2.2 Statistical inference

2.2.1 Setting the scene: Are you a Bayesian or a frequentist?

This question was posed by Thierry Appourchaux to a few of us, young asteroseismologists, during a doctoral school that took place in Tenerife in the autumn of 2010. The audience fell inconveniently silent as if no one had ever given it any thought.

It was a controversy between Ronald Fisher and Harold Jeffreys, dating back to the first half of the last century, that marked the beginning of two schools of thought with different views on probability and statistics, namely, that of the frequentists and that of the Bayesians. The debate between frequentists and Bayesians relates to the topic of objective versus subjective probabilities. For a frequentist, to whom the laws of physics are deterministic, the probability of an event is identified with the long-run relative frequency with which that event occurs in identical repeats of the experiment or observation. In the frequentist approach probabilities are only assigned to propositions about random variables. The Bayesian, on the other hand, regards the laws of physics as being operational. The Bayesian has recognized that the mathematical rules of probability are not only suitable for calculating relative frequencies of random variables, but can also be interpreted as valid principles of logic for directly computing the probability of any proposition or hypothesis of interest, based on our current state of knowledge. An excellent presentation of the topic of Bayesian logical data analysis is given in the book by Gregory (2005).

I leave the skeptical frequentist (presumably) reader with Edwin T. Jaynes' words on the topic of objectivity versus subjectivity: "The only thing objectivity requires of a scientific approach is that experimenters with the same state of knowledge reach the same conclusion."

2.2.2 Hypothesis testing

Inferring the truth of one or more hypotheses related to some physical phenomenon is one of the main goals in science. As a further matter, the information that we have available is always incomplete, meaning that our knowledge of nature is probabilistic. Consequently, the funny thing about it is that, due to our state of incomplete information, we can never prove any hypothesis is true. Bayesian inference comes to the rescue by allowing us to directly compute the probabilities of two or more competing hypotheses based on the current state of knowledge. On the other hand, the frequentist approach to hypothesis testing is rather indirect. The present discussion on hypothesis testing is adapted from Appourchaux et al. (2010).

2.2.2.1 Frequentist hypothesis testing

In the frequentist approach, the argument of a probability is restricted to a random variable. Since a given hypothesis cannot be considered a random variable, the truth of the hypothesis must be indirectly inferred. Frequentist hypothesis testing thus involves considering each hypothesis individually and deciding whether to reject that hypothesis or fail to reject it, based on the computed value of a suitable choice of statistic. In our case, we will be interested in testing the following two hypotheses:

- H_0 or null hypothesis: We observe pure noise;
- H_1 or alternative hypothesis: We observe a signal embedded in noise.

The test based on the H_0 hypothesis consists in determining a significance level for which peaks in the spectrum have a low probability of being due to noise. It thus tests for the presence of a signal in the data. The test based on the H_1 hypothesis, on the other hand, allows computing the probability that a signal can be detected given its characteristics.

For a mode with a lifetime much longer than the length of the observation, i.e., a long-lived mode, it is assumed that we search for a peak that is restricted to a single frequency bin in the power spectrum. An analytical example based on the detection of a long-lived mode in a power spectrum (e.g., a g mode in the power spectrum of the Sun or an unresolved solar/stellar p mode) will guide the reader throughout the discussion taking place in this and the following section.

Let us start by considering the H_0 hypothesis. The statistics of the power spectrum of a pure noise signal is assumed to be known and taken to be χ^2 with 2 degrees of freedom. I denote by Z the random variable representing the power level in a given bin, which is observed to take a particular value z (cf. Eq. 2.28). Our choice of statistic is simply that of Z[1]. Next we set the false alarm probability or p-value (Scargle 1982), thus defining the detection threshold z_{det}:

$$p = p(Z \geq z_{\mathrm{det}} | H_0) = \mathrm{e}^{-\frac{z_{\mathrm{det}}}{\langle z \rangle}} \, . \tag{2.59}$$

For instance, a confidence level of 95% or, equivalently, a false alarm probability of 5%, leads to a threshold given by $z_{\mathrm{det}} \approx 3\langle z \rangle$. Finally, the probability of having a value of the statistic at least as extreme as the one observed is computed (the so-called detection significance). We are now in a position to make a decision: If the observed power level z_{obs} is greater than z_{det}, then the H_0 hypothesis is rejected; otherwise we fail to reject the null hypothesis. In the former case, the detection significance, given by $p_{\mathrm{obs}} = \mathrm{e}^{-\frac{z_{\mathrm{obs}}}{\langle z \rangle}}$, is quoted. A test based on the H_0 hypothesis was used in helioseismology, for example, by Appourchaux et al. (2000), to impose an upper limit on g-mode amplitudes. A range of similar tests have been applied by Chaplin et al. (2002) in the search for low-degree, low-frequency solar p modes making use of 9 years of BiSON data. Figure 2.5 illustrates the application of a test based on the H_0 hypothesis to the detection of an

---

[1] Such a choice of statistic is not done ad hoc, but can be systematically derived using the Neyman-Pearson lemma (Neyman & Pearson 1933).

unresolved solar p mode. Figure 2.6, on the other hand, illustrates the application of a test based on the H_0 hypothesis to the detection of short-lived stellar p modes.

For the H_1 hypothesis, the characteristics of both the noise and the sought-after signal are assumed to be known. A significance level is then set that defines the acceptance or rejection of that hypothesis. It was based on the H_1 hypothesis that Gabriel et al. (2002) provided the probability of detecting a pure sine wave with given amplitude in GOLF data. Appourchaux (2004) provides tests based both on the H_0 and H_1 hypotheses. In that work, a false alarm test for detecting short-lived p modes is defined and the probability of detecting such modes is given subject to a set of assumptions about their characteristics.

Decisions based on hypothesis testing are prone to errors. For example, it may happen that the H_0 hypothesis be rejected when true (false positive or type I error) or accepted when false (false negative or type II error). A type I error is considered to be more serious[1]. It is not possible, however, to minimize both the type I and type II errors. The usual procedure is then to state the maximum size of the type I error that is tolerable and construct a test procedure that minimizes the type II error. Assuming, for instance, that one is willing to accept a maximum type I error of 5%, then setting $p=0.05$ will minimize the occurrence of a type II error.

The detection significance $p_{\rm obs}$ is often incorrectly regarded as the probability that H_0 is true. The point here is that any particular value of the detection significance may arise even in the event that the alternative hypothesis is true. The detection significance instead tells us how likely the observed data are given the null hypothesis and provided we could repeat our experiment ad infinitum. In the framework of Bayesian inference, one is not interested in the detection significance but in the posterior probability of H_0, viz., the likelihood that H_0 is true given the observed data, $p(H_0|z)$. This is the quantity that we really want to know and its computation will be the subject of the next section.

2.2.2.2 Bayesian hypothesis testing

A preliminary step should be to formally introduce Bayes' theorem (Bayes & Price 1763). Let us consider a set of competing hypotheses, $\{H_i\}$, assumed to be mutually

---

[1] A courtroom analogy would be that the possibility of convicting an innocent party is considered worse than the possibility of acquitting a guilty party.

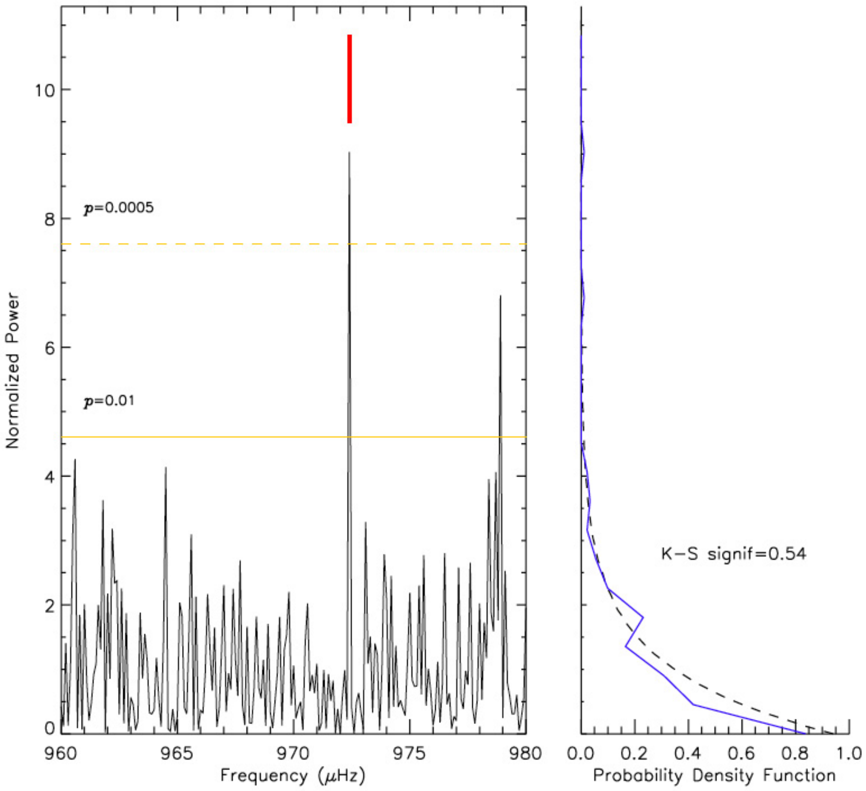

Figure 2.5: Application of a test based on the H_0 hypothesis to the detection of an unresolved solar p mode - The left-hand panel displays the simulated power spectrum of an isolated low-frequency solar $l=0$ mode (its true location being marked by a vertical red dash) normalized to the local background. The mode linewidth was taken to be one tenth of the bin width and its relative height was rather optimistically set to 10 for illustrative purposes only. The solid horizontal line corresponds to the detection threshold obtained by setting $p=0.01$ in Eq. (2.59). According to Eq. (2.30), the chance of finding at least one noise spike within the displayed window (containing 200 bins) at or above this detection threshhold is then of about 87% (with a total of 2 such spikes, on average, expected to be found). A more conservative approach would be to set to, say, 10%, the probability of finding at least one spike within the considered window (or a total of 0.1 spikes on average). This results in $p=0.0005$, corresponding to the dashed horizontal line. The right-hand panel displays the probability density function of the simulated spectral noise (solid curve) and the exponential distribution with unit mean and unit variance (dashed curve) from which noise samples have been drawn. The significance level of the Kolmogorov-Smirnov statistic is indicated, telling us how similar the corresponding cumulative distribution functions are.

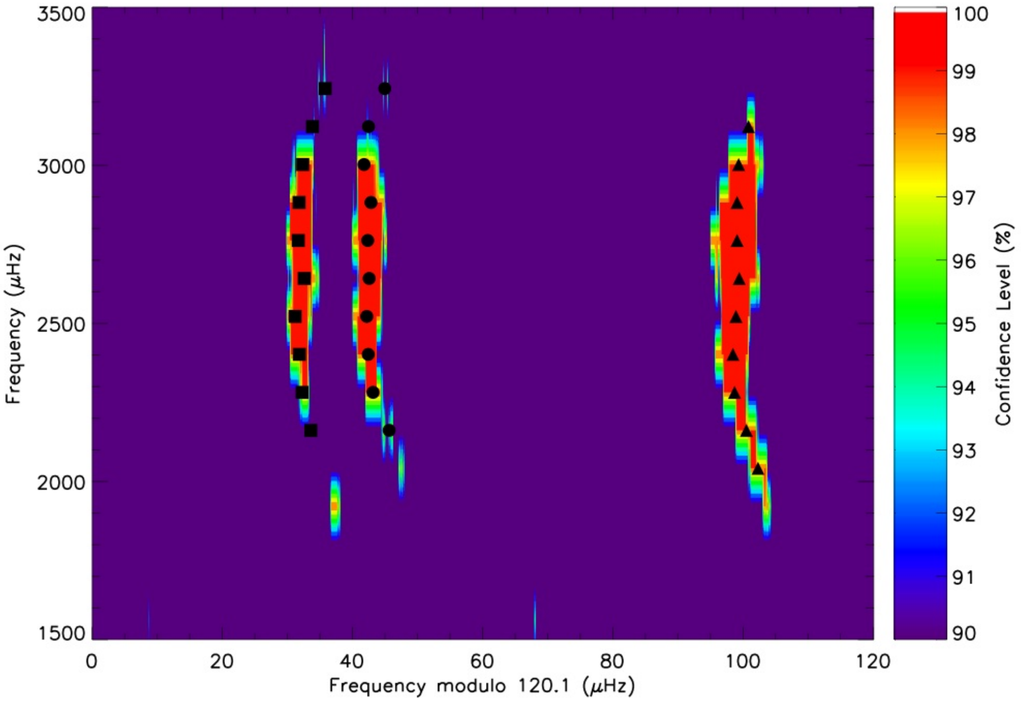

Figure 2.6: Application of a test based on the H_0 hypothesis to the detection of short-lived stellar p modes - In order to keep the discussion as concise as possible, the problem of detecting short-lived modes in a binned power spectrum has not been addressed. Nevertheless, an example is given here of the application of a test based on the H_0 hypothesis to the detection of short-lived modes (cf. Appourchaux 2004). What one may call a probabilistic échelle diagram (i.e., displaying probability instead of power) is plotted based on a 18-month-long time series of KIC 3427720. The displayed frequencies come from the analysis of a subseries of only 9 months long with symbol shapes indicating mode degree: $l=0$ (circles), $l=1$ (triangles), and $l=2$ (squares). A confidence level of, say, 95%, corresponds to a detection threshold such that the probability of finding at least one noise spike within the whole plotted window is 5%. Confidence levels have been clipped to a minimum of 90%. The inclusion of an extra 9 months of photometry allows detecting a few additional modes at the low-frequency range.

exclusive. One should be able to assign a probability, $p(H_i|D,I)$, to each hypothesis, taking into account the observed data, D, and any available prior information, I, arising from theoretical considerations and/or previous observations. This is done through Bayes' theorem:

$$p(H_i|D,I) = \frac{p(H_i|I)\,p(D|H_i,I)}{p(D|I)}\,. \tag{2.60}$$

The probability of the hypothesis H_i in the absence of D is called the *prior probability*, $p(H_i|I)$, whereas the probability including D is called the *posterior probability*, $p(H_i|D,I)$. The quantity $p(D|H_i,I)$ is called the *likelihood* of H_i, $p(D|I)$ being the *global likelihood* for the entire class of hypotheses. Bayesian inference thus encodes our current state of knowledge into a posterior probability concerning each member of the hypothesis space of interest. Moreover, the sum of the posterior probabilities over the hypothesis space of interest is unity, and hence one has:

$$p(D|I) = \sum_i p(H_i|I)\, p(D|H_i, I)\,. \tag{2.61}$$

It now becomes a trivial exercise to derive an expression for $p(H_0|z)$ as a function of $p(z|H_0)$ and $p(z|H_1)$ (Berger & Sellke 1987):

$$p(H_0|z) = \frac{p(H_0)\, p(z|H_0)}{p(H_0)\, p(z|H_0) + p(H_1)\, p(z|H_1)}\,, \tag{2.62}$$

where I believe the nomenclature to be self-explanatory. By setting the prior on H_0 as $p(H_0) = p_0$, one then necessarily has $p(H_1) = 1 - p_0$. The adopted value for p_0 thus reflects our prejudice on which hypothesis is more likely to be true. Finally, we obtain

$$p(H_0|z) = \left(1 + \frac{1-p_0}{p_0}\,\mathscr{L}\right)^{-1}\,, \tag{2.63}$$

where the likelihood ratio $\mathscr{L}$ is defined as:

$$\mathscr{L} = \frac{p(z|H_1)}{p(z|H_0)}\,. \tag{2.64}$$

Hereafter, we set $p_0 = 0.5$. The prescription of Berger et al. (1997) should then be used when performing hypothesis testing:

- If $\mathscr{L} > 1$, reject H_0 and report $p(H_0|z) = 1/(1+\mathscr{L})$;
- If $\mathscr{L} \leq 1$, accept H_0 and report $p(H_1|z) = 1/(1+\mathscr{L}^{-1})$.

Furthermore, Sellke et al. (2001) found that $p(H_0|z)$ has a lower bound given by

$$p(H_0|z) \geq \left(1 - \frac{1}{\mathrm{e}\, p\, \ln p}\right)^{-1}\,, \tag{2.65}$$

where the previously introduced detection significance, given by[1] $p = \mathrm{e}^{-z}$, has been incorporated.

---

[1] From now on we drop the subscript in p_{obs}.

We now recover our analytical example based on the detection of a long-lived mode in a power spectrum. The likelihood of H_0 is simply given by

$$p(z|H_0) = \mathrm{e}^{-z}\,, \tag{2.66}$$

where we have conveniently set the mean noise level to unity in Eq. (2.28), i.e., $\langle z \rangle = 1$. In order to define the likelihood of H_1, we assume that there is a peak corresponding to a long-lived mode. The mode is further assumed to be stochastically excited, being characterized by a known height H. This is a strong prior. The more realistic case of a mode with an unknown height is briefly mentioned below. Since the mean noise level is unity, H can be regarded as the signal-to-noise ratio. We are dealing with multiplicative noise and a proper expression for $p(z|H_1)$ can be found in Moreira et al. (2005):

$$p(z|H_1) = \frac{1}{1+H}\mathrm{e}^{-z/(1+H)}\,. \tag{2.67}$$

Finally, after some manipulation, we rewrite Eq. (2.63) as

$$p(H_0|z) = \left(1 + \frac{1}{1+H}\,p^{-H/(1+H)}\right)^{-1}\,. \tag{2.68}$$

It can be easily shown that Eq. (2.68) has a minimum at $H = -(\ln p + 1)$, where it takes the value:

$$p_{\min}(H_0|z) = \left(1 - \frac{1}{\mathrm{e}\,p\,\ln p}\right)^{-1}\,, \tag{2.69}$$

coinciding with the lower bound given in Eq. (2.65). Take a detection significance of 1% (i.e., $p = 0.01$). The odds against H_0 will then at most be of about 9 : 1 (cf. Eq. 2.69). This means that the likelihood of wrongly rejecting H_0 (type I error) is considerably higher than that suggested by the detection significance. This simple example brings to light a pitfall of frequentist hypothesis testing: the detection significance when rejecting the H_0 hypothesis can lead to the incorrect conclusion that the null hypothesis is unlike to occur at that level of significance (Appourchaux et al. 2009). In conclusion, it should be stated that the posterior probability of H_0 (Bayesian approach) provides a more conservative quantification of a detection when compared to the use of the detection significance (frequentist approach).

In the more realistic case of a mode with an unknown height, the posterior probability of H_0 is instead given by (Appourchaux et al. 2009):

$$p(H_0|z) = \left(1 + \frac{1}{H_\mathrm{u}}\int_0^{H_\mathrm{u}} \frac{1}{1+H'}\,p^{-H'/(1+H')}\,\mathrm{d}H'\right)^{-1}\,, \tag{2.70}$$

where a uniform prior for the mode height in the range $[0, H_\mathrm{u}]$ has been considered. Figure 2.7 displays the behavior of $p(H_1|z)$, i.e., $1-p(H_0|z)$, as a function of signal-to-noise ratio and detection significance p, for modes both with known and with unknown height. One immediately notices that, for a given p, assuming an unknown mode height intuitively causes the probability of detecting the mode to decrease for low to moderate SNR. This effect is reversed at high SNR, when $p(H_1|z)$ enters a downward trend, such trend being more accentuated for a mode with known height. This downward trend is contrary to our intuition and can be easily explained for the case of a mode with known height. In fact, our prior assumption of a high SNR is incorrect, viz., it does not find support in the data. As a consequence, $p(H_1|z)$ is penalized. Finally, the likelihood of wrongly rejecting H_0 (type I error) is considerably higher than that suggested by the value of p (recall discussion above), by a factor that progressively increases as the detection significance increases (i.e., as the magnitude of p decreases).

Broomhall et al. (2010) provide a comparison of frequentist and Bayesian approaches in the search for low-frequency p modes and g modes in Sun-as-a-star data. A Bayesian approach has also been used by Deheuvels et al. (2010) who, based upon posterior probability estimates, made decisions concerning the presence of $l=3$ modes and mixed modes in the power spectrum of the *CoRoT* target HD 49385.

2.2.3 Parameter estimation

2.2.3.1 Modeling the power spectrum

The very first step in such a parameter estimation problem consists in defining an appropriate model of the limit power spectrum. The model will be denoted by $\mathscr{P}(\nu; \boldsymbol{\lambda})$, being described by a set of parameters $\boldsymbol{\lambda}$ which contain the desired information on the physical processes at play. As I have already noted, the power spectrum is distributed around this limit (or mean) spectrum with an exponential distribution (see Sects. 1.4.1 and 2.1.5, as well as Eq. 2.76 below).

Neglecting any asymmetries in the mode profiles, we have seen that the mean spectrum of a single stochastically-excited mode follows a standard Lorentzian profile near the resonance (cf. Eq. 1.28):

$$\mathscr{M}(\nu; H, \nu_0, \Gamma) = \frac{H}{1+\left[\frac{2(\nu-\nu_0)}{\Gamma}\right]^2} \,, \tag{2.71}$$

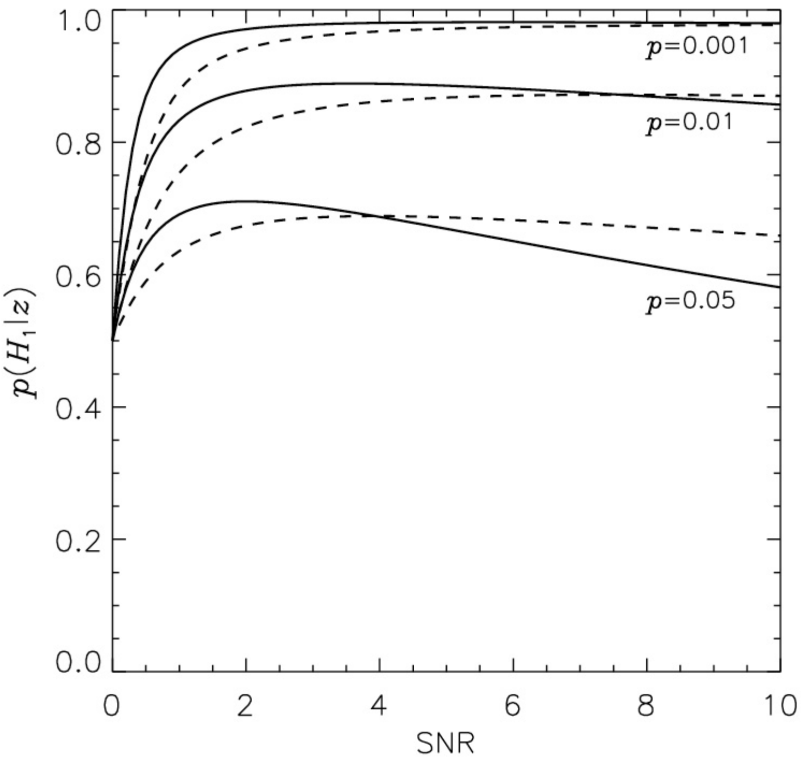

Figure 2.7: Posterior probability of detecting a stochastically-excited long-lived mode - The posterior probability of H_1, i.e., $1-p(H_0|z)$, is shown as a function of signal-to-noise ratio and detection significance p, for modes both with known (via Eq. 2.68; solid lines) and with unknown height (via Eq. 2.70; dashed lines).

where H is the mode height, ν_0 is the mode frequency, and Γ is the mode linewidth. Assuming energy equipartition between multiplet components with different azimuthal order, one may define the following overall profile for a (n, l) multiplet:

$$\mathscr{M}_{nl}(\nu; H_{nl}, \nu_{nlm}, \Gamma_{nlm}, i) = \sum_{m=-l}^{l} \mathscr{E}_{lm}(i)\, \mathscr{M}(\nu; H_{nl}, \nu_{nlm}, \Gamma_{nlm})\,, \tag{2.72}$$

where the $\mathscr{E}_{lm}(i)$ coefficients are given by Eq. (1.23). We have seen in Sect. 1.3.5 how departures from spherical symmetry, particularly when caused by rotation, will lift the degeneracy of the mode frequency ν_{nl}.

We are primarily interested in performing a so-called global fit (e.g., Appourchaux et al. 2008) to the observed power spectrum, whereby several radial orders are fitted simultaneously within a broad frequency range[1]. Therefore, one ends up modeling the limit acoustic power spectrum according to the following general relation:

$$\mathscr{P}(\nu;\boldsymbol{\lambda}) = \sum_n \sum_l \sum_{m=-l}^{l} \frac{\mathscr{E}_{lm}(i)\, H_{nl}}{1 + \left[\frac{2(\nu-\nu_{nlm})}{\Gamma_{nlm}}\right]^2} + S_{\rm bg}(\nu) + B\,, \tag{2.73}$$

where $S_{\rm bg}(\nu)$ has been introduced to describe the background signal (of both instrumental and stellar origin), while B is used to represent the photon shot noise. Depending on the model used, different assumptions are possible that concern the mode and background parameters, which may be extremely useful in order to reduce the dimension of parameter space (e.g., Handberg & Campante 2011).

The stellar background signal results from the superposition of several components related to activity, different scales of granulation, and even faculae. It may be modeled as (e.g., Harvey 1985; Harvey et al. 1993; Aigrain et al. 2004; Karoff 2012):

$$S_{\rm bg}(\nu) = \sum_j \frac{H_j}{1 + (2\pi\nu\tau_j)^{a_j}}\,, \tag{2.74}$$

where H_j is the height in the power spectrum at $\nu = 0$, τ_j is the characteristic time of the decaying autocorrelation function of the process, and a_j determines the slope of this so-called Harvey-like profile. Such functional form is representative of a random non-harmonic field whose autocorrelation decays exponentially with time. The original model by Harvey (1985), having $a_j = 2$, failed to reproduce the observed solar background signal above the acoustic cut-off frequency. Harvey et al. (1993) refined the original model by letting a_j be a free parameter and thus solved the misfit at high frequencies. The exponent a_j calibrates the amount of memory in the process and there is no physical reason why its value should be fixed or even the same for different components. Furthermore, Karoff (2012) argues that the slope of a given component should be different at low and high frequencies based on physical arguments. The instrumental background signal, being also a $1/f$-noise process, may just as well be incorporated in Eq. (2.74).

An important remark should be made at this stage on how we model the mode heights. Once again assuming energy equipartition between multiplet components with

---

[1] Conversely, pseudo-global (or local) fitting (e.g., Jiménez-Reyes et al. 2008) is an approach traditionally adopted for Sun-as-a-star data, whereby narrow frequency windows are considered at a time.

different azimuthal order, their heights may be expressed as:

$$H_{nlm} = \mathscr{E}_{lm}(i)\, H_{nl} = \mathscr{E}_{lm}(i)\, S_l^2\, \alpha_{nl}\,, \tag{2.75}$$

where S_l is the spatial response function introduced in Sect. 1.3.2, and the factor $\alpha_{nl} \approx \alpha(\nu_{nl})$ depends mainly on the frequency. This relation, however, is only strictly valid under one assumption: When the stellar flux is integrated over the full apparent disk, one must assume that the weighting function giving the contribution of a surface element to the integral is a function of the distance to the disk center alone. In that case, the apparent mode amplitude can effectively be separated into two factors: $\mathscr{E}_{lm}(i)$ and S_l^2. This assumption holds very well in the case of intensity measurements, since the weighting function is then mainly linked to the limb darkening, whereas for velocity measurements departures might be observed due to asymmetries in the velocity field induced by rotation (e.g., Ballot et al. 2006). As a means to reduce the number of parameters in our model, the heights of non-radial modes are commonly defined based on the heights of radial modes according to Eq. (2.75) and taking into account the S_l/S_0 ratios as given in Table 1.1.

The final model should be given by the convolution of the model in Eq. (2.73) with the power spectral window normalized to unit total area (Anderson et al. 1990), therefore taking into account the redistribution of power caused by gaps in the data. Inclusion of this last step may result in a computationally demanding implementation of the fitting problem, especially when using Monte Carlo techniques, and therefore should be well pondered.

2.2.3.2 Maximum Likelihood Estimation

In the case of a power spectrum of a solar-like oscillator, for which measurement errors are not normally distributed, one should employ the concept of Maximum Likelihood Estimation (MLE), thereby determining estimates of the parameters $\boldsymbol{\lambda}$ describing the model $\mathscr{P}(\nu;\boldsymbol{\lambda})$ that maximize the likelihood of the observed power spectrum. As an example, a fit to the power spectrum of α Cen A obtained with *WIRE* (Fletcher et al. 2006) is displayed in Fig. 2.8. It should be noted that this methodology is not equivalent to a traditional least-squares minimization problem, where it is implicitly assumed that the measurement errors are normally distributed.

The use of MLE for fitting solar power spectra was first mentioned by Duvall & Harvey (1986), being later applied and tested by Anderson et al. (1990). It has now been in use by helioseismologists for more than 20 years and has been applied in the analysis of low-degree modes as well as of medium- and high-degree modes (e.g., Schou 1992; Toutain & Appourchaux 1994; Appourchaux et al. 1998; Chaplin et al. 2006). Asteroseismologists, myself included, are now increasingly adopting this and other related approaches. As Sir Isaac Newton would say, we stand on the shoulders of giants.

I start by introducing the probability density function (pdf) at frequencies separated by $1/T$, T being the length of the observation (Duvall & Harvey 1986):

$$f(P_j;\boldsymbol{\lambda}) = \frac{1}{\mathscr{P}(\nu_j;\boldsymbol{\lambda})} \exp\left[-\frac{P_j}{\mathscr{P}(\nu_j;\boldsymbol{\lambda})}\right] \,, \tag{2.76}$$

where P_j is the observed power spectrum at frequency channel j. This equation is nothing but the χ^2_2 distribution scaled to the limit spectrum. As we have seen, an average power spectrum instead obeys a χ^2 probability distribution with $2k$ degrees of freedom, k being the number of combined spectra. In that case one has (Appourchaux 2003):

$$f(P_j;\boldsymbol{\lambda}) = \frac{k^{k-1}}{(k-1)!} \frac{P_j^{k-1}}{\mathscr{P}^k(\nu_j;\boldsymbol{\lambda})} \exp\left[-\frac{kP_j}{\mathscr{P}(\nu_j;\boldsymbol{\lambda})}\right] \,. \tag{2.77}$$

The next step is to specify the likelihood function, i.e., the joint pdf for the data sample $\{P_j\}$. Assuming that the frequency bins are uncorrelated, the joint pdf is simply given by the product of $f(P_j;\boldsymbol{\lambda})$ over some frequency interval of interest spanned by j:

$$L(\boldsymbol{\lambda}) = \prod_{j=1}^{N} f(P_j;\boldsymbol{\lambda}) \,. \tag{2.78}$$

In spite of Eq. (2.78) being valid for an uninterrupted data set, the same is not true when gaps are present in the time series. In that event, Stahn & Gizon (2008) have derived an expression for the joint pdf of solar-like oscillations in complex Fourier space, in agreement with the earlier work of Gabriel (1994). The last-mentioned pdf explicitly takes into account frequency correlations introduced by the convolution with the spectral window.

The basic idea behind MLE is to determine estimates $\tilde{\boldsymbol{\lambda}}$ so as to maximize the likelihood function of the observed power spectrum. Due to improved numerical stability,

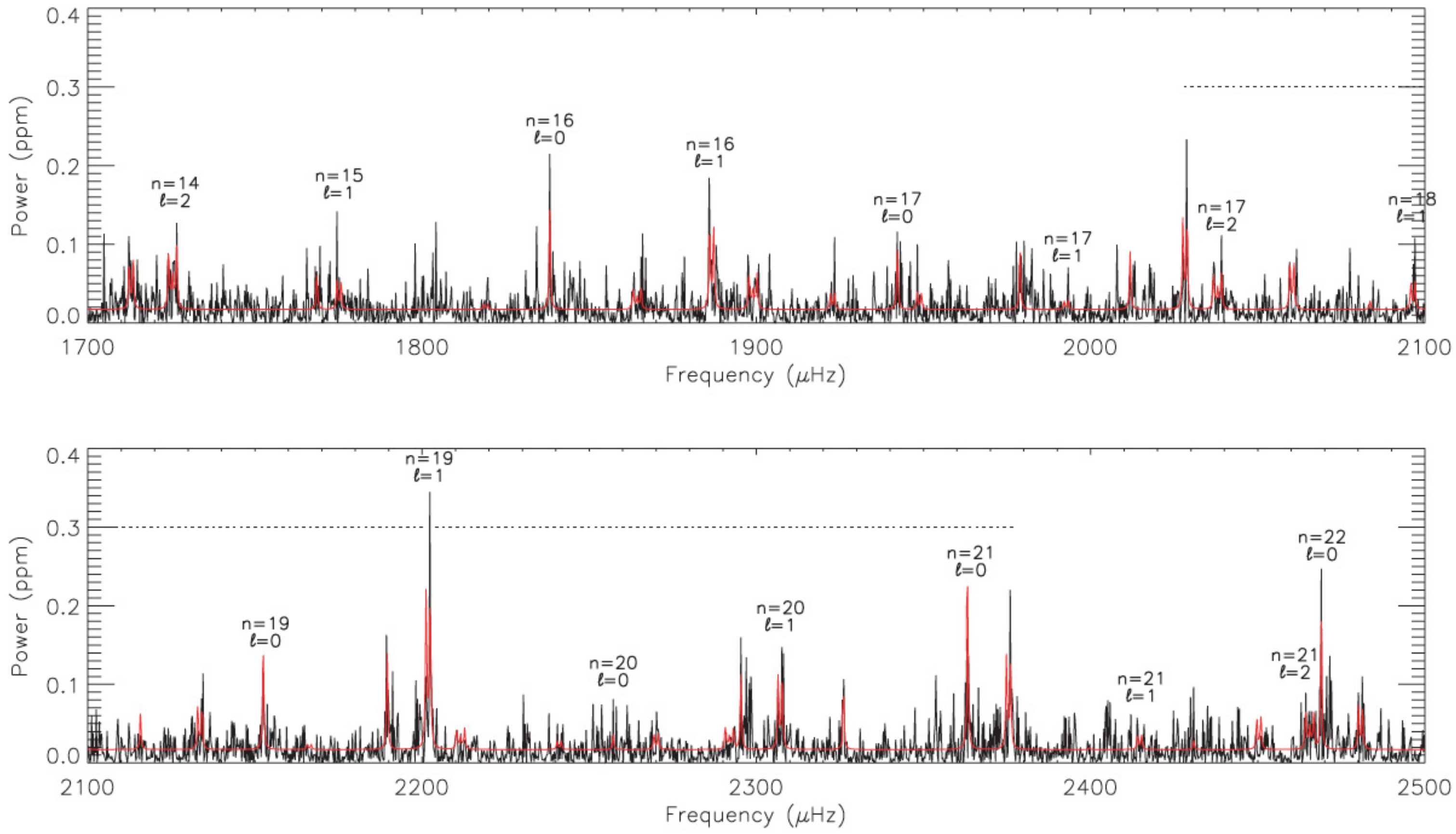

Figure 2.8: Fit to the *WIRE* power spectrum of α Cen A using MLE - The *WIRE* spectrum is shown with the fitted model overlaid in red. Fitted modes are labeled with the radial order n and degree l. The horizontal dotted lines, extending from the prominent peak at $\sim$2200 μHz, indicate the spacing at which the associated sidelobes caused by the severe window function are placed. From Fletcher et al. (2006).

however, it is more convenient to work with logarithmic probabilities. In practice, one ends up minimizing

$$\begin{aligned}\ell(\boldsymbol{\lambda}) &\equiv -\ln L(\boldsymbol{\lambda}) \\ &= \sum_{j=1}^{N} \left\{ \ln \mathscr{P}(\nu_j;\boldsymbol{\lambda}) + \frac{P_j}{\mathscr{P}(\nu_j;\boldsymbol{\lambda})} \right\} ,\end{aligned} \tag{2.79}$$

where Eq. (2.76) has been used in conjunction with Eq. (2.78). Symbolically, one thus has:

$$\tilde{\boldsymbol{\lambda}} = \arg\min_{\boldsymbol{\lambda}} \{\ell(\boldsymbol{\lambda})\} \ . \tag{2.80}$$

Finding the parameters $\tilde{\boldsymbol{\lambda}}$ that minimize $\ell(\boldsymbol{\lambda})$ may in principle be accomplished by employing, for instance, Powell's algorithm (Powell 1964). However, things are not that simple. Owing to the nonlinearity of the fitting problem in hand and to the large number of model parameters, one expects the likelihood to be multimodal. The risk of attaining a local minimum is real and further enhanced by the proneness of most standard algorithms to the initial guess parameters. Nevertheless, hope is not lost, since more sophisticated algorithms, such as Markov chain Monte Carlo techniques (see next section), are available.

The method of MLE possesses a number of attractive asymptotic properties (e.g., Kendall & Stuart 1979). Accordingly, in the limit of a very large sample (i.e., $N \to \infty$), the estimator $\tilde{\boldsymbol{\lambda}}$ is unbiased:

$$\lim_{N\to\infty} \mathrm{E}\left[\tilde{\boldsymbol{\lambda}}\right] = \boldsymbol{\lambda_0} \, , \tag{2.81}$$

where $\boldsymbol{\lambda_0}$ is the true parameter value. Moreover, the Cramér-Rao lower bound (Rao 1945; Cramér 1946) is reached:

$$\lim_{N\to\infty} \mathrm{cov}\left[\tilde{\boldsymbol{\lambda}}\right] = \mathsf{I}^{-1}(\boldsymbol{\lambda_0}) \, , \tag{2.82}$$

where $\mathsf{I}(\boldsymbol{\lambda})$ is the Fisher information matrix whose elements are given by

$$\mathsf{i}_{uv} = \mathrm{E}\left[\frac{\partial^2 \ell(\boldsymbol{\lambda})}{\partial\lambda_u \partial\lambda_v}\right] \ . \tag{2.83}$$

This means that no other asymptotically unbiased estimator has lower variance (minimum-variance unbiased estimator). Finally, the estimator $\tilde{\boldsymbol{\lambda}}$ is asymptotically normally distributed with mean $\boldsymbol{\lambda_0}$ and covariance matrix $\mathsf{I}^{-1}(\boldsymbol{\lambda_0})$.

Nonetheless, the world we live in is finite and hence there is no guarantee that the estimator $\tilde{\boldsymbol{\lambda}}$ will be normally distributed or even unbiased. Assuming that $\tilde{\boldsymbol{\lambda}}$ is approximately normally distributed, the covariance matrix is then given by the inverse of the Hessian matrix, $\mathsf{H}^{-1}(\boldsymbol{\lambda})$, computed at $\tilde{\boldsymbol{\lambda}}$. The elements of $\mathsf{H}(\boldsymbol{\lambda})$ are given by:

$$\mathsf{h}_{uv} = \frac{\partial^2 \ell(\boldsymbol{\lambda})}{\partial \lambda_u \partial \lambda_v} \,. \tag{2.84}$$

The so-called formal error bars on $\tilde{\boldsymbol{\lambda}}$ are given by the diagonal elements of the inverse of the Hessian matrix. Furthermore, the covariance matrix obeys the following inequality:

$$\mathrm{cov}\left[\tilde{\boldsymbol{\lambda}}\right] = \mathsf{H}^{-1}(\tilde{\boldsymbol{\lambda}}) \;\geq\; \mathsf{I}^{-1}(\boldsymbol{\lambda}_{\mathbf{0}}) \,, \tag{2.85}$$

meaning that the precision to which we can estimate $\tilde{\boldsymbol{\lambda}}$ is fundamentally limited by the Fisher information matrix.

Monte Carlo simulations. The considerations in the previous paragraph suggest that one should run Monte Carlo simulations on synthetic data as a means of validating the method (e.g., Anderson et al. 1990; Schou & Brown 1994; Toutain & Appourchaux 1994; Appourchaux et al. 1998; Gizon & Solanki 2003; Ballot et al. 2006, 2008). This is accomplished by fitting a large number of simulated realizations of a power spectrum in order to obtain the distributions of the fitted model parameters. Monte Carlo simulations enable us not only to determine the bias and precision associated with each parameter but also to assess the correlations between parameters. Besides, a matter of the utmost importance is the calibration of error bars. The procedure consists in calibrating the formal error bars such that the standard deviation of a given fitted parameter as obtained from Monte Carlo simulations equals the mean of the formal errors returned by the inverse Hessian, i.e., $\mathsf{H}(\tilde{\boldsymbol{\lambda}}) \approx \mathsf{I}(\boldsymbol{\lambda}_{\mathbf{0}})$.

Having defined a theoretical Hessian, Toutain & Appourchaux (1994) derived the following analytical expression for the frequency precision of a single p mode:

$$\begin{aligned} \sigma_\nu &= f(\beta)\sqrt{\frac{\Gamma}{4\pi T}} \\ &= \sqrt{\sqrt{\beta+1}\left(\sqrt{\beta+1}+\sqrt{\beta}\right)^3}\sqrt{\frac{\Gamma}{4\pi T}} \,, \end{aligned} \tag{2.86}$$

where β is the noise-to-signal ratio as before, and $f(\beta)$ is close to unity when β approaches 0. This is the same result as obtained in Libbrecht (1992). Equation

(2.86) is to be compared with Eq. (2.52) for a pure sine wave. Assuming white noise, $\sqrt{\beta} \sim \sigma/(A\sqrt{N})$ in the latter equation. Consequently, as the amplitude increases, the frequency precision of long-lived modes increases while that of short-lived modes reaches a limit. From Eq. (2.86) it becomes apparent that once a mode is resolved, and thus β cannot be improved with time (recall Eq. 2.32), frequency precision is expected to scale with the square root of time, i.e., $\sigma_\nu \propto T^{-1/2}$. This differs from the relation $\sigma_\nu \propto T^{-3/2}$ found in Eq. (2.52). Figure 2.9 displays the behavior of the frequency precision achievable for a stochastically-excited p mode as the length of the observation is increased. A transition between the unresolved ($T \ll 2\tau$) and resolved ($T \gg 2\tau$) regimes can be clearly seen.

Toutain & Appourchaux (1994) have also computed theoretical error bars for other parameters. To validate the approach, the theoretical precisions derived in their work were compared with those obtained from Monte Carlo simulations. Just like Anderson et al. (1990) before them, the authors realized that the amplitude, the linewidth, and the background noise tend to have a log-normal distribution. They suggest fitting the natural logarithm of these parameters instead, in order to derive meaningful error bars from the inverse of the Hessian.

I would also like to highlight a series of very instructive articles that have devoted particular attention to the issue of fitting the inclination of the rotation axis, i, and the rotational splitting[1], ν_s, of solar-like stars. Making use of extensive Monte Carlo simulations, Gizon & Solanki (2003) estimated the precision of the measurement of i. They found that the inclination angle can be retrieved accurately when $i \gtrsim 30^\circ$ for stars rotating at least twice as fast as the Sun that have been observed for 6 months, having further assumed solar linewidths. An extension of this analysis is provided by the same authors in Gizon & Solanki (2004), where they conclude that information can be obtained about the latitudinal differential rotation from observations of dipole and quadrupole modes, depending on the value of the mean rotation and on the inclination of the rotation axis. Ballot et al. (2006, 2008) emphasize the difficulties found when fitting these two quantities in the case of slow rotators, for which the splitting is comparable to the mode linewidth, thus leading to blending of the multiplet components. They explore in depth the correlations between the two parameters (see Fig. 2.10 for an example).

---

[1] In the asymptotic regime one has $\nu_\mathrm{s} \simeq \langle\Omega\rangle_{nl}/(2\pi)$ in Eq. (1.22).

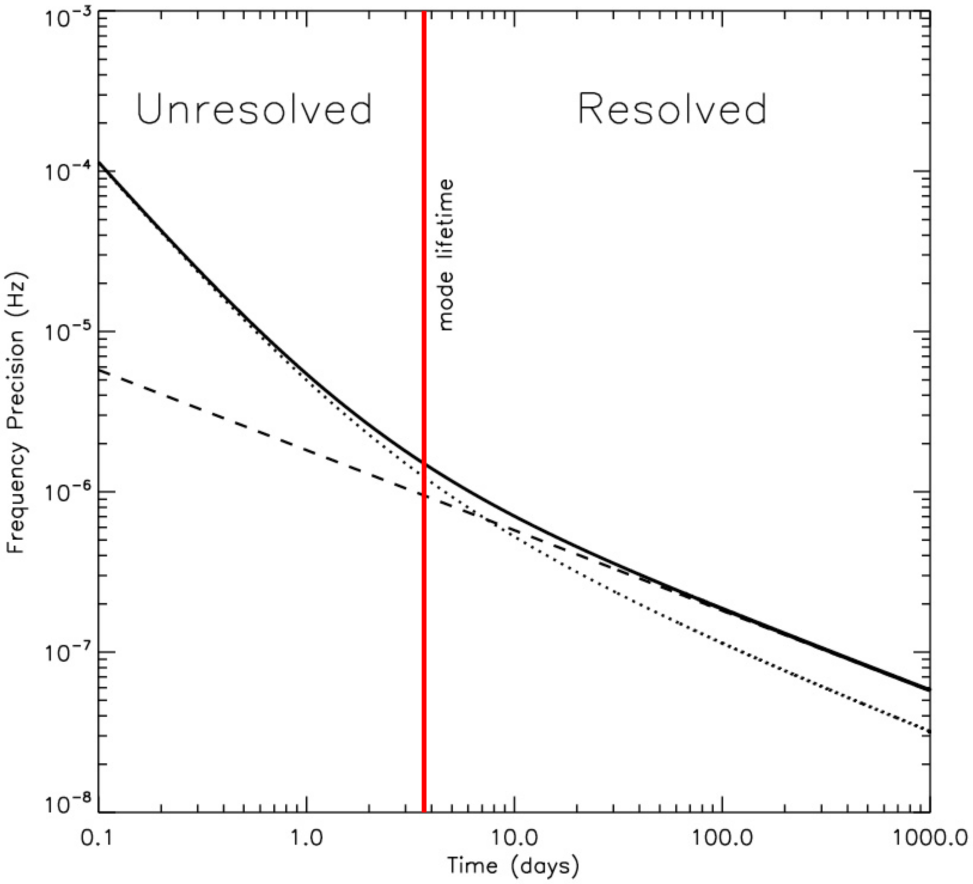

Figure 2.9: Frequency precision of a stochastically-excited p mode as a function of the length of the observation - Use has been made of Eq. (2.86) to compute the frequency precision. The definition of β entering that equation depends on whether or not the mode is resolved and is taken from Eq. (2.32). The dotted and dashed curves respectively represent the behavior of frequency precision in the unresolved and resolved regimes. Moreover, a more general expression, covering these two extreme regimes as well as the intermediate regime, has been computed for the frequency precision via Eq. (1.41) and is shown as a solid curve. The rms noise, σ_0, per $\Delta t = 58.85$s integration, was computed according to the empirical minimal-term model for the noise presented in Gilliland et al. (2010b) assuming a *Kepler* apparent magnitude of $Kp = 10$. The mode has a typical solar linewidth of 1 μHz and a rms amplitude $A_{\rm rms} = 2.68$ ppm, which corresponds to the maximum solar rms velocity amplitude of $0.16\,{\rm m\,s^{-1}}$ according to Eq. (1.34).

Parameter significance and the likelihood ratio. The discussion about MLE is not yet complete as one question still remains unanswered: How can one test the statistical significance of the fitted parameters? This can be done by employing the

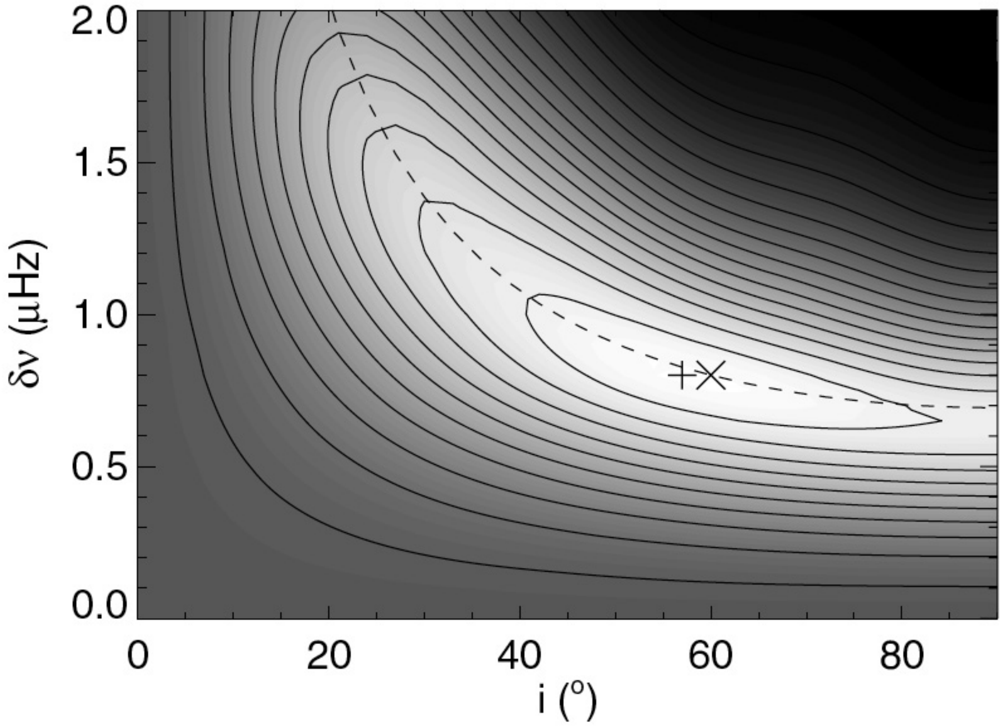

Figure 2.10: Correlation between maximum likelihood estimates of the inclination i and splitting $\nu_{\rm s}$ - The likelihood function for a simulated spectrum is shown in the plane $(i, \nu_{\rm s})$ of the space of parameters (notice that a different nomenclature is used for the splitting than the one in the text). Lighter tones correspond to higher likelihood and solid curves represent contours of constant likelihood. The cross ($\times$) marks the input pair $(i_0, \nu_{\rm s0})$ while the plus sign ($+$) marks the maximum of the likelihood. A clear correlation is seen between the two parameters whose values are organized along the dashed curve defined by $\nu_{\rm s} \sin i = \nu_{\rm s0} \sin i_0$. From Ballot et al. (2006).

so-called likelihood ratio test (Appourchaux et al. 1998). First, one starts by maximizing the likelihood $L(\boldsymbol{\lambda}_p)$ of the observed spectrum, where p parameters were used to construct the model. If one intends to model the same observed spectrum with n additional parameters, then the likelihood $L(\boldsymbol{\lambda}_{p+n})$ has to be maximized. The natural logarithm of the likelihood ratio $\mathscr{L}$ (cf. Eq. 2.64) is then given by:

$$\begin{aligned} \ln \mathscr{L} &= \ln L(\boldsymbol{\lambda}_p) - \ln L(\boldsymbol{\lambda}_{p+n}) \\ &= \ell(\boldsymbol{\lambda}_{p+n}) - \ell(\boldsymbol{\lambda}_p) \, . \end{aligned} \tag{2.87}$$

Clearly, when $\mathscr{L} \ll 1$ one has reasons to believe that the additional parameters are indeed significant. To assess how significant they are, an hypothesis test called likelihood ratio test may be performed. The null hypothesis is stated as: The n additional parameters are not needed to model the observed spectrum. Taking comfort in the knowledge that the statistical test $-2\ln\mathscr{L}$ approximately follows a χ^2 distribution with n degrees of freedom under the null hypothesis (Wilks 1938), one then proceeds with the computation of the detection significance (recall Sect. 2.2.2.1 for its definition).

Karoff (2012) employs the likelihood ratio test to assess the statistical significance of a facular component in power spectra of the Sun, having made use of 13 years of observations carried out by the VIRGO/SPM instrument. Figure 2.11 portrays the case of KIC 6603624, a main-sequence star exhibiting solar-like oscillations, for which the statistical significance of a facular component is over the 99.9% level according to the likelihood ratio test.

A rather interesting work on the reliability of the likelihood ratio when applied to mode identification (i.e., tagging of modes by degree l) in solar-like stars is presented in Salabert et al. (2010). It was also based on the likelihood ratio that Appourchaux et al. (2008) computed the posterior probabilities of the two competing mode identification scenarios in a study of the *CoRoT* F5 main-sequence star HD 49933. Their calculations were done in a way similar to the procedure outlined in Sect. 2.2.2.2, hence providing the statistical significance of either scenario. Mode identification was made difficult due to the conjugation of two factors, namely, a mode linewidth larger than solar together with a small frequency separation narrower than in the Sun. As a result, the $l=0,2$ and $l=1$ ridges were indistinguishable from one another. This has been coined the "F star problem" (Bedding 2011), which is also a problem in, e.g., Procyon (Bedding et al. 2010b; Bedding & Kjeldsen 2010) and θ Cyg (see Fig. 2.12). Notoriously, the preferred mode identification of Appourchaux et al. (2008) was proved to be wrong as soon as a longer time series became available for analysis (see Sect. 3.2.1; Benomar et al. 2009b). To be fair, it should be stressed that Appourchaux et al. (2008) were already envisaging the inclusion of prior knowledge through a full Bayesian approach as the next logical step to take. This would have saved the authors from all the controversy (Benomar et al. 2009a). Bayesian parameter estimation, including the analogous problem of model comparison, are the subjects of the next section.

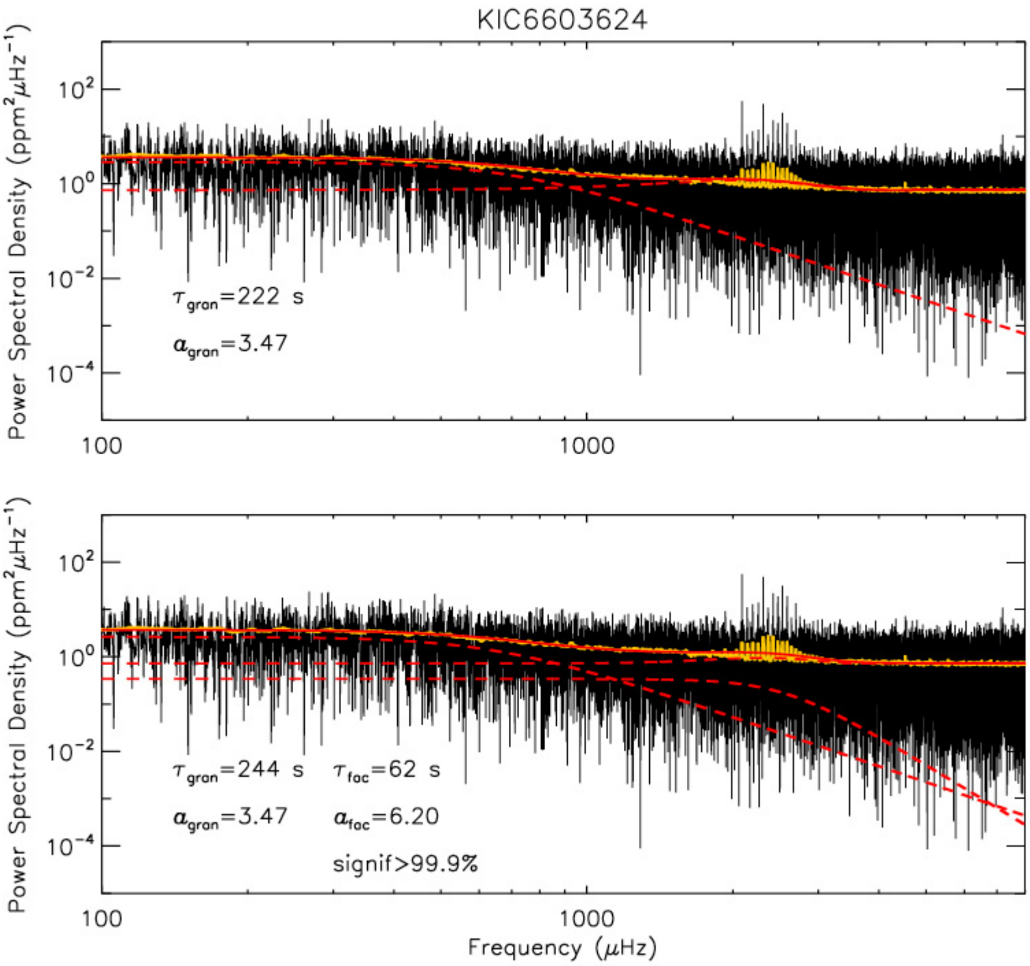

Figure 2.11: Presence of a facular signal in the power spectrum of KIC 6603624 - The power spectrum (black) has been computed from twelve months of *Kepler* photometry (Q5 to Q8). A smoothed version of the power spectrum (yellow) is also shown in order to visually enhance the acoustic signal centered at about 2.5 mHz. Besides a Gaussian component used to describe the p-mode power-excess hump (e.g., Kallinger et al. 2010b) and a flat component representing white noise, the background model also included both a granular and a facular signal (bottom panel) or else only a granular signal (top panel). The characteristic timescales ($\tau_{\rm gran}$ and $\tau_{\rm fac}$) and slopes ($a_{\rm gran}$ and $a_{\rm fac}$) of the corresponding Harvey-like profiles are indicated (cf. Eq. 2.74). The latter have been fixed to their solar values according to Karoff (2012).

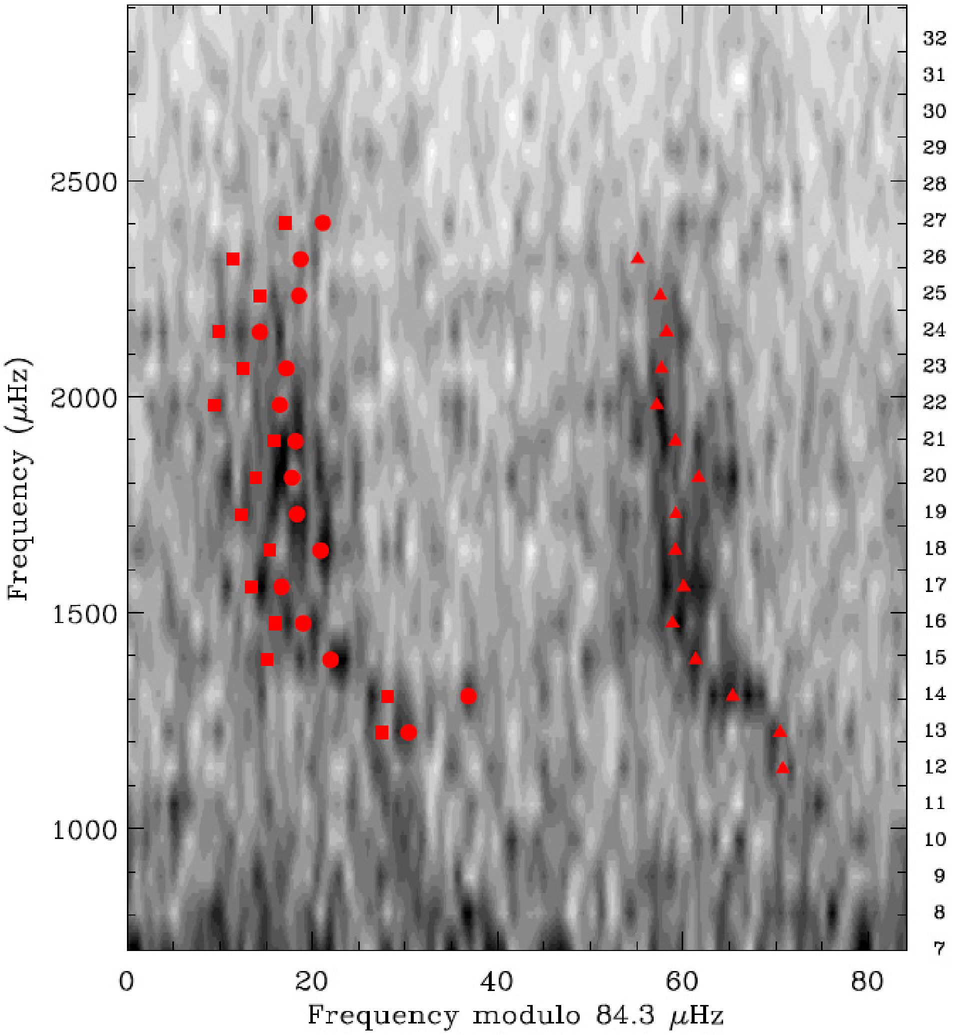

Figure 2.12: Échelle diagram of the power density spectrum of θ Cyg - θ Cyg is a very bright F-type dwarf. It has been observed with *Kepler* throughout Quarter 8 (Q8) using a special photometric mask. The resulting power density spectrum is shown in grayscale. Symbols in red represent the individual frequencies obtained from a provisional fit to the power spectrum using a regularized version of the MLE algorithm (or MAP; see discussion in the next section). Symbol shapes indicate mode degree: $l = 0$ (circles), $l = 1$ (triangles), and $l = 2$ (squares). Identification of the ridges from a simple visual inspection is far from evident. Another fit was performed assuming the alternative mode identification scenario. The plotted scenario was found to be statistically more likely based on the computation of the likelihood ratio, although not in a decisive way (only by a factor of ~3.7). At the time of writing a debate is still ongoing as to which is the correct scenario.

2.2.3.3 Bayesian parameter estimation using MCMC

The first attempt at applying a Bayesian approach to parameter estimation in asteroseismology is due to Brewer et al. (2007). However, their use of a time-based model consisting of pure sine waves incorrectly models the stochastic excitation of an harmonic oscillator. They have since improved their approach by considering damped oscillations and by modeling the asteroseismic data as a Gaussian process (Brewer & Stello 2009). It would then be the controversy surrounding the early work of Appourchaux et al. (2008) on HD 49933 to trigger the development of several Bayesian data analysis tools (Benomar et al. 2009a; Gruberbauer et al. 2009; Handberg & Campante 2011).

Herein, I highlight the main features of a Bayesian peak-bagging[1] tool that employs Markov chain Monte Carlo (MCMC) techniques. The following discussion is adapted from Handberg & Campante (2011), where the reader will find a comprehensive guide to the implementation of such a peak-bagging tool. This is unquestionably one of my main contributions to the field and, for that reason, the aforementioned article can be found as a supplement in Appendix D.

This tool is to be applied to the power spectra of solar-like oscillators and used as a means to infer both individual oscillation mode parameters and parameters describing non-resonant features. Besides making it possible to incorporate relevant prior information through Bayes' theorem, this tool also allows obtaining the marginal probability density function for each of the model parameters. Moreover, it provides larger error bars on the parameters than does MLE, thus making it a more conservative approach. Handberg & Campante (2011) apply this tool to a couple of recent asteroseismic data sets, namely, to *CoRoT* observations of HD 49933 and to ground-based observations of Procyon.

Having set up the model of the power spectrum in Sect. 2.2.3.1, I will start by introducing the Bayesian statistical framework to be used for estimating the model parameters and for comparing the merits of competing models. In the meantime, the reader should recall Eqs. (2.60) and (2.61), where Bayes' theorem was formally introduced and a posterior probability $p(H_i|D, I)$ was assigned to each member of the hypothesis space of interest, denoted by $\{H_i\}$.

---

[1] The term "peak-bagging", coined by Jesper Schou, a keen mountain climber, refers in the present context to the analysis of individual oscillation peaks in the power spectrum.

Parameter estimation. Very often, a particular hypothesis, i.e., a given model M of the power spectrum, is assumed true and the hypothesis space of interest then concerns the values taken by the model parameters $\boldsymbol{\lambda}$. These parameters are continuous, meaning that one will be interested in their probability density functions. The global likelihood of model M is then given by the continuous counterpart of Eq. (2.61):

$$p(D|I) = \int p(\boldsymbol{\lambda}|I)\, p(D|\boldsymbol{\lambda}, I)\, \mathrm{d}\boldsymbol{\lambda}\,. \tag{2.88}$$

Computation of the global likelihood is rather complex, but can be achieved rather straightforwardly by using the Metropolis-Hastings algorithm under parallel tempering (e.g., Gregory 2005; Handberg & Campante 2011).

We may also want to restate Bayes' theorem in order to account for this new formalism:

$$p(\boldsymbol{\lambda}|D, I) = \frac{p(\boldsymbol{\lambda}|I)\, p(D|\boldsymbol{\lambda}, I)}{p(D|I)}\,. \tag{2.89}$$

The terms entering this equation have exactly the same meaning as the corresponding terms entering Eq. (2.60). As a result, $p(D|\boldsymbol{\lambda}, I)$ is nothing but the likelihood function $L(\boldsymbol{\lambda})$ as given in Eq. (2.78). We are ultimately interested in using MCMC techniques to map the posterior pdf given by Eq. (2.89). This approach is exceedingly more powerful than the Bayesian point-estimation method of Maximum A Posteriori (MAP; e.g., Gaulme et al. 2009). The MAP approach can in fact be regarded as a regularized version of the frequentist MLE, also a point-estimation method. Drawing a parallelism with Eq. (2.80), one has symbolically:

$$\tilde{\boldsymbol{\lambda}}_{\mathrm{MAP}} = \arg\max_{\boldsymbol{\lambda}} \{p(\boldsymbol{\lambda}|I)\, L(\boldsymbol{\lambda})\}\ . \tag{2.90}$$

One of the main advantages of a Bayesian approach when compared to a frequentist approach resides in the fact that the posterior pdf, $p(\boldsymbol{\lambda}|D, I)$, is directly accessed, and not only the likelihood function. Moreover, the use of MCMC techniques to map the posterior pdf clearly supersedes the MLE approach, which only provides the location of the maximum of the likelihood. Another main advantage provided by the Bayesian framework is the ability to incorporate relevant prior information through Bayes' theorem and evaluate its effect on our conclusions. When basing the fitting/detection problem upon a priori theoretical knowledge, its outcome will effectively be restricted to what one can imagine or conceive (Appourchaux 2008). This is particularly useful when fitting a model to an acoustic power spectrum exhibiting low SNR in the p modes, a scenario where frequentist approaches tend to break down. Gregory (2005) provides useful insight on the use and effect of the prior in the framework of Bayesian data analysis.

The procedure of marginalization makes it possible to compute the marginal posterior pdf for a subset of parameters $\boldsymbol{\lambda}_{\mathrm{A}}$ by integrating over the remaining parameters $\boldsymbol{\lambda}_{\mathrm{B}}$, the so-called nuisance parameters:

$$p(\boldsymbol{\lambda}_{\mathrm{A}}|D,I) = \int p(\boldsymbol{\lambda}_{\mathrm{A}},\boldsymbol{\lambda}_{\mathrm{B}}|D,I)\,\mathrm{d}\boldsymbol{\lambda}_{\mathrm{B}}\,. \tag{2.91}$$

Furthermore, assuming that the prior on $\boldsymbol{\lambda}_{\mathrm{A}}$ is independent of the prior on $\boldsymbol{\lambda}_{\mathrm{B}}$, then by applying the product rule one has:

$$p(\boldsymbol{\lambda}_{\mathrm{A}},\boldsymbol{\lambda}_{\mathrm{B}}|I) = p(\boldsymbol{\lambda}_{\mathrm{A}}|I)\,p(\boldsymbol{\lambda}_{\mathrm{B}}|\boldsymbol{\lambda}_{\mathrm{A}},I) = p(\boldsymbol{\lambda}_{\mathrm{A}}|I)\,p(\boldsymbol{\lambda}_{\mathrm{B}}|I)\,. \tag{2.92}$$

In practice, one will be working with logarithmic probabilities. The global likelihood of the model plays the role of a normalization constant and we rewrite Eq. (2.89) as follows:

$$\ln p(\boldsymbol{\lambda}|D,I) = \mathrm{const.} + \ln p(\boldsymbol{\lambda}|I) - \ell(\boldsymbol{\lambda})\,, \tag{2.93}$$

where $\ell(\boldsymbol{\lambda})$ is given by Eq. (2.79).

Model comparison. As we will see below, the problem of model comparison is analogous to that of parameter estimation. When facing a situation in which several parameterized models are available for describing the same physical phenomenon, one expects Bayes' theorem to allow for a statistical comparison between such models. Bayesian model comparison has a built-in Occam's razor, a principle also known as lex parsimoniae, by which a complex model is automatically penalized, unless the available data justify its additional complexity. Notice that these competing models may be either intrinsically different models or else similar but with varying number of parameters (i.e., nested models), or even the same model with different priors affecting its parameters.

Given two or more competing models and our prior information, I, being in the current context that one and only one of the models is true, we can assign individual probabilities similarly to what has been done in Eq. (2.60), after replacing H_i by M_i:

$$p(M_i|D,I) = \frac{p(M_i|I)\,p(D|M_i,I)}{p(D|I)}\,, \tag{2.94}$$

Table 2.1: Jeffreys' scale - The usual scale by which to judge the evidences of two competing models.

$\ln B_{ij}$	Strength of evidence
< 1	Not worth more than a bare mention
1–2.5	Significant
2.5–5	Strong to very strong
> 5	Decisive

where the global likelihood of model M_i, $p(D|M_i,I)$, also called the evidence of the model, is given by Eq. (2.88). As stated above, after comparison of Eqs. (2.89) and (2.94), one realizes that the problem of model comparison is indeed analogous to the problem of parameter estimation.

Of particular interest is the computation of the ratio of the probabilities of two competing models:

$$O_{ij} \equiv \frac{p(M_i|D,I)}{p(M_j|D,I)} = \frac{p(M_i|I)\,p(D|M_i,I)}{p(M_j|I)\,p(D|M_j,I)} = \frac{p(M_i|I)}{p(M_j|I)} B_{ij}\,, \tag{2.95}$$

where O_{ij} is the odds ratio in favor of model M_i over model M_j, B_{ij} is the so-called Bayes' factor, and $p(M_i|I)/p(M_j|I)$ is the prior odds ratio. The Bayesian odds ratio closely resembles the frequentist likelihood ratio discussed in the previous section. However, the former ratio is the product of the ratio of the prior probabilities of the models and the ratio of their global likelihoods, in contrast to the ratio of point-like probability estimates in the latter case. Computation of O_{ij} is thus a means of assessing, for instance, which of two mode identification scenarios is statistically more likely (e.g., Benomar et al. 2009a; Bedding et al. 2010b; Handberg & Campante 2011). It is usual to assume that one has no prior information impelling us to prefer one model over the other, and in that case one sets $p(M_i|I)/p(M_j|I)=1$. This assumption should, however, be used with great care, especially when dealing with nested models which is often the case (e.g., Scott & Berger 2010). One is now in need of a scale by which to judge the ratio of the evidences of two competing models. The usual scale employed is Jeffreys' scale (Jeffreys 1961), which is displayed in Table 2.1 for convenience.

Moreover, the Bayesian framework makes it possible to extract parameter constraints even in the presence of model uncertainty, i.e., when the implementation of model selection has not been successful. This is done by simply combining the probability distribution of the parameters within each individual model, weighted by the model probability. This procedure, called Bayesian model averaging (e.g., Liddle 2009), is an analog of the superposition of eigenstates of an observable in quantum mechanics.

Markov chain Monte Carlo. After inspection of Eq. (2.91), the need becomes clear for a mathematical tool that is able to efficiently evaluate the multidimensional integrals required in the computation of the marginal distributions. This constitutes the rationale behind the method known as Markov chain Monte Carlo, first introduced in the early 1950s by statistical physicists and nowadays extensively used in all areas of science and economics.

The aim is to draw samples from the target distribution, $p(\boldsymbol{\lambda}|D,I)$, by constructing a pseudo-random walk in parameter space such that the number of samples drawn from a particular region is proportional to its posterior density. Such a pseudo-random walk is attained by generating a Markov chain, whereby a new sample, $\boldsymbol{\lambda}_{t+1}$, depends on the previous sample, $\boldsymbol{\lambda}_t$, according to a time-independent quantity called the transition kernel, $p(\boldsymbol{\lambda}_{t+1}|\boldsymbol{\lambda}_t)$. After a burn-in phase, $p(\boldsymbol{\lambda}_{t+1}|\boldsymbol{\lambda}_t)$ is able to generate samples of $\boldsymbol{\lambda}$ with a probability density converging on the target distribution.

An algorithm widely employed to generate a Markov chain was initially proposed by Metropolis et al. (1953), and subsequently generalized by Hastings (1970), this latter version being commonly referred to as the Metropolis-Hastings algorithm. It works in the following way: Suppose the current sample, at some instant denoted by t, is represented by $\boldsymbol{\lambda}_t$. We would like to steer the Markov chain toward the next sampling state, $\boldsymbol{\lambda}_{t+1}$, by first proposing a new sample to be drawn, $\boldsymbol{\xi}$, from a proposal distribution, $q(\boldsymbol{\xi}|\boldsymbol{\lambda}_t)$, that can have almost any form. Here, I specifically treat $q(\boldsymbol{\xi}|\boldsymbol{\lambda}_t)$ as being a multivariate normal distribution with covariance matrix $\boldsymbol{\Sigma}$. The proposal distributions for the individual parameters are further assumed to be independent, meaning that $\boldsymbol{\Sigma}$ is diagonal. The proposed sample is then accepted with a probability given by:

$$\alpha(\boldsymbol{\lambda}_t,\boldsymbol{\xi}) = \min(1,r) = \min\left[1, \frac{p(\boldsymbol{\xi}|D,I)}{p(\boldsymbol{\lambda}_t|D,I)}\frac{q(\boldsymbol{\lambda}_t|\boldsymbol{\xi})}{q(\boldsymbol{\xi}|\boldsymbol{\lambda}_t)}\right] , \tag{2.96}$$

where $\alpha(\boldsymbol{\lambda}_t,\boldsymbol{\xi})$ is the acceptance probability and r is called the Metropolis ratio. In the present case $q(\boldsymbol{\lambda}_t|\boldsymbol{\xi})=q(\boldsymbol{\xi}|\boldsymbol{\lambda}_t)$, since the proposal distribution is symmetric. As a result, if the posterior density for the proposed sample is greater than or equal to that of the current sample, i.e., $p(\boldsymbol{\xi}|D,I) \geq p(\boldsymbol{\lambda}_t|D,I)$, then the proposal will be accepted, otherwise it will be accepted with a probability given by the ratio of the posterior densities. If $\boldsymbol{\xi}$ is not accepted, then the chain will keep the current sampling state, i.e., $\boldsymbol{\lambda}_{t+1} = \boldsymbol{\lambda}_t$. The procedure just described is repeated for a predefined number of iterations or, alternatively, for a number of iterations determined by a convergence test applied to the Markov chain.

Once the posterior pdf, $p(\boldsymbol{\lambda}|D,I)$, has been mapped, the procedure of marginalization becomes trivial. The marginal posterior distribution of a given parameter λ, $p(\lambda|D,I)$, is then simply obtained by collecting its samples in an histogram and further normalizing it. An estimate of the kth moment of λ about the origin is then given by

$$\langle\lambda^k\rangle \equiv \int \lambda^k \, p(\lambda|D,I) \, \mathrm{d}\lambda \approx \frac{1}{N_{\mathrm{it}}} \sum_t \lambda_t^k \, , \tag{2.97}$$

where N_{it} is the total number of samples.

Automated MCMC and parallel tempering. The basic Metropolis-Hastings algorithm outlined above can be refined by incorporating a statistical control system that allows to automatically fine-tune the proposal distribution during the burn-in phase. Moreover, inclusion of parallel tempering will increase the mixing properties of the Markov chain and consequently reduce the risk of the algorithm becoming stuck in a local mode of the target distribution. The reader is referred to Handberg & Campante (2011) for how to implement these two features. Here, I only give a brief summary.

The basic Metropolis-Hastings algorithm runs a serious risk of becoming stuck in a local mode of the target distribution, thus failing to fully explore all regions of parameter space containing significant probability. A way of overcoming this difficulty is to employ parallel tempering (e.g., Earl & Deem 2005), whereby a discrete set of progressively flatter versions of the target distribution is created by introducing a temperature parameter, $\mathcal{T}$. In practice, use is made of its reciprocal, $\gamma = 1/\mathcal{T}$, referred to as the tempering parameter. We modify Eq. (2.89) to generate the tempered distributions as follows:

$$p(\boldsymbol{\lambda}|D,\gamma,I) = C \, p(\boldsymbol{\lambda}|I) \, p(D|\boldsymbol{\lambda},I)^{\gamma} \, , \;\; 0 < \gamma \leq 1 \, , \tag{2.98}$$

where C is a constant. For $\gamma = 1$, we retrieve the target distribution, also called the cold sampler, while for $\gamma < 1$, the hotter distributions are effectively flatter versions of the target distribution. By running such a set of chains in parallel (n_γ in total) and further allowing the swap of their respective parameter states, we enable the algorithm to sample the target distribution in a way that makes possible both the investigation of its overall features (low-γ chains) and the examination of the fine details of a local mode (high-γ chains). Figure 2.13 provides a pseudocode version of the Metropolis-Hastings algorithm with the inclusion of parallel tempering.

Based on a statistical control system similar to the one described in Gregory (2005), we may automate the process of calibration of the Gaussian proposal σ values, which specify the direction and step size in parameter space when proposing a new sample to be drawn. The optimal choice of $\{\sigma\}$ is closely related to the average rate at which proposed state changes are accepted, the so-called acceptance rate. The control system makes use of an error signal to steer the selection of the σ values during the burn-in phase of a single parallel tempering MCMC run, acting independently on each of the tempered chains. The error signal is proportional to the difference between the current acceptance rate and a target acceptance rate. As soon as the error signal for each of the tempered chains is less than a measure of the statistical fluctuation expected for a zero-mean error, the control system is turned off and the algorithm switches to the standard parallel tempering MCMC.

2.3 Getting practical: a pipeline for ***Kepler***

In the past few years, considerable effort has been invested in making preparations for the mode parameter analysis of *Kepler* data. This analysis involves the estimation of individual and global oscillation mode parameters, as well as estimation of parameters describing non-resonant signatures of convection and activity. An example of such an effort is the work conducted in the framework of the AsteroFLAG consortium (Chaplin et al. 2008a) which followed from the earlier work undertaken by the *CoRoT* data analysis team (Appourchaux et al. 2006a,b). This naturally paved the way for the development of a number of automated pipelines to measure global asteroseismic parameters of solar-like oscillators (Huber et al. 2009; Mosser & Appourchaux 2009; Roxburgh 2009a; Campante et al. 2010b; Hekker et al. 2010; Karoff et al. 2010; Mathur et al. 2010b; Verner & Roxburgh 2011).

In order to fully characterize a star using asteroseismology, it is desirable to have accurate estimates of individual p-mode parameters. These include the frequencies, amplitudes, and lifetimes of a large number of modes for which the angular degree l and radial order n have been identified. However, this is only possible for data above a certain signal-to-noise level. Global asteroseismic parameters, indicative of the global structure, are on the other hand readily obtainable using automated analysis methods that can incorporate data with a lower SNR and for which a full peak-bagging analysis is not always possible. Furthermore, the automated nature of these pipelines is required if we are to efficiently exploit the plenitude of data made available by *Kepler* on these targets. A thorough comparison of complementary analysis methods used to extract global asteroseismic parameters of main-sequence and subgiant solar-like oscillators is presented in Verner et al. (2011b) (see Sect. 3.3.1).

I have been personally involved in the development of two such automated pipelines, namely, the KAB and the AAU pipelines, as they are known internally. The KAB pipeline is fully described in Karoff et al. (2010). It operates based on a novel algorithm for modeling and fitting the autocovariance of the power spectrum, which has in turn been developed by Campante et al. (2010b). This algorithm overcomes the problem of mode identification and thus suits the automated nature of the pipeline, since there is no longer the need to make subjective choices during the analysis process. The article describing this algorithm can be found as a supplement in Appendix E.

Regarding the AAU pipeline, no work has unfortunately been published describing its methodology. That is, however, what I intend to do herein. The AAU pipeline is an automated pipeline designed to measure global asteroseismic parameters of main-sequence and subgiant solar-like oscillators, which is accomplished by using exclusively the time-series data as input. This pipeline is based on a series of programming modules that were passed to me by William J. Chaplin, hence explaining some of the similarities between the AAU and the Birmingham-Sheffield Hallam (Hekker et al. 2010) pipelines. The underlying methodology of the AAU pipeline is described below. The results obtained from the automated analysis – carried out using the methods of nine independent research teams – of 1948 main-sequence and subgiant *Kepler* survey stars are presented in Verner et al. (2011b). The AAU and KAB pipelines have taken part in this collective effort.

The AAU pipeline consists of a series of modules that aim at extracting the following information from the power spectra of the time-series data:

1. Frequency range of the oscillations;

2. Parameterization of the stellar and instrumental background signals;
3. Average large frequency separation, $\Delta\nu$;
4. Maximum mode amplitude, A_{max};
5. Frequency of maximum amplitude, ν_{max}.

2.3.1 Range of oscillations

We have seen in Sect. 1.5.1.1 that the quasi-regularity of the spectrum of high-order p modes constitutes one of the main signatures of the presence of solar-like oscillations. We thus look for a frequency range in the power spectrum in which peaks appear at nearly regular intervals. It should be noted that the assumption of quasi-regularity of the spectrum may be too strong in the case of subgiants due to the presence of g modes and mixed modes. Nevertheless, we start, from 100 μHz up to the Nyquist frequency ($\sim 8300\ \mu$Hz for short-cadence data), by partitioning the power spectrum into overlapping windows of variable width, w, which in turn depends on the value of the central frequency of the window, ν_{central}, with the successive ν_{central} separated by $w/20$. The values of ν_{central} are actually used as proxies for ν_{max}. Since the width of the p-mode hump roughly scales with ν_{max} (e.g., Stello et al. 2007; Mosser et al. 2010), w is defined as $w=(\nu_{\mathrm{central}}/\nu_{\mathrm{max},\odot})w_{\odot}$, with $\nu_{\mathrm{max},\odot}=3100\ \mu$Hz and $w_{\odot}=2000\ \mu$Hz, the latter being the expected value were the Sun to be observed as a bright star with *Kepler*.

The next step consists in computing the power spectrum of the power spectrum, PS$\otimes$PS, for each of the frequency windows. The presence of prominent features in the PS$\otimes$PS around the predicted values of $\Delta\nu/2$, $\Delta\nu/4$, and $\Delta\nu/6$ (the first, second, and third harmonics, respectively) is then examined. The predicted value of $\Delta\nu$ is computed according to the observed relation between $\Delta\nu$ and ν_{max} presented in Stello et al. (2009a), to be precise, $\Delta\nu \propto \nu_{\mathrm{central}}^{0.77}$. An hypothesis test is subsequently applied, whereby the presence of oscillations in a given window is established if the probability of the three above features being due to noise is less than 1% (i.e., a confidence level of 99% is required). The same considerations that allowed us to derive the statistics of the power spectrum in Sect. 2.1.5 are also applicable here, thus meaning that the PS$\otimes$PS follows a χ_2^2 distribution. Therefore, the probability that the peaks are due to noise is given by $(1-p)^{\zeta N}$, where p is the probability that a random variable following a χ^2_6 distribution is larger than the average normalized height of the three peaks in the PS⊗PS, ζ is an empirical correction factor that accounts for the effect of oversampling ($\zeta = 3$ when oversampling by a factor of 10; Gabriel et al. 2002), and N is the number of independent bins in the frequency window being considered. Finally, the frequency range of the oscillations is determined based on the overall span of the windows with confirmed oscillations.

In case the above strategy fails to detect oscillations, an alternative approach is used that no longer assumes $\Delta\nu$ to be constant with frequency, but instead takes into account its frequency dependency by slightly stretching (or compressing) the frequency axis of the power spectrum before computing the PS⊗PS for each of the windows. This aims at producing a nearly regular pattern of peaks in the stretched (compressed) power spectrum in contrast with the original spectrum, consequently enhancing the SNR of the features associated with the large frequency separation in the PS⊗PS. The details on how to implement this stretching can be found in Hekker et al. (2010) and only a summary is provided here. In short, the stretched frequencies are given by:

$$\nu_{\mathrm{stretch}} = (\nu - \nu_{\mathrm{central}}) - j\, s_{\max} \left(\frac{\nu}{\nu_{\mathrm{central}}} - 1 \right)^2 , \tag{2.99}$$

where j is an integer, and $s_{\max}$ is the maximum amount of stretching allowed. The optimal amount of stretching is then evaluated by looking for the value of j that minimizes the probability of the features in the PS⊗PS being due to noise.

2.3.2 Background signal

The model of the background signal is kept simple. We opt for a model merely containing a granulation component and white noise, and fit it to a power spectrum that has been previously smoothed. The smoothing implies Gaussian statistics and we therefore employ a nonlinear least-squares fit based on a gradient-expansion algorithm. The frequency range of the oscillations (see previous section) is excluded from the fitting window[1]. The fitting window starts at 100 μHz to allow for the decay of any possible activity component, characterized by considerably longer timescales, and extends all the way up to the Nyquist frequency. The granulation component is represented by a

---

[1] It should be noted, however, that a background fit is performed for all stars regardless of whether or not oscillations have been detected.

Harvey-like profile (cf. Eq. 2.74) to which an offset B is added containing mostly white noise, resulting in the following functional form of the model:

$$S_{\mathrm{bg}}(\nu) + B = \frac{H_{\mathrm{gran}}}{1 + (2\pi\nu\tau_{\mathrm{gran}})^a} + B\,, \tag{2.100}$$

where a is left as a free parameter. An example of a fit to the background signal is displayed in the top panel of Fig. 2.14.

A careful choice of the initial guesses for each model parameter proves critical for the convergence of the fitting procedure. H_{gran} is initially set to one thousandth of the maximum power in the smoothed spectrum. The input for τ_{gran} is computed on the assumption that it scales inversely with ν_{max} (Huber et al. 2009; Kjeldsen & Bedding 2011). Since at this stage an estimate of ν_{max} is not yet available, a proxy is used instead, namely, the midpoint of the frequency range of the oscillations. The exponent a is initially set to 2 following the original model of Harvey (1985). Finally, we choose as input for B the mean power at high frequencies, well beyond the range of oscillations.

The above might, however, not be enough to achieve convergence and hence a trap has been devised for the non-convergence of the fit. We start by randomly selecting an input parameter and make a random increment (or decrement) to it before performing the fit. This is repeated up to a maximum of a few hundred times until convergence is achieved. The fitting procedure is said to converge – for a given set of input parameters – when the relative decrease in χ^2 is less than $1{\times}10^{-6}$ in one iteration of the procedure. Failure to converge means that no other pipeline modules will be run on that particular star. Finally, the standard deviations of the model parameters are used as errors.

2.3.3 $\Delta\nu$

In order to estimate the average large frequency separation, $\Delta\nu$, we compute the PS⊗PS over the frequency range of the oscillations (see bottom panel of Fig. 2.14 for an example). Furthermore, the frequency dependence of $\Delta\nu$ is taken into account by computing the PS⊗PS for a power spectrum that has been optimally stretched (compressed). The feature at $\Delta\nu/2$ (first harmonic) in the PS⊗PS is then located and its power-weighted centroid computed to provide an estimate of $\Delta\nu$. The standard deviation of grouped data, given by $\sqrt{\left[\sum hx^2 - (\sum hx)^2/\sum h\right] / (\sum h - 1)}$, is also computed and used as the error on $\Delta\nu$, meaning that the feature in the PS⊗PS is interpreted as an assembly of spectral heights (h) over a number of bins (with midpoint x).

2.3.4 $A_{\max}$ and $\nu_{\max}$

We start by computing the power envelope for radial modes as a function of frequency according to Kjeldsen et al. (2008a). First, we subtract the fit to the background signal from the power spectrum. The residual spectrum thus obtained is then heavily smoothed over the range occupied by the p modes by convolving it with a Gaussian having a full width at half maximum of $4\Delta\nu$. Finally, we multiply the smoothed, residual spectrum by $\Delta\nu/c$, where c, defined as $c = \sum(S_l/S_0)^2$ (cf. Table 1.1), is a factor[1] measuring the effective number of modes per order and taken here to be 3.03.

The frequency at which the power envelope attains its maximum value is used next as a proxy for $\nu_{\max}$ in the estimation of the maximum mode power. An estimate of the maximum mode power is computed by averaging the spectrum over a rectangular window of width $2\Delta\nu$ centered at this proxy and converting to power per radial mode as seen above. Computation of the associated uncertainty is then greatly simplified and is given by the standard deviation of the powers in the bins within the rectangular window.

The amplitude envelope is obtained by taking the square root of the power envelope. This amplitude envelope is nothing but A_{rms} (see Eqs. 1.34 and 1.37). Velocity amplitude envelopes are also displayed in Fig. 1.18 for a number of stars. Once again, notice that we are dealing with amplitudes scaled to be equivalent radial-mode amplitudes. It follows that the maximum mode amplitude, $A_{\max}$, is given by the square root of the estimated maximum mode power. Moreover, the fractional error on the maximum mode amplitude is half that on the maximum mode power.

Finally, a proper estimate of $\nu_{\max}$ is provided. We average the p-mode spectrum over adjacent (independent) rectangular windows of width $2\Delta\nu$ and convert to power per radial mode. An estimate of $\nu_{\max}$ is then given by the power-weighted centroid, with an associated uncertainty derived from the standard deviation of grouped data.

---

[1] The dependence of c on limb darkening is ignored.

```
1:  procedure PARALLEL TEMPERING METROPOLIS-HASTINGS
2:      $\boldsymbol{\lambda}_{0,i} = \boldsymbol{\lambda}_0 \, , \; 1 \leq i \leq n_\gamma$
3:      for $t = 0, 1, \ldots, N_{\mathrm{it}} - 1$ do
4:          for $i = 1, 2, \ldots, n_\gamma$ do
5:              Propose a new sample to be drawn from a
                  proposal distribution: $\boldsymbol{\xi} \sim N(\boldsymbol{\lambda}_{t,i}; \Sigma_i)$
6:              Compute the Metropolis ratio:
                  $\ln r = \ln p(\boldsymbol{\xi}|D, \gamma_i, I) - \ln p(\boldsymbol{\lambda}_{t,i}|D, \gamma_i, I)$
7:              Sample a uniform random variable:
                  $U_1 \sim \mathrm{Uniform}(0, 1)$
8:              if $\ln U_1 \leq \ln r$ then
9:                  $\boldsymbol{\lambda}_{t+1,i} = \boldsymbol{\xi}$
10:             else
11:                 $\boldsymbol{\lambda}_{t+1,i} = \boldsymbol{\lambda}_{t,i}$
12:             end if
13:         end for
14:         $U_2 \sim \mathrm{Uniform}(0, 1)$
15:         if $U_2 \leq 1/n_{\mathrm{swap}}$ then
16:             Select random chain:
                  $i \sim \mathrm{UniformInt}(1, n_\gamma - 1)$
17:             Compute $r_{\mathrm{swap}}$:
                  $\ln r_{\mathrm{swap}} = \ln p(\boldsymbol{\lambda}_{t,i+1}|D, \gamma_i, I) + \ln p(\boldsymbol{\lambda}_{t,i}|D, \gamma_{i+1}, I)$
                      $- \ln p(\boldsymbol{\lambda}_{t,i}|D, \gamma_i, I) - \ln p(\boldsymbol{\lambda}_{t,i+1}|D, \gamma_{i+1}, I)$
18:             $U_3 \sim \mathrm{Uniform}(0, 1)$
19:             if $\ln U_3 \leq \ln r_{\mathrm{swap}}$ then
20:                 Swap parameter states of chains $i$ and $i + 1$:
                      $\boldsymbol{\lambda}_{t,i} \leftrightarrow \boldsymbol{\lambda}_{t,i+1}$
21:             end if
22:         end if
23:     end for
24:     return $\boldsymbol{\lambda}_{t,i} \, , \; \forall t \, , \; i\!:\!\gamma_i\!=\!1$
25: end procedure
```

Figure 2.13: Metropolis-Hastings algorithm - A pseudocode version of the Metropolis-Hastings algorithm with the inclusion of parallel tempering is given. For a complete understanding of the implementation of parallel tempering (lines 14 to 22) I refer the reader to Appendix D.

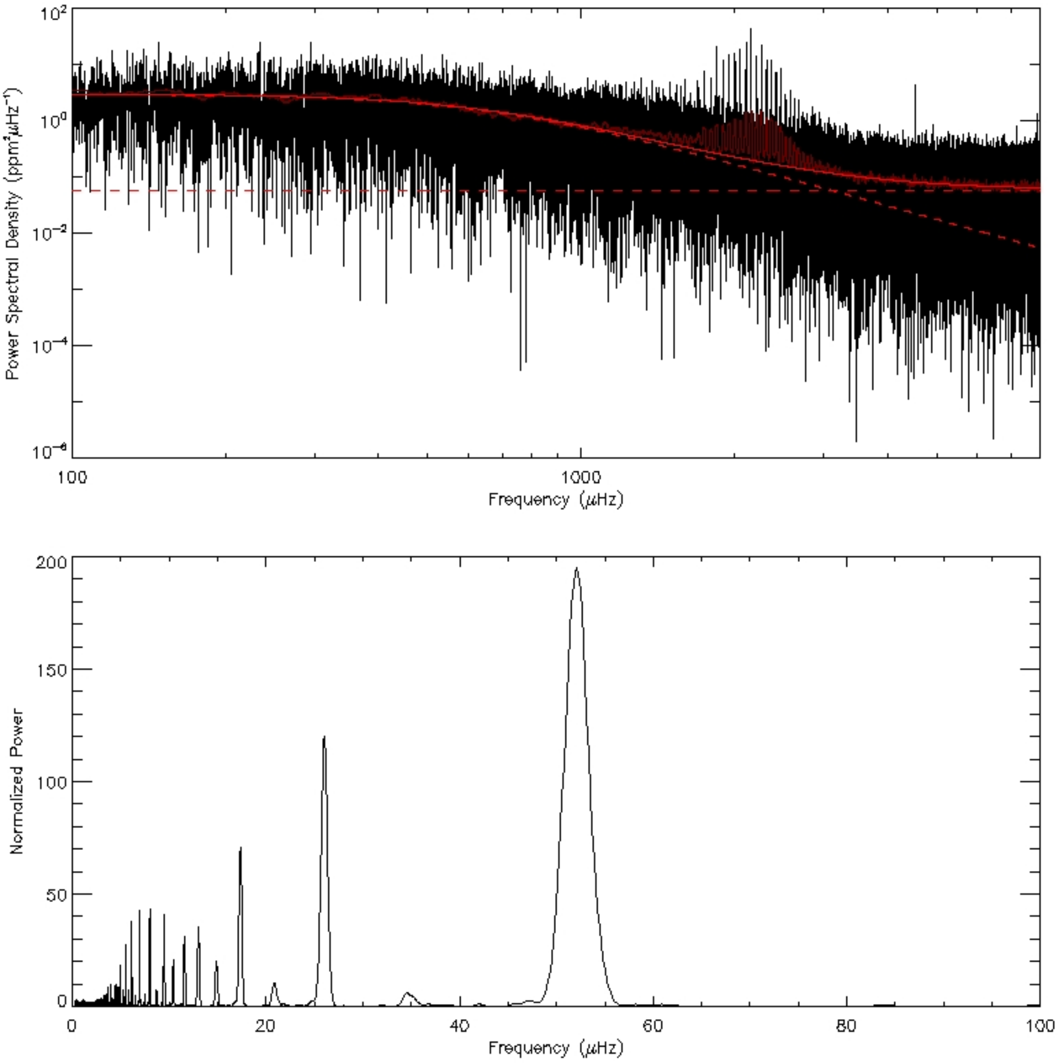

Figure 2.14: Pipeline output from the analysis of the light curve of the bright G-type dwarf 16 Cyg A - The solar analog 16 Cyg A is a member of a hierarchical triple system and has been observed with *Kepler* throughout Quarter 7 (Q7) using a special photometric mask. The top panel displays the smoothed power density spectrum (in dark red), used in the fit to the background signal, atop the original spectrum (in black), on a log-log scale. The fit to the background signal (red solid line) and both its components (red dashed lines) are also shown (see text for details). The bottom panel displays the PS$\otimes$PS over the frequency range of the oscillations. The features at $\Delta\nu/2$ ($\sim 52\,\mu$Hz), $\Delta\nu/4$ ($\sim 26\,\mu$Hz) and $\Delta\nu/6$ ($\sim 17\,\mu$Hz) are conspicuous.

Chapter 3

Selected results

In the course of the two previous chapters, I have made reference to a series of published works that have benefited to a great extent from my contribution. For that reason, I have decided to compile them in Appendices A to E. In the current chapter, I present the reader with a series of additional published results to which I have also contributed, although in a somewhat less determinant (but still significant) way. These scientific results are divided into three categories according to the origin of the acquired data, namely, arising from radial-velocity measurements taken during ground-based campaigns, from *CoRoT* photometry, or from *Kepler* photometry.

The above does not enclose my contribution to the field since, during the past three years, I have been involved (and continue to be) in a panoply of additional projects that have meanwhile been published or still await publication. However, I feel that the compendium of scientific results presented in this dissertation is fully representative of my work and technical expertise.

3.1 Results from ground-based campaigns

3.1.1 An asteroseismic and interferometric study of the solar twin 18 Scorpii

Solar twins, defined as having fundamental physical properties very similar or identical to solar (Cayrel de Strobel et al. 1981), are of great importance because they allow for a precise differential analysis relative to the Sun. In Bazot et al. (2011), our goal has been to use asteroseismology and interferometry on a study of 18 Scorpii, the brightest among the known solar twins. These techniques had already been combined to study the bright subgiant β Hyi (North et al. 2007), for which a mass was derived through the use of homology relations. In this study, we have applied a similar methodology to 18 Sco.

18 Scorpii, a 5th-magnitude star, has been observed for 12 nights with HARPS in May 2009 as part of the asteroseismic component of this study. Figure 3.1 displays the resulting power spectrum of radial-velocity measurements. An average large frequency separation of $134.4 \pm 0.3\ \mu$Hz has been estimated based on the autocorrelation of the time series. We have also performed long-baseline interferometry at visible wavelengths by using the PAVO beam-combiner (Ireland et al. 2008) at the CHARA array (ten Brummelaar et al. 2005). An angular diameter of 0.6759 ± 0.0062 mas has been estimated that, combined with the known parallax, leads to a radius of $1.010 \pm 0.009\,\mathrm{R}_\odot$. Using the homology relation given in Eq. (1.54), one obtains a mass of $1.02 \pm 0.03\,\mathrm{M}_\odot$ for 18 Sco. This value for the mass is in good agreement with previously published estimates derived from indirect methods, such as comparison between spectroscopic or photometric observations and stellar evolutionary tracks.

This work shows the possibilities offered by the synergy between asteroseismology, even if from a ground-based single site, and interferometry (for more on the combined application of these two techniques see Cunha et al. 2007). Our results confirm that 18 Sco is remarkably similar to the Sun in terms of both radius and mass. The next steps to be taken involve measuring the individual oscillation frequencies and performing full modeling using all the available observations.

3.1.2 Probing the core properties of α Centauri A with asteroseismology

The proximity of the visual binary system α Cen, allied to the similarity of its components to the Sun, caused this system to become a preferred asteroseismic target[1]. Moreover, its primary component, α Cen A (G2V), has a mass of $1.105 \pm 0.007\,\mathrm{M}_\odot$ (Pourbaix et al. 2002), very close to the limit above which main-sequence stars keep the convective core developed during the pre-main-sequence phase. For this reason, a

---

[1] An account is given in Sect. 1.6.2 of the asteroseismic campaigns dedicated to α Cen A during the last decade.

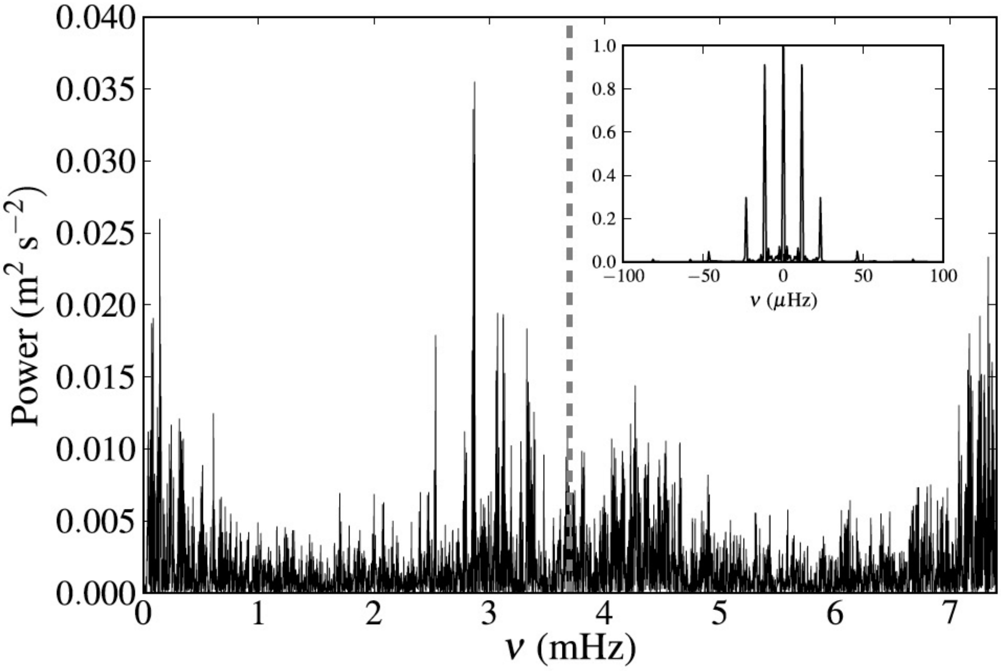

Figure 3.1: Power spectrum from radial-velocity measurements of 18 Sco - The vertical dashed line marks the location of the equivalent Nyquist frequency. The inset shows the spectral window, normalized to its maximum. The power spectrum shows a clear hump of excess power around 3 mHz, reaching $\sim 0.04\,\mathrm{m^2\,s^{-2}}$, which corresponds to amplitudes of $\sim 20\,\mathrm{cm\,s^{-1}}$. From Bazot et al. (2011).

theoretical study of α Cen A is particularly valuable for testing the poorly-modeled treatment of convection and extra mixing in the central regions of low-mass stars.

In de Meulenaer et al. (2010), we have combined and analysed the radial-velocity time series obtained in May 2001 with CORALIE (Bouchy & Carrier 2001, 2002), UVES and UCLES (Butler et al. 2004; Bedding et al. 2004). The aim has been to derive a precise set of asteroseismic constraints to be compared to models, that would eventually allow us to improve the knowledge of the interior of α Cen A, namely, by determining the nature of its core.

While the combined time series is as long as the CORALIE time series (12.45 days), it contains almost five times more data points, significantly reducing the daily aliases in the spectral window due to an enhanced time coverage (see Fig. 3.2). Three different weighting schemes have been used in the computation of a Lomb-Scargle periodogram

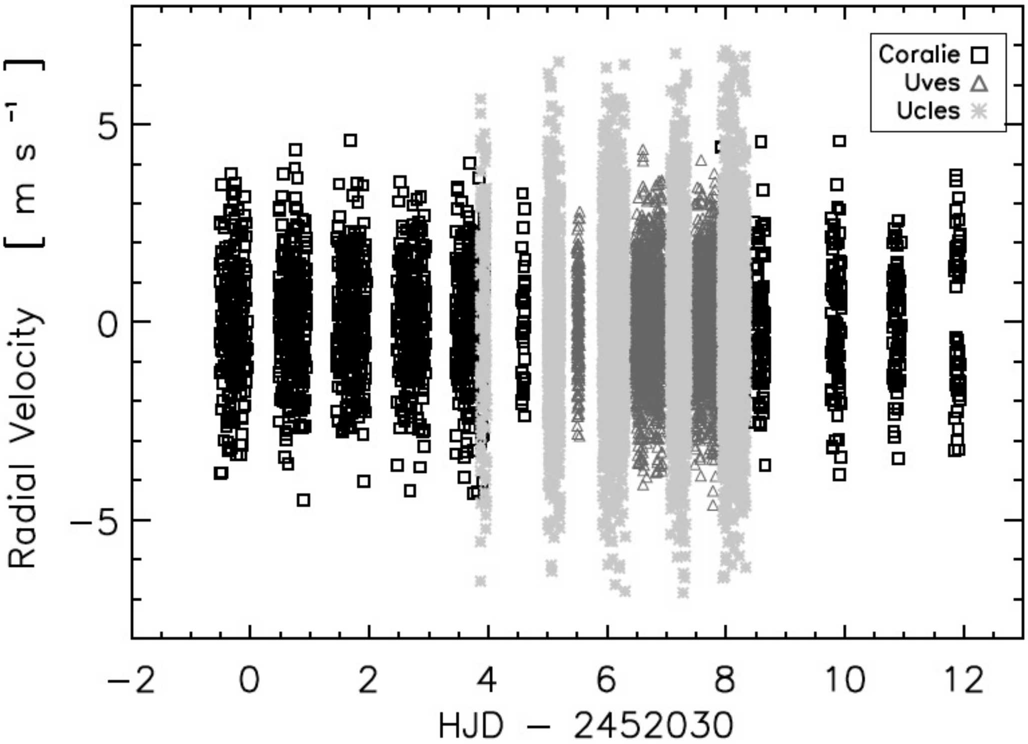

Figure 3.2: Combined time series obtained for α Cen A with CORALIE, UVES, and UCLES - Note that the UCLES data set, which has been obtained in Australia, fills several of the gaps in the time series left by the other two data sets, obtained in Chile. From de Meulenaer et al. (2010).

from the combined time series, thus resulting in three different power spectra. Since we have employed Iterative Sine-Wave Fitting for frequency estimation (with all its known problems concerning false detections and fatal error propagation; recall Sect. 2.1.9), we hoped to guarantee the genuineness of the detected frequencies by analysing three different power spectra. We have detected 44 modes with $l = 0, 1, 2, 3$, in overall good agreement with previous works, of which 14 showed possible rotational splittings. New average values have been derived for the large and small frequency separations.

Miglio & Montalbán (2005) have performed several calibrations of the α Cen system using both classical (photometric, spectroscopic, and astrometric) and asteroseismic constraints. They found that models with either a radiative or a convective core could equally well reproduce the classical constraints, and that an overshooting parameter $\alpha_{\rm ov} > 0.15$ is sufficient for a convective core to persist once the star leaves the pre-

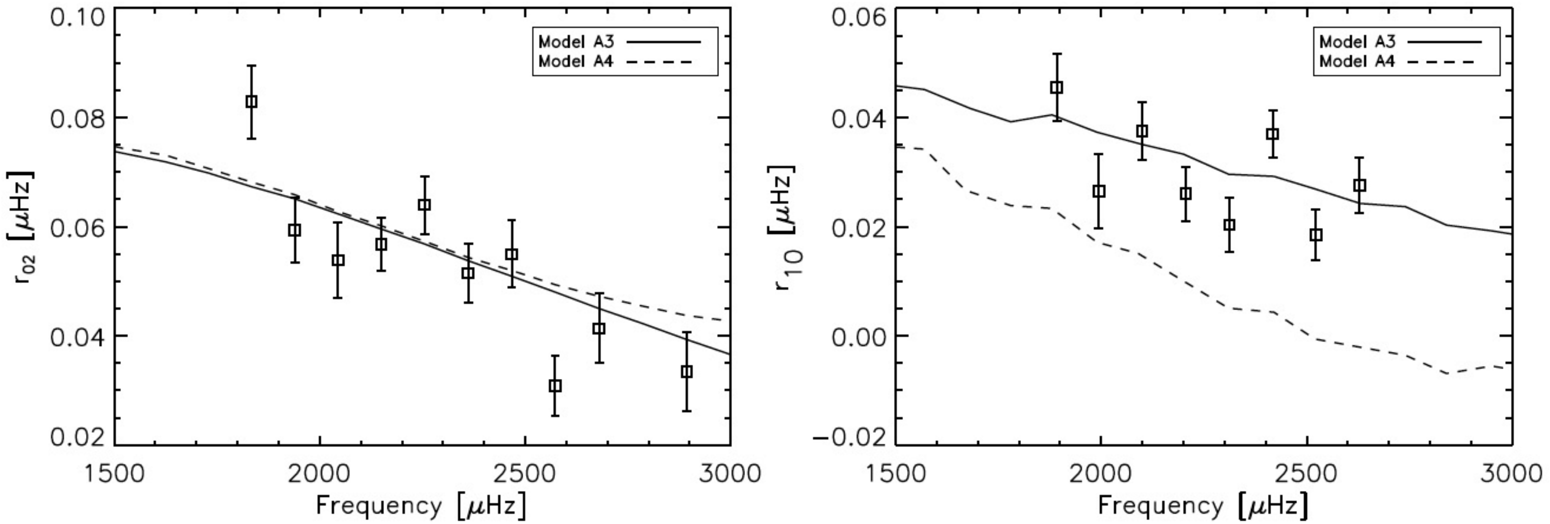

Figure 3.3: Comparison with models of α Cen A based on the ratios r_{02} and r_{10} - The left-hand (right-hand) panel shows a comparison of the observed ratio r_{02} (r_{10}) with that computed from a couple of models from Miglio & Montalbán (2005) (see text for details). From de Meulenaer et al. (2010).

main-sequence phase. They also realized that the structural differences in these two sets of models leave distinctive signatures on the oscillation frequencies, in particular on the ratios r_{02} (cf. Eq. 1.55) and r_{10} (cf. Eq. 1.56). In Fig. 3.3 we compare the observed ratios r_{02} and r_{10} – derived from the frequencies estimated in our study – with those computed from a couple of models from Miglio & Montalbán (2005), to be specific, their models A3 (radiative core and no overshooting) and A4 (convective core and $\alpha_{\rm ov} = 0.2$). Although the ratio r_{02} does not help discriminating between models, the ratio r_{10} allows us to reject model A4. Therefore, current observational constraints seem not to be in favor of a convective core in α Cen A. Moreover, we are able to set an upper limit to the amount of convective-core overshooting needed to model stars of mass and metallicity similar to those of α Cen A.

3.2 Results from *CoRoT*

3.2.1 A fresh look at the seismic spectrum of HD 49933

In Benomar et al. (2009b), we have analysed 180 days of *CoRoT* photometry on the F5 main-sequence star HD 49933. In 2007, *CoRoT* had already produced a 60-day time series on this target as a result of an initial short run. These initial data would be subsequently analysed by Appourchaux et al. (2008), thus providing the first asteroseismic results from *CoRoT* on a star displaying solar-like oscillations. A new and longer run of 137 days then followed in 2008. Note also that this star had been observed during 10 nights with HARPS (Mosser et al. 2005) previous to the advent of *CoRoT*.

The seismic spectrum of HD 49933 has proven very difficult to interpret. Mosser et al. (2005) were unable to isolate individual p modes in the power spectrum, but could still measure the large frequency separation. The data analysed by Appourchaux et al. (2008) clearly showed individual p-mode peaks in the power spectrum. However, they still had to face the problem of mode identification (recall the discussion on the "F star problem" in Sect. 2.2.3.2), which was apparently solved based on the computation of a likelihood ratio. This same time series would be the object of further studies. For instance, Benomar et al. (2009a), based on the computation of a Bayesian odds ratio (cf. Eq. 2.95), found mode identification to be ambiguous for this star. Needless to say, controversy arised.

As already stated above, in this work we have analysed 180 days of photometric data. Three power spectra were computed: from the initial 60-day run and from two non-overlapping subsets of 60 days each belonging to the second longer run. These spectra were then averaged, hence reducing the variance in the resulting average power spectrum. This final power spectrum was distributed to a number of fitters, who then fitted a common model to the spectrum using different methods (MLE, MAP and a Bayesian approach using MCMC techniques) or the same method applied in an independent manner. The different methods yielded consistent results, allowing us to make a robust identification of the modes in terms of the degree l (see Fig. 3.4). Our preferred mode identification, opposite to the one advanced by Appourchaux et al. (2008), was established with a very high confidence level. Moreover, the precision with which mode parameters were estimated has significantly increased, with the rotational splitting remaining the only mode parameter that is poorly constrained.

3.2.2 The *CoRoT* target HD 52265: a G0V metal-rich exoplanet-host star

HD 52265 is a G0V metal-rich exoplanet-host[1] star observed in the seismology field of the *CoRoT* space telescope from November 2008 to March 2009. The satellite collected 117 days of high-precision photometric data on this star with a duty cycle of 90%, allowing for a clear detection of solar-like oscillations. Complementary ground-based observations were obtained with the Narval spectrograph at the Pic du Midi observatory in December 2008 and January 2009, i.e., simultaneously with *CoRoT* observations.

In Ballot et al. (2011), our aim has been to characterize HD 52265 using both spectroscopic and seismic data. To date, only a handful of exoplanet-host stars have been the object of seismic studies: μ Ara (Bouchy et al. 2005), ι Hor (Vauclair et al. 2008), HD 46375 (Gaulme et al. 2010), HAT-P-7, HAT-P-11 and TrES-2 (Christensen-Dalsgaard et al. 2010). The high-quality *CoRoT* observations of HD 52265 have allowed us to determine its seismic properties with a precision never before obtained for any other exoplanet-host star.

Precise fundamental stellar parameters have been obtained: $T_{\mathrm{eff}} = 6100 \pm 60$ K, $\log g = 4.35 \pm 0.09$, $[\mathrm{M/H}] = 0.19 \pm 0.05$, as well as $v \sin i = 3.6^{+0.3}_{-1.0}\ \mathrm{km\,s^{-1}}$. We have

---

[1] A planet orbiting HD 52265 was independently discovered in 2000 by Butler et al. (2000) and Naef et al. (2001).

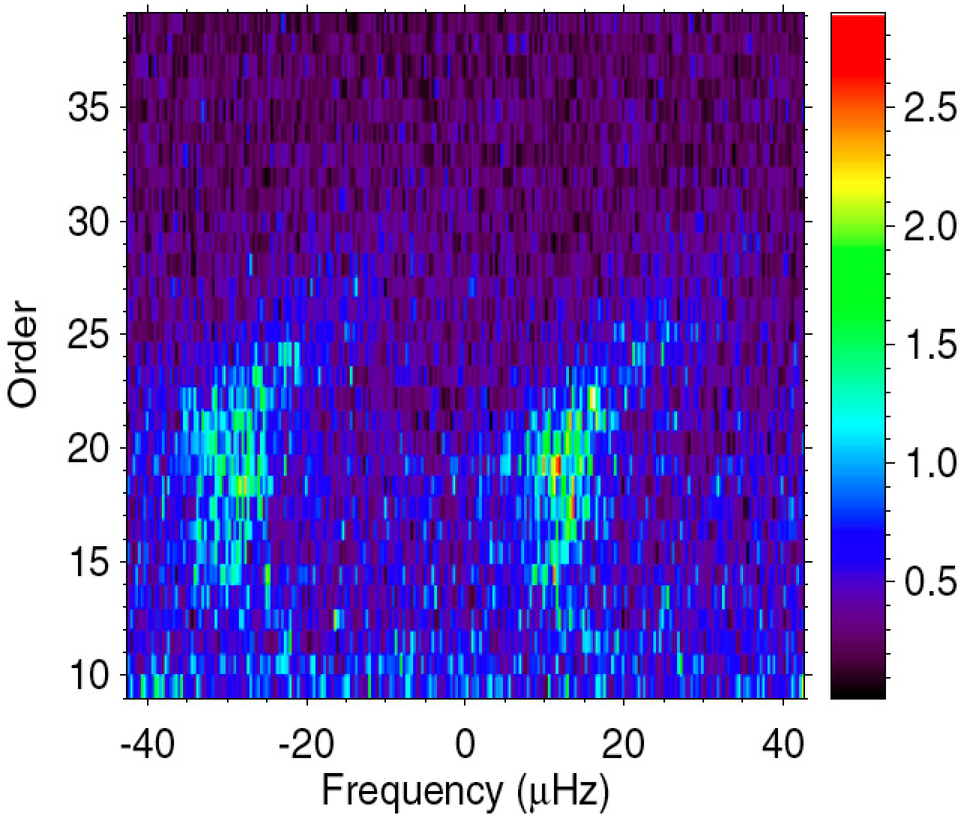

Figure 3.4: Average spectrum of HD 49933 in échelle format - This échelle diagram has been computed using a large frequency separation of 85 μHz and then smoothed to 0.8 μHz (4 bins). Identification of the ridges from a simple visual inspection is far from evident. In our preferred identification scenario, the left-hand ridge corresponds to $l=1$ and the right-hand ridge to $l=0,2$. From Benomar et al. (2009b).

derived the granulation properties and have analysed the signature of stellar rotation arising from the modulation of the light curve due to photospheric magnetic activity (see Fig. 3.5). Thanks to spot-modeling of the light curve, we have found a mean rotational period of $P_{\rm rot}=12.3 \pm 0.15$ days.

Parameters describing the observed p modes have been estimated using MLE. A global fit to the spectrum has been performed, over about ten radial orders, for degrees $l = 0, 1, 2$. The frequencies of 31 modes are reported in the range 1500–2550 μHz. The large separation exhibits a clear modulation around the mean value $\langle \Delta\nu \rangle = 98.3 \pm 0.1$ μHz, which we interpret as possibly being associated with the he-

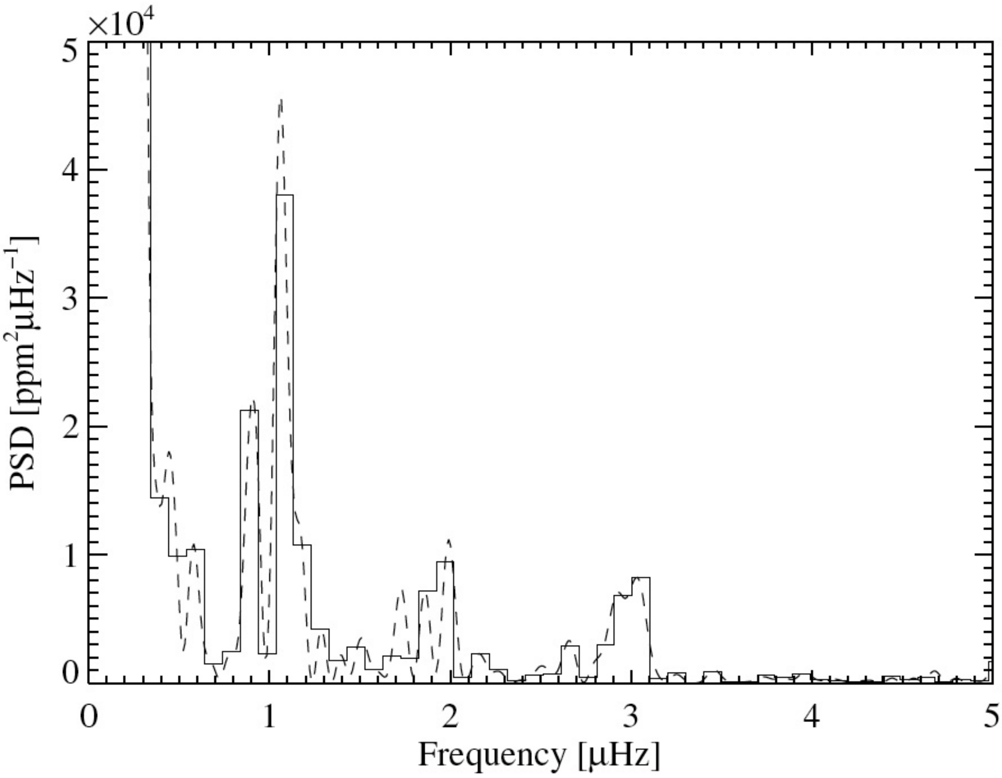

Figure 3.5: Power density spectrum of HD 52265 at the low-frequency end - The power density spectrum is represented by the solid line, while the dashed line corresponds to an oversampled version of the spectrum (by a factor of 10). The modulation of the light curve caused by photospheric spots produces a significant peak at 1.05 μHz and another very close one at 0.91 μHz. We interpret this broadened structure as being the signature of differential rotation. Peaks around 2 and 3 μHz are simply overtones of the rotational period. From Ballot et al. (2011).

lium second-ionization region. Mode linewidths vary with frequency along a S-shaped curve with a local maximum around 1800 μHz (see Fig. 3.6). Mode lifetimes range between 0.5 and 3 days, being shorter than solar, although significantly longer than those observed for F stars. Finally, amplitudes increase almost regularly until reaching a maximum around 2100 μHz, remaining close to that maximum before sharply dropping above 2450 μHz. The fitted maximum bolometric amplitude for radial modes is 3.96 ± 0.24 ppm.

Thanks to the precise estimates of mode frequencies (a precision of about 0.2 μHz has been achieved for the highest-amplitude modes) and fundamental parameters,

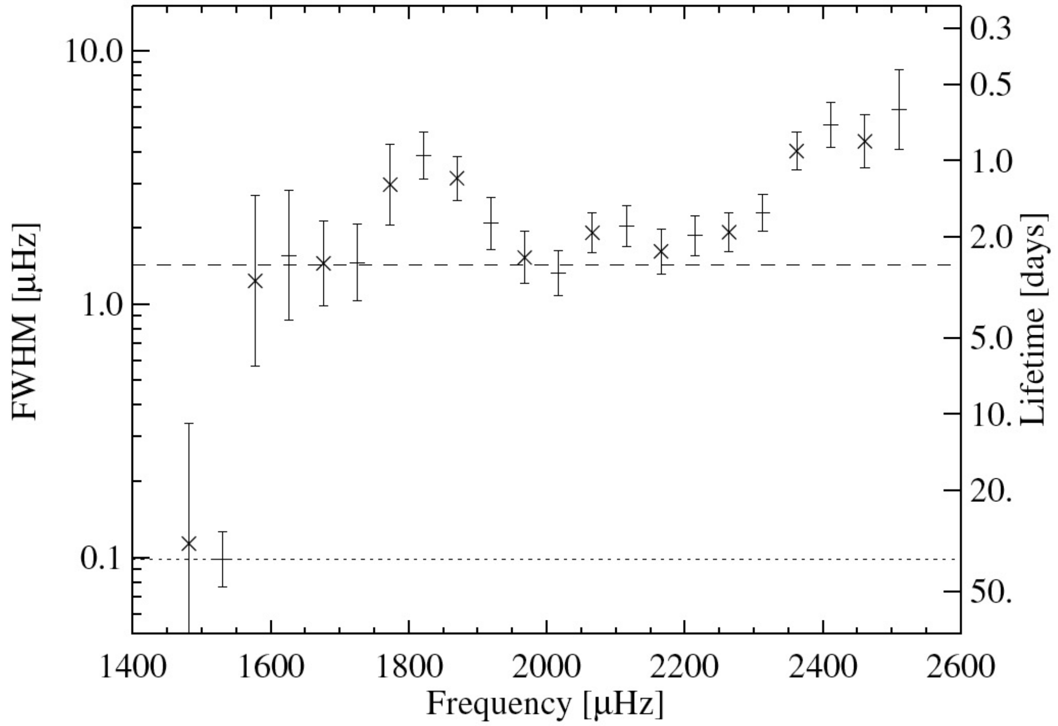

Figure 3.6: Mode linewidths as a function of frequency for HD 52265 - Crosses correspond to values obtained by fitting a common width for modes with $(n-1, l=1)$ and $(n, l=0)$, whereas plus signs correspond to values obtained by fitting a common width for modes with $(n, l=1)$ and $(n, l=0)$. The dotted line indicates the spectral resolution. The dashed line shows the prediction of Chaplin et al. (2009). From Ballot et al. (2011).

HD 52265 has become a promising object for stellar modeling. This seismic study will also help improving our knowledge of the planetary companion.

3.2.3 On the origin of the intermediate-order g modes observed in the hybrid γ Dor/δ Sct star HD 49434

γ Doradus stars pulsate in high-order g modes with periods of order 1 day, driven by convective-flux blocking at the base of their convective envelopes. δ Scuti stars, on the other hand, pulsate in low-order p modes with periods of order 2 hours, driven by the κ mechanism operating in the He II ionization zone. The two types of modes have their properties determined by different portions of the stellar interior. Therefore, hybrid γ Dor/δ Sct pulsators are of great interest because they offer additional constraints on stellar structure and may be used to test theoretical models (Grigahcène et al. 2010). Furthermore, in the same locus of the Hertzsprung-Russell diagram where the γ Dor and δ Sct instability strips overlap, solar-like oscillations are also predicted to occur for δ Sct stars (Houdek et al. 1999; Samadi et al. 2002), having actually been confirmed observationally for the very first time by Antoci et al. (2011).

In Campante et al. (2010a)[1], we have analysed the frequency power spectrum of HD 49434 resulting from 136.9 days of *CoRoT* photometry. HD 49434 (F1V) had been referenced as a candidate hybrid γ Dor/δ Sct star by Uytterhoeven et al. (2008), following an extensive photometric and spectroscopic ground-based campaign, a classification that Chapellier et al. (2011) could, however, not confirm. A compelling feature of its frequency power spectrum is the presence of intermediate-order g modes between the simultaneously excited high-order g modes (γ Dor regime) and low-order p modes (δ Sct regime). However, time-dependent convection models (Dupret et al. 2005; Grigahcène et al. 2005) predict the existence of a theoretical frequency gap that is stable to pulsations in the range 5–15 d^{-1} (i.e., between the two regimes just mentioned) for low-degree modes. This raises the question as to which mechanism is responsible for the excitation of the observed intermediate-order g modes.

In this work, we have addressed the possibility that such modes are excited by a stochastic mechanism. A search for the signature of stochastic excitation in a selection of modes within the theoretical frequency gap was carried out according to the statistical method described in Pereira & Lopes (2005) (recall the discussion in Sect. 1.4.4). Figure 3.7 displays the so-called excitation diagram for a selection of modes within the theoretical frequency gap. The fact that the observational results lie outside the confidence interval (for the two strongest modes) or just over the 1-σ lower bound (for the two faintest modes) may tempt one to conclude that these modes are not stochastically excited. However, we need to be cautious and a new analysis should be carried out that uses a larger number of amplitude measurements (i.e., using shorter subseries or, alternatively, based on a longer time series), thus increasing the significance of the statistic $\sigma(A)/\langle A\rangle$.

---

[1] This non-refereed proceedings paper resulted from a poster presentation at the Fourth HELAS International Conference, held in Lanzarote in February 2010.

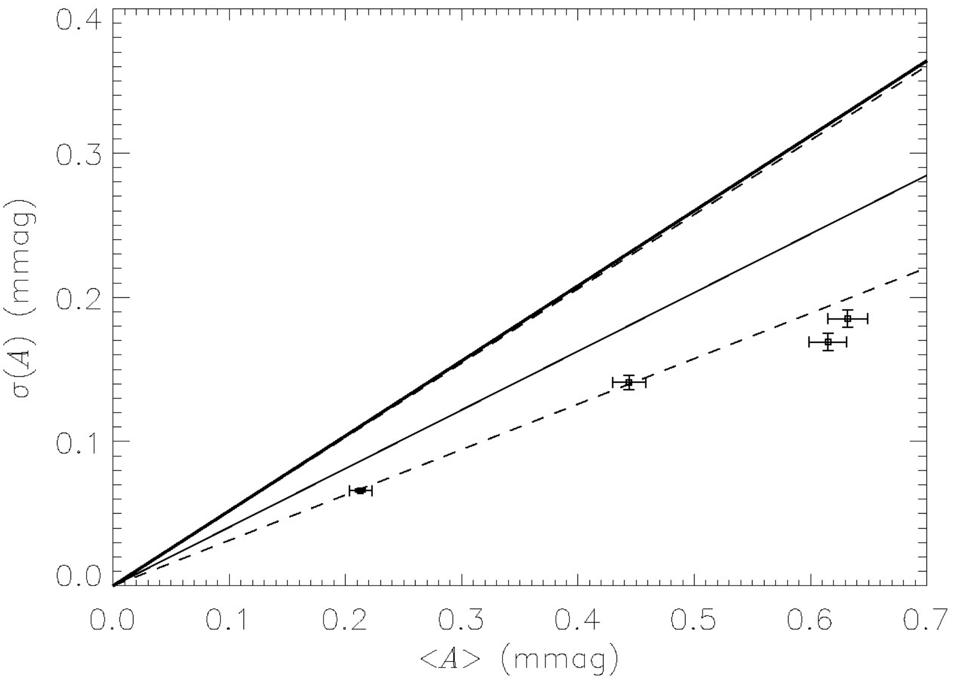

Figure 3.7: Excitation diagram for 4 selected modes within the frequency gap - Observational results for a selection of 4 modes within the gap are plotted with accompanying error bars. The thick solid line represents the theoretical relation $\sigma(A)=0.52\langle A\rangle$. The thin solid line represents the outcome of Monte Carlo simulations – assuming stochastic excitation and the same sampling used to obtain the observational results – which gave $\sigma(A)\approx 0.41\langle A\rangle$, with the corresponding 1-σ bounds represented by the dashed lines. From Campante et al. (2010a).

3.3 Results from *Kepler*

3.3.1 Global properties of solar-like oscillations observed by *Kepler*: a comparison of complementary analysis methods

In Sect. 2.3, I emphasized the main reasons why automated pipelines have been used to analyse *Kepler* data on main-sequence and subgiant solar-like oscillators. Firstly, global asteroseismic parameters are readily obtainable – even from data with low SNR – using automated analysis methods. Secondly, the automated nature of these pipelines is required to efficiently exploit the plenitude of data made available by *Kepler* on these targets.

In Verner et al. (2011b), we present the asteroseismic analysis of 1948 F-, G-, and K-type main-sequence and subgiant stars observed by *Kepler* during the first seven months of science operations. This incorporates all short-cadence observations of stars that have been identified as potentially showing solar-like oscillations. We have detected solar-like oscillations in 642 of these stars and have characterized them by their average large frequency separation ($\Delta\nu$), frequency of maximum amplitude ($\nu_{\max}$), and maximum mode amplitude ($A_{\max}$). This represents the largest cohort of main-sequence and subgiant solar-like oscillators observed to date. By combining results from the analysis methods of nine independent research teams (see Table 3.1), we have verified the detections, rejected outliers, and devised a method to ensure the results are consistent within an accurate uncertainty range. It is apparent that the formal uncertainties returned from automated analysis methods are often inconsistent with the actual precision of the results. Obtaining an accurate uncertainty on the global asteroseismic parameters is essential when using such results to model stellar structure.

We have correlated the fraction of stars for which we detected oscillations with the stellar parameters from the *Kepler* Input Catalog (KIC; e.g., Brown et al. 2011; Verner et al. 2011a), and found a significant reduction in the proportion of solar-like oscillators with effective temperatures in the range $5300\,\mathrm{K} \lesssim T_{\mathrm{eff}} \lesssim 5700\,\mathrm{K}$, viz., the temperature range that separates the distributions of main-sequence stars from subgiants. This has also been noted by Chaplin et al. (2011b), who have suggested that this absence of oscillators may be due to evolutionary effects that cause an increase in surface magnetic activity, thus reducing the detectability of oscillations. Moreover, a drop-off has been found in the relative number of detected oscillators approaching the red edge of the classical instability strip.

By characterizing the stars by $\Delta\nu$ or $\nu_{\max}$, we have clearly identified the separate main-sequence and subgiant populations (see Fig. 3.8). The distributions of these global asteroseismic parameters for the observed main-sequence stars show that we typically find values of $\Delta\nu$ and $\nu_{\max}$ smaller than solar. This reflects the increased amplitude of oscillations in stars with lower $\nu_{\max}$ and the higher intrinsic luminosity of such stars. The stars with asteroseismic parameters closer to those of the Sun also tend to be the brighter stars in the set.

By combining the scaling relations in Eqs. (1.32) and (1.54), Stello et al. (2009a) showed that the expected relationship between $\Delta\nu$ and $\nu_{\max}$ is almost independent of

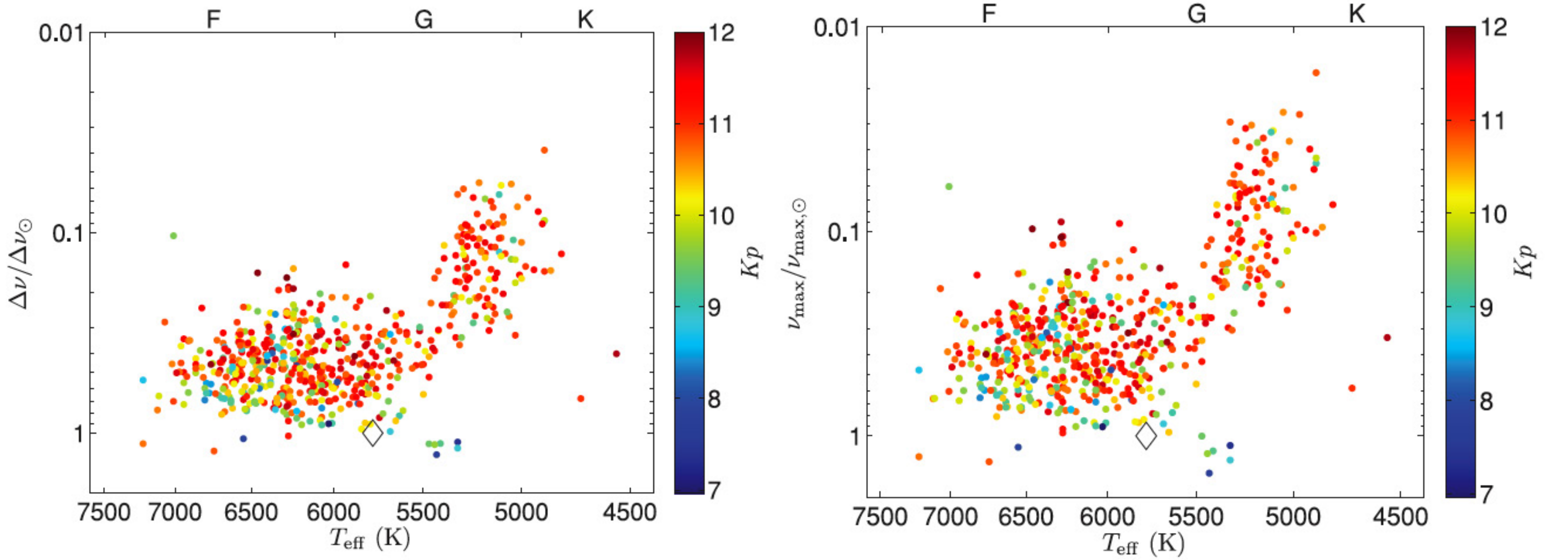

Figure 3.8: Asteroseismic population diagrams - These diagrams have been produced using the values of $\Delta\nu$ (left-hand panel) and $\nu_{\rm max}$ (right-hand panel). The subgiants are grouped in the upper right of the diagrams, with the main-sequence stars grouped in the lower left. The diamonds indicate the position of the Sun. Points are colored according to the corresponding apparent magnitude taken from the KIC. From Verner et al. (2011b).

Table 3.1: Summary of the methods used by each automated pipeline - Abbreviations used are SPS – smoothed power spectrum, PSPS – power spectrum of the power spectrum, TSACF – time series autocorrelation function, PSACF – power spectrum autocorrelation function, and K08 – method based on Kjeldsen et al. (2008a).

Pipeline	Method for $\Delta\nu$	Method for $\nu_{\max}$	Method for $A_{\max}$
A2Z[a]	Peak of PSPS	Fit to SPS	Fit to SPS (K08)
AAU[b]	Peak of PSPS	Peak of SPS	Peak of SPS
COR[c]	Fit to TSACF	Fit to SPS	Fit to TSACF
IAS	Peak of TSACF	Fit to SPS	Fit to SPS (K08)
OCT[d]	1: PSPS (full PS) 2: PSPS (Bayesian on full PS)[j] 3: PSPS (small ν range)[j] 4: PSPS (Bayesian on small ν range)[j]	1: Fit to SPS 2: Peak of SPS[j]	1: Peak of SPS 2: Fit to SPS 3: Fit to SPS (K08)
ORK[e]	Comb response function	CLEAN algorithm	—
QML[f]	1: Peak of TSACF 2: Fit to PSACF	Fit to PSACF	Fit to PSACF
KAB[g,h]	Fit to PSACF	1: Fit to PSACF 2: Fit to SPS	Fit to SPS
SYD[i]	Fit to PSACF	1: Peak of SPS 2: Fit to SPS	1: Peak of SPS (K08) 2: Fit to SPS (K08)

[a] Mathur et al. (2010b); [b] see Sect. 2.3; [c] Mosser & Appourchaux (2009); [d] Hekker et al. (2010); [e] Bonanno et al. (2008); [f] Verner & Roxburgh (2011); [g] Campante et al. (2010b); [h] Karoff et al. (2010); [i] Huber et al. (2009); [j] only used for the analysis of simulated data.

luminosity and only weakly dependent on mass and effective temperature. To a good approximation, we can assume

$$\frac{\Delta\nu}{\Delta\nu_{\odot}} \approx \left(\frac{\nu_{\max}}{\nu_{\max,\odot}}\right)^{a}, \tag{3.1}$$

after scaling by solar values. We have determined the exponents of power-law relationships between the verified $\Delta\nu$ and $\nu_{\max}$ values and found that the scatter in the results is at a level greater than the formal uncertainties obtained for the individual methods. Taking a weighted average of the exponents, we have determined a power-law exponent of $a = 0.795 \pm 0.007$, which is significantly higher than that found using data from a similar number of red giants: $a = 0.784 \pm 0.003$ (Hekker et al. 2009). This discrepancy can be explained by the different temperatures and evolutionary states of the stars in each study.

The maximum mode amplitudes obtained by each method have been used to determine the exponent s (cf. Eq. 1.33) relating the dependence of mode amplitude on

L/M. We have used bolometric-corrected amplitudes and set $r = 1.5$ (cf. Eq. 1.35) to find that a strong temperature dependence remains in s. This is not surprising, since setting $r = 1.5$ in Eq. (1.35) relies on a very simple adiabatic description of the stellar atmosphere. We have constrained this dependence by a linear relationship, which gives a value of s for stars in the red-giant regime that agrees with that determined in Mosser et al. (2010).

3.3.2 Ensemble asteroseismology of solar-type stars with *Kepler*

During the first seven months of science operations, more than 2000 stars have been selected for observation at short cadence for a 1-month period each, as part of an asteroseismic survey of the solar-type population in the *Kepler* field of view. These stars have magnitudes down to *Kepler* apparent magnitude $Kp \approx 12$ and have been selected as potential solar-type targets based upon parameters in the KIC. In Chaplin et al. (2011c), we report the detection of solar-like oscillations in 500 of these stars, an ensemble that is large enough to allow statistical studies of intrinsic stellar properties (such as mass, radius, and age) and to test theories of stellar evolution.

We have made use of the $\Delta\nu$ and $\nu_{\rm max}$ of the stars in the ensemble, together with estimates of $T_{\rm eff}$ derived from multicolor photometry available in the KIC, to estimate the masses and radii in a way that is independent of stellar evolutionary models. This so-called direct method of estimation uses the following relations (Kallinger et al. 2010b):

$$\frac{R}{\mathrm{R}_\odot} \approx \frac{\nu_{\rm max}}{\nu_{\rm max,\odot}} \left(\frac{\Delta\nu}{\Delta\nu_\odot}\right)^{-2} \left(\frac{T_{\rm eff}}{\mathrm{T}_{\rm eff,\odot}}\right)^{0.5} \tag{3.2}$$

and

$$\frac{M}{\mathrm{M}_\odot} \approx \left(\frac{\nu_{\rm max}}{\nu_{\rm max,\odot}}\right)^{3} \left(\frac{\Delta\nu}{\Delta\nu_\odot}\right)^{-4} \left(\frac{T_{\rm eff}}{\mathrm{T}_{\rm eff,\odot}}\right)^{1.5}, \tag{3.3}$$

which can be arrived at by combining Eqs. (1.32) and (1.54), and then solving for R and M, respectively. We have obtained a median fractional uncertainty of just over 10% in M and about 5.5% in R. The direct method gives larger uncertainties on M and on R than would be obtained from a grid-based method of estimation (i.e., matching the observations to stellar evolutionary tracks; e.g., Stello et al. 2009b; Basu et al. 2010; Quirion et al. 2010; Gai et al. 2011). However, the lack of precise independent constraints on the metallicities meant that the grid-based approach would be vulnerable to a systematic bias in the estimates of M (although not R).

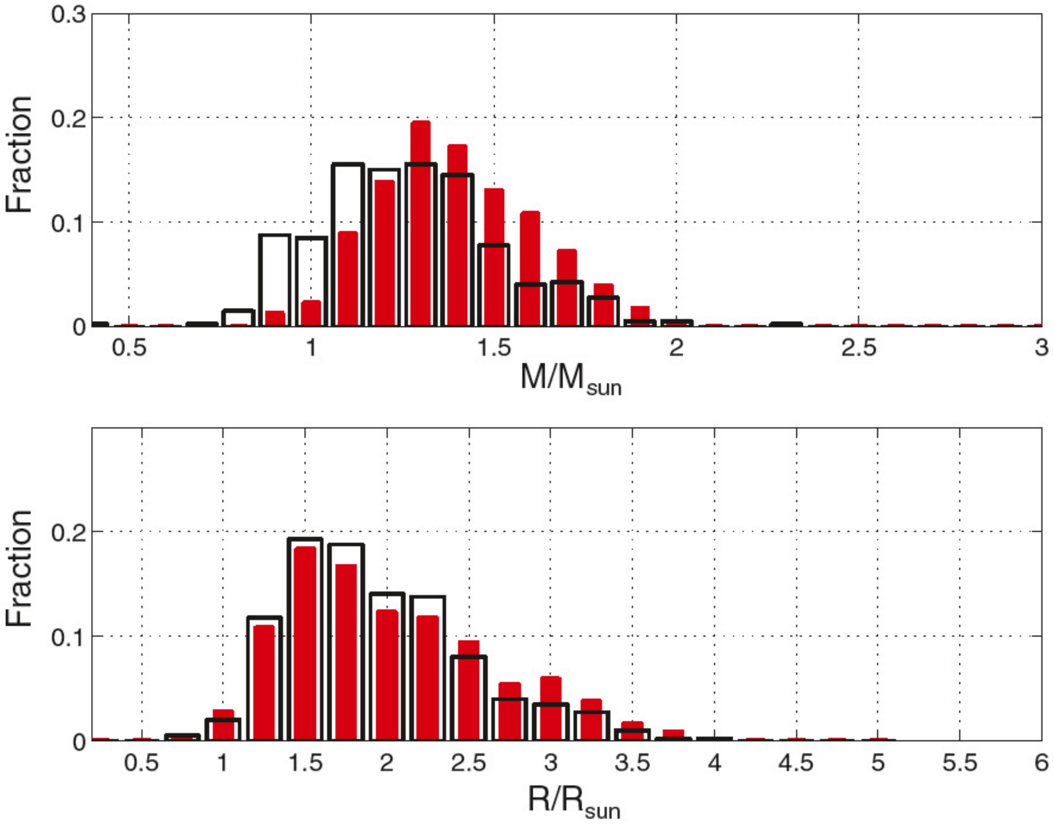

Figure 3.9: Observed versus predicted distributions of fundamental stellar parameters - Black lines show histograms of the observed distributions of masses (top panel) and radii (bottom panel). In red, the predicted distributions from population synthesis modeling, after correction for the effects of detection bias. From Chaplin et al. (2011c).

The observed distributions of stellar masses and radii have been compared with those predicted from synthetic stellar populations (see Fig. 3.9). The synthetic populations have been calculated by modeling the formation and evolution of stars in the *Kepler* field of view. This modeling requires descriptions of, for example, the star-formation history, the spatial density of stars in the disk of the Galaxy, and the rate at which the Galaxy is chemically enriched by stellar evolution. While the distributions of stellar radii are similar, the same cannot be said for the mass distributions. We have applied the Kolmogorov-Smirnov test in order to quantify differences between the observed and synthetic distributions. Differences in radius were found to be marginally significant at best. In contrast, those in mass were found to be highly significant

($> 99.99\%$). The observed distribution of masses is wider at its peak than the predicted distribution and is offset toward slightly lower masses. On the assumption that the observed masses and radii are robust, this result may have implications for both the star-formation rate and the initial mass function of stars.

3.3.3 Solar-like oscillations in KIC 11395018 and KIC 11234888 from eight months of *Kepler* data

Since the start of *Kepler* science operations in May 2009, a selection of survey stars have been continuously monitored at short cadence to test and validate the time-series photometry, five of which show evidence of solar-like oscillations. Such continuous and long observations are unprecedented for solar-type stars other than the Sun. In Mathur et al. (2011), we have analysed 8-month-long time series with a duty cycle in excess of 90% for two of these stars[1], namely, KIC 11395018 and KIC 11234888. The two stars selected for this study are relatively faint – KIC 11395018 (G-type) and KIC 11234888 (late F-type) have *Kepler* apparent magnitudes of $Kp = 10.8$ and $Kp = 11.9$, respectively – and display low SNR in the p-mode peaks. The light curves used in the analysis have been corrected for instrumental effects in a manner independent of the *Kepler* science pipeline (for details see García et al. 2011b).

Different fitting strategies have been employed to extract estimates of p-mode frequencies as well as of other individual mode parameters, from which we have selected frequency lists that will help constrain stellar models. A total of 22 and 16 modes of degree $l = 0, 1, 2$ have been identified for KIC 11395018 (in the range 600–1000 μHz) and KIC 11234888 (in the range 500–900 μHz), respectively. Moreover, two avoided crossings ($l = 1$ ridge) have been identified for KIC 11395018, while a more complex échelle spectrum has been found for KIC 11234888 displaying several avoided crossings (see Fig. 3.10). Both stars are thus thought to have evolved off the main sequence. These results confirm previous expectations that asteroseismology of solar-type survey targets is possible down to apparent magnitudes of 11 and fainter, provided we work with a multi-month time series (e.g., Stello et al. 2009b).

The global asteroseismic parameters reported for these stars, together with a detailed atmospheric analysis, should allow constraining their radii, masses and ages with

---

[1] Two other stars, namely, KIC 10273246 and KIC 10920273, are analysed in Campante et al. (2011).

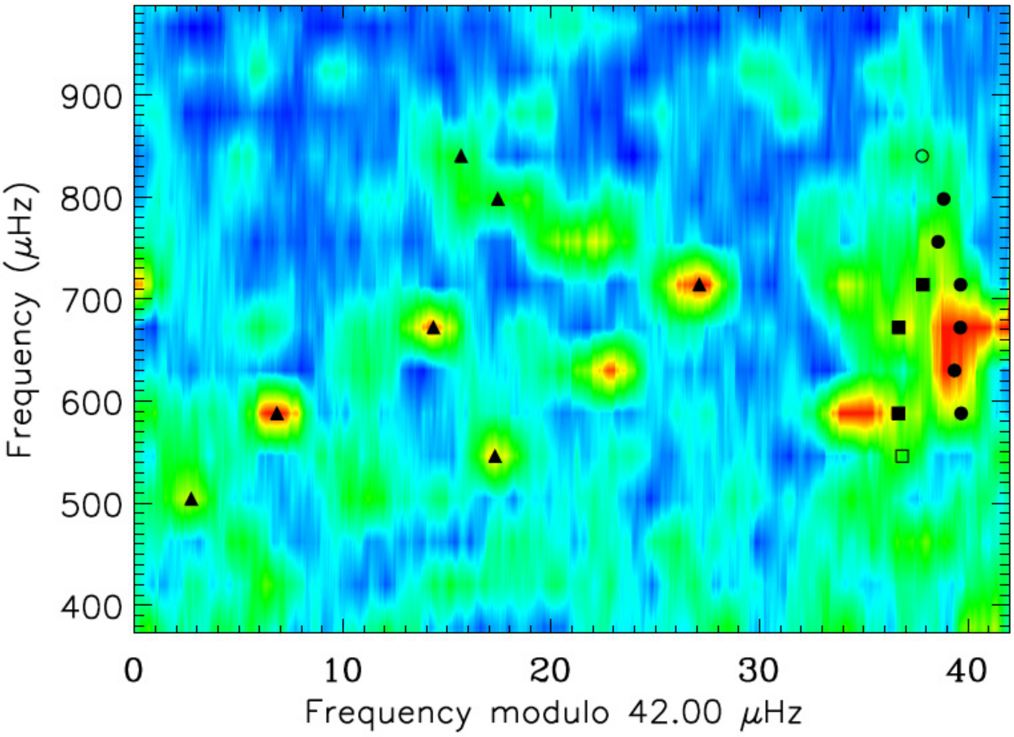

Figure 3.10: Échelle diagram of the power density spectrum of KIC 11234888 - The minimal (filled symbols) and maximal (filled and open symbols) frequency sets are displayed (for a definition see Campante et al. 2011). Symbol shapes indicate mode degree: $l=0$ (circles), $l=1$ (triangles), and $l=2$ (squares). From Mathur et al. (2011).

considerable precision (Creevey et al. 2012). Further insight into the physics of these evolved solar-type stars – based on detailed modeling and inversion techniques – is now possible due to the high quality of the seismic parameters found.

Bibliography

Abrams, D. & Kumar, P. 1996, ApJ, 472, 882

Aerts, C., Christensen-Dalsgaard, J., & Kurtz, D. W. 2010, Asteroseismology, 1st edn. (Springer)

Aigrain, S., Favata, F., & Gilmore, G. 2004, A&A, 414, 1139

Aizenman, M., Smeyers, P., & Weigert, A. 1977, A&A, 58, 41

Anderson, E. R., Duvall, Jr., T. L., & Jefferies, S. M. 1990, ApJ, 364, 699

Antoci, V., Handler, G., Campante, T. L., et al. 2011, Nature, 477, 570

Appourchaux, T. 2003, A&A, 412, 903

Appourchaux, T. 2004, A&A, 428, 1039

Appourchaux, T. 2008, Astronomische Nachrichten, 329, 485

Appourchaux, T. 2011, in Asteroseismology, Canary Islands Winter School of Astrophysics, ed. P. L. Pallé, Vol. XXII (Cambridge University Press)

Appourchaux, T., Belkacem, K., Broomhall, A.-M., et al. 2010, A&A Rev., 18, 197

Appourchaux, T., Benomar, O., Gruberbauer, M., et al. 2012, A&A, 537, A134

Appourchaux, T., Berthomieu, G., Michel, E., et al. 2006a, in ESA Special Publication, Vol. 1306, Proceedings of The *CoRoT* Mission Pre-Launch Status – Stellar Seismology and Planet Finding, ed. M. Fridlund, A. Baglin, J. Lochard, & L. Conroy, 377

Appourchaux, T., Berthomieu, G., Michel, E., et al. 2006b, in ESA Special Publication, Vol. 1306, Proceedings of The *CoRoT* Mission Pre-Launch Status – Stellar Seismology and Planet Finding, ed. M. Fridlund, A. Baglin, J. Lochard, & L. Conroy, 429

Appourchaux, T., Fröhlich, C., Andersen, B. N., et al. 2000, ApJ, 538, 401

Appourchaux, T., Gizon, L., & Rabello-Soares, M. 1998, A&AS, 132, 107

Appourchaux, T., Michel, E., Auvergne, M., et al. 2008, A&A, 488, 705

Appourchaux, T., Samadi, R., & Dupret, M.-A. 2009, A&A, 506, 1

Arentoft, T., Kjeldsen, H., & Bedding, T. R. 2009, in Astronomical Society of the Pacific Conference Series, ed. M. Dikpati, T. Arentoft, I. González Hernández, C. Lindsey, & F. Hill, Vol. 416, 347

Arentoft, T., Kjeldsen, H., Bedding, T. R., et al. 2008, ApJ, 687, 1180

Auvergne, M., Bodin, P., Boisnard, L., et al. 2009, A&A, 506, 411

Baglin, A., Michel, E., Auvergne, M., & the *CoRoT* Team. 2006, in ESA Special Publication, Vol. 624, Proceedings of *SOHO* 18/GONG 2006/HELAS I, Beyond the spherical Sun

Ballot, J. 2010, Astronomische Nachrichten, 331, 933

Ballot, J., Appourchaux, T., Toutain, T., & Guittet, M. 2008, A&A, 486, 867

Ballot, J., García, R. A., & Lambert, P. 2006, MNRAS, 369, 1281

Ballot, J., Gizon, L., Samadi, R., et al. 2011, A&A, 530, A97

Ballot, J., Turck-Chièze, S., & García, R. A. 2004, A&A, 423, 1051

Balona, L. A., Pigulski, A., De Cat, P., et al. 2011, MNRAS, 413, 2403

Barban, C., Deheuvels, S., Baudin, F., et al. 2009, A&A, 506, 51

Basu, S. & Antia, H. M. 2008, Phys. Rep., 457, 217

Basu, S., Chaplin, W. J., & Elsworth, Y. 2010, ApJ, 710, 1596

Basu, S., Grundahl, F., Stello, D., et al. 2011, ApJ, 729, L10

Basu, S., Mazumdar, A., Antia, H. M., & Demarque, P. 2004, MNRAS, 350, 277

Batchelor, G. K. 1953, The Theory of Homogeneous Turbulence, 1st edn. (Cambridge University Press)

Baudin, F., Barban, C., Belkacem, K., et al. 2011, A&A, 529, A84

Bayes, T. & Price, R. 1763, Philosophical Transactions, 53, 370

Bazot, M., Bouchy, F., Kjeldsen, H., et al. 2007, A&A, 470, 295

Bazot, M., Ireland, M. J., Huber, D., et al. 2011, A&A, 526, L4

Bazot, M., Vauclair, S., Bouchy, F., & Santos, N. C. 2005, A&A, 440, 615

Beck, P. G., Bedding, T. R., Mosser, B., et al. 2011, Science, 332, 205

Bedding, T. R. 2003, Ap&SS, 284, 61

Bedding, T. R. 2011, in Asteroseismology, Canary Islands Winter School of Astrophysics, ed. P. L. Pallé, Vol. XXII (Cambridge University Press)

Bedding, T. R., Brun, A. S., Christensen-Dalsgaard, J., et al. 2007a, Highlights of Astronomy, 14, 491

Bedding, T. R., Butler, R. P., Kjeldsen, H., et al. 2001, ApJ, 549, L105

Bedding, T. R., Huber, D., Stello, D., et al. 2010a, ApJ, 713, L176

Bedding, T. R. & Kjeldsen, H. 2003, PASA, 20, 203

Bedding, T. R. & Kjeldsen, H. 2008, in Astronomical Society of the Pacific Conference Series, Vol. 384, 14th Cambridge Workshop on Cool Stars, Stellar Systems, and the Sun, ed. G. van Belle, 21

Bedding, T. R. & Kjeldsen, H. 2010, Communications in Asteroseismology, 161, 3

Bedding, T. R., Kjeldsen, H., Arentoft, T., et al. 2007b, ApJ, 663, 1315

Bedding, T. R., Kjeldsen, H., Bouchy, F., et al. 2005, A&A, 432, L43

Bedding, T. R., Kjeldsen, H., Butler, R. P., et al. 2004, ApJ, 614, 380

Bedding, T. R., Kjeldsen, H., Campante, T. L., et al. 2010b, ApJ, 713, 935

Bedding, T. R., Kjeldsen, H., Reetz, J., & Barbuy, B. 1996, MNRAS, 280, 1155

Bedding, T. R., Mosser, B., Huber, D., et al. 2011, Nature, 471, 608

Belkacem, K., Goupil, M.-J., Dupret, M.-A., et al. 2011, A&A, 530, A142

Belkacem, K., Samadi, R., Goupil, M.-J., et al. 2009, Science, 324, 1540

Benomar, O., Appourchaux, T., & Baudin, F. 2009a, A&A, 506, 15

Benomar, O., Baudin, F., Campante, T. L., et al. 2009b, A&A, 507, L13

Berger, J. O., Boukai, B., & Wang, Y. 1997, Statistical Science, 12, 133

Berger, J. O. & Sellke, T. 1987, Journal of the American Statistical Association, 82, 112

Blackman, R. B. & Tukey, J. W. 1958a, Bell System Technical Journal, 37, 185

Blackman, R. B. & Tukey, J. W. 1958b, Bell System Technical Journal, 37, 485

Böhm-Vitense, E. 2007, ApJ, 657, 486

Bonanno, A., Benatti, S., Claudi, R., et al. 2008, ApJ, 676, 1248

Borucki, W. J., Koch, D., Basri, G., et al. 2010, Science, 327, 977

Bouchy, F., Bazot, M., Santos, N. C., Vauclair, S., & Sosnowska, D. 2005, A&A, 440, 609

Bouchy, F. & Carrier, F. 2001, A&A, 374, L5

Bouchy, F. & Carrier, F. 2002, A&A, 390, 205

Bourguignon, S., Carfantan, H., & Böhm, T. 2007, A&A, 462, 379

Brandão, I. M., Doğan, G., Christensen-Dalsgaard, J., et al. 2011, A&A, 527, A37

Breger, M., Stich, J., Garrido, R., et al. 1993, A&A, 271, 482

Bretthorst, G. L. 1988, Bayesian Spectrum Analysis and Parameter Estimation (New York: Springer-Verlag)

Bretthorst, G. L. 2000, in Bulletin of the American Astronomical Society, Vol. 32, American Astronomical Society Meeting Abstracts, 1438

Bretthorst, G. L. 2001a, in American Institute of Physics Conference Series, Vol. 568, Bayesian Inference and Maximum Entropy Methods in Science and Engineering, ed. A. Mohammad-Djafari, 241–245

Bretthorst, G. L. 2001b, in American Institute of Physics Conference Series, Vol. 568, Bayesian Inference and Maximum Entropy Methods in Science and Engineering, ed. A. Mohammad-Djafari, 246–251

Brewer, B. J., Bedding, T. R., Kjeldsen, H., & Stello, D. 2007, ApJ, 654, 551

Brewer, B. J. & Stello, D. 2009, MNRAS, 395, 2226

Brookes, J. R., Isaak, G. R., & van der Raay, H. B. 1978, MNRAS, 185, 19

Broomhall, A.-M., Chaplin, W. J., Elsworth, Y., Appourchaux, T., & New, R. 2010, MNRAS, 406, 767

Broomhall, A.-M., Chaplin, W. J., Elsworth, Y., & New, R. 2009, in Astronomical Society of the Pacific Conference Series, ed. M. Dikpati, T. Arentoft, I. González Hernández, C. Lindsey, & F. Hill, Vol. 416, 245

Brown, T. M., Gilliland, R. L., Noyes, R. W., & Ramsey, L. W. 1991, ApJ, 368, 599

Brown, T. M., Kennelly, E. J., Korzennik, S. G., et al. 1997, ApJ, 475, 322

Brown, T. M., Latham, D. W., Everett, M. E., & Esquerdo, G. A. 2011, AJ, 142, 112

Bruntt, H., Kjeldsen, H., Buzasi, D. L., & Bedding, T. R. 2005, ApJ, 633, 440

Butler, R. P., Bedding, T. R., Kjeldsen, H., et al. 2004, ApJ, 600, L75

Butler, R. P., Vogt, S. S., Marcy, G. W., et al. 2000, ApJ, 545, 504

Buzasi, D. L. 2002, in Astronomical Society of the Pacific Conference Series, Vol. 259, IAU Colloq. 185: Radial and Nonradial Pulsations as probes of Stellar Physics, ed. C. Aerts, T. R. Bedding, & J. Christensen-Dalsgaard, 616

Campante, T. L., Grigahcène, A., Suárez, J. C., & Monteiro, M. J. P. F. G. 2010a, Astronomische Nachrichten, in press [arXiv:1003.4427v1]

Campante, T. L., Handberg, R., Mathur, S., et al. 2011, A&A, 534, A6

Campante, T. L., Karoff, C., Chaplin, W. J., et al. 2010b, MNRAS, 408, 542

Carrier, F., Bouchy, F., Kienzle, F., et al. 2001, A&A, 378, 142

Carrier, F., De Ridder, J., Baudin, F., et al. 2010, A&A, 509, A73

Carrier, F., Eggenberger, P., & Bouchy, F. 2005, A&A, 434, 1085

Catala, C. 2009, Experimental Astronomy, 23, 329

Cayrel de Strobel, G., Knowles, N., Hernandez, G., & Bentolila, C. 1981, A&A, 94, 1

Chapellier, E., Rodríguez, E., Auvergne, M., et al. 2011, A&A, 525, A23

Chaplin, W. J. 2011, in Asteroseismology, Canary Islands Winter School of Astrophysics, ed. P. L. Pallé, Vol. XXII (Cambridge University Press)

Chaplin, W. J. & Appourchaux, T. 1999, MNRAS, 309, 761

Chaplin, W. J., Appourchaux, T., Arentoft, T., et al. 2008a, Astronomische Nachrichten, 329, 549

Chaplin, W. J., Appourchaux, T., Baudin, F., et al. 2006, MNRAS, 369, 985

Chaplin, W. J., Appourchaux, T., Elsworth, Y., et al. 2010, ApJ, 713, L169

Chaplin, W. J. & Basu, S. 2008, Sol. Phys., 251, 53

Chaplin, W. J., Bedding, T. R., Bonanno, A., et al. 2011a, ApJ, 732, L5

Chaplin, W. J., Elsworth, Y., Houdek, G., & New, R. 2007, MNRAS, 377, 17

Chaplin, W. J., Elsworth, Y., Howe, R., et al. 1997a, MNRAS, 287, 51

Chaplin, W. J., Elsworth, Y., Isaak, G. R., et al. 2002, MNRAS, 336, 979

Chaplin, W. J., Elsworth, Y., Isaak, G. R., et al. 1997b, MNRAS, 288, 623

Chaplin, W. J., Elsworth, Y., Isaak, G. R., et al. 2003, A&A, 398, 305

Chaplin, W. J., Houdek, G., Appourchaux, T., et al. 2008b, A&A, 485, 813

Chaplin, W. J., Houdek, G., Elsworth, Y., et al. 2005, MNRAS, 360, 859

Chaplin, W. J., Houdek, G., Karoff, C., Elsworth, Y., & New, R. 2009, A&A, 500, L21

Chaplin, W. J., Kjeldsen, H., Bedding, T. R., et al. 2011b, ApJ, 732, 54

Chaplin, W. J., Kjeldsen, H., Christensen-Dalsgaard, J., et al. 2011c, Science, 332, 213

Christensen-Dalsgaard, J. 1984, in Space Research in Stellar Activity and Variability, ed. A. Mangeney & F. Praderie, 11

Christensen-Dalsgaard, J. 1988, in IAU Symposium, Vol. 123, Advances in Helio- and Asteroseismology, ed. J. Christensen-Dalsgaard & S. Frandsen, 295

Christensen-Dalsgaard, J. 1989, MNRAS, 239, 977

Christensen-Dalsgaard, J. 2002, Reviews of Modern Physics, 74, 1073

Christensen-Dalsgaard, J. 2004, Sol. Phys., 220, 137

Christensen-Dalsgaard, J., Carpenter, K. G., Schrijver, C. J., Karovska, M., & the SI Team. 2011, Journal of Physics Conference Series, 271, 012085

Christensen-Dalsgaard, J. & Frandsen, S. 1983, Sol. Phys., 82, 469

Christensen-Dalsgaard, J. & Gough, D. O. 1980, Nature, 288, 544

Christensen-Dalsgaard, J. & Houdek, G. 2010, Ap&SS, 328, 51

Christensen-Dalsgaard, J., Kjeldsen, H., Brown, T. M., et al. 2010, ApJ, 713, L164

Christensen-Dalsgaard, J., Kjeldsen, H., & Mattei, J. A. 2001, ApJ, 562, L141

Claverie, A., Isaak, G. R., McLeod, C. P., van der Raay, H. B., & Roca Cortés, T. 1979, Nature, 282, 591

Cooley, J. W. & Tukey, J. W. 1965, Mathematics of Computing, 19, 297

Cox, J. P. & Whitney, C. 1958, ApJ, 127, 561

Cramér, H. 1946, Mathematical Methods of Statistics (Princeton University Press)

Creevey, O. L., Doğan, G., Frasca, A., et al. 2012, A&A, 537, A111

Cunha, M. S., Aerts, C., Christensen-Dalsgaard, J., et al. 2007, A&A Rev., 14, 217

Cunha, M. S. & Brandão, I. M. 2011, A&A, 529, A10

Cunha, M. S. & Metcalfe, T. S. 2007, ApJ, 666, 413

Cuypers, J. 1987, Medelingen van de Koninklijke Academie voor Wetenschappen, Letteren en Schone Kunsten van Belgïe, 49, 1

de Meulenaer, P., Carrier, F., Miglio, A., et al. 2010, A&A, 523, A54

De Ridder, J., Barban, C., Baudin, F., et al. 2009, Nature, 459, 398

Deeming, T. J. 1975, Ap&SS, 36, 137

Deheuvels, S., Bruntt, H., Michel, E., et al. 2010, A&A, 515, A87

Deheuvels, S. & Michel, E. 2010, Ap&SS, 328, 259

Deubner, F. & Gough, D. O. 1984, ARA&A, 22, 593

di Mauro, M. P., Christensen-Dalsgaard, J., Kjeldsen, H., Bedding, T. R., & Paternò, L. 2003, A&A, 404, 341

Doğan, G., Bonanno, A., Bedding, T. R., et al. 2010, Astronomische Nachrichten, 331, 949

Dupret, M.-A., Grigahcène, A., Garrido, R., Gabriel, M., & Scuflaire, R. 2005, A&A, 435, 927

Duvall, Jr., T. L. & Harvey, J. W. 1986, in NATO ASIC Proc. 169: Seismology of the Sun and the Distant Stars, ed. D. O. Gough, 105–116

Duvall, Jr., T. L., Jefferies, S. M., Harvey, J. W., Osaki, Y., & Pomerantz, M. A. 1993, ApJ, 410, 829

Dziembowski, W. A. & Soszyński, I. 2010, A&A, 524, A88

Earl, D. J. & Deem, M. W. 2005, Physical Chemistry Chemical Physics (Incorporating Faraday Transactions), 7, 3910

Eddington, A. S. 1926, The Internal Constitution of the Stars (Cambridge University Press)

Ferraz-Mello, S. 1981, AJ, 86, 619

Fletcher, S. T., Chaplin, W. J., Elsworth, Y., Schou, J., & Buzasi, D. L. 2006, MNRAS, 371, 935

Foster, G. 1996, AJ, 111, 541

Frandsen, S., Bruntt, H., Grundahl, F., et al. 2007, A&A, 475, 991

Frandsen, S., Carrier, F., Aerts, C., et al. 2002, A&A, 394, L5

Fröhlich, C., Andersen, B. N., Appourchaux, T., et al. 1997, Sol. Phys., 170, 1

Fröhlich, C., Romero, J., Roth, H., et al. 1995, Sol. Phys., 162, 101

Gabriel, A. H., Baudin, F., Boumier, P., et al. 2002, A&A, 390, 1119

Gabriel, A. H., Grec, G., Charra, J., et al. 1995, Sol. Phys., 162, 61

Gabriel, M. 1994, A&A, 287, 685

Gai, N., Basu, S., Chaplin, W. J., & Elsworth, Y. 2011, ApJ, 730, 63

García, R. A. 2011, in Proceedings of the IX Scientific Meeting of the Spanish Astronomical Society, Highlights of Spanish Astrophysics VI, in press [arXiv:1101.0236v1]

García, R. A. & Ballot, J. 2008, A&A, 477, 611

García, R. A., Ceillier, T., Campante, T. L., et al. 2011a, Astronomical Society of the Pacific, in press [arXiv:1109.6488v1]

García, R. A., Hekker, S., Stello, D., et al. 2011b, MNRAS, 414, L6

García, R. A., Mathur, S., Salabert, D., et al. 2010, Science, 329, 1032

García, R. A., Régulo, C., Samadi, R., et al. 2009, A&A, 506, 41

Gaulme, P., Appourchaux, T., & Boumier, P. 2009, A&A, 506, 7

Gaulme, P., Deheuvels, S., Weiss, W. W., et al. 2010, A&A, 524, A47

Gilliland, R. L. 2008, AJ, 136, 566

Gilliland, R. L., Brown, T. M., Christensen-Dalsgaard, J., et al. 2010a, PASP, 122, 131

Gilliland, R. L., Brown, T. M., Kjeldsen, H., et al. 1993, AJ, 106, 2441

Gilliland, R. L., Jenkins, J. M., Borucki, W. J., et al. 2010b, ApJ, 713, L160

Gilliland, R. L., McCullough, P. R., Nelan, E. P., et al. 2011, ApJ, 726, 2

Gizon, L. & Solanki, S. K. 2003, ApJ, 589, 1009

Gizon, L. & Solanki, S. K. 2004, Sol. Phys., 220, 169

Goldreich, P. & Keeley, D. A. 1977, ApJ, 212, 243

Gough, D. O. 1986, in Hydrodynamic and Magnetodynamic Problems in the Sun and Stars, ed. Y. Osaki, 117

Gough, D. O. 1993, in Astrophysical Fluid Dynamics – Les Houches 1987, ed. J.-P. Zahn & J. Zinn-Justin, 399–560

Grec, G., Fossat, E., & Pomerantz, M. A. 1983, Sol. Phys., 82, 55

Gregory, P. C. 2005, Bayesian Logical Data Analysis for the Physical Sciences: A Comparative Approach with 'Mathematica' Support (Cambridge University Press)

Grigahcène, A., Antoci, V., Balona, L. A., et al. 2010, ApJ, 713, L192

Grigahcène, A., Dupret, M.-A., Gabriel, M., Garrido, R., & Scuflaire, R. 2005, A&A, 434, 1055

Grigahcène, A., Dupret, M.-A., Sousa, S. G., et al. 2011, Ap&SS, in press [arXiv:1112.5961v1]

Gruberbauer, M., Kallinger, T., Weiss, W. W., & Guenther, D. B. 2009, A&A, 506, 1043

Grundahl, F., Christensen-Dalsgaard, J., Arentoft, T., et al. 2009a, Communications in Asteroseismology, 158, 345

Grundahl, F., Christensen-Dalsgaard, J., Kjeldsen, H., et al. 2009b, in Astronomical Society of the Pacific Conference Series, ed. M. Dikpati, T. Arentoft, I. González Hernández, C. Lindsey, & F. Hill, Vol. 416, 579

Grundahl, F., Kjeldsen, H., Christensen-Dalsgaard, J., Arentoft, T., & Frandsen, S. 2007, Communications in Asteroseismology, 150, 300

Guenther, D. B., Kallinger, T., Reegen, P., et al. 2005, ApJ, 635, 547

Handberg, R. & Campante, T. L. 2011, A&A, 527, A56

Harvey, J. W. 1985, in ESA Special Publication, Vol. 235, Future Missions in Solar, Heliospheric & Space Plasma Physics, ed. E. Rolfe & B. Battrick, 199–208

Harvey, J. W. 1988, in IAU Symposium, Vol. 123, Advances in Helio- and Asteroseismology, ed. J. Christensen-Dalsgaard & S. Frandsen, 497

Harvey, J. W., Duvall, Jr., T. L., Jefferies, S. M., & Pomerantz, M. A. 1993, in Astronomical Society of the Pacific Conference Series, Vol. 42, GONG 1992. Seismic Investigation of the Sun and Stars, ed. T. M. Brown, 111

Hastings, W. K. 1970, Biometrika, 57, 97

Hekker, S., Basu, S., Stello, D., et al. 2011a, A&A, 530, A100

Hekker, S., Broomhall, A.-M., Chaplin, W. J., et al. 2010, MNRAS, 402, 2049

Hekker, S., Elsworth, Y., De Ridder, J., et al. 2011b, A&A, 525, A131

Hekker, S., Kallinger, T., Baudin, F., et al. 2009, A&A, 506, 465

Hoffleit, D. 1997, Journal of the American Association of Variable Star Observers (JAAVSO), 25, 115

Högbom, J. A. 1974, A&AS, 15, 417

Horne, J. H. & Baliunas, S. L. 1986, ApJ, 302, 757

Houdek, G. 2006, in ESA Special Publication, Vol. 624, Proceedings of *SOHO* 18/GONG 2006/HELAS I, Beyond the spherical Sun

Houdek, G., Balmforth, N. J., Christensen-Dalsgaard, J., & Gough, D. O. 1999, A&A, 351, 582

Houdek, G. & Gough, D. O. 2007, MNRAS, 375, 861

Howe, R. 2009, Living Reviews in Solar Physics, 6, 1

Huber, D., Bedding, T. R., Arentoft, T., et al. 2011a, ApJ, 731, 94

Huber, D., Bedding, T. R., Stello, D., et al. 2011b, ApJ, in press [arXiv:1109.3460v1]

Huber, D., Bedding, T. R., Stello, D., et al. 2010, ApJ, 723, 1607

Huber, D., Stello, D., Bedding, T. R., et al. 2009, Communications in Asteroseismology, 160, 74

Ireland, M. J., Mérand, A., ten Brummelaar, T. A., et al. 2008, in Society of Photo-Optical Instrumentation Engineers Conference Series, Vol. 7013, Presented at the Society of Photo-Optical Instrumentation Engineers (SPIE) Conference

Jaynes, E. T. 1987, in Maximum-Entropy and Bayesian Analysis and Estimation Problems. Proceedings of the Third Workshop on Maximum Entropy and Bayesian Methods in Applied Statistics, ed. C. R. Smith & G. J. Erickson (Reidel, Dordrecht, Netherlands), 1–37

Jeffreys, H. 1961, Theory of Probability, 3rd edn. (Oxford University Press)

Jenkins, G. M. & Watts, D. G. 1968, Spectral Analysis and its Applications (San Francisco: Holden Day)

Jenkins, J. M., Caldwell, D. A., Chandrasekaran, H., et al. 2010, ApJ, 713, L120

Jiménez-Reyes, S. J., Chaplin, W. J., García, R. A., et al. 2008, MNRAS, 389, 1780

Kallinger, T., Mosser, B., Hekker, S., et al. 2010a, A&A, 522, A1

Kallinger, T., Weiss, W. W., Barban, C., et al. 2010b, A&A, 509, A77

Karoff, C. 2012, MNRAS, in press [arXiv:1201.2539v1]

Karoff, C., Campante, T. L., & Chaplin, W. J. 2010, Astronomische Nachrichten, in press [arXiv:1003.4167v1]

Karoff, C., Metcalfe, T. S., Chaplin, W. J., et al. 2009, MNRAS, 399, 914

Kendall, M. & Stuart, A. 1979, The Advanced Theory of Statistics. Vol. 2: Inference and Relationship, 4th edn. (Macmillan)

Khintchine, A. 1934, Mathematische Annalen, 109, 604

Kiss, L. L. & Bedding, T. R. 2003, MNRAS, 343, L79

Kjeldsen, H. & Bedding, T. R. 1995, A&A, 293, 87

Kjeldsen, H. & Bedding, T. R. 2011, A&A, 529, L8

Kjeldsen, H., Bedding, T. R., Arentoft, T., et al. 2008a, ApJ, 682, 1370

Kjeldsen, H., Bedding, T. R., Baldry, I. K., et al. 2003, AJ, 126, 1483

Kjeldsen, H., Bedding, T. R., Butler, R. P., et al. 2005, ApJ, 635, 1281

Kjeldsen, H., Bedding, T. R., & Christensen-Dalsgaard, J. 2008b, ApJ, 683, L175

Kjeldsen, H., Bedding, T. R., Viskum, M., & Frandsen, S. 1995, AJ, 109, 1313

Koch, D. G., Borucki, W. J., Basri, G., et al. 2010, ApJ, 713, L79

Koen, C. 1999, MNRAS, 309, 769

Kumar, P., Franklin, J., & Goldreich, P. 1988, ApJ, 328, 879

Lamb, H. 1932, Hydrodynamics, 6th edn. (Dover Publications)

Leavitt, H. S. 1908, Annals of Harvard College Observatory, 60, 87

Leavitt, H. S. & Pickering, E. C. 1912, Harvard College Observatory Circular, 173, 1

Ledoux, P. 1951, ApJ, 114, 373

Leighton, R. B., Noyes, R. W., & Simon, G. W. 1962, ApJ, 135, 474

Libbrecht, K. G. 1992, ApJ, 387, 712

Liddle, A. R. 2009, Annual Review of Nuclear and Particle Science, 59, 95

Lomb, N. R. 1976, Ap&SS, 39, 447

Martić, M., Schmitt, J., Lebrun, J., et al. 1999, A&A, 351, 993

Mathur, S., García, R. A., Catala, C., et al. 2010a, A&A, 518, A53

Mathur, S., García, R. A., Régulo, C., et al. 2010b, A&A, 511, A46

Mathur, S., Handberg, R., Campante, T. L., et al. 2011, ApJ, 733, 95

Matthews, J. M., Kuschnig, R., Guenther, D. B., et al. 2004, Nature, 430, 51

Mayor, M., Pepe, F., Queloz, D., et al. 2003, The Messenger, 114, 20

Mazumdar, A., Basu, S., Collier, B. L., & Demarque, P. 2006, MNRAS, 372, 949

Mazumdar, A. & Michel, E. 2010, Astronomische Nachrichten, in press [arXiv:1004.2739v1]

Metcalfe, T. S., Dziembowski, W. A., Judge, P. G., & Snow, M. 2007, MNRAS, 379, L16

Metcalfe, T. S., Monteiro, M. J. P. F. G., Thompson, M. J., et al. 2010, ApJ, 723, 1583

Metropolis, N., Rosenbluth, A. W., Rosenbluth, M. N., Teller, A. H., & Teller, E. 1953, J. Chem. Phys., 21, 1087

Michel, E., Baglin, A., Auvergne, M., et al. 2008, Science, 322, 558

Miglio, A. & Montalbán, J. 2005, A&A, 441, 615

Miglio, A., Montalbán, J., Baudin, F., et al. 2009, A&A, 503, L21

Miglio, A., Montalbán, J., Carrier, F., et al. 2010, A&A, 520, L6

Monteiro, M. J. P. F. G., Christensen-Dalsgaard, J., & Thompson, M. J. 2000, MNRAS, 316, 165

Monteiro, M. J. P. F. G., Christensen-Dalsgaard, J., & Thompson, M. J. 2002, in ESA Special Publication, Vol. 485, Stellar Structure and Habitable Planet Finding, ed. B. Battrick, F. Favata, I. W. Roxburgh, & D. Galadi, 291–298

Montgomery, M. H. & O'Donoghue, D. 1999, Delta Scuti Star Newsletter, 13, 28

Moreira, O., Appourchaux, T., Berthomieu, G., & Toutain, T. 2005, MNRAS, 357, 191

Mosser, B. & Appourchaux, T. 2009, A&A, 508, 877

Mosser, B., Appourchaux, T., Catala, C., Buey, J., & the SIAMOIS Team. 2008, Journal of Physics Conference Series, 118, 012042

Mosser, B., Barban, C., Montalbán, J., et al. 2011a, A&A, 532, A86

Mosser, B., Belkacem, K., Goupil, M.-J., et al. 2011b, A&A, 525, L9

Mosser, B., Belkacem, K., Goupil, M.-J., et al. 2010, A&A, 517, A22

Mosser, B., Bouchy, F., Catala, C., et al. 2005, A&A, 431, L13

Mosser, B., Michel, E., Appourchaux, T., et al. 2009, A&A, 506, 33

Naef, D., Mayor, M., Pepe, F., et al. 2001, A&A, 375, 205

Neyman, J. & Pearson, E. S. 1933, Royal Society of London Philosophical Transactions Series A, 231, 289

Nigam, R. & Kosovichev, A. G. 1998, ApJ, 505, L51

Nigam, R., Kosovichev, A. G., Scherrer, P. H., & Schou, J. 1998, ApJ, 495, L115

North, J. R., Davis, J., Bedding, T. R., et al. 2007, MNRAS, 380, L80

Nyquist, H. 1928, Transactions of the AIEE, 47, 617

Osaki, J. 1975, PASJ, 27, 237

Parseval des Chênes, M.-A. 1806, Mémoires présentés à l'Institut des Sciences, Lettres et Arts, pars divers savans, et lus dans ses assemblées. Sciences, mathématiques et physiques. (Savans étrangers.), 1, 638

Peligrad, M. & Wu, W. B. 2010, Annals of Probability, 38, 2009

Pereira, T. M. D. & Lopes, I. P. 2005, ApJ, 622, 1068

Pereira, T. M. D., Suárez, J. C., Lopes, I. P., et al. 2007, A&A, 464, 659

Pourbaix, D., Nidever, D., McCarthy, C., et al. 2002, A&A, 386, 280

Powell, M. J. D. 1964, Computer Journal, 7, 155

Press, W. H. & Rybicki, G. B. 1989, ApJ, 338, 277

Quirion, P.-O., Christensen-Dalsgaard, J., & Arentoft, T. 2010, ApJ, 725, 2176

Rao, C. R. 1945, Bulletin of the Calcutta Mathematical Society, 37, 81

Reegen, P. 2004, in IAU Symposium, Vol. 224, The A-Star Puzzle, ed. J. Zverko, J. Ziznovsky, S. J. Adelman, & W. W. Weiss, 791–798

Roberts, D. H., Lehar, J., & Dreher, J. W. 1987, AJ, 93, 968

Roxburgh, I. W. 2009a, A&A, 506, 435

Roxburgh, I. W. 2009b, A&A, 493, 185

Roxburgh, I. W. & Vorontsov, S. V. 2003, A&A, 411, 215

Saio, H. 1981, ApJ, 244, 299

Salabert, D., Ballot, J., & García, R. A. 2011, A&A, 528, A25

Salabert, D., García, R. A., & Mathur, S. 2010, Astronomische Nachrichten, in press [arXiv:1003.6076v3]

Samadi, R., Georgobiani, D., Trampedach, R., et al. 2007, A&A, 463, 297

Samadi, R., Goupil, M.-J., & Houdek, G. 2002, A&A, 395, 563

Scargle, J. D. 1982, ApJ, 263, 835

Scargle, J. D. 1989, ApJ, 343, 874

Schou, J. 1992, PhD thesis, Aarhus University, Aarhus, Denmark

Schou, J. & Brown, T. M. 1994, A&AS, 107, 541

Schou, J. & Buzasi, D. L. 2001, in ESA Special Publication, Vol. 464, *SOHO* 10/GONG 2000 Workshop: Helio- and Asteroseismology at the Dawn of the Millennium, ed. A. Wilson & P. L. Pallé, 391–394

Schuster, A. 1905, Proceedings of the Royal Society of London, 77, 136

Scott, J. G. & Berger, J. O. 2010, Annals of Statistics, 38, 2587

Sellke, T., Bayarri, M. J., & Berger, J. O. 2001, American Statistician, 55, 62

Severino, G., Magrì, M., Oliviero, M., Straus, T., & Jefferies, S. M. 2001, ApJ, 561, 444

Shannon, C. E. 1949, Proceedings of the Institute of Radio Engineers, 37, 10

Shapley, H. 1914, ApJ, 40, 448

Silva Aguirre, V., Ballot, J., Serenelli, A. M., & Weiss, A. 2011a, A&A, 529, A63

Silva Aguirre, V., Chaplin, W. J., Ballot, J., et al. 2011b, ApJ, 740, L2

Smeyers, P. 1968, Annales d'Astrophysique, 31, 159

Soriano, M. & Vauclair, S. 2008, A&A, 488, 975

Stahn, T. & Gizon, L. 2008, Sol. Phys., 251, 31

Stello, D., Basu, S., Bruntt, H., et al. 2010, ApJ, 713, L182

Stello, D., Bruntt, H., Kjeldsen, H., et al. 2007, MNRAS, 377, 584

Stello, D., Chaplin, W. J., Basu, S., Elsworth, Y., & Bedding, T. R. 2009a, MNRAS, 400, L80

Stello, D., Chaplin, W. J., Bruntt, H., et al. 2009b, ApJ, 700, 1589

Tarrant, N. J., Chaplin, W. J., Elsworth, Y., Spreckley, S. A., & Stevens, I. R. 2007, MNRAS, 382, L48

Tarrant, N. J., Chaplin, W. J., Elsworth, Y., Spreckley, S. A., & Stevens, I. R. 2008, A&A, 483, L43

Tassoul, M. 1980, ApJS, 43, 469

ten Brummelaar, T. A., McAlister, H. A., Ridgway, S. T., et al. 2005, ApJ, 628, 453

Torrence, C. & Compo, G. P. 1998, Bulletin of the American Meteorological Society, 79, 61

Toutain, T. & Appourchaux, T. 1994, A&A, 289, 649

Uytterhoeven, K., Mathias, P., Poretti, E., et al. 2008, A&A, 489, 1213

Vandakurov, Y. V. 1967, AZh, 44, 786

Vauclair, S., Laymand, M., Bouchy, F., et al. 2008, A&A, 482, L5

Verner, G. A., Chaplin, W. J., Basu, S., et al. 2011a, ApJ, 738, L28

Verner, G. A., Chaplin, W. J., & Elsworth, Y. 2006, ApJ, 638, 440

Verner, G. A., Elsworth, Y., Chaplin, W. J., et al. 2011b, MNRAS, 415, 3539

Verner, G. A. & Roxburgh, I. W. 2011, Astronomische Nachrichten, in press [arXiv:1104.0631v1]

Walker, G. A. H. 2008, Journal of Physics Conference Series, 118, 012013

Walker, G. A. H., Matthews, J. M., Kuschnig, R., et al. 2003, PASP, 115, 1023

White, T. R., Bedding, T. R., Stello, D., et al. 2011a, ApJ, 742, L3

White, T. R., Bedding, T. R., Stello, D., et al. 2011b, ApJ, in press [arXiv:1109.3455v1]

White, T. R., Brewer, B. J., Bedding, T. R., Stello, D., & Kjeldsen, H. 2010, Communications in Asteroseismology, 161, 39

Wiener, N. 1930, Acta Mathematica, 55, 117

Wilks, S. S. 1938, Annals of Mathematical Statistics, 9, 60

Woodard, M. F. 1984, PhD thesis, University of California, San Diego, USA

Zechmeister, M. & Kürster, M. 2009, A&A, 496, 577

Zhevakin, S. A. 1963, ARA&A, 1, 367

Zwintz, K., Kuschnig, R., Weiss, W. W., Gray, R. O., & Jenkner, H. 1999, A&A, 343, 899

Appendices

Appendix A

LETTER

doi:10.1038/nature10389

The excitation of solar-like oscillations in a δ Sct star by efficient envelope convection

V. Antoci[1], G. Handler[1,2], T. L. Campante[3,4], A. O. Thygesen[4,5], A. Moya[6], T. Kallinger[1,7,8], D. Stello[9], A. Grigahcène[3], H. Kjeldsen[4], T. R. Bedding[9], T. Lüftinger[1], J. Christensen-Dalsgaard[4], G. Catanzaro[10], A. Frasca[10], P. De Cat[11], K. Uytterhoeven[12,13,14,15], H. Bruntt[4], G. Houdek[1], D. W. Kurtz[16], P. Lenz[2], A. Kaiser[1], J. Van Cleve[17], C. Allen[18] & B. D. Clarke[17]

Delta Scuti (δ Sct)[1] stars are opacity-driven pulsators with masses of 1.5–2.5$M_\odot$, their pulsations resulting from the varying ionization of helium. In less massive stars[2] such as the Sun, convection transports mass and energy through the outer 30 per cent of the star and excites a rich spectrum of resonant acoustic modes. Based on the solar example, with no firm theoretical basis, models predict that the convective envelope in δ Sct stars extends only about 1 per cent of the radius[3], but with sufficient energy to excite solar-like oscillations[4,5]. This was not observed before the Kepler mission[6], so the presence of a convective envelope in the models has been questioned. Here we report the detection of solar-like oscillations in the δ Sct star HD 187547, implying that surface convection operates efficiently in stars about twice as massive as the Sun, as the *ad hoc* models predicted.

Thirty days of continuous observations of HD 187547 (KIC 7548479) by the Kepler mission with a cadence of 1 min led to its identification as a δ Sct pulsator (Fig. 1a, b). In contrast to the non-uniformly distributed signals at low frequencies, the observed regularly spaced peaks at high frequencies (Fig. 1c) suggest that we also observe high-radial-order overtones as expected for stochastically excited solar-like oscillations. For such oscillations the observed comb-like frequency structure (with the large frequency separation $\Delta\nu$ indicating the frequency separation between consecutive radial overtones of like degree) is the result of mainly radial and dipolar pulsation modes, whereas for δ Sct stars it is not clear which modes are excited to observable amplitudes. The strikingly broadened structures observed only at high frequencies (Figs 1f and 2b, c) suggest that each is due either to single damped and stochastically re-excited oscillations or to very close unresolved frequencies of coherent oscillations.

Here we use spectroscopic observations to derive an effective temperature $T_{\rm eff} = 7{,}500 \pm 250$ K, a surface gravity of $\log g = 3.90 \pm 0.25$ dex (c.g.s.) and a projected rotational velocity of $v \sin i = 10.3 \pm 2.3$ km s^{-1} (see Supplementary Information for details). We identify HD 187547 as an Am star from chemical element abundance analysis, which is consistent with the observed low $v \sin i$ typical for these stars. Am stars are stars of spectral type A showing atmospheric underabundance when compared with the Sun in the chemical elements Sc and Ca, and an overabundance of Ba, Sr and Y (ref. 7). We compute a photospheric metallicity (all elements except H and He) of $Z = 0.017$, which is larger than the solar value of $Z = 0.0134$ (ref. 8).

About two-thirds of Am stars are primary components of spectroscopic binary systems[9]. The Am phenomenon is connected to slow rotation, which is not common in A type stars. Binarity is believed to act as a braking mechanism slowing down the rotation and allowing spectral peculiarities to occur as a result of element diffusion[10]. Pulsating Am stars still represent a challenge to theory, because He is expected to settle gravitationally and should only partly be present in the He II ionization zone where the δ Sct pulsations are excited. In other words, theoretical models predict that the hottest and youngest A-type stars should not pulsate[10], which is in contradiction with recent observations[11]. As the stars evolve, their convective envelopes deepen and efficiently mix the stellar matter, erasing the observed chemical peculiarities in the atmospheres, allowing the opacity mechanism to drive pulsation in the He II ionization zone. Using the observed solar-like oscillations reported here, the depth of the convective envelope can be derived (hence the mixing length), probing the diffusion of He and heavy elements in this star. This will contribute significantly to revising the interaction between pulsation and diffusion in models of Am stars.

Seven radial velocity measurements of HD 187547, spread over 153 days, give no evidence for a short-period binary system. In addition, the absence of any detectable contribution by a potential close companion to the spectrum implies a considerably less luminous star of spectral type G or later. The expected amplitudes and frequency of maximum oscillation power for such a star are inconsistent with the observations, leading to the conclusion that the signal observed in Fig. 1c cannot originate from a companion. The observed amplitude spectrum of HD 187547 is not affected by a background star because the fraction of light in the aperture from neighbouring stars is only 1.5%. Other chemically peculiar pulsating stars situated, as the δ Sct stars, in the classical instability strip in the Hertzsprung–Russell diagram[12] are the rapidly oscillating Ap stars. Their high-radial-order pulsation modes are triggered by the opacity mechanism acting in the hydrogen ionization zone, often showing equidistant multiplets in the frequency spectrum as a result of the alignment of the pulsation axes with strong magnetic fields[13]. The strong magnetic fields as seen in rapidly oscillating Ap stars are, however, not observed in Am stars[14]. We therefore exclude the possibility that HD 187547 is a hybrid of a δ Sct and a rapidly oscillating Ap star.

In Fig. 3 we show an échelle diagram comparing the observed frequencies with a model of a star similar to HD 187547, demonstrating again the clear structures separated by $\Delta\nu$ at high frequencies and the non-structured distribution at lower frequencies. For the high-frequency modes we derive a mean large frequency separation $\Delta\nu$ of 40.5 ± 0.6 μHz. Using the empirical relation[15]

---

[1]Institute of Astronomy, University of Vienna, Türkenschanzstraße 18, A-1180 Vienna, Austria. [2]Copernicus Astronomical Center, Bartycka 18, 00-716 Warsaw, Poland. [3]Centro de Astrofísica, Departamento de Física e Astronomia-Faculdade de Ciências, Universidade do Porto, Rua das Estrelas, 4150-762 Porto, Portugal. [4]Department of Physics and Astronomy, Aarhus University, Ny Munkegade 120, DK-8000 Aarhus C, Denmark. [5]Nordic Optical Telescope, Apartado 474, E-38700 Santa Cruz de La Palma, Santa Cruz de Tenerife, Spain. [6]Departamento de Astrofísica, Centro de Astrobiología, Instituto Nacional de Técnica Aeroespacial – Consejo Superior de Investigaciones Científicas, PO Box 78, E-28691, Villanueva de la Cañada, Madrid, Spain. [7]Department of Physics and Astronomy, University of British Columbia, 6224 Agricultural Road, Vancouver, British Columbia V6T 1Z1, Canada. [8]Instituut voor Sterrenkunde, University of Leuven, Celestijnenlaan 200D, 3001 Leuven, Belgium. [9]Sydney Institute for Astronomy (SIfA), School of Physics, University of Sydney, New South Wales 2006, Australia. [10]Istituto Nazionale di Astrofisica – Osservatorio Astrofisico di Catania, via S. Sofia 78, I-95123 Catania, Italy. [11]Royal Observatory of Belgium, Ringlaan 3, B-1180 Brussels, Belgium. [12]Laboratoire AIM, CEA/DSM-CNRS Université Paris Diderot, Commissariat à l'Energie Atomique et aux Energies Alternatives, Institut de Recherche sur Les Lois Fondamentales, Service d'Astrophysique, Centre de Saclay, F-91191, Gif-sur-Yvette, France. [13]Kiepenheuer-Institut für Sonnenphysik, Schöneckstrasse 6, 79104 Freiburg, Germany. [14]Instituto de Astrofísica de Canarias, 38200 La Laguna, Tenerife, Spain. [15]Departamento de Astrofísica, Universidad de La Laguna, 38205 La Laguna, Tenerife, Spain. [16]Jeremiah Horrocks Institute, University of Central Lancashire, Preston PR1 2HE, UK. [17]SETI Institute/NASA Ames Research Center, Moffett Field, California 94035, USA. [18]Orbital Sciences Corporation/NASA Ames Research Center, Moffett Field, California 94035, USA.

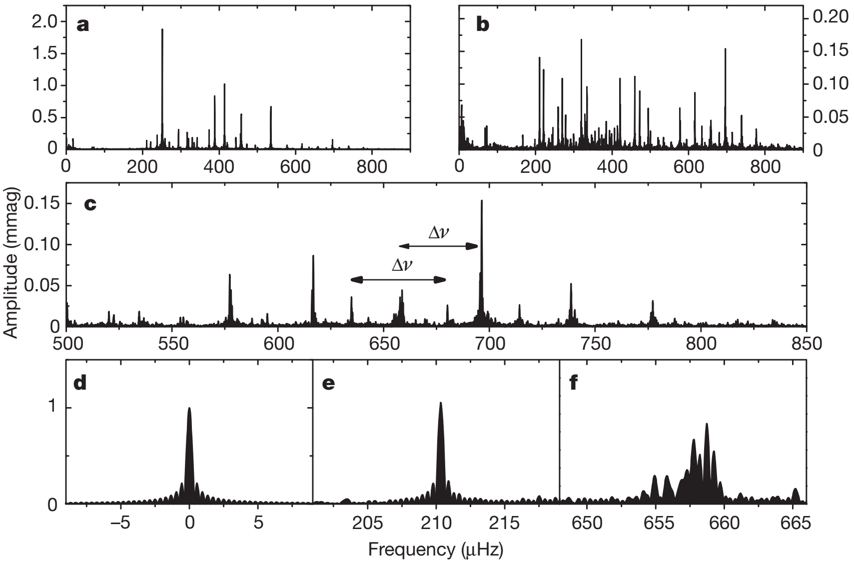

Figure 1 | Fourier amplitude spectra of the Kepler light curve of HD 187547. a, Fourier spectrum covering the entire frequency range in which significant signals were observed with a dominant frequency at 251 μHz and an amplitude of 2 mmag, typical for a δ Sct star. **b**, The multimode oscillations of HD 187547 are shown by subtracting 16 sinusoids corresponding to the most prominent oscillations, revealing a large number of additional significant frequencies. **c**, The region between 500 and 850 μHz shows a clear pattern of roughly equally spaced peaks, which we interpret as high-order consecutive radial overtones. The comb-like structure expected for high-order radial overtones is clearly visible. The broadened peaks suggest damped/re-excited solar-like oscillations. The black arrows denoted Δ*ν* indicate the large separation between consecutive radial and dipole modes. **d**, Spectral window. The shape of the window function is defined by the length and sampling of the data set. Any coherent signal will have the same profile. **e**, Example for one of the modes driven by the opacity mechanism in HD 187547. **f**, A supposed solar-like oscillation mode observed in HD 187547, displaying a broadened structure suggestive of a short mode lifetime.

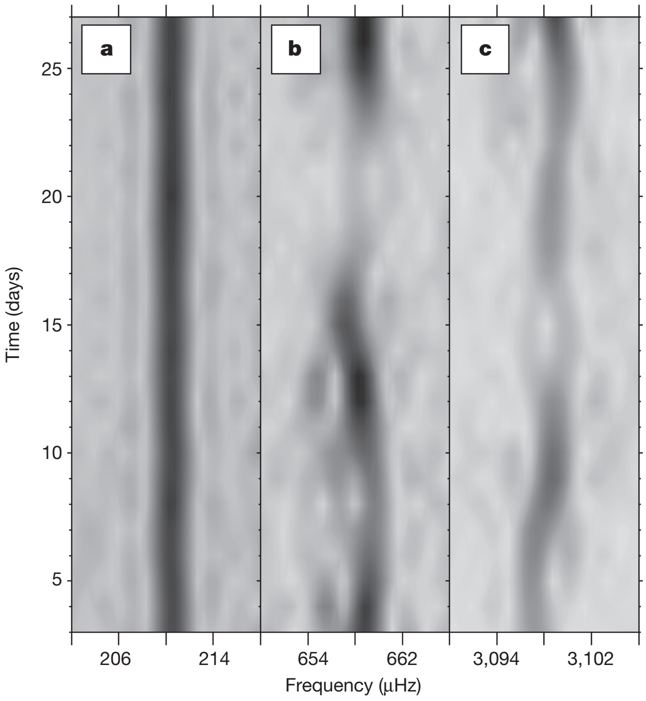

Figure 2 | Time-Fourier spectrum. Here we again highlight the difference in temporal variability between the modes interpreted as stochastic modes and the coherent, opacity-driven peaks at low frequencies. The time-fourier spectrum was computed with a running filter of full-width at half-maximum = 5 days, comparable to the mean mode lifetime. **a**, An opacity-driven mode (the same as in Fig. 1e) showing temporal stability in the δ Sct frequency region. **b**, Stochastic mode observed in HD 187547, showing an erratic behaviour as expected for solar-like oscillations (the same as in Fig. 1f). **c**, For comparison, a stochastic oscillation mode observed in the Sun. The solar data were obtained from the SOHO VIRGO instrument. The data set has the same length and sampling as for HD 187547; that is, 30 days and 1 min, respectively. Further details of frequency analyses and tests on artificial data sets (Supplementary Fig. 1) to verify our interpretation are in the Supplementary Information.

$\Delta\nu = (0.263 \pm 0.009)\,\mu\mathrm{Hz}(\nu_{\mathrm{max}}\,\mu\mathrm{Hz}^{-1})^{0.772 \pm 0.005}$ we obtain a frequency of maximum power $\nu_{\mathrm{max}} = 682^{+41}_{-43}$ μHz. This is in very good agreement with the highest-amplitude mode in the supposed stochastic frequency region at 696 μHz. The possibility that what we observe is $0.5\Delta\nu$ in the frequency spectrum is ruled out because this would require a ν_{max} at about 1,673 μHz, where no signal is observed. We can also exclude the observation of $2\Delta\nu$ because that would place ν_{max} at 277 μHz, close to the dominant opacity-driven mode at 251 μHz.

The amplitudes of solar-like oscillations are determined by the interaction between driving and damping defined by different physical processes[2], such as modulation of the turbulent momentum and heat fluxes by pulsation. The exact contribution to driving and damping by each of these processes is still not well understood, resulting in uncertainties in the predictions of the stochastically excited mode amplitudes[16], particularly in hotter stars[2,3] in which the convective envelopes are shallow. We expect the mixing length, the amplitudes and mode lifetimes to constrain the anisotropy of the convective velocity field, parameters that all semi-analytical convection models rely on[17].

For HD 187547 we measure a peak-amplitude per radial mode[18] for the assumed stochastic signal of 56 ± 2 p.p.m., which after bolometric correction[19] results in 67 ± 3 p.p.m. (see Supplementary Information for details). From the empirical scaling relation[20] and using a bolometric solar peak-amplitude of 3.6 p.p.m. (ref. 21) we obtain a predicted peak amplitude of $A = 14 \pm 9$ p.p.m. The mean mode lifetimes are measured[22] as 5.7 ± 0.8 days. Empirical relations predict a mode lifetime for a star with $T_{\mathrm{eff}} = 7{,}500 \pm 250$ K of the order of one day[23] or shorter[24], which is not in agreement with what we measure for HD 187547. However, these scaling relations (for amplitude and mode lifetimes) are based on few observed stars, and none of them is calibrated in the temperature domain of our target, for which the physical conditions in the convection zone are expected to be very different. Furthermore, given that HD 187547 is metal overabundant in comparison with the Sun, the observed amplitude is expected to be higher[3,25] than predicted from simple scaling, which is indeed the case. The power of a mode is directly proportional to the mode lifetime provided that the energy supply rate over the mode inertia is constant[26], which further supports

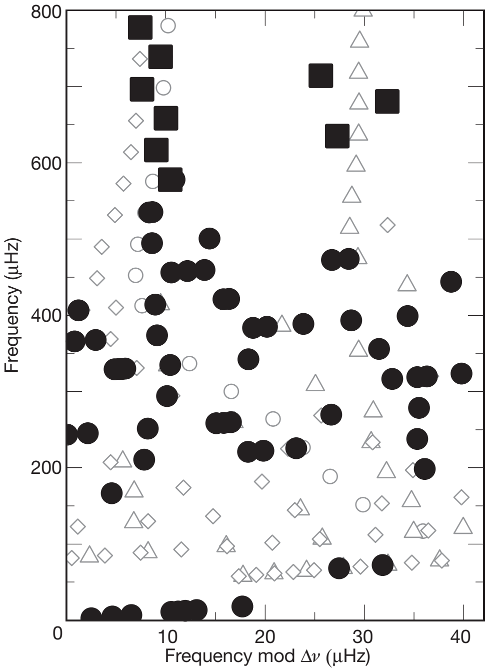

Figure 3 | Échelle diagram of HD 187547. Here we plot 69 extracted frequencies as a function of frequency modulo the large separation ($\Delta\nu = 40.5$ μHz). Frequencies equally spaced by $\Delta\nu$ will form vertical ridges in the échelle diagram. To guide the eye, we show theoretically predicted frequencies of pulsation modes for a $1.85M_\odot$ stellar model. Ridges of $l = 0$ modes are represented by open circles, $l = 1$ by open triangles and $l = 2$ by open diamonds. Detailed modelling of the star is beyond the scope of this paper. The supposed solar-like modes (filled squares) between 500 and 870 μHz show clear ridges, as expected for high-order acoustic oscillations similar to what is observed in solar-like stars. The lower frequencies that we attribute to δ Sct pulsation (filled circles) excited by the opacity mechanism show no obvious regular patterns.

the higher amplitude because the observed mode lifetimes are also longer than expected. An additional factor that is not considered in any scaling relations is the chemical peculiarity of our target. In summary, these factors make HD 187547 an intriguing case for further theoretical analyses of stochastic oscillations and the potential interaction with the opacity mechanism in δ Sct stars.

The amplitude distribution for stochastic pulsation can be described as a Rayleigh distribution, provided that the examined time series are much shorter than the mode lifetimes. The relation between the mean amplitude $\langle A\rangle$ and its standard deviation $\sigma(A)$ can then be written as[27] $(4/\pi - 1)^{0.5}\langle A\rangle \approx 0.52\langle A\rangle$. This is not valid for opacity-driven pulsation. For HD 187547 we therefore expect to obtain two different regimes of the ratio $\sigma(A)/\langle A\rangle$ for the two groups of oscillation modes (Supplementary Fig. 2). Indeed, we see that the δ Sct frequencies have a lower value of $\sigma(A)/\langle A\rangle$ than the supposed solar-like modes, giving further evidence for the stochastic nature of the latter (see Supplementary Information for details).

We cannot strictly exclude the possibility that the signals between 578 and 868 μHz are due to unresolved modes of pulsation excited by the opacity mechanism, because high-radial-order acoustic modes can also be observed in hot δ Sct stars. Nevertheless, as shown in Fig. 1 this would imply that δ Sct pulsation covers the region between 205 and 870 μHz continuously. According to current theory, the opacity mechanism acting in the He II ionization zone cannot excite modes spanning 16 radial orders for a star with parameters like those of HD 187547 (ref. 28). Further support for the discovery of solar-like oscillations comes from spectroscopic observations that also indicate the presence of convective motions in the atmospheres of A and Am stars[29]. In addition, signatures of granulation noise in δ Sct stars have been reported from photometric measurements[3]. Opacity-driven pulsations are also observed in more massive stars (8–$16M_\odot$), known as β Cephei stars (in this case the opacity mechanism acts in the ionization region of the iron-group elements). The unexpected detection of solar-like oscillations in such a star[30] (with a mass of $10M_\odot$) suggests that both types of pulsation, opacity-driven and stochastically excited, can coexist and can have overlapping frequency domains. The similar timescales of the different oscillation types imply a possible interaction between the two mechanisms.

Received 7 April; accepted 26 July 2011.
Published online 14 September; corrected 29 September 2011 (see full-text HTML version for details).

1. Breger, M. in *Delta Scuti and Related Stars* (ASP Conf. Ser. Vol. 210) (eds Breger, M. & Montgomery, M.) 3–42 (Astronomical Society of the Pacific, 2000).
2. Chaplin, W. J. *et al.* Ensemble asteroseismology of solar-type stars with the NASA Kepler mission. *Science* **332,** 213–216 (2011).
3. Kallinger, T. & Matthews, J. M. Evidence for granulation in early A-type stars. *Astrophys. J.* **711,** L35–L39 (2010).
4. Houdek, G., Balmforth, N. J., Christensen-Dalsgaard, J. & Gough, D. O. Amplitudes of stochastically excited oscillations in main-sequence stars. *Astron. Astrophys.* **351,** 582–596 (1999).
5. Samadi, R., Goupil, M.-J. & Houdek, G. Solar-like oscillations in delta Scuti stars. *Astron. Astrophys.* **395,** 563–571 (2002).
6. Koch, D. G. *et al.* Kepler mission design, realized photometric performance, and early science. *Astrophys. J.* **713,** L79–L86 (2010).
7. Preston, G. W. The chemically peculiar stars of the upper main sequence. *Annu. Rev. Astron. Astrophys.* **12,** 257–277 (1974).
8. Asplund, M., Grevesse, N., Sauval, A. J. & Scott, P. The chemical composition of the Sun. *Annu. Rev. Astron. Astrophys.* **47,** 481–522 (2009).
9. Carquillat, J.-M. & Prieur, J.-L. Contribution to the search for binaries among Am stars. VIII. New spectroscopic orbits of eight systems and statistical study of a sample of 91 Am stars. *Mon. Not. R. Astron. Soc.* **380,** 1064–1078 (2007).
10. Turcotte, S., Richer, J., Michaud, G. & Christensen-Dalsgaard, J. The effect of diffusion on pulsations of stars on the upper main sequence—δ Scuti and metallic A stars. *Astron. Astrophys.* **360,** 603–616 (2000).
11. Balona, L. *et al.* Kepler observations of Am stars. *Mon. Not. R. Astron. Soc.* **414,** 792–800 (2011).
12. Handler, G. Confirmation of simultaneous p and g mode excitation in HD 8801 and γ Peg from time-resolved multicolour photometry of six candidate 'hybrid' pulsators. *Mon. Not. R. Astron. Soc.* **398,** 1339–1351 (2009).
13. Kurtz, D. W. Rapidly oscillating AP stars. *Mon. Not. R. Astron. Soc.* **200,** 807–859 (1982).
14. Aurière, M. *et al.* No detection of large-scale magnetic fields at the surfaces of Am and HgMn stars. *Astron. Astrophys.* **523,** A40, doi:10.1051/0004-6361/201014848 (2010).
15. Stello, D., Chaplin, W. J., Basu, S., Elsworth, Y. & Bedding, T. R. The relation between $\Delta\nu$ and ν_{max} for solar-like oscillations. *Mon. Not. R. Astron. Soc.* **400L,** L80–L84 (2009).
16. Houdek, G. Solar-type variables. *AIP Conf. Proc.* **1170,** 519–530 (2009).
17. Samadi, R., Belkacem, K., Goupil, M.-J., Kupka, F. & Dupret, M.-A. Solarlike oscillation amplitudes and line-widths as a probe for turbulent convection in stars. *Proc. Int. Astron. Un.* **239,** 349–357 (2007).
18. Kjeldsen, H. *et al.* The amplitude of solar oscillations using stellar techniques. *Astrophys. J.* **682,** 1370–1375 (2008).
19. Ballot, J., Barban, C. & van't Veer-Menneret, C. Visibilities and bolometric corrections for stellar oscillation modes observed by Kepler. *Astron. Astrophys.* **531,** A124, doi:10.1051/0004-6361/201016230 (2011).
20. Kjeldsen, H. & Bedding, T. R. Amplitudes of solar-like oscillations: a new scaling relation. *Astron. Astrophys.* **529,** L8, doi:10.1051/0004-6361/201116789 (2011).
21. Michel, E. *et al.* Intrinsic photometric characterisation of stellar oscillations and granulation. *Astron. Astrophys.* **495,** 979–987 (2009).
22. Gruberbauer, M., Kallinger, T., Weiss, W. W. & Guenther, D. B. On the detection of Lorentzian profiles in a power spectrum: a Bayesian approach using ignorance priors. *Astron. Astrophys.* **506,** 1043–1053 (2009).
23. Chaplin, W. J., Houdek, G., Karoff, C., Elsworth, Y. & New, R. Mode lifetimes of stellar oscillations. Implications for asteroseismology. *Astron. Astrophys.* **500,** L21–L24 (2009).
24. Baudin, F. *et al.* Amplitudes and lifetimes of solar-like oscillations observed by CoRoT. Red-giant versus main-sequence stars. *Astron. Astrophys.* **529,** A84, doi:10.1051/0004-6361/201014037 (2011).
25. Samadi, R., Ludwig, H.-G., Belkacem, K., Goupil, M. J. & Dupret, M.-A. The CoRoT target HD 49933. I. Effect of the metal abundance on the mode excitation rates. *Astron. Astrophys.* **509,** A15, doi:10.1051/0004-6361/200911867 (2010).
26. Chaplin, W. J. *et al.* On model predictions of the power spectral density of radial solar p modes. *Mon. Not. R. Astron. Soc.* **360,** 859–868 (2005).
27. Chang, H.-Y. & Gough, D. O. On the power distribution of solar p modes. *Solar Phys.* **181,** 251–263 (1998).
28. Pamyatnykh, A. A. in *Delta Scuti and Related Stars* (ASP Conf. Ser. Vol. 210) (eds Breger, M. & Montgomery, M.) 215–246 (Astronomical Society of the Pacific, 2000).

29. Landstreet, J. D. *et al.* Atmospheric velocity fields in tepid main sequence stars. *Astron. Astrophys.* **503,** 973–984 (2009).
30. Belkacem, K. *et al.* Solar-like oscillations in a massive star. *Science* **324,** 1540–1542 (2009).

Supplementary Information is linked to the online version of the paper at www.nature.com/nature.

Acknowledgements We thank the entire Kepler team, without whom these results would not be possible. V.A., G.Ha. and G.Ho. were supported by the Austrian Fonds zur Förderung der wissenschaftlichen Forschung. V.A. also thanks L. Fossati for his help. A.M. acknowledges the funding of AstroMadrid, who was also supported by Spanish grants. T.R.B. and D.S. acknowledge support from the Australian Reseach Council. T.L was supported by the Austrian Agency for International Cooperation in Education and Research. K.U. acknowledges financial support from the Deutsche Forschungsgemeinschaft. Funding for this Discovery mission is provided by NASA's Science Mission Directorate.

Author Contributions V.A. discovered the star among the Kepler targets, analysed it and found the solar-like oscillations (as a part of her PhD thesis), did spectroscopic analyses, frequency analyses, the test on the stochastic nature of the signal, and interpretations, and wrote the paper. G.Ha. had the idea for this project and supervised V.A., helped with analyses, interpretations and writing the paper. T.L.C. contributed to the analyses of the stochastic modes and also to the test on the stochastic nature of the signal. A.O.T. observed the target spectroscopically at Nordic Optical Telescope, identified the star as an Am star and did spectroscopic analyses. A.M. contributed to the statistical test on the nature of the stochastic signal. T.K. helped interpretations, data analyses and writing the paper, and delivered the mode lifetimes. D.S. helped with data analyses, writing the paper and made Fig. 2. A.G. helped with theoretical interpretations and the time-Fourier analyses. T.R.B. helped with interpretations and writing the paper. H.K. contributed to the analyses, also by supervising V.A., and is a member of the Kepler Asteroseismic Investigation Steering Committee. J.C-D. helped with the theoretical support, writing the paper and is a member of the Kepler Asteroseismic Investigation Steering Committee. T.L. confirmed the Am identification, excluding the Ap character of the star. G.C., A.F. and A.K. did spectroscopic analyses. P.D.C. was Principal Investigator and observer for the spectroscopic data from McDonald observatory. K.U. was Co-Investigator of the McDonald data and coordinated the ground-based observations. H.B. was Principal Investigator for the observations with the NARVAL spectrograph and did spectroscopic analyses. G.Ho. and P.L. helped with theoretical interpretations and writing the paper. D.W.K. helped with the Am classification and writing the paper and is leader of the delta Scuti working group of the Kepler Asteroseismic Science Consortium. J.V.C., C.A. and B.D.C. are part of the Kepler team and were involved in designing and operating the satellite. All co-authors contributed to discussions and commented on the manuscript.

Author Information Reprints and permissions information is available at www.nature.com/reprints. The authors declare no competing financial interests. Readers are welcome to comment on the online version of this article at www.nature.com/nature. Correspondence and requests for materials should be addressed to V.A. (victoria.antoci@univie.ac.at).

Appendix B

The Astrophysical Journal, 713:935–949, 2010 April 20 doi:10.1088/0004-637X/713/2/935

A MULTI-SITE CAMPAIGN TO MEASURE SOLAR-LIKE OSCILLATIONS IN PROCYON. II. MODE FREQUENCIES

Timothy R. Bedding[1], Hans Kjeldsen[2], Tiago L. Campante[2,3], Thierry Appourchaux[4], Alfio Bonanno[5], William J. Chaplin[6], Rafael A. Garcia[7], Milena Martić[8], Benoit Mosser[9], R. Paul Butler[10], Hans Bruntt[1,11], László L. Kiss[1,12], Simon J. O'Toole[13], Eiji Kambe[14], Hiroyasu Ando[15], Hideyuki Izumiura[14], Bun'ei Sato[16], Michael Hartmann[17], Artie Hatzes[17], Caroline Barban[11], Gabrielle Berthomieu[18], Eric Michel[11], Janine Provost[18], Sylvaine Turck-Chièze[7], Jean-Claude Lebrun[8], Jerome Schmitt[19], Jean-Loup Bertaux[8], Serena Benatti[20], Riccardo U. Claudi[21], Rosario Cosentino[5], Silvio Leccia[22], Søren Frandsen[2], Karsten Brogaard[2], Lars Glowienka[2], Frank Grundahl[2], Eric Stempels[23], Torben Arentoft[2], Michaël Bazot[2], Jørgen Christensen-Dalsgaard[2], Thomas H. Dall[24], Christoffer Karoff[2], Jens Lundgreen-Nielsen[2], Fabien Carrier[25], Patrick Eggenberger[26], Danuta Sosnowska[27], Robert A. Wittenmyer[28,29], Michael Endl[28], Travis S. Metcalfe[30], Saskia Hekker[6,31], and Sabine Reffert[32]

[1] Sydney Institute for Astronomy (SIfA), School of Physics, University of Sydney, NSW 2006, Australia; bedding@physics.usyd.edu.au
[2] Danish AsteroSeismology Centre (DASC), Department of Physics and Astronomy, Aarhus University, DK-8000 Aarhus C, Denmark
[3] Centro de Astrofísica da Universidade do Porto, Rua das Estrelas, 4150-762 Porto, Portugal
[4] Institut d'Astrophysique Spatiale, Université Paris XI-CNRS, Bâtiment 121, 91405 Orsay Cedex, France
[5] INAF—Osservatorio Astrofisico di Catania, via S. Sofia 78, 95123 Catania, Italy
[6] School of Physics and Astronomy, University of Birmingham, Edgbaston, Birmingham B15 2TT, UK
[7] DAPNIA/DSM/Service d'Astrophysique, CEA/Saclay, 91191 Gif-sur-Yvette Cedex, France
[8] LATMOS, University of Versailles St Quentin, CNRS, BP 3, 91371 Verrieres le Buisson Cedex, France
[9] LESIA, CNRS, Université Pierre et Marie Curie, Université Denis Diderot, Observatoire de Paris, 92195 Meudon Cedex, France
[10] Carnegie Institution of Washington, Department of Terrestrial Magnetism, 5241 Broad Branch Road NW, Washington, DC 20015-1305, USA
[11] Laboratoire AIM, CEA/DSM—CNRS–Université Paris Diderot—IRFU/SAp, 91191 Gif-sur-Yvette Cedex, France
[12] Konkoly Observatory of the Hungarian Academy of Sciences, H-1525 Budapest, P.O. Box 67, Hungary
[13] Anglo-Australian Observatory, P.O. Box 296, Epping, NSW 1710, Australia
[14] Okayama Astrophysical Observatory, National Astronomical Observatory of Japan, National Institutes of Natural Sciences, 3037-5 Honjyo, Kamogata, Asakuchi, Okayama 719-0232, Japan
[15] National Astronomical Observatory of Japan, National Institutes of Natural Sciences, 2-21-1 Osawa, Mitaka, Tokyo 181-8588, Japan
[16] Global Edge Institute, Tokyo Institute of Technology 2-12-1-S6-6, Ookayama, Meguro-ku, Tokyo 152-8550, Japan
[17] Thüringer Landessternwarte Tautenburg, Sternwarte 5, 07778 Tautenburg, Germany
[18] Université de Nice Sophia-Antipolis, CNRS UMR 6202, Laboratoire Cassiopée, Observatoire de la Côte d'Azur, BP 4229, 06304 Nice Cedex, France
[19] Observatoire de Haute Provence, 04870 St Michel l'Observatoire, France
[20] CISAS—University of Padova, Via Venezia 5, 35131, Padova, Italy
[21] INAF—Astronomical Observatory of Padua, Vicolo Osservatorio 5, 35122 Padova, Italy
[22] INAF—Osservatorio Astronomico di Capodimonte, Salita Moiariello 16, 80131 Napoli, Italy
[23] Department of Physics and Astronomy, P.O. Box 516, SE-751 20 Uppsala, Sweden
[24] European Southern Observatory, D-85748 Garching, Germany
[25] Instituut voor Sterrenkunde, Katholieke Universiteit Leuven, Celestijnenlaan 200 B, 3001 Leuven, Belgium
[26] Observatoire de Genève, Université de Genève, Ch. des Maillettes 51, CH-1290 Sauverny, Switzerland
[27] Laboratoire d'astrophysique, EPFL Observatoire CH-1290 Versoix, Switzerland
[28] McDonald Observatory, University of Texas at Austin, Austin, TX 78712, USA
[29] School of Physics, University of New South Wales, NSW 2052, Australia
[30] High Altitude Observatory, National Centre for Atmospheric Research, Boulder, CO 80307-3000, USA
[31] Leiden Observatory, Leiden University, 2300 RA Leiden, The Netherlands
[32] ZAH-Landessternwarte, 69117 Heidelberg, Germany

Received 2010 January 19; accepted 2010 February 26; published 2010 March 29

ABSTRACT

We have analyzed data from a multi-site campaign to observe oscillations in the F5 star Procyon. The data consist of high-precision velocities that we obtained over more than three weeks with 11 telescopes. A new method for adjusting the data weights allows us to suppress the sidelobes in the power spectrum. Stacking the power spectrum in a so-called échelle diagram reveals two clear ridges, which we identify with even and odd values of the angular degree ($l = 0$ and 2, and $l = 1$ and 3, respectively). We interpret a strong, narrow peak at 446 μHz that lies close to the $l = 1$ ridge as a mode with mixed character. We show that the frequencies of the ridge centroids and their separations are useful diagnostics for asteroseismology. In particular, variations in the large separation appear to indicate a glitch in the sound-speed profile at an acoustic depth of $\sim$1000 s. We list frequencies for 55 modes extracted from the data spanning 20 radial orders, a range comparable to the best solar data, which will provide valuable constraints for theoretical models. A preliminary comparison with published models shows that the offset between observed and calculated frequencies for the radial modes is very different for Procyon than for the Sun and other cool stars. We find the mean lifetime of the modes in Procyon to be $1.29^{+0.55}_{-0.49}$ days, which is significantly shorter than the 2–4 days seen in the Sun.

Key words: stars: individual (Procyon A) – stars: oscillations

1. INTRODUCTION

The success of helioseismology and the promise of asteroseismology have motivated numerous efforts to measure oscillations in solar-type stars. These began with ground-based observations (for recent reviews see Bedding & Kjeldsen 2007; Aerts et al. 2008) and now extend to space-based photometry, particularly with the *CoRoT* and *Kepler* Missions (e.g., Michel et al. 2008; Gilliland et al. 2010).

We have carried out a multi-site spectroscopic campaign to measure oscillations in the F5 star Procyon A (HR 2943; HD 61421; HIP 37279). We obtained high-precision velocity observations over more than three weeks with 11 telescopes, with almost continuous coverage for the central 10 days. In Arentoft et al. (2008, hereafter Paper I) we described the details of the observations and data reduction, measured the mean oscillation amplitudes, gave a crude estimate for the mode lifetime and discussed slow variations in the velocity curve that we attributed to rotational modulation of active regions. In this paper, we describe the procedure used to extract the mode parameters, provide a list of oscillation frequencies, and give an improved estimate of the mode lifetimes.

2. PROPERTIES OF SOLAR-LIKE OSCILLATIONS

We begin with a brief summary of the relevant properties of solar-like oscillations (for reviews see, for example, Brown & Gilliland 1994; Bedding & Kjeldsen 2003; Christensen-Dalsgaard 2004).

To a good approximation, in main-sequence stars the cyclic frequencies of low-degree *p*-mode oscillations are regularly spaced, following the asymptotic relation (Tassoul 1980; Gough 1986):

$$\nu_{n,l} \approx \Delta\nu(n + \tfrac{1}{2}l + \epsilon) - l(l+1)D_0. \tag{1}$$

Here, n (the radial order) and l (the angular degree) are integers, $\Delta\nu$ (the large separation) depends on the sound travel time across the whole star, D_0 is sensitive to the sound speed near the core and ϵ is sensitive to the reflection properties of the surface layers. It is conventional to define three so-called small frequency separations that are sensitive to the sound speed in the core: $\delta\nu_{02}$ is the spacing between adjacent modes with $l = 0$ and $l = 2$ (for which n will differ by 1); $\delta\nu_{13}$ is the spacing between adjacent modes with $l = 1$ and $l = 3$ (ditto); and $\delta\nu_{01}$ is the amount by which $l = 1$ modes are offset from the midpoint of the $l = 0$ modes on either side.[33] To be explicit, for a given radial order, n, these separations are defined as follows:

$$\delta\nu_{02} = \nu_{n,0} - \nu_{n-1,2}, \tag{2}$$

$$\delta\nu_{01} = \tfrac{1}{2}(\nu_{n,0} + \nu_{n+1,0}) - \nu_{n,1}, \tag{3}$$

$$\delta\nu_{13} = \nu_{n,1} - \nu_{n-1,3}. \tag{4}$$

If the asymptotic relation (Equation (1)) were to hold exactly, it would follow that all of these separations would be independent of n and that $\delta\nu_{02} = 6D_0$, $\delta\nu_{13} = 10D_0$, and $\delta\nu_{01} = 2D_0$. In practice, Equation (1) is only an approximation. In the Sun and other stars, theoretical models and observations show that $\Delta\nu$, D_0, and ϵ vary somewhat with frequency, and also with l. Consequently, the small separations also vary with frequency.

The mode amplitudes are determined by the excitation and damping, which are stochastic processes involving near-surface convection. We typically observe modes over a range of frequencies, which in Procyon is especially broad (about 400–1400 μHz; see Paper I). The observed amplitudes also depend on l via various projection factors (see Table 1 of Kjeldsen et al. 2008a). Note, in particular, that velocity measurements are much more sensitive to modes with $l = 3$ than are intensity measurements. The mean mode amplitudes are modified for a given observing run by the stochastic nature of the excitation, resulting in considerable scatter of the peak heights about the envelope.

Oscillations in the Sun are long-lived compared to their periods, which allows their frequencies to be measured very precisely. However, the lifetime is not infinite and the damping results in each mode in the power spectrum being split into multiple peaks under a Lorentzian profile. The FWHM of this Lorentzian, which is referred to as the linewidth Γ, is inversely proportional to the mode lifetime: $\Gamma = 1/(\pi\tau)$. We follow the usual definition that τ is the time for the mode amplitude to decay by a factor of e. The solar value of τ for the strongest modes ranges from 2 to 4 days, as a decreasing function of frequency (e.g., Chaplin et al. 1997).

Procyon is an evolved star, with theoretical models showing that it is close to, or just past, the end of the main sequence (e.g., Guenther & Demarque 1993; Barban et al. 1999; Chaboyer et al. 1999; Di Mauro & Christensen-Dalsgaard 2001; Kervella et al. 2004; Eggenberger et al. 2005; Provost et al. 2006; Bonanno et al. 2007; Guenther et al. 2008). As such, its oscillation spectrum may show deviations from the regular comb-like structure described by Equation (1), especially at low frequencies. This is because some modes, particularly those with $l = 1$, are shifted by avoided crossings with gravity modes in the stellar core (also called "mode bumping"; see Osaki 1975; Aizenman et al. 1977). These so-called "mixed modes" have *p*-mode character near the surface but *g*-mode character in the deep interior. Some of the theoretical models of Procyon cited above indeed predict these mixed modes, depending on the evolutionary state of the star, and we must keep this in mind when attempting to identify oscillation modes in the power spectrum. The mixed modes are rich in information because they probe the stellar core and are very sensitive to age, but they complicate the task of mode identification.

We should also keep in mind that mixed modes are expected to have lower amplitudes and longer lifetimes (smaller linewidths) than regular *p*-modes because they have larger mode inertias (e.g., Christensen-Dalsgaard 2004). Hence, for a data series that is many times longer than the lifetime of the pure *p*-modes, a mixed mode may appear in the power spectrum as a narrow peak that is higher than the others, even though its power (amplitude squared) is not especially large.

Another potential complication is that stellar rotation causes modes with $l \geqslant 1$ to split into multiplets. The peaks of these multiplets are characterized by the azimuthal degree m, which takes on values of $m = 0, \pm 1, \ldots, \pm l$, with a separation that directly measures the rotation rate averaged over the region of the star that is sampled by the mode. The measurements are particularly difficult because a long time series is needed to resolve the rotational splittings. We argue in Appendix A that the low value of $v \sin i$ observed in Procyon implies that rotational splitting of frequencies is not measurable in our observations.

---

[33] One can also define an equivalent quantity, $\delta\nu_{10}$, as the offset of $l = 0$ modes from the midpoint between the surrounding $l = 1$ modes, so that $\delta\nu_{10} = \nu_{n,0} - \frac{1}{2}(\nu_{n-1,1} + \nu_{n,1})$.

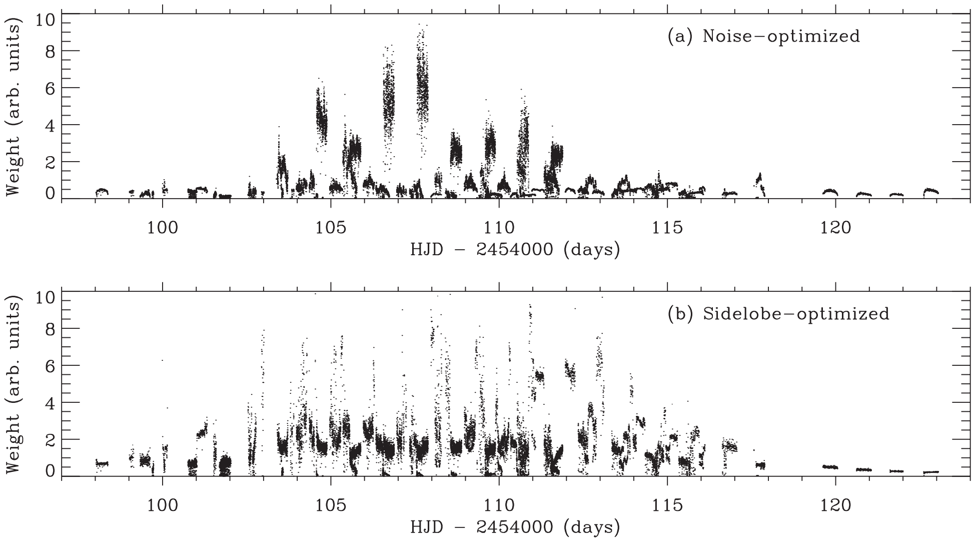

Figure 1. Weights for time series of velocity observations of Procyon, optimized to minimize: (a) the noise level and (b) the height of the sidelobes.

3. WEIGHTING THE TIME SERIES

The time series of velocity observations was obtained over 25 days using 11 telescopes at eight observatories and contains just over 22,500 data points. As discussed in Paper I, the velocity curve shows slow variations that we attribute to a combination of instrumental drifts and rotational modulation of stellar active regions. We have removed these slow variations by subtracting all the power below 280 μHz, to prevent spectral leakage into higher frequencies that would degrade the oscillation spectrum. We take this high-pass-filtered time series of velocities, together with their associated measurement uncertainties, as the starting point in our analysis.

3.1. Noise-optimized Weights

Using weights when analyzing ground-based observations of stellar oscillations (e.g., Gilliland et al. 1993; Frandsen et al. 1995) allows one to take into account the significant variations in data quality during a typical observing campaign, especially when two or more telescopes are used. The usual practice, which we followed in Paper I, is to calculate the weights for a time series from the measurement uncertainties, σ_i, according to $w_i = 1/\sigma_i^2$.

These "raw" weights can then be adjusted to minimize the noise level in the final power spectrum by identifying and revising those uncertainties that are too optimistic, and at the same time rescaling the uncertainties to be in agreement with the actual noise levels in the data. This procedure is described in Paper I and references therein. The time series of these noise-optimized weights is shown in Figure 1(a). These are the same as those shown in Figure 1(d) of Paper I, but this time as weights rather than uncertainties.

The power spectrum of Procyon based on these noise-optimized weights is shown in Figure 2(a). This is the same as shown in Paper I (lower panel of Figure 6), except that the power at low frequencies, which arises from the slow variations, has been removed. As described in Paper I, the noise level above 3 mHz in this noise-optimized spectrum is 1.9 cm s^{-1} in amplitude. This includes some degree of spectral leakage from the oscillations and if we high-pass filter the spectrum up to 3 mHz to remove the oscillation signal, the noise level drops to 1.5 cm s^{-1} in amplitude.

The task of extracting oscillation frequencies from the power spectrum is complicated by the presence of structure in the spectral window, which are caused by gaps or otherwise uneven coverage in the time series. The spectral window using the noise-optimized weights is shown in Figure 3(a). Prominent sidelobes at ±11.57 μHz correspond to aliasing at one cycle per day. Indeed, the prospect of reducing these sidelobes is the main reason for acquiring multi-site observations. However, even with good coverage the velocity precision varies greatly, both for a given telescope during the run and from one telescope to another (see Figure 1(a)). As pointed out in Paper I, using these measurement uncertainties as weights has the effect of increasing the sidelobes in the spectral window. We now discuss a technique for addressing this issue.

3.2. Sidelobe-optimized Weights

Adjusting the weights allows one to suppress the sidelobe structure; the trade-off is an increase in the noise level. This technique is routinely used in radio astronomy when synthesizing images from interferometers (e.g., Högbom & Brouw 1974). An extreme case is to set all weights to be equal, which is the same as not using weights at all. This is certainly not optimal because it produces a power spectrum with greatly increased noise (by a factor of 2.3) but still having significant sidelobes, as can be seen in Figure 6(a) of Paper I. Adjusting the weights on a night-by-night basis in order to minimize the sidelobes was used in the analysis of dual-site observations of α Cen A (Bedding et al. 2004), α Cen B (Kjeldsen et al. 2005), and β Hyi (Bedding et al. 2007). For our multi-site Procyon data, this is impractical because of the large number of (partly overlapping) telescope nights. We have developed a more general algorithm for adjusting weights to minimize the sidelobes (H. Kjeldsen et al. 2010, in preparation). The new method, which is superior because it does not assume the oscillations are coherent over the whole observing run, is based on the principle that equal weight is given to all segments of the time series. The method produces the cleanest possible spectral window in terms of suppressing the sidelobes, and we have tested it with good results using published data for α Cen A and B and β Hyi (Arentoft et al. 2010).

The new method operates with two timescales, T_1 and T_2. All data segments of length T_1 (=2 hr, in this case) are required to

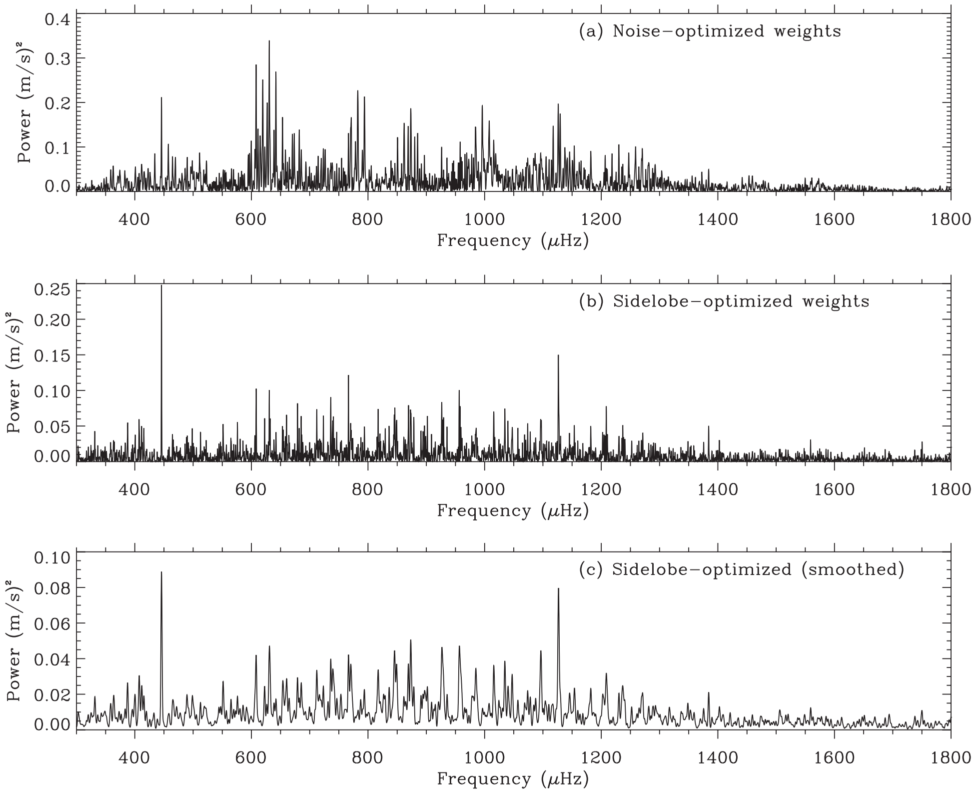

Figure 2. Power spectrum of oscillations in Procyon: (a) using the noise-optimized weights; (b) using the sidelobe-optimized weights; (c) using the sidelobe-optimized weights and smoothing by convolution with a Gaussian with FWHM 2 μHz.

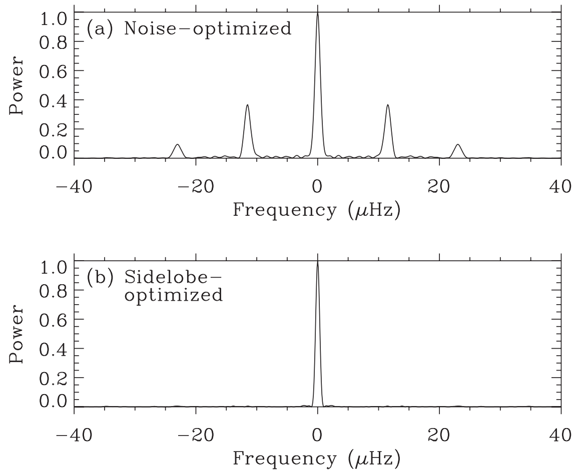

Figure 3. Spectral window for the Procyon observations using (a) noise-optimized weights and (b) sidelobe-optimized weights.

have the same total weight throughout the time series, with the relaxing condition that variations on timescales longer than T_2 (=12 hr) are retained. To be explicit, the algorithm works as follows. We adjust the weights so that all segments of length T_1 have the same total weight. That is, for each point w_i in the time series of weights, define $\{S_i\}$ to be the set of weights in a segment of width T_1 centered at that time stamp, and divide each w_i by the sum of the weights in $\{S_i\}$. However, this adjustment suffers from edge effects, since it gives undue weight to points adjacent to a gap. To compensate, we also divide by an asymmetry factor

$$R = 1 + \left| \frac{\Sigma_{\rm left} - \Sigma_{\rm right}}{\Sigma_{\rm left} + \Sigma_{\rm right}} \right| . \tag{5}$$

Here, $\Sigma_{\rm left}$ is the sum of the weights in the segment $\{S_i\}$ that have time stamps less than t_i, and $\Sigma_{\rm right}$ is the sum of the weights in the segment $\{S_i\}$ that have time stamps greater than t_i. Note that R ranges from 1, for points that are symmetrically placed in their T bin, up to 2 for points at one edge of a gap.

Once the above procedure is done for T_1, which is the shortest timescale on which we wish to adjust the weights, we do it again with T_2, which is the longest timescale for adjusting the weights. Finally, we divide the first set of adjusted weights by the second set, and this gives the weights that we adopt (Figure 1(b)).

3.3. The Sidelobe-optimized Power Spectrum

Figure 2(b) shows the power spectrum of Procyon based on the sidelobe-optimized weights. The spectral window has improved tremendously (Figure 3(b)), while the noise level at high frequencies (above 3 mHz) has increased by a factor of 2.0.

The power spectrum now clearly shows a regular series of peaks, which are even more obvious after smoothing (Figure 2(c)). We see that the large separation of the star is about 55 μHz, confirming the value indicated by several previous studies (Mosser et al. 1998; Martić et al. 1999, 2004; Eggenberger et al. 2004; Régulo & Roca Cortés 2005; Leccia et al. 2007; Guenther et al. 2008). The very strong peak at 446 μHz appears to be a candidate for a mixed mode, especially given its narrowness (see Section 2).

Plotting the power spectrum in échelle format using a large separation of 56 μHz (Figure 4) clearly shows two ridges, as

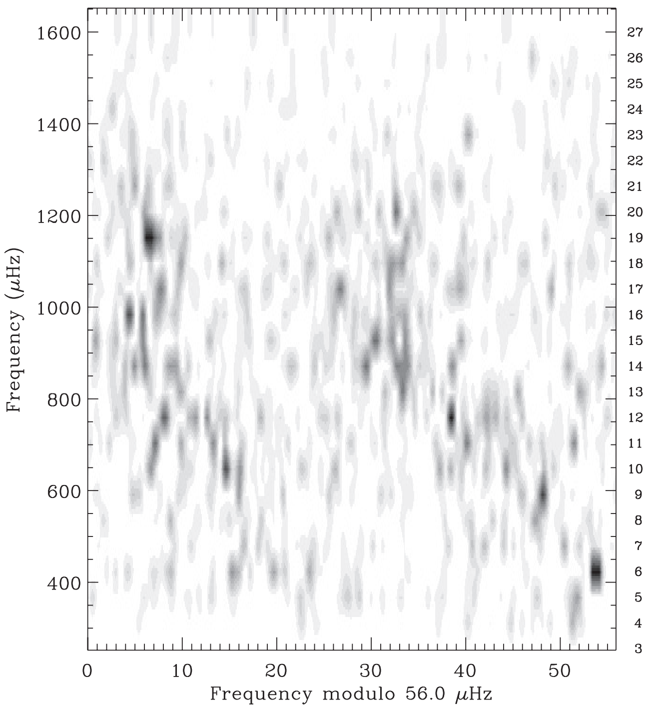

Figure 4. Power spectrum of Procyon in échelle format using a large separation of 56 μHz, based on the sidelobe-optimized weights. Two ridges are clearly visible. The upper parts are vertical but the lower parts are tilted, indicating a change in the large separation as a function of frequency. The orders are numbered sequentially on the right-hand side.

expected.[34] The upper parts are vertical but the lower parts are tilted, indicating a change in the large separation as a function of frequency. This large amount of curvature in the échelle diagram goes a long way toward explaining the lack of agreement between previous studies on the mode frequencies of Procyon (see the list of references given in the previous paragraph).

The advantage of using the sidelobe-optimized weights is demonstrated by Figure 5. This is the same as Figure 4 but for the noise-optimized weights and the ridges are no longer clearly defined.

4. IDENTIFICATION OF THE RIDGES

We know from asymptotic theory (see Equation (1)) that one of the ridges in the échelle diagram (Figure 4) corresponds to modes with even degree ($l = 0$ and 2) and the other to modes with odd degree ($l = 1$ and 3). However, it is not immediately obvious which is which. We also need to keep in mind that the asymptotic relation in evolved stars does not hold exactly. We designate the two possibilities Scenario A, in which the left-hand ridge in Figure 4 corresponds to modes with odd degree, and Scenario B, in which the same ridge corresponds to modes with even degree. Figure 6 shows the Procyon power spectrum collapsed along several orders. We now see double peaks that suggest the identifications shown, which corresponds to Scenario B.

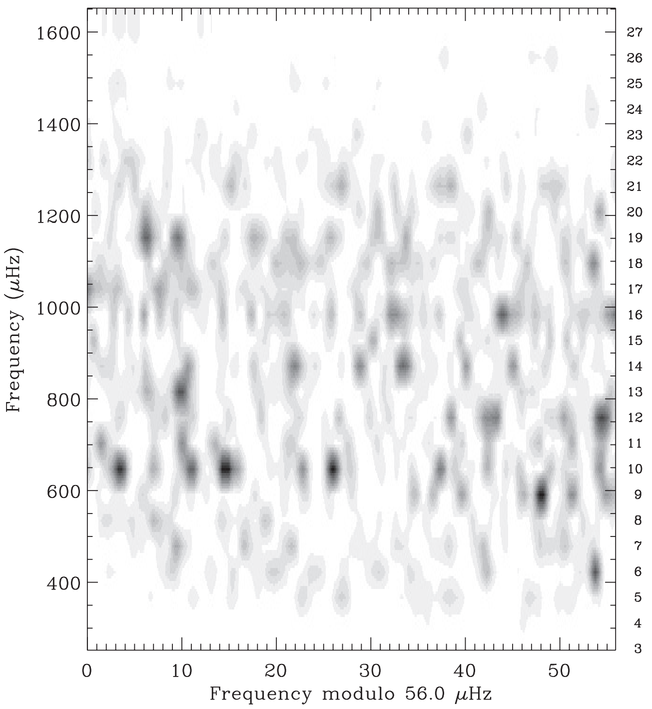

Figure 5. Same as Figure 4, but for the noise-optimized weights. The sidelobes from daily aliasing mean that the ridges can no longer be clearly distinguished.

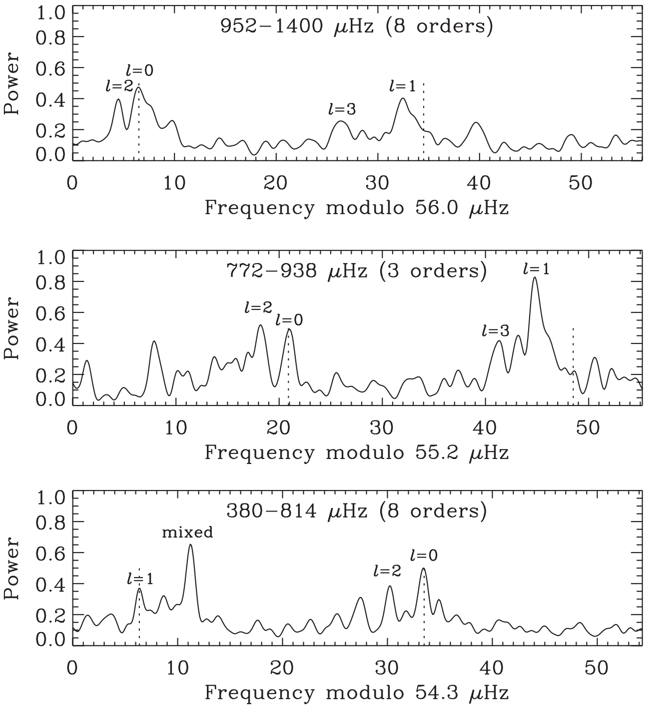

Figure 6. Power spectrum of Procyon collapsed along several orders. Note that the power spectrum was first smoothed slightly by convolving with a Gaussian with FWHM 0.5 μHz. The dotted lines are separated by exactly $\Delta\nu/2$, to guide the eye in assessing the 0–1 small separation.

We can check that the small separation $\delta\nu_{01}$ has the expected sign. According to asymptotic theory (Equation (1)), each $l = 1$ mode should be at a slightly lower frequency than the midpoint of the adjacent $l = 0$ modes. This is indeed the case for the identifications given in Figure 6, but would not be if the even

---

[34] When making an échelle diagram, it is common to plot ν versus (ν mod $\Delta\nu$), in which case each order slopes slightly upward. However, for gray-scale images, it is preferable to keep the orders horizontal, as was done in the original presentation of the diagram (Grec et al. 1983). We have followed that approach in this paper, and the value given on the vertical axis indicates the frequency at the middle of each order.

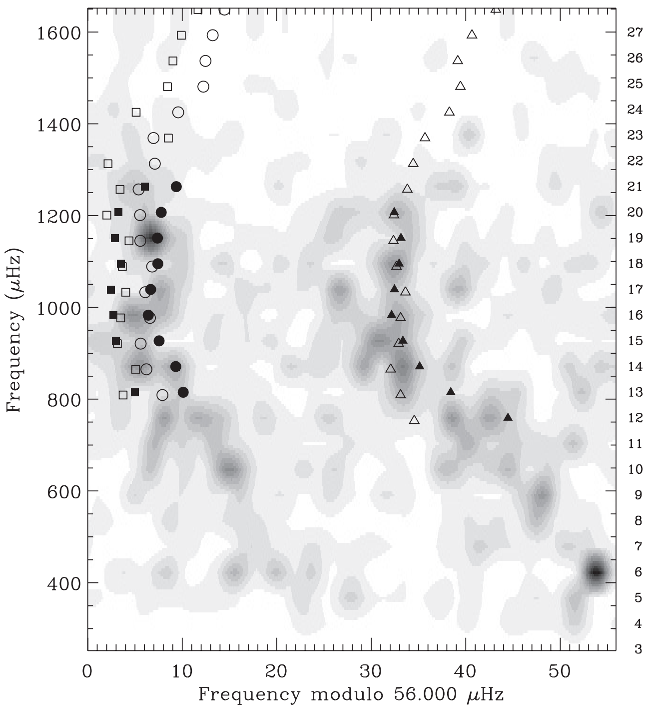

Figure 7. Échelle diagram for Procyon smoothed to 2 μHz (grayscale) overlaid with scaled frequencies for two stars observed by *CoRoT*. The filled symbols are oscillation frequencies for HD 49385 reported by Deheuvels et al. (2010), after multiplying by 0.993. Open symbols are oscillation frequencies for HD 49933 from the revised identification by Benomar et al. (2009b, Scenario B) after multiplying by 0.6565. Symbol shapes indicate mode degree: $l = 0$ (circles), $l = 1$ (triangles), and $l = 2$ (squares).

and odd degrees were reversed. We should be careful, however, since $\delta\nu_{01}$ has been observed to have the opposite sign in red giant stars (Carrier et al. 2010; Bedding et al. 2010).

The problem of ridge identification in F stars was first encountered by Appourchaux et al. (2008) when analyzing *CoRoT* observations of HD 49933 and has been followed up by numerous authors (Benomar et al. 2009a, 2009b; Gruberbauer et al. 2009; Mosser & Appourchaux 2009; Roxburgh 2009; Kallinger et al. 2010). Two other F stars observed by *CoRoT* have presented the same problem, namely HD 181906 (García et al. 2009) and HD 181420 (Barban et al. 2009). A discussion of the issue was recently given by Bedding & Kjeldsen (2010), who proposed a solution to the problem that involves comparing two (or more) stars on a single échelle diagram after first scaling their frequencies.

Figure 7 shows the échelle diagram for Procyon overlaid with scaled frequencies for two stars observed by *CoRoT*, using the method described by Bedding & Kjeldsen (2010). The filled symbols are scaled oscillation frequencies for the G0 star HD 49385 observed by *CoRoT* (Deheuvels et al. 2010). The scaling involved multiplying all frequencies by a factor of 0.993 before plotting them, with this factor being chosen to align the symbols as closely as possible with the Procyon ridges. For this star, the *CoRoT* data gave an unambiguous mode identification, which is indicated by the symbol shapes. This confirms that the left-hand ridge of Procyon corresponds to modes with even l (Scenario B).

The open symbols in Figure 7 are oscillation frequencies for HD 49933 from the revised identification by Benomar et al. (2009b, Scenario B), after multiplying by a scaling factor of 0.6565. The alignment with HD 49385 was already demonstrated by Bedding & Kjeldsen (2010). We show HD 49933 here for comparison and to draw attention to the different amounts of bending at the bottom of the right-hand ($l = 1$) ridge for the three stars. The *CoRoT* target that is most similar to Procyon is HD170987 but unfortunately the signal-to-noise ratio (S/N) is too low to provide a clear identification of the ridges (Mathur et al. 2010).

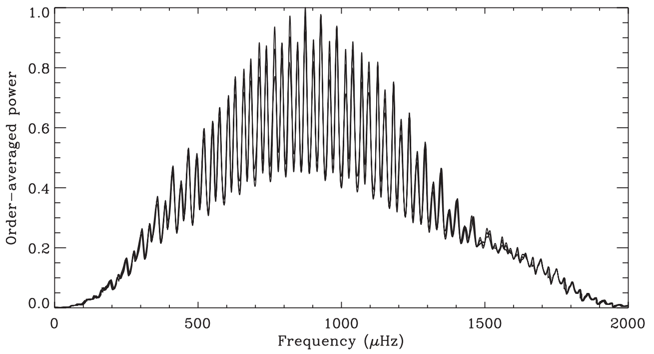

Figure 8. Order-averaged power spectrum (OAPS), where smoothing was done with a FWHM of 4.0 orders (see the text). The OAPS is plotted for three values of the large separations (54, 55, and 56 μHz), and we see that the positions of the maxima are not very sensitive to the value of $\Delta\nu$.

The above considerations give us confidence that Scenario B in Procyon is the correct identification, and we now proceed on that basis.

5. FREQUENCIES OF THE RIDGE CENTROIDS

Our next step in the analysis was to measure the centroids of the two ridges in the échelle diagram. We first removed the strong peak at 446 μHz (it was replaced by the mean noise level). We believe this to be a mixed mode and its extreme power means that it would significantly distort the result. We then smoothed the power spectrum to a resolution of 10 μHz (FWHM). To further improve the visibility of the ridges, we also averaged across several orders, which corresponds to smoothing in the vertical direction in the échelle diagram (Bedding et al. 2004; Kjeldsen et al. 2005; Karoff 2007). That is, for a given value of $\Delta\nu$, we define the "order-averaged" power spectrum to be

$$\mathrm{OAPS}(\nu, \Delta\nu) = \sum_{j=-4}^{4} c_j \mathrm{PS}(\nu + j\Delta\nu). \tag{6}$$

The coefficients c_j are chosen to give a smoothing with a FWHM of $k\Delta\nu$:

$$c_j = c_{-j} = \frac{1}{1 + (2j/k)^2}. \tag{7}$$

We show in Figure 8 the OAPS based on smoothing over 4 orders ($k = 4.0$), and so we used $(c_0, \ldots, c_4) = (1, 0.8, 0.5, 0.31, 0.2)$. The OAPS is plotted for three values of the large separations (54, 55, and 56 μHz), and they are superimposed. The three curves are hardly distinguishable, and we see that the positions of the maxima are not sensitive to the value of $\Delta\nu$.

We next calculated a modified version of the OAPS in which the value at each frequency is the maximum value of the OAPS over a range of large separations (53–57 μHz). This is basically the same as the comb response, as used previously by several authors (Kjeldsen et al. 1995; Mosser et al. 1998; Martić et al. 1999; Leccia et al. 2007). The maxima of this function define the centroids of the two ridges, which are shown in Figure 9.

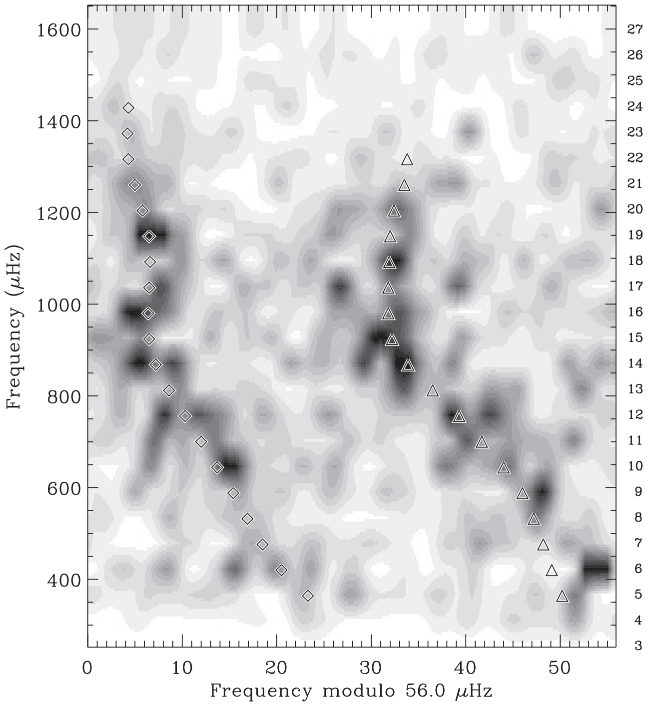

Figure 9. Centroids of the two ridges, as measured from the comb response. The grayscale shows the sidelobe-optimized power spectrum from which the peaks were calculated.

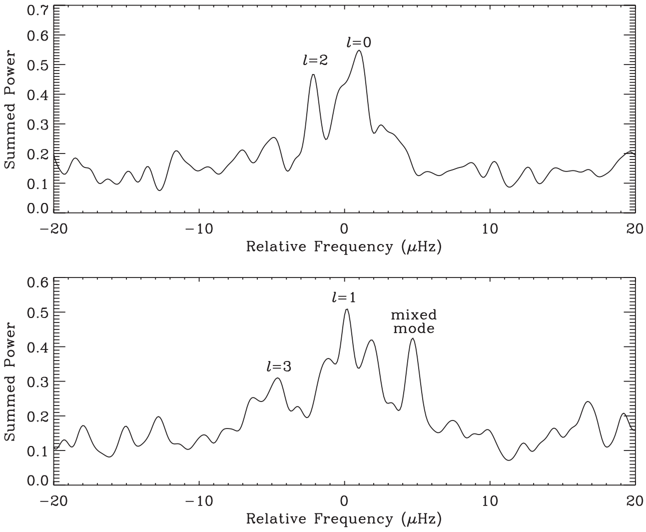

Figure 10. Power spectrum of Procyon collapsed along the ridges, over the full range of oscillations (18 orders). The upper panel shows the left-hand ridge, which we identify with modes having even degree, and the lower panel shows the right-hand ridge (odd degree). Note that the power spectrum was first smoothed slightly by convolving with a Gaussian with FWHM 0.6 μHz.

In Figure 10, we show the full power spectrum of Procyon (using sidelobe-optimized weights) collapsed along the ridges. This is similar to Figure 6 except that each order was shifted before the summation, so as to align the ridge peaks (symbols in Figure 9) and hence remove the curvature. This was done separately for both the even- and odd-degree ridges, as shown in the two panels of Figure 10. The collapsed spectrum clearly shows the power corresponding to $l = 0$–3, as well as the extra power from the mixed modes (for this figure, the peak at 446 μHz has not been removed).

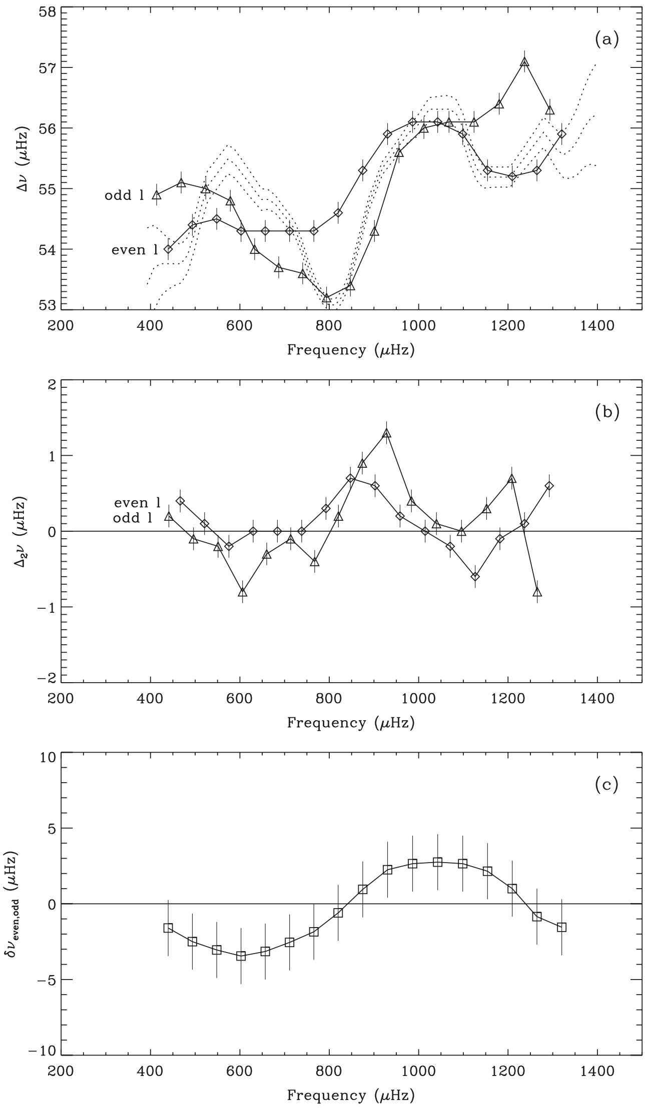

Figure 11. Symbols show the frequency separations in Procyon as a function of frequency, as measured from the ridge centroids: (a) large frequency separation, (b) second differences, and (c) small frequency separation. The dotted lines in panel *a* show the variation in $\Delta\nu$ (with $\pm 1\sigma$ range) calculated from the autocorrelation of the time series—see the text.

In Section 6 below, we use the ridges to guide our identification of the individual modes. First, however, we show that some asteroseismological inferences can be made solely from the ridges themselves. This is explained in more detail in Appendix B.

5.1. Large Separation of the Ridges

Figure 11(a) shows the variation with frequency of the large separation for each of the two ridges (diamonds and triangles). The smoothing across orders (Equation (6)) means that the ridge frequencies are correlated from one order to the next and so we used simulations to estimate uncertainties for the ridge centroids.

The oscillatory behavior of $\Delta\nu$ as a function of frequency seen in Figure 11(a) is presumably a signature of the helium ionization zone (e.g., Gough 1990). The oscillation is also seen in Figure 11(b), which shows the second differences for the two ridges, defined as follows (see Gough 1990; Ballot et al. 2004;

Houdek & Gough 2007):

$$\Delta_2 \nu_{n,\mathrm{even}} = \nu_{n-1,\mathrm{even}} - 2\nu_{n,\mathrm{even}} + \nu_{n+1,\mathrm{even}}, \tag{8}$$

$$\Delta_2 \nu_{n,\mathrm{odd}} = \nu_{n-1,\mathrm{odd}} - 2\nu_{n,\mathrm{odd}} + \nu_{n+1,\mathrm{odd}}. \tag{9}$$

The period of the oscillation is ∼500 μHz, which implies a glitch at an acoustic depth that is approximately twice the inverse of this value (Gough 1990; Houdek & Gough 2007), namely ∼1000 s. To determine this more precisely, we calculated the power spectrum of the second differences for both the odd and even ridges, and measured the highest peak. We found the period of the oscillation in the second differences to be 508 ± 18 μHz. Comparing this result with theoretical models will be the subject of a future paper.

The dotted lines in Figure 11(a) show the variation of $\Delta\nu$ with frequency calculated from the autocorrelation of the time series using the method of Mosser & Appourchaux (2009; see also Roxburgh & Vorontsov 2006). The mixed mode at 446 μHz was first removed and the smoothing filter had FWHM equal to 3 times the mean large separation. We see general agreement with the values calculated from the ridge separations. Some of the differences presumably arise because the autocorrelation analysis of the time series averages the large separation over all degrees.

5.2. *Small Separation of the Ridges*

Using only the centroids of the ridges, we can measure a small separation that is useful for asteroseismology. By analogy with $\delta\nu_{01}$ (see Equation (3)), we define it as the amount by which the odd ridge is offset from the midpoint of the two adjacent even ridges, with a positive value corresponding to a leftward shift (as observed in the Sun). That is,

$$\delta\nu_{\mathrm{even,odd}} = \frac{\nu_{n,\mathrm{even}} + \nu_{n+1,\mathrm{even}}}{2} - \nu_{n,\mathrm{odd}}. \tag{10}$$

Figure 11(c) shows our measurements of this small separation.[35] It is related in a simple way to the conventional small separations $\delta\nu_{01}$, $\delta\nu_{02}$, and $\delta\nu_{13}$ (see Appendix B for details) and so, like them, it gives information about the sound speed in the core. Our measurements of this small separation can be compared with theoretical models using the equations in Appendix B (e.g., see Christensen-Dalsgaard & Houdek 2009).

6. FREQUENCIES OF INDIVIDUAL MODES

We have extracted oscillation frequencies from the time series using the standard procedure of iterative sine-wave fitting. Each step of the iteration involves finding the strongest peak in the sidelobe-optimized power spectrum and subtracting the corresponding sinusoid from the time series. Figure 12 shows the result. The two ridges are clearly visible but the finite mode lifetime causes many modes to be split into two or more peaks. We might also be tempted to propose that some of the multiple peaks are due to rotational splitting but, as shown in Appendix A, this is unlikely to be the case.

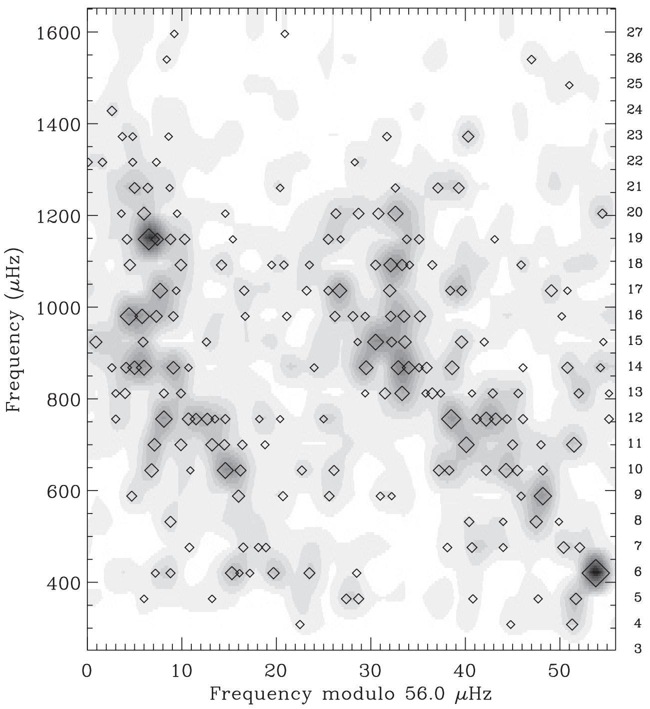

Figure 12. Peaks extracted from sidelobe-optimized power spectrum using iterative sine-wave fitting. Symbol size is proportional to amplitude (after the background noise has been subtracted). The grayscale shows the sidelobe-optimized power spectrum on which the fitting was performed, to guide the eye.

Deciding on a final list of mode frequencies with correct l identifications is somewhat subjective. To guide this process, we used the ridge centroids shown in Figure 9 as well as the small separations $\delta\nu_{02}$ and $\delta\nu_{13}$ from the collapsed power spectrum (see Figures 6 and 10). Each frequency extracted using iterative sine-wave fitting that lay close to a ridge was assigned an l value and multiple peaks from the same mode were averaged. The final mode frequencies are listed in Table 1, while peaks with S/N $\geqslant$ 3.5 that we have not identified are listed in Table 2. Figures 13 and 14 show these peaks overlaid on the sidelobe-optimized power spectrum. Figure 15 shows the three small separations (Equations (2)–(4)) as calculated from the frequencies listed in Table 1. The uncertainties in the mode frequencies are shown in parentheses in Table 1. These depend on the S/N of the peak and were calibrated using simulations (e.g., see Bedding et al. 2007).

The entries in Table 2 are mostly false peaks due to noise and to residuals from the iterative sine-wave fitting, but may include some genuine modes. To check whether some of them may be daily aliases of each other or of genuine modes, we calculated the differences of all combinations of frequencies in Tables 1 and 2. The histogram of these pairwise differences was flat in the vicinity of 11.6 μHz and showed no excess, confirming that daily aliases do not contribute significantly to the list of frequencies in the tables.

We also checked whether the number peaks in Table 2 agrees with expectations. We did this by analyzing a simulated time series that matched the observations in terms of oscillations properties (frequencies, amplitudes, and mode lifetimes), noise level, window function, and distribution of weights. We extracted peaks from the simulated power spectrum using iterative sine-wave fitting, as before, and found the number of "extra" peaks (not coinciding with the oscillation ridges) to be similar to that seen in Figure 12. Finally, we remark that the peak at 408 μHz is a candidate for a mixed mode with $l = 1$, given that

---

[35] We could also define a small separation $\delta\nu_{\mathrm{odd,even}}$ to be the amount by which the centroid of the even ridge is offset rightward from the midpoint of the adjacent odd ridges. This gives similar results.

Table 1

Oscillation Frequencies in Procyon (in μHz)

Order	$l = 0$	$l = 1$	$l = 2$	$l = 3$
4	...	331.3 (0.8)	...	...
5	...	387.7 (0.7)	...	...
6	415.5 (0.8)	445.8 (0.3)	411.7 (0.7)	...
7	466.5 (1.0)	498.6 (0.7)	464.5 (0.9)	488.7 (0.9)
8	...	551.5 (0.7)	...	544.4 (0.9)
9	576.0 (0.7)	608.2 (0.5)	...	...
10	630.7 (0.6)	660.6 (0.7)	627.0 (1.1)	653.6 (0.8)
11	685.6 (0.7)	712.1 (0.5)	681.9 (0.7)	...
12	739.2 (0.7)	766.5 (0.5)	736.2 (0.5)	...
13	793.7 (0.9)	817.2 (0.6)	792.3 (0.9)	...
14	849.1 (0.7)	873.5 (0.6)	845.4 (0.6)	869.5 (0.6)
15	901.9 (0.8)	929.2 (0.7)	...	926.6 (0.6)
16	957.8 (0.6)	985.3 (0.7)	956.4 (0.5)	980.4 (0.9)
17	1015.8 (0.6)	1040.0 (0.7)	...	1034.5 (0.7)
18	1073.9 (0.7)	1096.5 (0.7)	1068.5 (0.7)	...
19	1126.7 (0.5)	1154.6 (0.9)	1124.3 (0.9)	...
20	1182.0 (0.7)	1208.5 (0.6)	1179.9 (1.0)	...
21	1238.3 (0.9)	1264.6 (1.0)	1237.0 (0.8)	...
22	1295.2 (1.0)	...	1292.8 (1.0)	...
23	1352.6 (1.1)	1375.7 (1.0)	1348.2 (1.0)	...

Table 2

Unidentified Peaks with S/N $\geqslant 3.5$

ν (μHz)	S/N
407.6 (0.8)	3.5
512.8 (0.8)	3.6
622.8 (0.6)	4.3
679.1 (0.7)	4.0
723.5 (0.6)	4.7
770.5 (0.7)	4.1
878.5 (0.6)	4.4
890.8 (0.7)	3.6
935.6 (0.7)	3.9
1057.2 (0.7)	3.7
1384.3 (0.7)	3.6

it lies in the same order as the previously identified mixed mode at 446 μHz (note that we expect one extra $l = 1$ mode to occur at an avoided crossing).

The modes listed in Table 1 span 20 radial orders and more than a factor of 4 in frequency. This range is similar to that obtained from long-term studies of the Sun (e.g., Broomhall et al. 2009) and is unprecedented in asteroseismology. It was made possible by the unusually broad range of excited modes in Procyon and the high S/N of our data. Since the stellar background at low frequencies in intensity measurements is expected to be much higher than for velocity measurements, it seems unlikely that even the best data from the *Kepler* Mission will return such a wide range of frequencies in a single target.

7. MODE LIFETIMES

As discussed in Section 2, if the time series is sufficiently long then damping causes each mode in the power spectrum to be split into a series of peaks under a Lorentzian envelope having FWHM $\Gamma = 1/(\pi\tau)$, where τ is the mode lifetime. Our observations of Procyon are not long enough to resolve the modes into clear Lorentzians, and instead we see each mode as a small number of peaks (sometimes one). Furthermore, the centroid of these peaks may be offset from the position of the true mode, as illustrated in Figure 1 of Anderson et al. (1990). This last feature allows one to use the scatter of the extracted frequencies about smooth ridges in the échelle diagram, calibrated using simulations, to estimate the mode lifetime (Kjeldsen et al. 2005; Bedding et al. 2007). That method cannot be applied to Procyon because the $l = 0$ and $l = 2$ ridges are not well resolved and the $l = 1$ ridge is affected by mixed modes.

Rather than looking at frequency shifts, we have estimated the mode lifetime from the variations in mode amplitudes (again calibrated using simulations). This method is less precise but has the advantage of being independent of the mode identifications (e.g., Leccia et al. 2007; Carrier et al. 2007; Bedding et al. 2007). In Paper I, we calculated the smoothed amplitude curve for Procyon in 10 two-day segments and used the fluctuations about the mean to make a rough estimate of the mode lifetime: $\tau = 1.5^{+1.9}_{-0.8}$ days. We have attempted to improve on that estimate by considering the amplitude fluctuations of individual modes, as has been done for the Sun (e.g., Toutain & Fröhlich 1992; Baudin et al. 1996; Chang & Gough 1998), but were not able to produce well-calibrated results for Procyon.

Instead, we have measured the "peakiness" of the power spectrum (see Bedding et al. 2007) by calculating the ratio between the square of the mean amplitude of the 15 highest peaks in the range 500–1300 μHz (found by iterative sine-wave fitting) and the mean power in the same frequency range. The value for this ratio from our observations of Procyon is 6.9. We made a large number of simulations (3600) having a range of mode lifetimes and with the observed frequency spectrum, noise level, window function, and weights. Comparing the simulations with the observations led to a mode lifetime for Procyon of $1.29^{+0.55}_{-0.49}$ days.

This agrees with the value found in Paper I but is more precise, confirming that modes in Procyon are significantly more short-lived than those of the Sun. As discussed in Section 2, the dominant modes in the Sun have lifetimes of 2–4 days (e.g., Chaplin et al. 1997). The tendency for hotter stars to have shorter mode lifetimes has recently been discussed by Chaplin et al. (2009).

8. FITTING TO THE POWER SPECTRUM

Extracting mode parameters by fitting directly to the power spectrum is widely used in helioseismology, where the time series extends continuously for months or even years, and so the individual modes are well resolved (e.g., Anderson et al. 1990). Mode fitting has not been applied to ground-based observations of solar-type oscillations because these data typically have shorter durations and significant gaps. Global fitting has been carried out on spacecraft data, beginning with the 50-day time series of α Cen A taken with the *WIRE* spacecraft (Fletcher et al. 2006) and the 60-day light curve of HD 49933 from *CoRoT* (Appourchaux et al. 2008). Our observations of Procyon are much shorter than either of these cases but, given the quality of the data and the spectral window, we considered it worthwhile to attempt a fit.

Global fits to the Procyon power spectrum were made by several of us. Here, we present results from a fit using a Bayesian approach (e.g., Gregory 2005), which allowed us to include in a straightforward way our prior knowledge of the oscillation properties. The parameters to be extracted were the frequencies, heights, and linewidths of the modes. To obtain the marginal probability distributions of these parameters

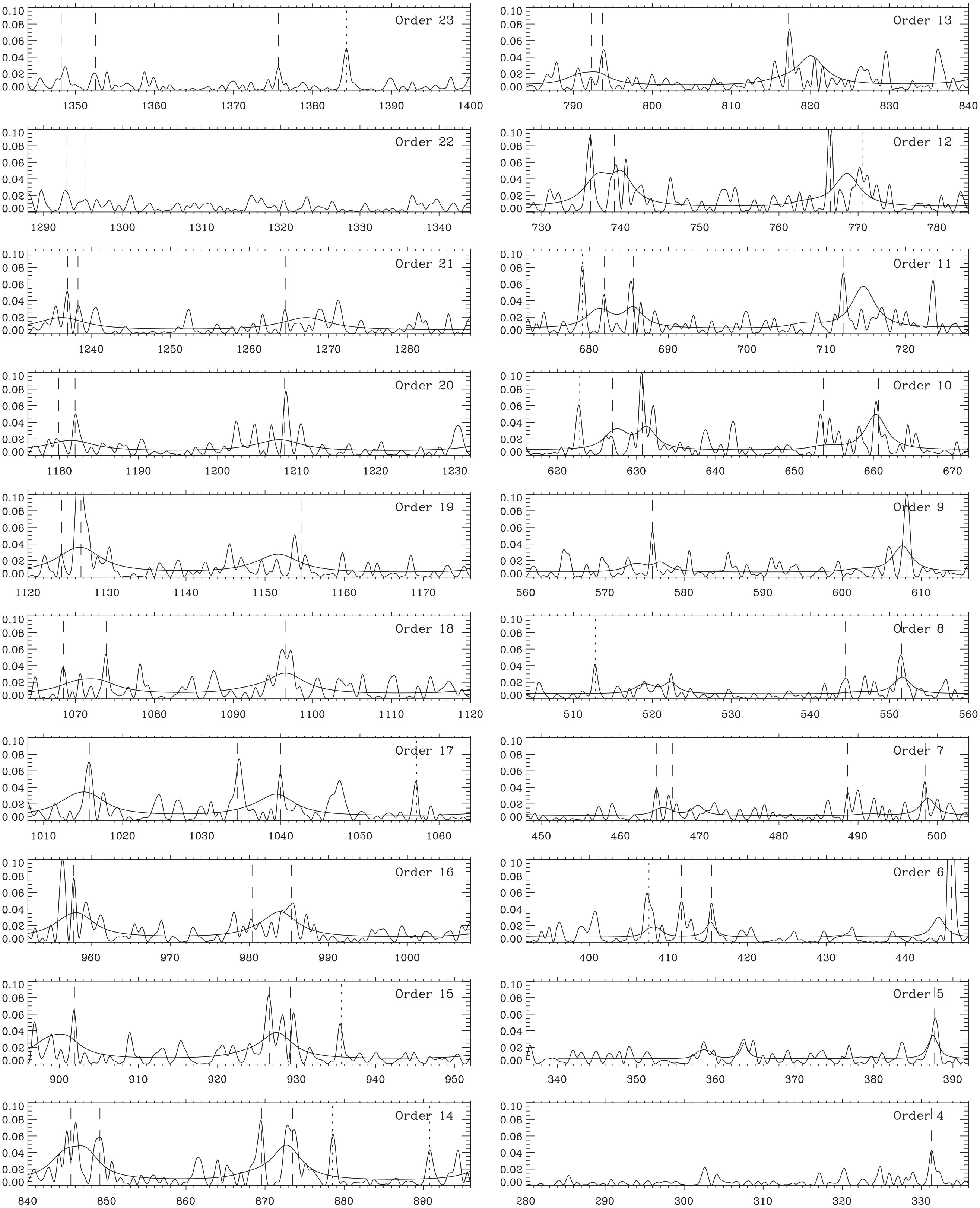

Figure 13. Power spectrum of Procyon at full resolution, with the orders in each column arranged from top to bottom, for easy comparison with the échelle diagrams. Vertical dashed lines show the mode frequencies listed in Table 1 and dotted lines show the peaks that have not been identified, as listed in Table 2. The smooth curve shows the global fit to the power spectrum for Scenario B (see Section 8).

and their associated uncertainties, we employed an Automated Parallel Tempering Markov Chain Monte Carlo (APT MCMC) algorithm. It implements the Metropolis–Hastings sampler by performing a random walk in parameter space while drawing

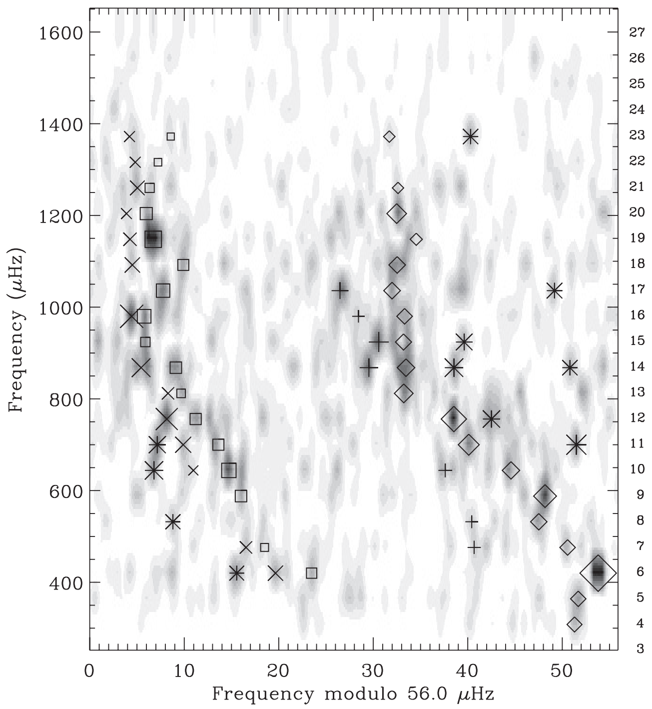

Figure 14. Power spectrum of Procyon overlaid with mode frequencies listed in Table 1. Symbols indicate angular degree (squares: $l = 0$; diamonds: $l = 1$; crosses: $l = 2$; pluses: $l = 3$). Asterisks show the peaks that have not been identified, as listed in Table 2.

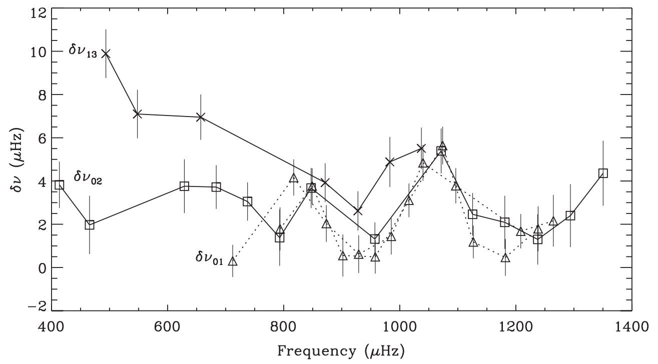

Figure 15. Small frequency separations in Procyon, as measured from the mode frequencies listed in Table 1.

samples from the posterior distribution (Gregory 2005). Further details of our implementation of the algorithm will be given elsewhere (T. L. Campante et al. 2010, in preparation).

The details of the fitting are as follows.

1. The fitting was performed over 17 orders (5–21) using the sidelobe-optimized power spectrum. In each order, we fitted modes with $l = 0$, 1, and 2, with each individual profile being described by a symmetric Lorentzian with FWHM Γ and height H. The mode frequencies were constrained to lie close to the ridges and to have only small jumps from one order to the next (a Gaussian prior with $\sigma = 3\ \mu$Hz). The S/Ns of modes with $l = 3$ were too low to permit a fit. In order to take their power into account, we included them in the model with their frequencies fixed by the asymptotic relation (Equation (1)).
2. The data are not good enough to provide a useful estimate of the linewidth of every mode, or even of every order. Therefore, the linewidth was parameterized as a linear function of frequency, defined by two parameters Γ_{600} and Γ_{1200}, which are the values at 600 and 1200 μHz. These parameters were determined by the fit, in which both were assigned a uniform prior in the range 0–10 μHz.
3. The height of each mode is related to the linewidth and amplitude according to (Chaplin et al. 2005):

$$H = \frac{2A^2}{\pi\Gamma}. \tag{11}$$

The amplitudes A of the modes were determined as follows. For the radial modes ($l = 0$), we used the smoothed amplitude curve measured from our observations, as shown in Figure 10 of Paper I. The amplitudes of the non-radial modes ($l = 1$–3) were then calculated from the radial modes using the ratios given in Table 1 of Kjeldsen et al. (2008a), namely, $S_0 : S_1 : S_2 : S_3 = 1.00 : 1.35 : 1.02 : 0.47$.
4. The background was fitted as a flat function.
5. We calculated the rotationally split profiles of the non-radial modes using the description given by Gizon & Solanki (2003). The inclination angle of the rotation axis was fixed at 31°, which is the inclination of the binary orbit (Girard et al. 2000) and, as discussed in Paper I (Section 4.1), is consistent with the rotational modulation of the velocity curve. The rotational splitting was fixed at 0.7 μHz, which was chosen to match the observed value of $v \sin i = 3.16$ km s^{-1} (Allende Prieto et al. 2002), given the known radius of the star. As discussed in Appendix A, choosing different values for the inclination (and hence the splitting) does not affect the mode profile, assuming reasonable values of the linewidth.

Table 3
Frequencies from Global Fit Using Scenario B (in μHz, with −/+ Uncertainties)

Order	$l = 0$	$l = 1$	$l = 2$
5	363.6 (0.8/0.9)	387.5 (0.6/0.6)	358.5 (1.3/1.2)
6	415.3 (3.3/1.0)	. . .	408.1 (1.0/3.7)
7	469.7 (1.6/2.1)	498.8 (0.7/0.8)	465.3 (1.1/1.3)
8	522.3 (1.4/1.4)	551.6 (0.8/0.7)	519.0 (1.5/1.6)
9	577.0 (1.6/2.5)	607.6 (0.6/0.7)	573.9 (2.2/2.8)
10	631.3 (0.8/0.8)	660.3 (1.0/1.3)	627.4 (2.1/2.8)
11	685.6 (1.2/1.6)	714.7 (1.4/1.2)	681.2 (2.3/1.9)
12	740.1 (1.6/1.7)	768.6 (0.9/1.0)	737.0 (1.5/1.7)
13	793.2 (1.3/1.7)	820.0 (1.7/1.2)	790.9 (2.0/1.9)
14	847.3 (1.2/1.4)	872.7 (1.1/0.9)	844.7 (1.7/1.5)
15	901.0 (1.8/1.7)	927.5 (0.8/0.8)	898.6 (2.1/2.1)
16	958.7 (1.4/1.1)	983.9 (1.0/1.3)	957.2 (1.0/1.3)
17	1015.9 (1.5/1.8)	1039.5 (1.6/1.7)	1014.0 (1.8/2.4)
18	1073.2 (1.5/2.2)	1096.6 (1.1/1.0)	1070.3 (2.2/2.3)
19	1127.2 (1.0/1.3)	1151.8 (1.4/1.4)	1125.9 (1.3/1.4)
20	1182.3 (1.5/1.4)	1207.9 (1.4/1.1)	1180.5 (1.6/1.6)
21	1236.9 (1.7/1.6)	1267.4 (1.7/1.5)	1235.5 (2.0/1.7)

We carried out the global fit using both scenarios discussed in Section 4. The fit for Scenario B is shown as the smooth curve in Figure 13 and the fitted frequencies are given in Table 3. Note that the mixed mode at 446 μHz was not properly fitted because it lies too far from the ridge (see point 1 above). To check the agreement with the results discussed in Section 6, we examined the differences betweens the frequencies in Tables 1 and 3. We found a reduced χ^2 of 0.74, which indicates good agreement. A

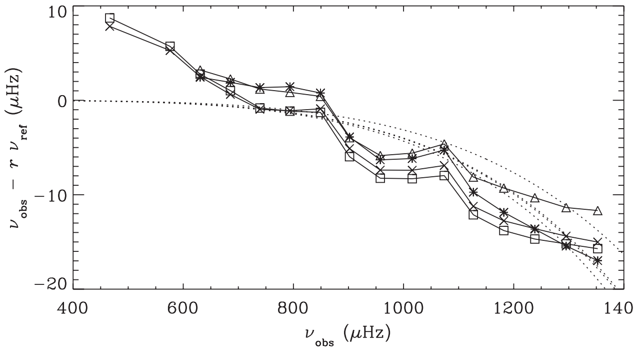

Figure 16. Difference between observed frequencies of radial modes in Procyon and those of scaled models. The symbols indicate different models, as follows: squares from Chaboyer et al. (1999, Table 2), crosses from Di Mauro & Christensen-Dalsgaard (2001), asterisks from Kervella et al. (2004, Table 4), and triangles from Eggenberger et al. (2005, model M1a). In each case, the dotted curve shows the correction calculated using Equation (4) of Kjeldsen et al. (2008b).

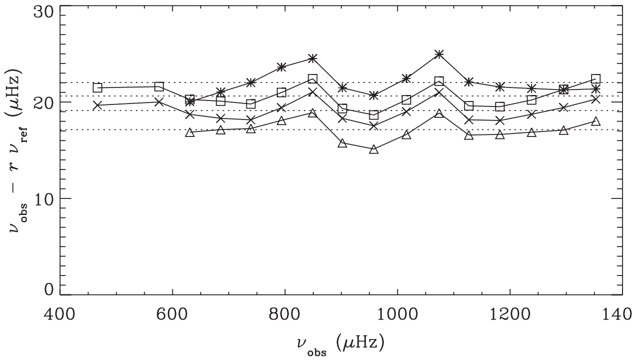

Figure 17. Same as Figure 16, but with a constant near-surface correction ($b = 0$).

Table 4
Frequencies from Global Fit Using Scenario A (in μHz, with −/+ Uncertainties)

Order	$l = 0$	$l = 1$	$l = 2$
5	387.7 (1.9/1.8)	361.9 (1.8/2.0)	385.1 (1.9/2.6)
6	. . .	412.5 (1.7/2.3)	439.3 (2.6/2.6)
7	498.7 (1.1/1.6)	467.6 (1.4/1.3)	493.2 (2.6/2.0)
8	552.2 (1.5/1.5)	520.7 (1.2/1.3)	549.3 (2.2/2.0)
9	607.8 (1.0/0.9)	576.2 (1.1/1.4)	605.4 (2.2/2.3)
10	661.3 (1.3/1.5)	631.1 (0.7/0.8)	657.1 (1.7/1.6)
11	716.8 (1.3/1.7)	684.7 (1.2/1.2)	712.6 (1.2/1.2)
12	769.9 (1.2/1.3)	739.1 (1.1/1.2)	766.6 (1.4/1.4)
13	822.7 (1.9/2.7)	792.9 (1.3/1.3)	817.8 (1.3/1.4)
14	874.5 (1.3/1.3)	846.4 (0.9/0.8)	869.9 (1.6/1.3)
15	928.8 (1.2/1.2)	900.0 (1.3/1.4)	925.9 (1.3/1.1)
16	985.1 (1.0/1.1)	958.2 (0.8/0.8)	980.9 (1.9/1.6)
17	1043.4 (2.8/2.8)	1015.7 (1.0/0.9)	1035.2 (1.0/0.8)
18	1097.6 (1.5/0.9)	1072.5 (1.1/1.2)	1091.8 (3.7/4.2)
19	1153.7 (0.9/0.8)	1126.9 (0.5/0.6)	1146.8 (1.3/1.0)
20	1209.1 (0.8/0.9)	1181.8 (1.0/0.9)	1204.8 (1.3/1.4)
21	1269.2 (1.0/1.1)	1237.1 (0.9/0.9)	1264.8 (1.5/1.5)

value less than 1 is not surprising given that both methods were constrained to find modes close to the ridges.

The fitted linewidths (assumed to be a linear function of frequency, as described above) gave mode lifetimes of 1.5 ± 0.4 days at 600 μHz and 0.6 ± 0.3 days at 1200 μHz. These agree with the single value of $1.29^{+0.55}_{-0.49}$ days found above (Section 7), and indicate that the lifetime increases toward lower frequencies, as is the case for the Sun and for the F-type *CoRoT* targets HD 49933 (Benomar et al. 2009b) and HD 181420 (Barban et al. 2009).

We also carried out the global fit using Scenario A. We found through Bayesian model selection that Scenario A was statistically favored over Scenario B by a factor of 10:1. This factor classifies as "significant" on the scale of Jeffreys (1961; see Table 1 of Liddle 2009). On the same scale, posterior odds of at least ~13:1 are required for a classification of "strong to very strong," and "decisive" requires at least ~150:1. In our Bayesian fit to Procyon, the odds ratio in favor of Scenario A did not exceed 13:1, even when different sets of priors were imposed.

In light of the strong arguments given in Section 4 in favor of Scenario B, we do not consider the result from Bayesian model selection to be sufficiently compelling to cause us to reverse our identification. Of course, it is possible that Scenario A is correct and, for completeness, we show these fitted frequencies in Table 4. The fit using Scenario A gave mode lifetimes of 0.9 ± 0.2 days at 600 μHz and 1.0 ± 0.3 days at 1200 μHz.

9. PRELIMINARY COMPARISON WITH MODELS

A detailed comparison of the observed frequencies of Procyon with theoretical models is beyond the scope of this paper, but we will make some preliminary comments on the systematic offset between the two. It is well established that incorrect modeling of the surface layers of the Sun is responsible for discrepancies between the observed and calculated oscillation frequencies (Christensen-Dalsgaard et al. 1988; Dziembowski et al. 1988; Rosenthal et al. 1999; Li et al. 2002).

To address this problem for other stars, Kjeldsen et al. (2008b) proposed an empirical correction to be applied to model frequencies that takes advantage of the fact that the offset between observations and models is independent of l and goes to zero with decreasing frequency. They measured the offset for the Sun to be a power law with exponent $b = 4.9$ and applied this correction to the radial modes of other stars, finding very good results that allowed them to estimate mean stellar densities very accurately (better than 0.5%).

We have applied this method to Procyon, comparing our observed frequencies for the radial modes with various published models to determine the scaling factor r and the offset (see Kjeldsen et al. 2008b for details of the method). The results are shown in Figure 16. Interestingly, the offset between the observations and scaled models does not go to zero with decreasing frequency. This contrasts with the G- and K-type stars investigated by Kjeldsen et al. (2008b), namely, the Sun, α Cen A and B, and β Hyi.

The method of Kjeldsen et al. (2008b) assumes the correction to be applied to the models to have the same form as in the Sun, namely, a power law with an exponent of $b = 4.9$. The fit in Figure 16 is poor and is not improved by modest adjustments to b. Instead, the results seem to imply an offset that is constant. Setting $b = 0$ and repeating the calculations produce the results shown in Figure 17, where we indeed see a roughly constant offset between the models and the observations of about 20 μHz.

As a check, we can consider the density implied for Procyon. The stellar radius can be calculated from the interferometric radius and the parallax. The angular diameter of 5.404 ± 0.031 mas (Aufdenberg et al. 2005, their Table 7) and the revised *Hipparcos* parallax of 285.93 ± 0.88 mas (van Leeuwen 2007) gives a radius of 2.041 ± 0.015 $R_\odot$.

Procyon is in a binary system (the secondary is a white dwarf), allowing the mass to be determined from astrometry. Girard et al. (2000) found a value of $1.497 \pm 0.037\ M_\odot$, while Gatewood & Han (2006) found $1.431 \pm 0.034\ M_\odot$ (see Guenther et al. 2008 for further discussion).

The density obtained using the fits shown in Figure 16 is in the range 0.255–0.258 g cm^{-3}. Combining with the radius implies a mass in the range 1.54–1.56 $M_\odot$. The density obtained using the fits shown in Figure 17 is in the range 0.242–0.244 g cm^{-3}, implying a mass of 1.46–1.48 $M_\odot$. The latter case seems to be in much better agreement with the astrometrically determined mass, lending some support to the idea that the offset is constant.

We can also consider the possibility that our mode identification is wrong and that Scenario A is the correct one (see Sections 4 and 8). With this reversed identification, the radial modes in Procyon are those in Table 1 listed as having $l = 1$. Assuming these to be radial modes, the offset between them and the model frequencies is again constant, as we would expect, but this time with a mean value close to zero. The implied density for Procyon is again consistent with the observed mass and radius.

The preceding discussion makes it clear that the correction that needs to be applied to models of Procyon is very different from that for the Sun and other cool stars, regardless of whether Scenario B or A is correct. In particular, the substantial nearly constant offset implied by Figure 16 would indicate errors in the modeling extending well beyond the near-surface layers. We also note that in terms of the asymptotic expression (Equation (1)) a constant offset would imply an error in the calculation of ϵ.

10. CONCLUSION

We have analyzed results from a multi-site campaign on Procyon that obtained high-precision velocity observations over more than three weeks (Paper I). We developed a new method for adjusting the weights in the time series that allowed us to minimize the sidelobes in the power spectrum that arise from diurnal gaps and so to construct an échelle diagram that shows two clear ridges of power. To identify the odd and even ridges, we summed the power across several orders. We found structures characteristic of $l = 0$ and 2 in one ridge and $l = 1$ and 3 in the other. This identification was confirmed by comparing our Procyon data in a scaled échelle diagram (Bedding & Kjeldsen 2010) with other stars for which the ridge identification is known. We showed that the frequencies of the ridge centroids and their large and small separations are easily measured and are useful diagnostics for asteroseismology. In particular, an oscillation in the large separation appears to indicate a glitch in the sound-speed profile at an acoustic depth of ~1000 s.

We identify a strong narrow peak at 446 μHz, which falls slightly away from the $l = 1$ ridge, as a mixed mode. In Table 1, we give frequencies, extracted using iterative sine-wave fitting, for 55 modes with angular degrees l of 0–3. These cover 20 radial orders and a factor of more than 4 in frequency, which reflects the broad range of excited modes in Procyon and the high S/N of our data, especially at low frequencies. Intensity measurements will suffer from a much higher stellar background at low frequencies, making it unlikely that even the best data from the *Kepler* Mission will yield the wide range of frequencies found here. This is a strong argument in favor of continuing efforts toward ground-based Doppler studies, such as the Stellar Observations Network Group (SONG; Grundahl et al. 2008), which is currently under construction, and the proposed Antarctic instrument Seismic Interferometer to Measure Oscillations in the Interior of Stars (SIAMOIS; Mosser et al. 2008).

We estimated the mean lifetime of the modes by comparing the "peakiness" of the power spectrum with simulations and found a value of $1.29^{+0.55}_{-0.49}$ days, significantly below that of the Sun. A global fit to the power spectrum using Bayesian methods confirmed this result and provided evidence that the lifetime increases toward lower frequencies. It also casts some doubt on the mode identifications. We still favor the identification discussed above, but leave open the possibility that this may need to be reversed. Finally, comparing the observed frequencies of radial modes in Procyon with published theoretical models showed an offset that appears to be constant with frequency, making it very different from that seen in the Sun and other cool stars. Detailed comparisons of our results with theoretical models will be carried out in future papers.

We would be happy to make the data presented in this paper available on request.

This work was supported financially by the Australian Research Council, the Danish Natural Science Research Council, the Swiss National Science Foundation, NSF grant AST-9988087 (R.P.B.), and by SUN Microsystems. We gratefully acknowledge support from the European Helio- and Asteroseismology Network (HELAS), a major international collaboration funded by the European Commission's Sixth Framework Programme.

APPENDIX A

ROTATIONAL SPLITTING

We expect non-radial modes to be split due to the rotation of the star. The rotation period of Procyon is not known, although slow variations in our velocity observations (Paper I) indicated a value of either 10.3 days or twice that value. The projected rotational velocity has been measured spectroscopically. Allende Prieto et al. (2002) determined a value of $v \sin i = 3.16 \pm 0.50$ km s^{-1}, although they note that the actual value may be lower by about 0.5 km s^{-1}.

Gizon & Solanki (2003) have studied the effect of rotation on the profiles of solar-like oscillations as a function of inclination and mode lifetime (see also Ballot et al. 2006). We have repeated their calculations for our observations of Procyon (with sidelobe-optimized weights). The results are shown in Figure 18, which shows the effects of rotational splitting, inclination angle, and mode lifetime on the theoretical profile of the modes.[36] Note that the calculations do not include the stochastic nature of the excitation and so the function shown here should properly be called the expectation value of the power spectrum, also known as the *limit spectrum*. Figure 18 is similar to Figure 2 of Gizon & Solanki (2003) except that instead of fixing the rotation period, we have fixed $v \sin i$ to be the measured value. For $l = 0$, the profile does not depend on the inclination angle, while for $l = 1$, 2, and 3 the solid and dashed lines show calculations for $i = 30^\circ$ ($P_{\rm rot} = 16.4$ days) and $i = 80^\circ$ ($P_{\rm rot} = 32.3$ days), respectively. In each panel, results are shown for three values of the mode lifetime: 1.5 days (top curve), 3 days (middle curve), and infinite (bottom curve). For each mode lifetime, the curves for different i and l are all normalized to have the same area.

---

[36] Note that we have made the quite reasonable assumption that the internal rotation has a similar period to the surface rotation.

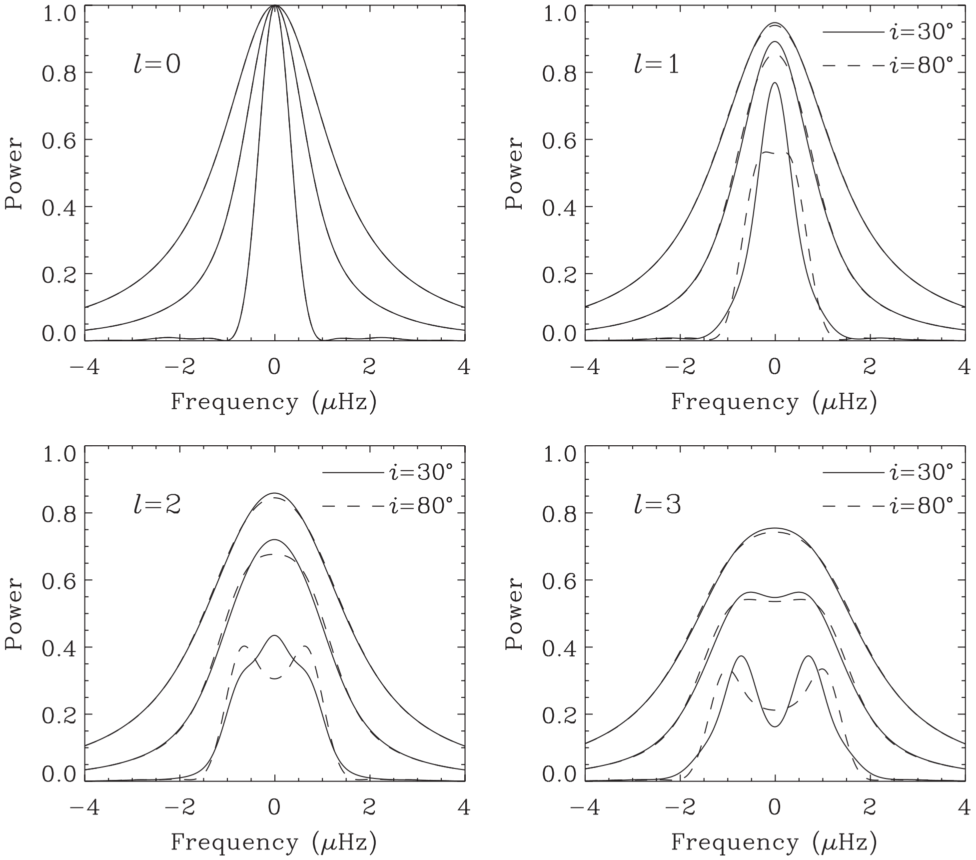

Figure 18. Theoretical line profiles showing rotational splitting for different mode degrees, similar to Figure 2 of Gizon & Solanki (2003) but here using a fixed value of $v \sin i$, namely 3.16 km s^{-1}, as measured for Procyon (Allende Prieto et al. 2002). For $l = 0$, the profile does not depend on the inclination angle, while for $l = 1$, 2, and 3 the solid and dashed lines show calculations for $i = 30°$ ($P_{\rm rot} = 16.4$ days) and $i = 80°$ ($P_{\rm rot} = 32.3$ days), respectively. In each panel, results are shown for three values of the mode lifetime: 1.5 days (top curve), 3 days (middle curve), and infinite (bottom curve). For each mode lifetime, the curves for different i and l are all normalized to have the same area.

We see from Figure 18 that for a fixed $v \sin i$, the width of the profile stays roughly constant as a function of inclination. If the rotation axis of the star happens to be in the plane of the sky ($i = 90°$), then the rotation period is too low to produce a measurable splitting. At the other extreme, if the inclination is small (so that the rotation is close to pole-on), then the rotational splitting will be large but most of the power will be in the central peak ($m = 0$). Either way, once the profile has been broadened by the mode lifetime, the splitting will be unobservable.

We conclude that for realistic values of the mode lifetime, our observations are not long enough to detect rotational splitting in Procyon. The line profiles are broadened by rotation, but it is not possible to disentangle the rotation rate from the inclination angle. Rotational splitting is not measurable in Procyon, except perhaps with an extremely long data set. The detection of rotational splitting requires choosing a star with a larger $v \sin i$ or a longer mode lifetime, or both.

APPENDIX B

RELATING RIDGE CENTROIDS TO MODE FREQUENCIES

As discussed in Section 5, the frequencies of the ridge centroids are useful for asteroseismology in cases where it is difficult to resolve the ridges into their component modes. In this appendix, we relate the frequencies of the ridge centroids to those of the underlying modes, which allows us to express the small separation of the ridges (Equation (10)) in terms of the conventional small separations ($\delta\nu_{01}$, $\delta\nu_{02}$, and $\delta\nu_{13}$). These relationships will allow the observations to be compared with theoretical models.

The ridge centroids depend on the relative contributions of modes with $l = 0$, 1, 2, and 3. The power in the even ridge is approximately equally divided between $l = 0$ and $l = 2$, while the odd ridge is dominated by $l = 1$ but with some contribution from $l = 3$. The exact ratios depend on the observing method, as discussed by Kjeldsen et al. (2008a). For velocity measurements, such as those presented in this paper for Procyon, the amplitude ratios given by Kjeldsen et al. (2008a, their Table 1) yield the following expressions for the centroids in power:

$$\nu^{\rm vel}_{n,{\rm even}} = 0.49\nu_{n,0} + 0.51\nu_{n-1,2}, \tag{B1}$$

$$\nu^{\rm vel}_{n,{\rm odd}} = 0.89\nu_{n,1} + 0.11\nu_{n-1,3}, \tag{B2}$$

where the superscript indicates these apply to velocity measurements.

For photometric measurements, such as those currently being obtained with the *CoRoT* and *Kepler* Missions, the relative contributions from the various l values are different. Table 1 of Kjeldsen et al. (2008a) gives response factors for intensity measurements in the three VIRGO passbands, namely, 402, 500, and 862 nm. For *CoRoT* and *Kepler*, it is appropriate to use a central wavelength of 650 nm. Using the same method as Kjeldsen et al. (2008a), we find the ratios (in amplitude) for this case to be $S_0 : S_1 : S_2 : S_3 = 1.00 : 1.23 : 0.71 : 0.14$. The ridge centroids measured from such data would then be

$$\nu^{650}_{n,\mathrm{even}} = 0.66\nu_{n,0} + 0.34\nu_{n-1,2}, \tag{B3}$$

$$\nu^{650}_{n,\mathrm{odd}} = 0.99\nu_{n,1} + 0.01\nu_{n-1,3}. \tag{B4}$$

We can express the new small separation of the ridge centroids (Equation (10)) in terms of the conventional ones. For velocity, we have

$$\delta\nu^{\mathrm{vel}}_{\mathrm{even,odd}} = \delta\nu_{01} - 0.51\delta\nu_{02} + 0.11\delta\nu_{13}; \tag{B5}$$

and for photometry, we have

$$\delta\nu^{650}_{\mathrm{even,odd}} = \delta\nu_{01} - 0.34\delta\nu_{02} + 0.01\delta\nu_{13}. \tag{B6}$$

Finally, we can express these in terms of D_0 under the assumption that the asymptotic relation (Equation (1)) holds exactly, although in fact this is not likely to be the case:

$$\delta\nu^{\mathrm{vel}}_{\mathrm{even,odd}} = 0.04D_0 \tag{B7}$$

and

$$\delta\nu^{650}_{\mathrm{even,odd}} = 0.06D_0. \tag{B8}$$

REFERENCES

Aerts, C., Christensen-Dalsgaard, J., Cunha, M., & Kurtz, D. W. 2008, Sol. Phys., 251, 3

Aizenman, M., Smeyers, P., & Weigert, A. 1977, A&A, 58, 41

Allende Prieto, C., Asplund, M., López, R. J. G., & Lambert, D. L. 2002, ApJ, 567, 544

Anderson, E. R., Duvall, T. L., & Jefferies, S. M. 1990, ApJ, 364, 699

Appourchaux, T., et al. 2008, A&A, 488, 705

Arentoft, T., Kjeldsen, H., & Bedding, T. R. 2010, in ASP Conf. Ser. 416, GONG 2008/*SOHO* XXI Meeting on Solar-Stellar Dynamos as Revealed by Helio- and Asteroseismology, ed. M. Dikpati et al. (San Francisco, CA: ASP), in press (arXiv:0901.3632)

Arentoft, T., et al. 2008, ApJ, 687, 1180 (Paper I)

Aufdenberg, J. P., Ludwig, H.-G., & Kervella, P. 2005, ApJ, 633, 424

Ballot, J., García, R. A., & Lambert, P. 2006, MNRAS, 369, 1281

Ballot, J., Turck-Chièze, S., & García, R. A. 2004, A&A, 423, 1051

Barban, C., Michel, E., Martić, M., Schmitt, J., Lebrun, J. C., Baglin, A., & Bertaux, J. L. 1999, A&A, 350, 617

Barban, C., et al. 2009, A&A, 506, 51

Baudin, F., Gabriel, A., Gibert, D., Pallé, P. L., & Régulo, C. 1996, A&A, 311, 1024

Bedding, T. R., & Kjeldsen, H. 2003, PASA, 20, 203

Bedding, T. R., & Kjeldsen, H. 2007, in AIP Conf. Proc. 948, Unsolved Problems in Stellar Physics: A Conference in Honour of Douglas Gough, ed. R. J. Stancliffe et al. (Melville, NY: AIP), 117

Bedding, T. R., & Kjeldsen, H. 2010, Commun. Asteroseismol., 161, 3

Bedding, T. R., Kjeldsen, H., Butler, R. P., McCarthy, C., Marcy, G. W., O'Toole, S. J., Tinney, C. G., & Wright, J. T. 2004, ApJ, 614, 380

Bedding, T. R., et al. 2007, ApJ, 663, 1315

Bedding, T. R., et al. 2010, ApJ, in press (arXiv:1001.0229)

Benomar, O., Appourchaux, T., & Baudin, F. 2009a, A&A, 506, 15

Benomar, O., et al. 2009b, A&A, 507, L13

Bonanno, A., Küker, M., & Paternò, L. 2007, A&A, 462, 1031

Broomhall, A.-M., Chaplin, W. J., Davies, G. R., Elsworth, Y., Fletcher, S. T., Hale, S. J., Miller, B., & New, R. 2009, MNRAS, 396, L100

Brown, T. M., & Gilliland, R. L. 1994, ARA&A, 32, 37

Carrier, F., et al. 2007, A&A, 470, 1059

Carrier, F., et al. 2010, A&A, 55, A73

Chaboyer, B., Demarque, P., & Guenther, D. B. 1999, ApJ, 525, L41

Chang, H.-Y., & Gough, D. O. 1998, Sol. Phys., 181, 251

Chaplin, W. J., Elsworth, Y., Isaak, G. R., McLeod, C. P., Miller, B. A., & New, R. 1997, MNRAS, 288, 623

Chaplin, W. J., Houdek, G., Elsworth, Y., Gough, D. O., Isaak, G. R., & New, R. 2005, MNRAS, 360, 859

Chaplin, W. J., Houdek, G., Karoff, C., Elsworth, Y., & New, R. 2009, A&A, 500, L21

Christensen-Dalsgaard, J. 2004, Sol. Phys., 220, 137

Christensen-Dalsgaard, J., Däppen, W., & Lebreton, Y. 1988, Nature, 336, 634

Christensen-Dalsgaard, J., & Houdek, G. 2009, Ap&SS, in press (arXiv:0911.4629)

Deheuvels, S., et al. 2010, A&A, submitted

Di Mauro, M. P., & Christensen-Dalsgaard, J. 2001, in IAU Symp. 203, Recent Insights into the Physics of the Sun and Heliosphere: Highlights from SOHO and Other Space Missions, ed. P. Brekke, B. Fleck, & J. B. Gurman (San Francisco, CA: ASP), 94

Dziembowski, W. A., Paternó, L., & Ventura, R. 1988, A&A, 200, 213

Eggenberger, P., Carrier, F., & Bouchy, F. 2005, New Astron., 10, 195

Eggenberger, P., Carrier, F., Bouchy, F., & Blecha, A. 2004, A&A, 422, 247

Fletcher, S. T., Chaplin, W. J., Elsworth, Y., Schou, J., & Buzasi, D. 2006, MNRAS, 371, 935

Frandsen, S., Jones, A., Kjeldsen, H., Viskum, M., Hjorth, J., Andersen, N. H., & Thomsen, B. 1995, A&A, 301, 123

García, R. A., et al. 2009, A&A, 506, 41

Gatewood, G., & Han, I. 2006, AJ, 131, 1015

Gilliland, R. L., et al. 1993, AJ, 106, 2441

Gilliland, R. L., et al. 2010, PASP, 122, 131

Girard, T. M., et al. 2000, AJ, 119, 2428

Gizon, L., & Solanki, S. K. 2003, ApJ, 589, 1009

Gough, D. O. 1986, in Hydrodynamic and Magnetodynamic Problems in the Sun and Stars, ed. Y. Osaki (Tokyo: Univ. Tokyo Press), 117

Gough, D. O. 1990, in Lecture Notes in Physics, Vol. 367, Progress of Seismology of the Sun and Stars, ed. Y. Osaki & H. Shibahashi (Berlin: Springer), 283

Grec, G., Fossat, E., & Pomerantz, M. A. 1983, Sol. Phys., 82, 55

Gregory, P. C. 2005, Bayesian Logical Data Analysis for the Physical Sciences (Cambridge: Cambridge Univ. Press)

Gruberbauer, M., Kallinger, T., Weiss, W. W., & Guenther, D. B. 2009, A&A, 506, 1043

Grundahl, F., Christensen-Dalsgaard, J., Arentoft, T., Frandsen, S., Kjeldsen, H., Jørgensen, U. G., & Kjaergaard, P. 2008, Commun. Asteroseismol., 157, 273

Guenther, D. B., & Demarque, P. 1993, ApJ, 405, 298

Guenther, D. B., et al. 2008, ApJ, 687, 1448

Högbom, J. A., & Brouw, W. N. 1974, A&A, 33, 289

Houdek, G., & Gough, D. O. 2007, MNRAS, 375, 861

Jeffreys, H. 1961, Theory of Probability (3rd ed.; New York: Oxford Univ. Press)

Kallinger, T., Gruberbauer, M., Guenther, D. B., Fossati, L., & Weiss, W. W. 2010, A&A, 510, A106

Karoff, C. 2007, MNRAS, 381, 1001

Kervella, P., Thévenin, F., Morel, P., Berthomieu, G., Bordé, P., & Provost, J. 2004, A&A, 413, 251

Kjeldsen, H., Bedding, T. R., & Christensen-Dalsgaard, J. 2008b, ApJ, 683, L175

Kjeldsen, H., Bedding, T. R., Viskum, M., & Frandsen, S. 1995, AJ, 109, 1313

Kjeldsen, H., et al. 2005, ApJ, 635, 1281

Kjeldsen, H., et al. 2008a, ApJ, 682, 1370

Leccia, S., Kjeldsen, H., Bonanno, A., Claudi, R. U., Ventura, R., & Paternò, L. 2007, A&A, 464, 1059

Li, L. H., Robinson, F. J., Demarque, P., Sofia, S., & Guenther, D. B. 2002, ApJ, 567, 1192

Liddle, A. R. 2009, Annu. Rev. Nucl. Part. Sci., 59, 95

Martić, M., Lebrun, J.-C., Appourchaux, T., & Korzennik, S. G. 2004, A&A, 418, 295

Martić, M., et al. 1999, A&A, 351, 993

Mathur, S., et al. 2010, A&A, submitted

Michel, E., et al. 2008, Science, 322, 558

Mosser, B., & Appourchaux, T. 2009, A&A, 508, 877

Mosser, B., Appourchaux, T., Catala, C., Buey, J., & SIAMOIS team 2008, J. Phys. Conf. Ser., 118, 012042

Mosser, B., Maillard, J. P., Mékarnia, D., & Gay, J. 1998, A&A, 340, 457

Osaki, J. 1975, PASJ, 27, 237

Provost, J., Berthomieu, G., Martić, M., & Morel, P. 2006, A&A, 460, 759

Régulo, C., & Roca Cortés, T. 2005, A&A, 444, L5

Rosenthal, C. S., Christensen-Dalsgaard, J., Nordlund, Å., Stein, R. F., & Trampedach, R. 1999, A&A, 351, 689

Roxburgh, I. W. 2009, A&A, 506, 435

Roxburgh, I. W., & Vorontsov, S. V. 2006, MNRAS, 369, 1491

Tassoul, M. 1980, ApJS, 43, 469

Toutain, T., & Fröhlich, C. 1992, A&A, 257, 287

van Leeuwen, F. 2007, Hipparcos, the New Reduction of the Raw Data (Dordrecht: Springer)

Appendix C

A&A 534, A6 (2011)
DOI: 10.1051/0004-6361/201116620

Astronomy & Astrophysics

Asteroseismology from multi-month *Kepler* photometry: the evolved Sun-like stars KIC 10273246 and KIC 10920273

T. L. Campante[1,2], R. Handberg[2], S. Mathur[3], T. Appourchaux[4], T. R. Bedding[5], W. J. Chaplin[6], R. A. García[7], B. Mosser[8], O. Benomar[4], A. Bonanno[9], E. Corsaro[9], S. T. Fletcher[10], P. Gaulme[4], S. Hekker[6,11], C. Karoff[2], C. Régulo[12,13], D. Salabert[12,13], G. A. Verner[6,14], T. R. White[5,15], G. Houdek[16], I. M. Brandão[1], O. L. Creevey[12,13], G. Doğan[2], M. Bazot[1], J. Christensen-Dalsgaard[2], M. S. Cunha[1], Y. Elsworth[6], D. Huber[5], H. Kjeldsen[2], M. Lundkvist[2], J. Molenda-Żakowicz[17], M. J. P. F. G. Monteiro[1], D. Stello[5], B. D. Clarke[18], F. R. Girouard[19], and J. R. Hall[19]

[1] Centro de Astrofísica, DFA-Faculdade de Ciências, Universidade do Porto, Rua das Estrelas, 4150-762 Porto, Portugal
e-mail: `campante@astro.up.pt`
[2] Department of Physics and Astronomy, Aarhus University, 8000 Aarhus C, Denmark
e-mail: `campante@phys.au.dk`
[3] High Altitude Observatory, National Center for Atmospheric Research, Boulder, Colorado 80307, USA
[4] Institut d'Astrophysique Spatiale, Université Paris XI – CNRS (UMR8617), Bâtiment 121, 91405 Orsay Cedex, France
[5] Sydney Institute for Astronomy (SIfA), School of Physics, University of Sydney, NSW 2006, Australia
[6] School of Physics and Astronomy, University of Birmingham, Edgbaston, Birmingham B15 2TT, UK
[7] Laboratoire AIM, CEA/DSM-CNRS-Université Paris Diderot, IRFU/SAp, Centre de Saclay, 91191 Gif-sur-Yvette, France
[8] LESIA, CNRS, Université Pierre et Marie Curie, Université Paris Diderot, Observatoire de Paris, 92195 Meudon Cedex, France
[9] INAF Osservatorio Astrofisico di Catania, via S. Sofia 78, 95123 Catania, Italy
[10] Materials Engineering Research Institute, Faculty of Arts, Computing, Engineering and Sciences, Sheffield Hallam University, Sheffield S1 1WB, UK
[11] Astronomical Institute Anton Pannekoek, University of Amsterdam, Science Park 904, 1098 XH Amsterdam, The Netherlands
[12] Departamento de Astrofísica, Universidad de La Laguna, 38206 La Laguna, Tenerife, Spain
[13] Instituto de Astrofísica de Canarias, 38200 La Laguna, Tenerife, Spain
[14] Astronomy Unit, Queen Mary, University of London, Mile End Road, London E1 4NS, UK
[15] Australian Astronomical Observatory, PO Box 296, Epping NSW 1710, Australia
[16] Institute of Astronomy, University of Vienna, 1180 Vienna, Austria
[17] Astronomical Institute, University of Wrocław, ul. Kopernika 11, 51-622 Wrocław, Poland
[18] SETI Institute/NASA Ames Research Center, Moffett Field, CA 94035, USA
[19] Orbital Sciences Corporation/NASA Ames Research Center, Moffett Field, CA 94035, USA

Received 1 February 2011 / Accepted 16 August 2011

ABSTRACT

Context. The evolved main-sequence Sun-like stars KIC 10273246 (F-type) and KIC 10920273 (G-type) were observed with the NASA *Kepler* satellite for approximately ten months with a duty cycle in excess of 90%. Such continuous and long observations are unprecedented for solar-type stars other than the Sun.
Aims. We aimed mainly at extracting estimates of p-mode frequencies – as well as of other individual mode parameters – from the power spectra of the light curves of both stars, thus providing scope for a full seismic characterization.
Methods. The light curves were corrected for instrumental effects in a manner independent of the *Kepler* science pipeline. Estimation of individual mode parameters was based both on the maximization of the likelihood of a model describing the power spectrum and on a classic prewhitening method. Finally, we employed a procedure for selecting frequency lists to be used in stellar modeling.
Results. A total of 30 and 21 modes of degree $l = 0, 1, 2$ – spanning at least eight radial orders – have been identified for KIC 10273246 and KIC 10920273, respectively. Two avoided crossings ($l = 1$ ridge) have been identified for KIC 10273246, whereas one avoided crossing plus another likely one have been identified for KIC 10920273. Good agreement is found between observed and predicted mode amplitudes for the F-type star KIC 10273246, based on a revised scaling relation. Estimates are given of the rotational periods, the parameters describing stellar granulation and the global asteroseismic parameters $\Delta\nu$ and $\nu_{\max}$.

Key words. stars: oscillations – methods: data analysis – asteroseismology – stars: solar-type – stars: individual: KIC 10273246 – stars: individual: KIC 10920273

1. Introduction

The NASA *Kepler* mission was designed to use the transit method to detect Earth-like planets in and near the habitable zones of late-type main-sequence stars (Borucki et al. 2010; Koch et al. 2010). The satellite consists of a 0.95-m aperture telescope with a CCD array and is capable of producing photometric observations with a precision of a few parts-per-million (ppm) during a period of 4–6 years. The high-quality data provided by *Kepler* are also well suited for conducting asteroseismic studies of stars as part of the *Kepler* asteroseismic investigation (KAI; Gilliland et al. 2010a). Photometry of the vast

Table 1. Information given in the *Kepler* input catalog.

Star	2MASS ID	Kp	$T_{\rm eff}$ (K)	Recalibrated[a] $T_{\rm eff}$ (K)	$\log g$ (dex)	[Fe/H] (dex)	R ($R_\odot$)
KIC 10273246	19260576+4721300	10.90	6074 ± 200	6380 ± 76	4.2 ± 0.5	−0.3 ± 0.5	1.506
KIC10920273	19274576+4819454	11.93	5574 ± 200	5880 ± 53	4.1 ± 0.5	−0.4 ± 0.5	1.594

Notes. [a] A recalibration of the KIC photometry has posteriorly been performed by Pinsonneault et al. (in prep.).

majority of these stars is conducted at long cadence (29.4 min), while a revolving selection of up to 512 stars are monitored at short cadence (58.85 s). Short-cadence data allow us to investigate solar-like oscillations in main-sequence stars and subgiants, whose dominant periods are of the order of several minutes (Chaplin et al. 2010; Christensen-Dalsgaard et al. 2010; Metcalfe et al. 2010).

The information contained in solar-like oscillations allows fundamental stellar properties (e.g., mass, radius and age) to be determined (e.g., Stello et al. 2009b; Christensen-Dalsgaard et al. 2010; Kallinger et al. 2010a). The internal stellar structure can be constrained to unprecedented levels, provided that individual oscillation mode parameters are extracted (e.g., Cunha et al. 2007). This is possible in the case of the highest signal-to-noise ratio (*SNR*) observations, leading us to hope that asteroseismology will produce significant improvement on the theories related to stellar structure and evolution, on topics as diverse as energy generation and transport, rotation and stellar cycles (e.g., Karoff et al. 2009; García et al. 2010).

Solar-like oscillations in a few tens of main-sequence stars and subgiants have been previously measured using ground-based high-precision spectroscopy (e.g., Bedding et al. 2010b) and the space-based photometric mission CoRoT (e.g., Michel et al. 2008). During the first seven months of *Kepler* science operations, an asteroseismic survey of solar-type stars made it possible to detect solar-like oscillations in about 500 targets (Chaplin et al. 2011b). This constitutes an increase of one order of magnitude in the number of such stars with confirmed oscillations. This large, homogeneous data sample opens the possibility of conducting ensemble asteroseismology.

Since the start of *Kepler* science operations in 2009 May, a selection of solar-type stars have been continuously monitored at short cadence for more than seven months in order to test and validate the time-series photometry. Such continuous and long observations, also previously achieved by CoRoT (e.g., Benomar et al. 2009b), are unprecedented for solar-type stars other than the Sun. We present herein the analysis of two of these stars[1], namely, KIC 10273246 and KIC 10920273, both displaying relatively low *SNR* in the p-mode peaks. Two other stars, namely, KIC 11395018 and KIC 11234888, are analysed in a companion paper (Mathur et al. 2011). The analysis of these four stars has been conducted in a way so as to group together stars observed for the same length of time.

The two solar-type stars selected for this study are relatively faint (see Table 1) if we bear in mind that the apparent magnitude target range for detection of solar-like oscillations with *Kepler* spans $Kp \approx 6.5$ to $Kp \approx 12.5$ (see Fig. 5 of Chaplin et al. 2011a). The *Kepler* Input Catalog[2] (KIC; e.g., Latham et al. 2005; Batalha et al. 2010; Brown et al. 2011), from which all KASC targets have been selected, classifies KIC 10273246 as an F-type star and KIC 10920273 as a G-type star (Table 1). The atmospheric parameters provided by the KIC – as derived from photometric observations acquired in the Sloan filters – do not have sufficient precision for asteroseismology. Although we can apply scaling relations to convert the KIC parameters of these targets into predicted seismic and non-resonant background parameters, as well as fundamental stellar properties, caution is needed if use is to be made of these derived quantities. Tighter constraints on $T_{\rm eff}$, $\log g$ and [Fe/H] will be obtained from spectra collected for these two targets with the FIES spectrograph at the Nordic Optical Telescope (Creevey et al., in prep.).

The outline of the paper is as follows: we start in Sect. 2 by providing some background information on the properties of solar-like oscillations. In Sect. 3 we give an overview of the different peak-bagging[3] strategies employed and define a recipe for selecting frequency lists. Section 4 is devoted to a thorough analysis of the power spectra of the time series. A summary and conclusions are presented in Sect. 5.

2. Properties of solar-like oscillations

Solar-like oscillations are predominantly global standing acoustic waves. These are p modes (pressure playing the role of the restoring force) and are characterized by being intrinsically damped while simultaneously stochastically excited by near-surface convection (e.g., Christensen-Dalsgaard 2004). Therefore, all stars cool enough to harbor an outer convective envelope – whose locus in the H-R diagram approximately extends from the cool edge of the Cepheid instability strip and includes the red giant branch – may be expected to exhibit solar-like oscillations.

Modes of oscillation are characterized by three quantum numbers: n, l and m. The radial order n characterizes the behavior of the mode in the radial direction. The degree l and the azimuthal order m determine the spherical harmonic describing the properties of the mode as a function of colatitude and longitude. In the case of stellar observations, the associated whole-disk light integration and consequent lack of spatial resolution strongly suppress the signal from all but the modes of the lowest degree (with $l \leq 3$). For a spherically symmetric non-rotating star, mode frequencies depend only on n and l.

The observed modes of oscillation are typically high-order acoustic modes. If interaction with a g mode (gravity playing the role of the restoring force) can be neglected, linear, adiabatic, high-order acoustic modes, in a spherically symmetric star, satisfy an asymptotic relation for the frequencies (Vandakurov 1967; Tassoul 1980):

$$\nu_{nl} \sim \Delta\nu \, (n + l/2 + \varepsilon) - l(l+1)D_0, \tag{1}$$

where the large frequency separation $\Delta\nu$ is the inverse of the sound travel time across the stellar diameter, ε is a phase mostly

---

[1] Within the *Kepler* Asteroseismic Science Consortium (KASC), KIC 10273246 is referred to as "Mulder" and KIC 10920273 as "Scully".

[2] `http://archive.stsci.edu/kepler/kepler_fov/search.php`

[3] The term *peak-bagging* refers to the extraction of individual mode parameters from the power spectrum of a light curve.

sensitive to the properties of the near-surface region, and D_0 is a parameter sensitive to the sound-speed gradient near the core. The regular spacing of the frequency spectrum as conveyed by Eq. (1) is a characteristic feature of solar-like oscillations. We should, however, bear in mind that Eq. (1) is only an approximation. The large frequency separation does in fact depend both on frequency and on mode degree, being defined as

$$\Delta\nu_{nl} = \nu_{nl} - \nu_{n-1\,l} \approx \Delta\nu. \tag{2}$$

It is also conventional to define a so-called small frequency separation, also varying with frequency:

$$\delta\nu_{nl} = \nu_{nl} - \nu_{n-1\,l+2} \approx (4l+6)D_0. \tag{3}$$

The large frequency separation essentially scales with the square root of the mean stellar density (e.g., Brown & Gilliland 1994). Furthermore, the small frequency separation is sensitive to the structure of the core, decreasing with increasing stellar age. These two quantities thus have great diagnostic potential (e.g., Christensen-Dalsgaard 1993; Deheuvels et al. 2010b).

Sharp variations in the stellar interior cause detectable oscillatory signals in the frequencies, also visible in the behavior of $\Delta\nu$ as a function of frequency (e.g., Monteiro et al. 2000; Ballot et al. 2004; Basu et al. 2004; Cunha & Metcalfe 2007; Houdek & Gough 2007). These sharp features are mainly linked to borders of convection zones and to regions of rapid variation in the sound speed due to ionization of a dominant element. Their combined signature is detectable in frequencies of low-degree modes and such an analysis becomes possible in the stellar case once frequency precision is sufficiently high.

Stellar rotation, as well as any other physical process resulting in departure from spherical symmetry, introduces a dependence of the frequencies of non-radial modes on m. When the cyclic rotational frequency of the star, $\nu_{\rm rot}$, is small and in the case of rigid-body rotation dominated by advection, the cyclic frequency of a non-radial mode is given to first order by (Ledoux 1951):

$$\nu_{nlm} = \nu_{nl0} + m\,\nu_{\rm rot}\,, \quad |m| \le l\,. \tag{4}$$

To a second order of approximation, centrifugal effects that disrupt the equilibrium structure of the star are taken into account through an additional frequency perturbation (independent of the sign of m). This perturbation in turn scales as the ratio of the centrifugal to the gravitational forces at the stellar surface, i.e., $\Omega^2 R^3/(GM)$, where Ω denotes the surface angular velocity, R the radius of the star, M its mass, and G the universal gravitational constant. Although negligible in the Sun, these effects may be significant for faster-rotating solar-type stars (e.g., Ballot 2010). Large-scale magnetic fields may also introduce further corrections to the oscillation frequencies.

The frequency dependence of the mode surface amplitudes is determined both by (i) the frequency dependence of the stochastic process of excitation (mode energies result from a balance between the frequency-dependent energy input and the damping rate) and by (ii) the mode properties in the region of vigorous convection (e.g., Houdek et al. 1999; Samadi et al. 2007). The stochastic process of excitation is characterized by a relatively slow variation with frequency, meaning that it excites modes over a large frequency interval to comparable surface amplitudes. At low frequencies modes are evanescent in the region of efficient excitation, leading to small surface amplitudes. At high frequencies – greater than or equal to the acoustic cut-off frequency – modes undergo considerable energy loss through running waves in the atmosphere. Excitation is most efficient for those modes whose periods match the timescale of the near-surface convection. Also, the frequency of maximum amplitude, $\nu_{\rm max}$, is supposed to scale with the acoustic cut-off frequency, $\nu_{\rm ac}$ (Brown et al. 1991; Kjeldsen & Bedding 1995). All this gives rise to a characteristic distribution of power with frequency which is a signature of the presence of solar-like oscillations.

Substantial changes in the properties of solar-like oscillations occur with stellar evolution, particularly following the exhaustion of hydrogen in the core. Most noticeable is the occurrence of avoided crossings due to coupling between p and g modes of like degree (Osaki 1975; Aizenman et al. 1977), which lead to significant departures from the regular frequency spacing described by Eq. (1) in the case of evolved stars. The frequencies of non-radial modes, in particular those of $l = 1$ modes, are shifted by avoided crossings when they couple with g modes trapped in the deep stellar interior. At the avoided crossings these modes have a mixed nature, with both p- and g-mode behavior. Provided they are excited to observable amplitudes (their high mode inertia reduces their surface amplitude), these so-called mixed modes are of great diagnostic potential because they probe the stellar core and are very sensitive to stellar age.

3. On extracting estimates of mode frequencies

3.1. Overview of the different fitting strategies

We computed the power density spectrum (PDS) of the time series based on the implementation of the Lomb-Scargle periodogram (Lomb 1976; Scargle 1982) presented in Press & Rybicki (1989). This algorithm carries out reverse interpolation of the data onto a regular mesh and subsequently employs the fast Fourier transform. The power spectrum was then calibrated so that it satisfies Parseval's theorem, i.e., so that the total power in the positive-frequency side of the spectrum is equal to the variance of the time series (single-sided calibration). The effect of the window function is further taken into account when normalizing the PDS.

A total of eleven individual fitters (A2Z_CR, A2Z_DS, A2Z_RG, AAU, IAS_OB, IAS_PG, IAS_TA, OCT, ORK, QML and SYD) extracted estimates of the p-mode frequencies for at least one of the two stars and subsequently uploaded their results to the Cat Basket[4] data exchange facility. Different fitting strategies have been adopted and sometimes the same fitting strategy has been applied in an independent manner. All the fitting strategies adopted are, however, based on Fourier methods, the main idea behind them being either the maximization of the likelihood of a multi-parameter model describing the data or a classic prewhitening method.

A frequency-domain representation of the data aims at modeling the limit PDS of the time series. Such a model typically includes a sum of symmetric Lorentzian profiles meant to describe the individual p modes, together with a flat term and a number of additional terms describing both instrumental and stellar background noise (Anderson et al. 1990):

$$P(\nu) = \sum_{n,l,m} \frac{H_{nlm}}{1 + [2(\nu - \nu_{nlm})/\Gamma_{nlm}]^2} + B(\nu)\,, \tag{5}$$

where H is the mode height, Γ is the mode linewidth (related to the mode lifetime or amplitude e-folding time, $\tau_{\rm mode}$, through $\pi\Gamma = 1/\tau_{\rm mode}$), and $B(\nu)$ represents the background signal. The

---

[4] `http://bison.ph.bham.ac.uk/kcatbasket/`

components arising from the decay of active regions, granulation and faculae are commonly represented using a Harvey-like model (Harvey 1985; Aigrain et al. 2004):

$$B(\nu) = \sum_k \frac{4\,\sigma_k^2 \tau_k}{1 + (2\pi\nu\,\tau_k)^{s_k}} + W, \tag{6}$$

where $\{\sigma_k\}$ are the amplitudes, $\{\tau_k\}$ are the characteristic timescales, $\{s_k\}$ are the slopes of the individual power laws in the denominator, and W is a constant representing white noise (mainly due to photon shot noise). Equations (5) and (6) are representative of the models employed and individual fitters were further allowed to customize their own models. Hence we cannot talk of a reference model, as was done in Appourchaux et al. (2008).

Most fitters opted for performing a global fit (e.g., Appourchaux et al. 2008) – whereby the whole set of free parameters needed to describe the observed spectrum was optimized simultaneously – while there was still room for pseudo-global (or local) fitting (e.g., Jiménez-Reyes et al. 2008), an approach traditionally adopted for Sun-as-a-star data, whereby narrow frequency windows are considered at a time.

Statistical inference from the data was either frequentist or Bayesian in nature. The former approach relies on the straightforward application of a maximum likelihood estimator (MLE) taking into account the correct statistics of the spectrum (e.g., Toutain & Appourchaux 1994; Appourchaux et al. 2008) or, in the special case of Gaussian statistics, a least squares estimator (LSE). To be specific: A2Z_CR applied a global LSE to a smoothed version of the spectrum; A2Z_DS applied a local MLE; IAS_TA, OCT and QML applied a global MLE. The latter approach makes it possible to incorporate relevant prior information through Bayes' theorem. A regularized version of a MLE, known as maximum a posteriori (MAP; e.g., Gaulme et al. 2009), is a Bayesian point estimation method and was applied (globally) by A2Z_RG and IAS_PG. AAU and IAS_OB also performed global fits but instead used Markov chain Monte Carlo (MCMC) techniques to map the posterior probability distributions of the frequency parameters (e.g., Benomar et al. 2009a; Gruberbauer et al. 2009; Handberg & Campante 2011). With the exception of AAU and IAS_OB, who estimated the frequency uncertainties based on the posterior distributions of these same parameters, all the remaining fitters provided formal error bars derived from the inverse Hessian matrix.

ORK and SYD adopted a different approach, which did not involve fitting a model to the power density spectrum. ORK applied a procedure known as iterative sine-wave fitting (ISWF; e.g., Bedding et al. 2007; Bonanno et al. 2008; White et al. 2010): it iteratively removes sinusoidal components from the data, which are identified as the maxima of the Fourier spectrum of the residuals. Since the number of oscillation modes present in the data is unknown a priori, the algorithm requires a stopping rule that associates some degree of confidence to the amplitude of each extracted sinusoidal component. For the analysis by SYD, the power spectrum was smoothed by convolving with a Gaussian with full width at half maximum of 1.4 μHz (comparable to the intrinsic linewidth of the modes) and the frequencies of the highest peaks were measured. Mode identification (assigning l values) was done using the échelle diagram (Grec et al. 1983) both by ORK and SYD. Finally, frequency uncertainties are estimated either analytically (ORK) or by performing Monte Carlo simulations with artificial data (SYD).

3.2. Procedure for selecting frequency lists

A procedure for selecting relevant frequency lists to be used in stellar modeling has been described in Metcalfe et al. (2010). However, we have opted for revising that procedure. This has been motivated, at first, by the fact that different fitting strategies provided frequency uncertainties that differed greatly. For instance, uncertainties that had been underestimated would undesirably upweight the respective individual frequency sets. Consequently, a more robust method of frequency selection was needed. Other refinements were also made and we give below a detailed description of the new, revised procedure.

We aim at selecting, for a given star and for a given mode degree identification, two frequency sets – a *minimal frequency set* and a *maximal frequency set* – that will provide initial constraints for the modeling and allow for refined model-fitting, respectively. As before, we would like to determine individual sets, as opposed to averaged sets, meaning that these sets are fully reproducible.

We start by constructing both a *minimal list* and a *maximal list* of modes. Take N as being the total number of individual fitters providing peak-bagging results for a given star and assume for now that $N > 2$. For each $\{n, l\}$ pair, we apply Peirce's criterion (see Appendix A for its implementation; Peirce 1852; Gould 1855) for the rejection of outliers and assess how many frequency estimates are retained. Inclusion or not of the mode in the *minimal list* then results from a vote including all (N) fitters: If the number of frequencies retained is greater than[5] $\lfloor N/2 \rfloor$ then the mode is added to the *minimal list*. Inclusion or not of the mode in the *maximal list* is decided as follows: If the number of frequencies retained is at least 2 then the mode is added to the *maximal list*. The *minimal list* is thus a subset of the *maximal list*. For $N = 2$ the *minimal* and *maximal lists* are degenerate and will coincide.

In the final stage of the procedure, we compute for each of the N individual frequency sets the normalized root-mean-square deviation (nrmsd) with respect to the frequencies averaged over all contributing fitters, $\{\bar{\nu}_{nl}\}$, belonging to the *minimal list* of modes:

$$\mathrm{nrmsd} = \sqrt{\frac{\sum_{n,l} (\nu_{nl} - \bar{\nu}_{nl})^2/\sigma_{nl}^2}{N_1}}, \tag{7}$$

where σ_{nl} is the uncertainty in ν_{nl}, and N_1 is the number of modes in a particular individual set that actually belong to the *minimal list*. The *best fit* is defined as being the individual set with the smallest normalized rms deviation. Note that by *best fit* we mean here the most representative fit among the N available sets and not necessarily the one closest to the truth. The *minimal* and *maximal frequency sets* are finally given by those modes provided by the *best fit* that belong to the *minimal* and *maximal lists*, respectively. The homogeneous character of the revised procedure is reassured by generating the *minimal* and *maximal frequency sets* from the same individual set. The corresponding frequency uncertainties are simply those associated with the *best fit*. When $N = 2$ a *single frequency set* is defined, the same happening for $N = 1$ in which case it coincides with the only available individual set.

Although having been revised, this procedure is still subject to future improvement. The main reason for this is the fact that we assume the l values to be correctly assigned to modes by all the fitters. A way of overcoming this would be to implement a

---

[5] $\lfloor x \rfloor$ returns the closest integer less than or equal to x.

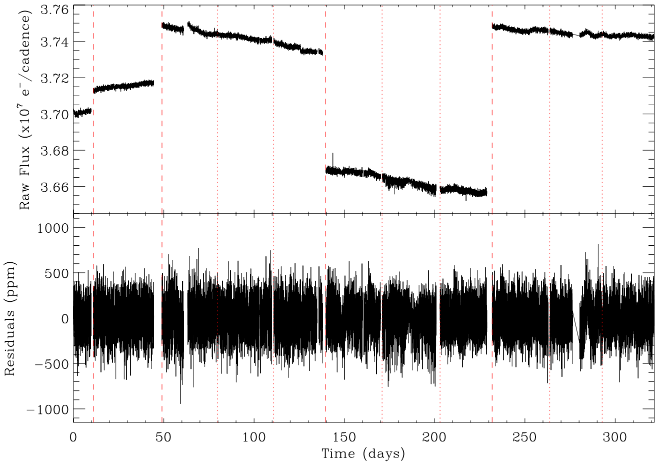

Fig. 1. Raw-flux time series corrected only for outliers (*top panel*) and corrected relative time series (*bottom panel*) for the case of KIC 10273246. Vertical dashed lines mark the beginning of each Quarter, whereas vertical dotted lines separate the segments within a Quarter.

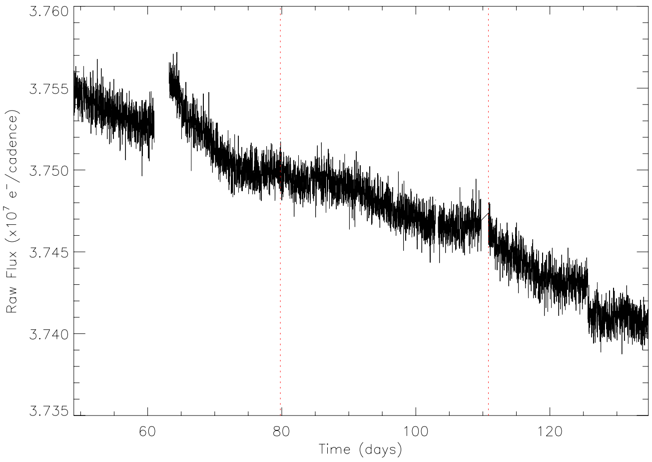

Fig. 2. Raw-flux time series (corrected only for outliers) of Quarter 2 for the case of KIC 10273246. Vertical dotted lines separate the three segments of Q2. The induced thermal drift after a safe-mode event is visible between the 60th and 70th days.

clustering algorithm that groups frequencies and posteriorly tags them with a mode degree based on a vote. Another issue concerns the possibility that the *best fit* misses some modes from the *minimal* and *maximal lists*. A solution for this would be to ask the fitter providing the *best fit* to reanalyse the power spectrum. One last drawback of this procedure is the possibility that the *minimal* and *maximal frequency sets* may contain some outliers, i.e., frequency estimates that have been ruled out according to Peirce's criterion.

4. Data analysis

4.1. Time series preparation

The stars were observed from 2009 May 2 to 2010 March 19, i.e., from Quarter 0 (Q0) to Quarter 4 (Q4). The duty cycle over the course of the approximately 10 months of observations was above 90%. Available time series suffered from several instrumental perturbations, and we have thus decided to develop our own corrections (García et al. 2011), independently from the presearch data conditioning module of the *Kepler* science pipeline (Jenkins et al. 2010), which generates corrected light curves for transiting-planet search.

The raw-flux time series were corrected for three types of effects: outliers, jumps and drifts. Data points considered to be outliers exhibit point-to-point deviations greater than $3\sigma_{\rm diff}$, where $\sigma_{\rm diff}$ is the standard deviation of the first differences of the time series. This correction removed approximately 1% of the data points. Jumps are sudden changes in the mean value of the time series caused by, e.g., attitude adjustments or a drop in pixel sensitivity (see Fig. 1). They were identified as causing spurious differences in the mean power of contiguous bins spanning one day. In cases where we know the photometric apertures to have changed, we by default check for jumps (only implemented in segments Q2.1 and Q4.1). Each jump has been manually validated. Finally, drifts are small, low-frequency perturbations due to temperature changes (e.g., after a long safe-mode event) and lasting for a few days (see Fig. 2). The corrections are based on the software developed to deal with high-voltage perturbations in the GOLF/SoHO instrument (García et al. 2005). We fit a 2nd- or 3rd-order polynomial function to the section of the time series where a thermal drift has been observed after comparing several light curves of the same Quarter. The fitted polynomial is then subtracted and another polynomial function of 1st- or 2nd-order – used as a reference – is added, which has been computed based on the observations done before and after the affected section. If the correction has to be applied to a border of the time series, then only one side of the light curve is processed.

Once the aforementioned corrections have been applied, we merge the data of the different Quarters into a single time series, after equalizing the average counting-rate level between the Quarters (or sometimes even within a Quarter when some instrumental parameters have been changed). In order to do so, and to allow conversion into units of ppm, we use a series of 6th-order polynomial fits, one for each segment. Finally, we normalize the standard deviation of the data obtained during Q3 to the average of the other Quarters, since Q3 is considerably noisier for the two stars. This normalization proved to be a good compromise between using the noisy Q3 data and not using them at all. Given the insufficient technical information available, it is not possible to know whether or not there is a variation in the gain of the CCD module during Q3. If such a gain variation is indeed present, the mode amplitudes would be affected and the adopted normalization will then correct these amplitudes toward something closer to their real value. If, on the other hand, no gain variation is present, then the adopted correction will effectively reduce the mode amplitudes. Having reduced the standard deviation of the data in Q3 by 34% for KIC 10273246 and 49% for KIC 10920273, and given that Q3 represents 3/7 of the total length of the time series used for peak-bagging (i.e., from Q0 to Q3; see Sect. 4.5), then mode amplitudes would be reduced by about 14% and 21%, respectively. However, we believe this latter scenario to be less likely and hence the quoted values of 14% and 21% can only be regarded as upper limits to mode amplitude reduction, which in reality may be much smaller.

4.2. Rotational modulation

To investigate the stellar rotational period ($P_{\rm rot}$) of these stars we seek high-*SNR* peaks in the low-frequency end of the PDS. However, the procedure for merging the different data sets described in the previous paragraph filters out the power density below 1 μHz. Therefore, starting with the corrected data, we have generated new merged time series in which a triangular

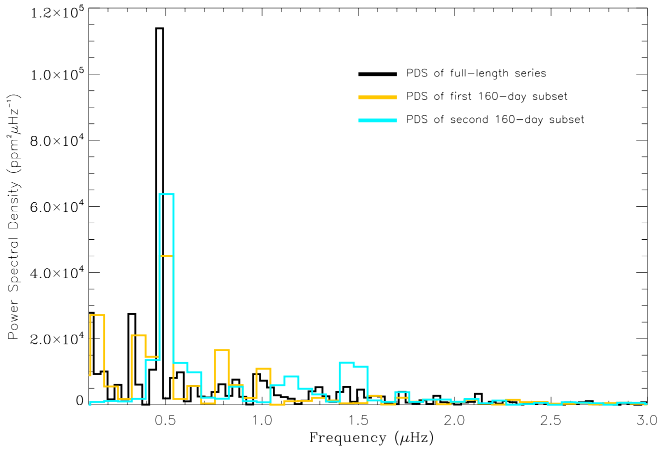

Fig. 3. Low-frequency end – between 0.1 and 3 μHz – of the power density spectrum of KIC 10273246.

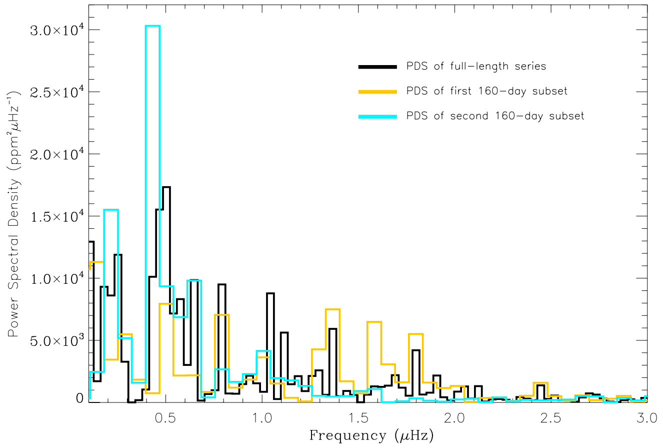

Fig. 4. Similar to Fig. 3 but for the case of KIC 10920273.

smoothing – over a period selected from the range of 12–20 days – has been used to normalize the light curves instead of the 6th-order polynomial fit (for details, see García et al. 2011). Finally, we computed the PDS of the full-length time series and also of two subsets of 160 days each. The low-frequency ends of the PDS are shown in Figs. 3 and 4 for KIC 10273246 and KIC 10920273, respectively. A different pattern of peaks appears for each star. In the case of KIC 10273246 (Fig. 3), the highest peak is seen at about 0.50 μHz ($P_{\rm rot} \approx 23$ days) in the three spectra considered, without any signature of differential rotation. This turns out to be a reliable signature of rotational modulation, since comparison with the power spectra of other stars observed with the same CCD module ruled out the possibility of an instrumental artifact. On the other hand, KIC 10920273 (Fig. 4) exhibits a high peak at about 0.43 μHz, though mostly during the second subset of 160 days. Indeed, this peak is not very significant, and during the first subset it is at the same level as that of the adjacent peaks. The PDS of the full-length time series also reveals itself as being rather noisy, and it is difficult to disentangle the stellar rotational period from it. Therefore, while a cyclic rotational frequency of 0.43 μHz ($P_{\rm rot} \approx 27$ days) seems plausible, we cannot exclude the possibility that this peak is associated with the roll schedule of the telescope. One of several alternative explanations for the low-*SNR* peaks would be that this star was observed during a low magnetic-activity period, with a small number of spots on its surface. A deeper study based on a longer data set is necessary to confirm the rotational rate of KIC 10920273.

Table 2. Background model parameters describing non-resonant features.

Star	$\sigma_{\rm gran}$ (ppm)	$\tau_{\rm gran}$ (s)	$s_{\rm gran}{}^{a}$	W (ppm$^2\,\mu$Hz^{-1})
KIC 10273246	69.9 ± 0.8	390 ± 12	3	4.15 ± 0.02
KIC 10920273	80.1 ± 0.4	351 ± 4	3	11.58 ± 0.02

Notes. [a] The slope of both Harvey-like terms has been fixed.

4.3. Power spectral density of the background

The power density spectra – based on the first seven months of observations, i.e., from Q0 to Q3 – of KIC 10273246 and KIC 10920273 are displayed in Fig. 5. The background signal rises toward the low-frequency end of the spectra with contributions from granulation and activity. At the high-frequency end, the spectra are dominated by photon shot noise. Also visible at the high-frequency end are a number of peaks corresponding to harmonics of the inverse of the long-cadence period, an artifact appearing in power spectra of short-cadence time series (Gilliland et al. 2010b) but having negligible influence on the current study. In between these two frequency regimes there is a conspicuous cluster of power due to the presence of p modes, with the hotter and brighter target KIC 10273246 displaying the higher *SNR*.

We fitted a model similar to the one described in Eq. (6) to a heavily smoothed version of both spectra. This model included an additional Gaussian function aimed at describing the p-mode power-excess hump (e.g., Kallinger et al. 2010b). The fitting window was from 100 μHz up to the Nyquist frequency, hence we did not consider a term accounting for the decay of active regions, whose typical timescale is considerably longer. We found no evidence for a facular component based on a simple visual inspection of the spectra, thus having not included such a component in the background model. Faculae had previously been reported on a couple of *Kepler* solar-type targets by Chaplin et al. (2010). A component carrying the signature of stellar granulation is, however, clearly displayed by both stars. Figure 5 displays the fitted models, while values of the fitted parameters are given in Table 2. Note that the slope of both granulation components has been fixed at the same value, i.e., $s_{\rm gran} = 3$, which is closer to solar (e.g., Michel et al. 2009) than the value of 2 originally proposed by Harvey (1985). Although we lack a physical reason for fixing this slope, the intention is to facilitate the comparison between the values of $\tau_{\rm gran}$.

The high-frequency noise power spectral density (W) is approximately 14% and 16% higher than predictions in the cases of KIC 10273246 and KIC 10920273, respectively. These predictions have been computed according to the empirical minimal term model for the noise presented in Gilliland et al. (2010b), which takes into account the *Kepler*-band magnitude of the star and the performance of the instrument. Noise levels are thus close to being Poisson-limited. A likely source of this extra noise is the larger scatter in Q3.

4.4. The global asteroseismic parameters $\Delta\nu$, $\nu_{\rm max}$ and $\delta\nu_{n0}$

In the past few years, a number of automated pipelines have been developed to measure global asteroseismic parameters of

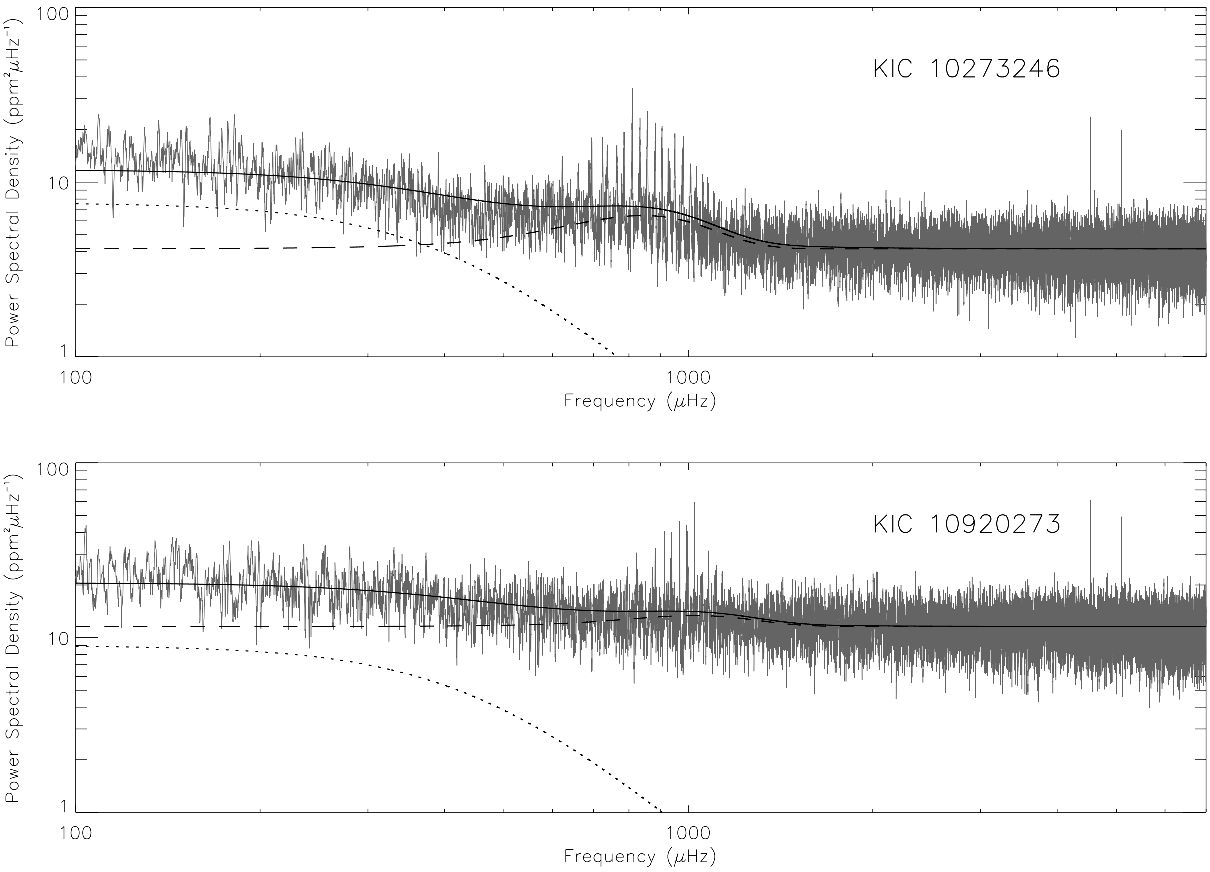

Fig. 5. Power density spectra – smoothed over 1 μHz in order to enhance p-mode visibility – of KIC 10273246 (*top panel*) and KIC 10920273 (*bottom panel*), plotted on a log-log scale. The solid black lines represent the fits described in the text. The remaining lines represent different components of the fitting model: the power envelope due to oscillations added to the offset from white noise (dashed), and granulation (dotted).

Table 3. Estimates of the global asteroseismic parameters $\Delta\nu$, $\nu_{\max}$ and $\delta\nu_{n0}$.

Star	$\langle\Delta\nu\rangle$ (μHz)	Range (μHz)	$\nu_{\max}$ (μHz)	$\langle\delta\nu_{n0}\rangle$ (μHz)
KIC 10273246	48.2 ± 0.5	[537, 1140]	839 ± 51	5.6 ± 1.2
KIC 10920273	57.3 ± 0.8	[757, 1290]	1024 ± 64	6.0 ± 1.5

solar-like oscillators (Huber et al. 2009; Mosser & Appourchaux 2009; Roxburgh 2009; Campante et al. 2010; Hekker et al. 2010; Karoff et al. 2010; Mathur et al. 2010b). Most of them have already been successfully tested on CoRoT data (e.g., Mathur et al. 2010a). The automated nature of these pipelines is required if we are to efficiently exploit the plenitude of data made available by *Kepler* on these targets. A thorough comparison of complementary analysis methods used to extract global asteroseismic parameters of main-sequence and subgiant solar-like oscillators is presented in Verner et al. (2011).

The results of the different pipelines on global parameter extraction have also been uploaded to the Cat Basket. For a given global parameter, some groups submitted results using more than one method or on more than one data release. In Table 3 we give a representative set of estimates of $\Delta\nu$ and $\nu_{\max}$ for the two stars in our study. These estimates were supplied by one of the pipelines, namely, the one described in Mosser & Appourchaux (2009), and are based on the analysis of the full-length time series. The large separation is a function of frequency. Consequently, the extent of variation of its mean value will depend upon the variation in frequency range adopted for its computation. However, as long as this frequency range includes $\nu_{\max}$, the impact of small differences in the range can be neglected. For the sake of completeness, we give the adopted frequency ranges in Table 3. An observed relation between $\Delta\nu$ and $\nu_{\max}$ for solar-like oscillations in main-sequence stars is presented in Stello et al. (2009a):

$$\Delta\nu \propto \nu_{\max}^{0.77}. \quad (8)$$

The values quoted in Table 3 for these two global parameters satisfy this relation, as can be seen in Fig. 6. Also, $\tau_{\rm gran}$ is seen to scale inversely with $\nu_{\max}$, as predicted by Kjeldsen & Bedding (2011).

The same pipeline has provided estimates of $\delta\nu_{n0}$ based on the analysis of seven months of data. These are also given in Table 3.

4.5. Mode frequencies

Estimates of mode frequencies were obtained by several individual fitters for both stars, based on the first seven months of observations (from Q0 to Q3). The procedure described in Sect. 3.2 was then used to select *minimal* and *maximal frequency sets*. An ad hoc step was, however, implemented at this stage, that aimed at removing doubtful modes from these sets based on *SNR* considerations. This quality control led to the removal of a few modes at the low- and high-frequency ends of the sets.

Another issue relates to the presence of mixed modes in the power spectrum. As we will see below, the *best fit* relies, for both

Table 4. Summary of the *best fits*.

Star	Method	Height (H)	Linewidth (Γ)	Splitting ($\nu_{\rm rot}$)	Inclination[a] (i)
KIC 10273246	Global MAP	One free parameter ($H_{l=0}$) per order No prior $H_{l=1}/H_{l=0}$ = 1.5 (fixed) $H_{l=2}/H_{l=0}$ = 0.5 (fixed)	One free parameter per order No prior	Free No prior	Free No prior
KIC 10920273	Global MAP	One free parameter ($H_{l=0}$) per order No prior $H_{l=1}/H_{l=0}$ = 1.5 (fixed) $H_{l=2}/H_{l=0}$ = 0.5 (fixed)	One free parameter per order Gaussian prior	Fixed at 0 μHz	Fixed at 0°

Notes. [a] Introduced in Eq. (15).

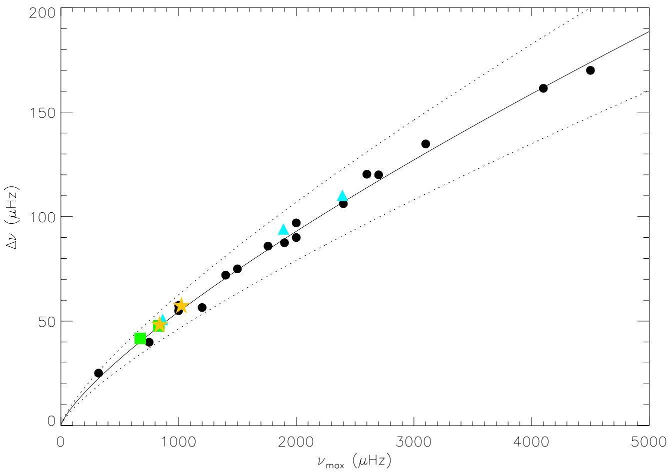

Fig. 6. Observed relation between $\Delta\nu$ and $\nu_{\rm max}$. Here we reproduce Fig. 2 of Stello et al. (2009a) in linear scale, where only stars whose $\nu_{\rm max}$ is greater than the Nyquist frequency for long-cadence sampling are displayed. The solid line is the power-law fit in their Eq. (1) with the corresponding ±15% deviations shown as dotted lines. We added to the plot the two stars being considered in this study (five-pointed stars), the two stars (squares) of Mathur et al. (2011), and the three bright G-type stars (triangles) of Chaplin et al. (2010).

stars, on an algorithm based on a frequency-domain representation of the data (cf. Eq. (5)). Moreover, the deterministic models that have been used only contained modes of degree up to $l = 2$, with three modes per radial order, one of each degree. The presence of an extra mixed mode in the vicinity of a mode with low *SNR* therefore greatly complicates the fit due to the inadequacy of the model. As a result, we opted for prewhitening the longer-lived mixed modes and give their frequencies a posteriori, while discarding any neighboring power structure with low *SNR* fitted by the MLE-based algorithm.

Eleven individual fitters (A2Z_CR, A2Z_DS, A2Z_RG, AAU, IAS_OB, IAS_PG, IAS_TA, OCT, ORK, QML and SYD) have provided results for KIC 10273246. A summary of the anonymous *best fit* is given in Table 4. The fitter has also imposed priors on the parameters used to describe the background signal, which were based on the output of a previous fit to the background alone. Table 5 and Fig. 7 combine the *minimal* and *maximal frequency sets* (recall that the former is a subset of the latter). We have identified a total of 30 modes of degree $l = 0, 1, 2$ that span a frequency range of width $\approx 10\,\Delta\nu$. The mode at 1122.70 μHz has only been reported by two fitters, who have identified it as being a radial mode despite its alignment with the $l = 2$ ridge. Given its very low power and the known convergence issues experienced by MLE-based methods under such low *SNR* conditions, we have decided to change its tagging a posteriori from $l = 0$ to $l = 2$. This mode should thus be considered with caution.

Table 5. The *minimal* and *maximal frequency sets* of observed oscillation frequencies for KIC 10273246.

l	Frequency (μHz)	Uncertainty (μHz)
0	737.90	0.30
0	785.40	0.20
0	833.90	0.20
0	883.50	0.20
0	932.70	0.50
0	981.10	0.30
0	1030.70	0.40
0	1079.30	0.20
1	622.80	0.20
1	661.90	0.50
1	695.75[b]	0.27
1	724.70	0.20
1	764.30	0.30
1	809.80	0.20
1	857.30	0.20
1	905.60	0.30
1	950.00	0.30
1	1008.60	0.40
1	1056.30	0.20
1	1103.30	0.40
2	688.50	0.70
2	734.80	0.60
2	779.50	0.40
2	830.30	0.40
2	880.60	0.50
2	927.50	0.40
2	977.60	0.40
2	1025.30	1.30
2	1073.70	0.20
2	1122.70[a,c]	0.40

Notes. [a] Mode belonging exclusively to the *maximal frequency set*. [b] $l = 1$ mixed mode introduced a posteriori. [c] Tagging changed a posteriori from $l = 0$ to $l = 2$.

The problem of ridge identification (i.e., the tagging of modes by degree l) in F stars dates back to when CoRoT observations of HD 49933 were first analysed by Appourchaux et al. (2008). In the present case such an identification can be simply done by visual inspection of the échelle diagram in Fig. 7. Nonetheless, two of the fitters (IAS_OB and IAS_TA) provided

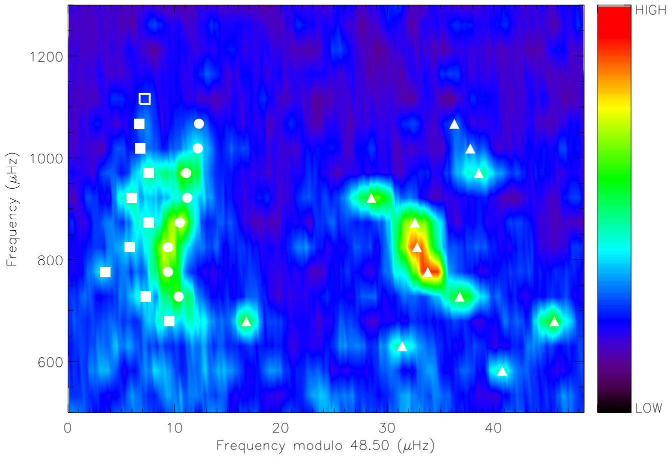

Fig. 7. Échelle diagram of the power density spectrum of KIC 10273246 (the colorbar decodes the power density level). The *minimal* (filled symbols) and *maximal* (filled and open symbols) *frequency sets* are displayed. Symbol shapes indicate mode degree: $l = 0$ (circles), $l = 1$ (triangles) and $l = 2$ (squares).

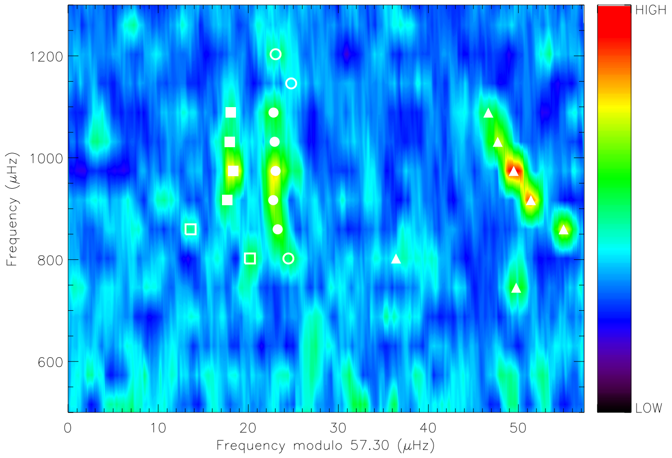

Fig. 8. Similar to Fig. 7 but for the case of KIC 10920273.

Table 6. The *minimal* and *maximal frequency sets* of observed oscillation frequencies for KIC 10920273.

l	Frequency (μHz)	Uncertainty (μHz)
0	826.66[a]	0.25
0	882.77	0.20
0	939.58	0.16
0	997.14	0.18
0	1054.33	0.30
0	1111.51	0.25
0	1170.77[a]	0.33
0	1226.34[a]	0.33
1	794.65[b]	0.32
1	838.61[b]	0.25
1	914.52	0.16
1	968.19	0.13
1	1023.58	0.14
1	1079.10	0.31
1	1135.36[d]	0.31
2	822.39[a]	0.28
2	873.10[a,c]	0.32
2	934.49	0.22
2	992.44	0.13
2	1049.36	0.39
2	1106.76	0.34

Notes. [a] Mode belonging exclusively to the *maximal frequency set*. [b] $l = 1$ mixed mode introduced a posteriori. [c] Possible $l = 2$ mixed mode introduced a posteriori. [d] Mode very close to the second harmonic of the inverse of the long-cadence period.

results for the two complementary identification scenarios. From the results provided by IAS_TA we are able to compute the likelihood ratio (e.g., Appourchaux et al. 1998) in favor of our preferred scenario, whereas computation of its Bayesian counterpart, the more conservative Bayes' factor (e.g., Liddle 2009; Handberg & Campante 2011), is possible based on the results provided by IAS_OB. Both approaches returned conclusive values in support of the adopted scenario.

Ten individual fitters (A2Z_CR, A2Z_DS, A2Z_RG, IAS_OB, IAS_PG, IAS_TA, OCT, ORK, QML and SYD) have provided results for KIC 10920273. A summary of the anonymous *best fit* is given in Table 4. In addition to the information provided in that table, it should also be mentioned that a Gaussian prior has been imposed on $\delta\nu_{n0}$. Table 6 and Fig. 8 combine the *minimal* and *maximal frequency sets*. We have identified a total of 21 modes – considerably less than for KIC 10273246 – of degree $l = 0, 1, 2$ that span a frequency range of width ≈8 $\Delta\nu$. The $l = 1$ mode at 1135.36 μHz is very close to the second harmonic ($2\times566.391\,\mu$Hz) of the long-cadence sampling. Although this anomaly is known to be more prominent for intermediate harmonics, we nonetheless follow the recommendation of Gilliland et al. (2010b) to flag this mode as suspect.

The quasi-regularity of the small ($\delta\nu_{n0}$) and large frequency separations ($\Delta\nu_{n0}$ and $\Delta\nu_{n2}$) is evident from Figs. 7 and 8. Notice that if these stars were to strictly obey the asymptotic relation in Eq. (1), they would then exhibit vertical ridges in the échelle diagram provided use of the correct $\Delta\nu$. The small separation $\delta\nu_{n0}$ is, however, more clearly distinguished in the case of KIC 10920273, which might be an indication of smaller mode linewidths in this cooler star (see Sect. 4.6 for a discussion on mode linewidths).

A striking feature in both échelle diagrams is the jagged appearance of the $l = 1$ ridge, a trademark of the presence of avoided crossings and an indicator of the evolved nature of these stars. These same features have also been seen in the cases of ground-based observations of η Boo (Kjeldsen et al. 2003), β Hyi (Bedding et al. 2007) and possibly Procyon (Bedding et al. 2010b), as well as in the cases of the CoRoT target HD 49385 (Deheuvels et al. 2010a), and KASC survey targets KIC 11026764 (Metcalfe et al. 2010), KIC 11395018 and KIC 11234888 (Mathur et al. 2011). Figure 9 displays a so-called p-g diagram as introduced by Bedding (2011), where the frequencies of the avoided crossings (i.e., the frequencies of the pure g modes in the core cavity) for a number of stars are plotted against the large separation of the p modes. Much of the diagnostic potential of mixed modes can be captured in this way, since their overall pattern is determined by the mode bumping at each avoided crossing, which in turn is determined by the g modes trapped in the core. This diagram could prove to be an instructive way to display results of many stars and to allow for a first comparison with theoretical models. We also report here the possible presence of a $l = 2$ mixed mode in the power spectrum of KIC 10920273 (at 873.10 μHz) that should, however, be confirmed by stellar models.

Table 7. Linewidths, heights, and bolometric amplitudes of radial modes for KIC 10273246 returned by the *best fit* (these are not provided for the radial mode of highest frequency since convergence was not properly achieved).

Frequency (μHz)	Linewidth (μHz)	Uncertainty (μHz)	Height (ppm^2 μHz^{-1})	Uncertainty (ppm^2 μHz^{-1})	Amplitude (ppm)	Uncertainty (ppm)
737.90	1.6	+0.5/−0.4	10.4	+3.3/−2.5	5.48	±0.81
785.40	1.7	+0.4/−0.3	11.4	+3.0/−2.4	5.90	±0.80
833.90	1.5	+0.3/−0.3	19.2	+4.7/−3.8	7.17	±0.75
883.50	1.8	+0.4/−0.3	15.9	+3.6/−2.9	7.14	±0.75
932.70	2.3	+0.5/−0.4	10.6	+2.4/−2.0	6.60	±0.77
981.10	1.9	+0.5/−0.4	12.9	+3.3/−2.6	6.61	±0.73
1030.70	2.6	+0.8/−0.6	5.5	+1.5/−1.2	5.09	±0.83
1079.30	…	…	…	…	…	…

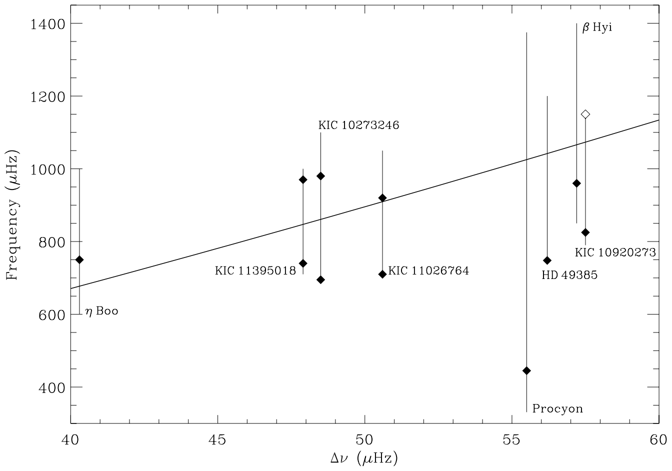

Fig. 9. p-g diagram showing the frequencies of avoided crossings (diamonds) plotted against the large separation for a number of stars. The vertical lines show the range over which the $l = 1$ ridge is clearly seen. The inclined line is the observed relation between $\Delta\nu$ and $\nu_{\max}$ of Stello et al. (2009a). For KIC 10273246 there are two clear avoided crossings, whereas for KIC 10920273 there is only one clear crossing plus another likely one (open symbol).

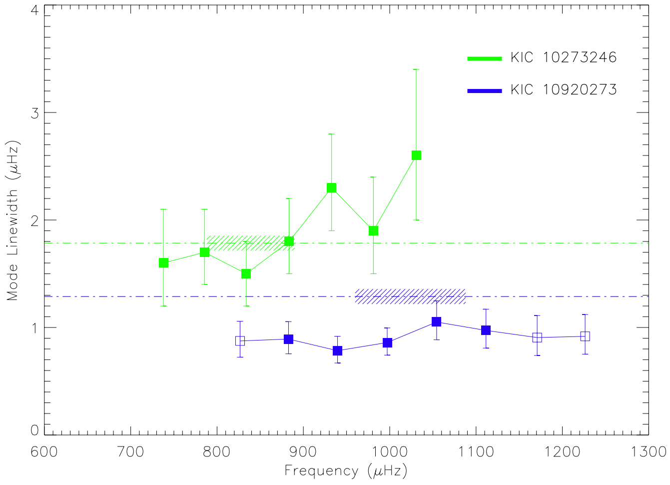

Fig. 10. Linewidths of the radial modes returned for KIC 10273246 and KIC 10920273 by the respective *best fit*. Modes represented by open symbols belong exclusively to the *maximal frequency set*. Dot-dashed lines mark the predicted mean linewidths of the most prominent modes using Eq. (9). The horizontal dimension of the line-filled areas represents the uncertainty in $\nu_{\max}$.

Detection of $l = 3$ modes with photometric observations is made very difficult due to geometric cancellation effects. Solar-like oscillations with $l = 3$ from *Kepler* photometry have nonetheless been reported for a set of low-luminosity red giants by Bedding et al. (2010a). Deheuvels et al. (2010a) have also reported the presence of $l = 3$ modes for the CoRoT target HD 49385. We should bear in mind that, except for ORK and SYD, all the remaining fitters used deterministic models in their frequency-domain representations of the data that only contained modes of degree up to $l = 2$, meaning that a statistical assessment of the presence or not of $l = 3$ modes could not be done. ORK and SYD, which were the only fitters that did not make any prior assumptions about the degree of the modes, have not reported the detection of modes that could be interpreted as $l = 3$ modes.

4.6. A word on mode linewidths, heights, and amplitudes

A thorough discussion of the mode linewidths, heights, and amplitudes goes beyond the scope of this work. However, there are some aspects we would like to mention here.

The intrinsic frequency resolution of the spectra (≈0.05 μHz) makes it possible to resolve the modes. This condition is obeyed provided the observation length $T \gg 2\tau_{\text{mode}}$ (Chaplin et al. 2003). Figure 10 displays, for each star, the linewidths of the radial modes returned by the respective *best fit* (see also Tables 7 and 8). The radial modes considered are those belonging to the *maximal frequency set*. Notice the near-constancy with frequency of the mode linewidths in the case of KIC 10920273, whereas for KIC 10273246 the linewidths increase steadily, although with considerably larger error bars (note that both sets of error bars were derived from the inverse Hessian matrix). Using pulsation computations of a grid of stellar models and the first asteroseismic results on mode lifetimes of solar-like stars, Chaplin et al. (2009) suggested a simple scaling relation between the mean mode linewidth of the most prominent p modes and T_{eff}:

$$\langle\Gamma\rangle \propto T_{\text{eff}}^4. \tag{9}$$

Figure 10 also displays the resulting predictions of mean linewidths of the most prominent modes (we have considered $\langle\Gamma\rangle_\odot \approx 1.2\,\mu$Hz and $T_{\text{eff}\odot} = 5777$ K, and taken the recalibrated KIC temperatures). The agreement with the observed values is fairly good in the case of KIC 10273246. On the other hand, the predicted value obtained for KIC 10920273 using Eq. (9) overestimates the observed linewidths. Assuming validity of this equation, this might be the result of the combination of two factors,

Table 8. Linewidths, heights, and bolometric amplitudes of radial modes for KIC 10920273 returned by the *best fit*.

Frequency (μHz)	Linewidth (μHz)	Uncertainty (μHz)	Height (ppm^2 μHz^{-1})	Uncertainty (ppm^2 μHz^{-1})	Amplitude (ppm)	Uncertainty (ppm)
826.66	0.88	+0.18/−0.15	9.10	+4.27/−2.91	3.75	±1.32
882.77	0.89	+0.16/−0.14	18.56	+5.30/−4.12	5.18	±1.08
939.58	0.78	+0.13/−0.11	26.28	+6.91/−5.47	5.74	±1.02
997.14	0.86	+0.14/−0.12	42.21	+9.71/−7.90	7.56	±0.99
1054.33	1.05	+0.20/−0.16	15.43	+4.57/−3.53	5.13	±1.11
1111.51	0.97	+0.20/−0.16	12.83	+4.36/−3.25	4.54	±1.16
1170.77	0.91	+0.20/−0.17	3.77	+3.26/−1.75	2.97	±1.88
1226.34	0.92	+0.20/−0.17	5.99	+3.34/−2.14	3.26	±1.46

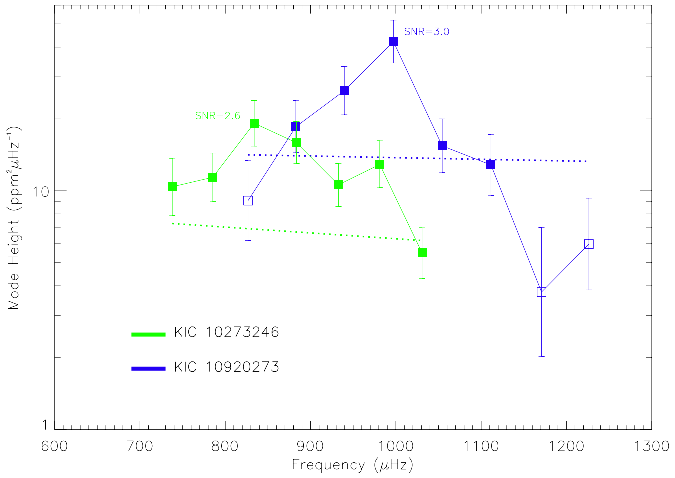

Fig. 11. Heights of the radial modes returned for KIC 10273246 and KIC 10920273 by the respective *best fit*, plotted on a log-linear scale. Modes represented by open symbols belong exclusively to the *maximal frequency set*. Also indicated is the *SNR* of the strongest modes as well as the background fits of Fig. 5 (dotted lines).

namely, an overestimation of $T_{\rm eff}$ and an overestimation of the fitted background that leads to underestimated fitted linewidths. Nonetheless, the F-type star KIC 10273246 exhibits the larger mode linewidths, as expected from Eq. (9). We should also note that Baudin et al. (2011) found a much stronger dependence of the mean mode linewidth on $T_{\rm eff}$.

When a mode is resolved, as is the case here, it is the mode height, H, that determines the *SNR* in power, viz., the height-to-background ratio. Figure 11 displays, for each star, the heights of the radial modes returned by the respective *best fit* (see also Tables 7 and 8). The modes are the same as shown in Fig. 10. We also indicate in Fig. 11 the *SNR* of the strongest radial modes, as well as the background fits of Fig. 5 (which are an indicator of *SNR* = 1). Overall, KIC 10273246 exhibits a higher *SNR* if we take into account the whole plotted frequency bands. Also apparent is the larger width of the p-mode hump of KIC 10920273, which roughly scales with $\nu_{\rm max}$ (e.g., Stello et al. 2007; Mosser et al. 2010).

Furthermore, we computed the rms amplitudes of the radial modes, A_{n0}, according to (e.g., Chaplin et al. 2003):

$$A_{n0} = \sqrt{\frac{\pi}{2}\Gamma_{n0}H_{n0}}. \tag{10}$$

Amplitudes are always better constrained than the heights and the linewidths themselves. We were careful enough to compute errors on the amplitudes that took into account the correlations between the fitted parameters Γ_{n0} and H_{n0} (e.g., Appourchaux 2011). These amplitudes were then scaled to their bolometric equivalent using the bolometric correction derived from the spectral response of the *Kepler* passband (Ballot et al. 2011). Finally, we obtained a maximum bolometric amplitude of $A^{(\rm max)}_{n0,\rm bol} = 7.17 \pm 0.75$ ppm (at 833.90 μHz) for KIC 10273246 (cf. Table 7), and of $A^{(\rm max)}_{n0,\rm bol} = 7.56 \pm 0.99$ ppm (at 997.14 μHz) for KIC 10920273 (cf. Table 8). These values were computed based on the results returned by the respective *best fit* and were found to be consistent with the values obtained from the other fitters' results.

Kjeldsen & Bedding (1995) have suggested an empirical scaling relation to predict the amplitudes of solar-like oscillations that, although extensively used, predicts amplitudes in F-type stars that are higher than actually observed (e.g., Michel et al. 2008). Recently, the same authors have proposed a new scaling relation for the amplitudes which is based on simple physical arguments (Kjeldsen & Bedding 2011):

$$A_{\rm bol} \propto \frac{L\,\tau^{0.5}_{\rm mode}}{M^{1.5}\,T^{1.25+r}_{\rm eff}}, \tag{11}$$

where L is the stellar luminosity, and the value of r is chosen to be either $r = 1.5$ (assuming adiabatic oscillations) or $r = 2$ (following a fit to observational data in Kjeldsen & Bedding 1995). By assuming that $\nu_{\rm max}$ is a fixed fraction of the acoustic cut-off frequency, i.e.,

$$\nu_{\rm max} \propto \nu_{\rm ac} \propto \frac{M\,T^{3.5}_{\rm eff}}{L}, \tag{12}$$

and adopting a scaling relation for the stellar mass based on seismic parameters (e.g., Kallinger et al. 2010b),

$$M \propto \Delta\nu^{-4}\,\nu^{3}_{\rm max}\,T^{1.5}_{\rm eff}, \tag{13}$$

we can combine Eqs. (11)–(13) to obtain the following relation (normalized with respect to values in the Sun):

$$A^{(\rm max)}_{n0,\rm bol} = A^{(\rm max)}_{n0,\rm bol\odot}\left(\frac{T_{\rm eff}}{T_{\rm eff\odot}}\right)^{1.5-r}\left(\frac{\nu_{\rm max}}{\nu_{\rm max\odot}}\right)^{-2.5}\left(\frac{\Delta\nu}{\Delta\nu_\odot}\right)^{2}\left(\frac{\Gamma}{\Gamma_\odot}\right)^{-0.5}, \tag{14}$$

where $A^{(\rm max)}_{n0,\rm bol\odot} = 2.53$ ppm, $\nu_{\rm max\odot} = 3050$ μHz, and $\Delta\nu_\odot = 135$ μHz. Note that by setting $r = 1.5$ (as we will be assuming hereafter), the dependence of Eq. (14) on $T_{\rm eff}$ is canceled and this scaling relation then solely depends on seismic parameters. Finally, use of this relation gives a predicted maximum bolometric amplitude of $A^{(\rm max)}_{n0,\rm bol} = 7.27 \pm 1.33$ ppm for KIC 10273246,

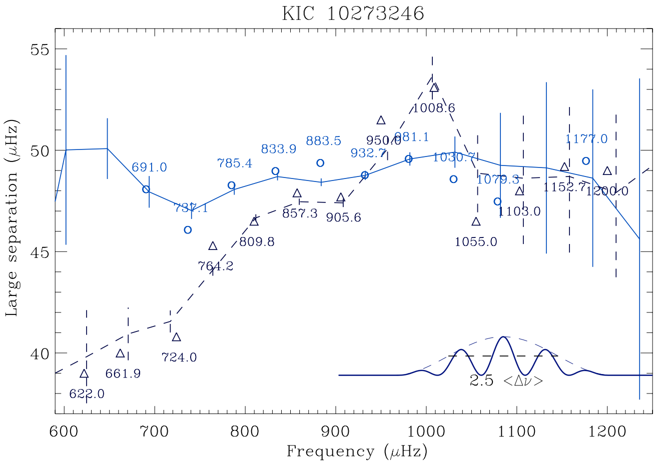

Fig. 12. Variation of $\Delta\nu_{\text{odd}}$ and $\Delta\nu_{\text{even}}$ with frequency for KIC 10273246. The dashed line corresponds to the odd ridge, whereas the solid line corresponds to the even ridge. Error bars are given with the same linestyles. Proxies of the mode frequencies derived with the EACF have been superimposed and their values appended: $l = 0$ (circles) and $l = 1$ (triangles). The inset shows the comb filter used in the analysis.

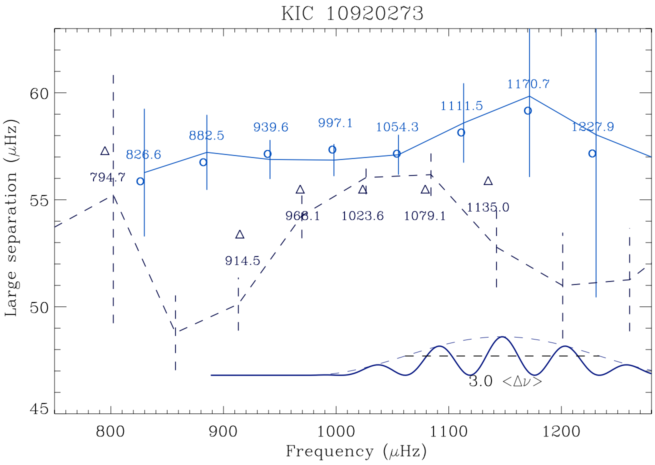

Fig. 13. Similar to Fig. 12 but for the case of KIC 10920273.

and of $A^{(\max)}_{n0,\text{bol}} = 8.24 \pm 1.44$ ppm for KIC 10920273, with the relatively large uncertainties dominated by the errors on $\nu_{\max}$. These values agree with the observed values at the 1-σ level. This is a particularly interesting result, since no discrepancy is seen between the predicted and observed amplitudes for the F-type star KIC 10273246.

4.7. Variation of $\Delta\nu$ with frequency

An independent methodology has been used to estimate the large frequency separation and the mode frequencies, which is based on the analysis of the spectrum with the envelope autocorrelation function (EACF; Mosser & Appourchaux 2009). As initially proposed by Roxburgh & Vorontsov (2006), the autocorrelation of the time series – or, equivalently, the power spectrum of the power spectrum – windowed with a narrow filter gives the variation of the large separation with frequency, $\Delta\nu(\nu)$. Mosser (2010) has shown that, with a dedicated comb filter for analysing the power spectrum, it is possible to obtain independently the values of the large separation for the odd ($l = 1$) and even ($l = 0, 2$) ridges. We denote them by $\Delta\nu_{\text{odd}}$ and $\Delta\nu_{\text{even}}$. Proxies of the mode frequencies can then be integrated from the $\Delta\nu(\nu)$ frequency pattern. In practice, they are derived from the correlation between the observed PDS and a synthetic spectrum based on the $\Delta\nu(\nu)$ pattern.

The values of $\Delta\nu_{\text{odd}}$ and $\Delta\nu_{\text{even}}$ for KIC 10273246 are given in Fig. 12. Notice the agreement between the proxies of the frequencies derived with the EACF and the frequencies of the *maximal frequency set* (Table 5). The EACF emphasizes the low values of $\Delta\nu_{\text{odd}}$ as well as its large gradient at the low-frequency end. Also clear is the large discrepancy relative to a regular échelle spectrum around 1000 μHz. The only mode present in the *maximal frequency set* and not detected with the EACF is the mixed mode at 695.75 μHz. This peak appears as supernumerary when compared to the regular agency of the modes. The EACF makes it possible to derive the large separation one radial order further than does peak-bagging.

Results for KIC 10920273 are given in Fig. 13. The lower *SNR* is counterbalanced by using a broader filter when computing the EACF. Again, the analysis is not conclusive for one mixed mode at low frequency, but it is able to recover the $l = 1$ ridge. We note that the even ridge is affected by the proximity of mixed modes. As opposed to the case of KIC 10273246, the EACF does not provide any further modes.

4.8. Rotational splitting and inclination

Stellar rotation removes the $(2l + 1)$-fold degeneracy of the frequencies of non-radial modes, allowing for a direct measurement of the stellar angular velocity averaged over the regions probed by these modes, as conveyed by Eq. (4). Using the radii and masses computed from model-grid-based methods by Creevey et al. (in prep.) together with the estimates of P_{rot}, we have computed the ratio of the surface angular velocity to the Keplerian break-up velocity, i.e., $\Omega/\sqrt{GM/R^3}$, which returned a value of approximately 1% for both stars, indicating that these are most likely slow rotators. In view of this and given the precision achievable from the spectra, we have thus decided not to include any second-order effects on the rotational splitting.

The overall profile of a non-radial multiplet thus consists of the sum of $2l + 1$ Lorentzian profiles regularly spaced in frequency, and scaled in height according to the $\mathscr{E}_{lm}(i)$ factors (Dziembowski 1977; Dziembowski & Goode 1985; Gizon & Solanki 2003):

$$\mathscr{E}_{lm}(i) = \frac{(l-|m|)!}{(l+|m|)!}\left[P_l^{|m|}(\cos i)\right]^2, \tag{15}$$

where i is the inclination angle between the direction of the stellar rotation axis and the line of sight, and $P_l^m(x)$ are the associated Legendre functions. Note that $\sum_m \mathscr{E}_{lm}(i) = 1$, meaning that the $\mathscr{E}_{lm}(i)$ factors represent the relative power contained in the modes within a multiplet.

While we are not able to robustly constrain the rotational splitting and inclination for both stars, we are however in a position to impose loose constraints on these parameters. Figures 14 and 15 map the two-dimensional posterior probability distributions of these parameters respectively for KIC 10273246 and KIC 10920273, based on the samples from a MCMC analysis of the ten-month-long time series by IAS_OB. We have overlaid each of these correlation maps with curves representing the estimate of P_{rot} given in Sect. 4.2 and the $P_{\text{rot}}(i)$ relation of Creevey et al. (in prep.), obtained by combining the projected rotational velocity ($v \sin i$) with the stellar radius.

For KIC 10273246, a comparison of the estimate of the rotational period with the $P_{\text{rot}}(i)$ relation implies that $i \gtrsim 20°$, which is also corroborated by the underlying correlation map.

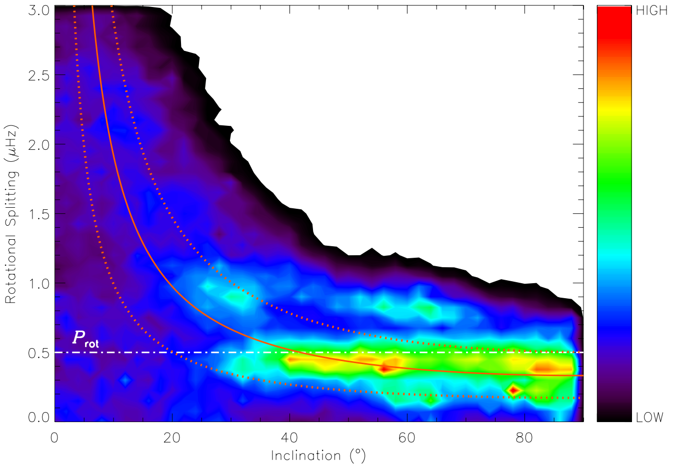

Fig. 14. Two-dimensional posterior probability distribution of $\nu_{\rm rot}$ and i for KIC 10273246 (the colorbar decodes the probability density level). The prior on i is uniform over the plotted range, whereas the prior on $\nu_{\rm rot}$ is uniform over the interval 0–2 μHz with a decaying Gaussian wing for higher values of the splitting. The dot-dashed line marks the estimate of the stellar rotational period given in Sect. 4.2. Furthermore, the $P_{\rm rot}(i)$ relation (solid curve) of Creevey et al. (in preparation) is shown together with the corresponding confidence interval (dotted curves).

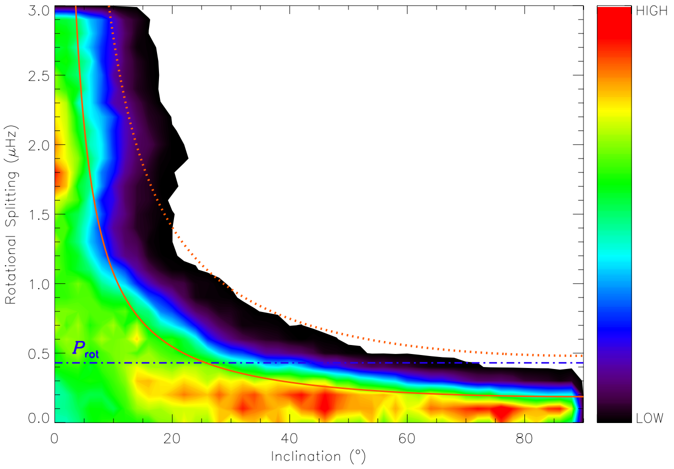

Fig. 15. Similar to Fig. 14 but for the case of KIC 10920273. Given the possibility that $v \sin i \approx 0$ km s^{-1}, the lower bound of the confidence interval of $P_{\rm rot}(i)$ will coincide with the horizontal axis.

Moreover, we notice that the marginal posterior probability distribution of $\nu_{\rm rot}$ is unimodal and points toward an interior rotating roughly as fast as the surface. We are however cautious not to claim to have robustly constrained the rotational splitting, since changes in the model – as well as in the priors on its parameters – used to represent the background signal may lead to significant alterations in the correlation map.

For KIC 10920273, no constraints on i are possible from a comparison of the estimate of the rotational period with the $P_{\rm rot}(i)$ relation. We should nevertheless remind the reader that the estimate of $P_{\rm rot}$ is somewhat doubtful (see Sect. 4.2). Although not completely apparent from Fig. 15, the marginal posterior probability distribution of i favors the scenario of a star seen pole-on (i.e., $i \approx 0°$). Consequently, according to Eq. (15), this would make inviable an inference of the rotational splitting. Going back to the discussion in Sect. 4.2, the possibility that this star is seen pole-on gains strength in explaining the low-*SNR* peaks at the low-frequency end of the PDS. There is however an alternative interpretation of the correlation map shown in Fig. 15 that should not be neglected: the high sensitivity of the parameter i to realization noise may lead to what is known as fit locking at 0° (e.g., Gizon & Solanki 2003; Ballot et al. 2008).

5. Summary and conclusions

The evolved Sun-like stars KIC 10273246 and KIC 10920273, respectively of spectral types F and G, were observed with *Kepler* at short cadence for approximately ten months (from Q0 to Q4) with a duty cycle in excess of 90%. The light curves used in the present analysis have been corrected for instrumental effects in a manner independent of the *Kepler* science pipeline. Both stars are relatively faint and display low *SNR* in the p-mode peaks.

Different fitting strategies have been employed to extract estimates of p-mode frequencies as well as of other individual mode parameters, from which we have selected frequency lists that will help constraining stellar models. A total of 30 and 21 modes of degree $l = 0, 1, 2$ have been identified for KIC 10273246 and KIC 10920273, respectively. These span at least eight radial orders. Furthermore, two avoided crossings ($l = 1$ ridge) have been identified for KIC 10273246, whereas one avoided crossing plus another likely one have been identified for KIC 10920273. These avoided crossings yield strong constraints – although model-dependent – on stellar age. Such results confirm previous expectations that asteroseismology of solar-type KASC survey targets is possible down to apparent magnitudes of 11 and fainter, provided we work with a multi-month time series (e.g., Stello et al. 2009b).

The peak-bagging results presented in Sect. 4.5 are based on the analysis of data from the first seven months of observations. A smaller number of individual fitters also analysed the ten-month-long time series (from Q0 to Q4). In spite of realization noise being expected to scale as $1/\sqrt{T}$ (Libbrecht 1992; Toutain & Appourchaux 1994; Stahn & Gizon 2008) thus making it possible to increase measurement precisions, there was barely any gain in terms of the number of modes detected. This is actually not surprising as, once a mode is resolved, the background-to-signal ratio in the power spectrum cannot be improved with time (e.g., Chaplin et al. 2003). The only exceptions would be (i) a radial mode at 690.34 ± 0.23 μHz for KIC 10273246, which is, however, detected with the EACF and shown in Fig. 12, and (ii) a $l = 2$ mode at 818.73 ± 0.23 μHz for KIC 10920273.

Good agreement is found between the observed and predicted mode amplitudes for the F-type star KIC 10273246, based on the revised scaling relation of Kjeldsen & Bedding (2011). This is a particularly interesting result that calls for further tests of this scaling relation using the large sample of *Kepler* stars.

Despite blending of the multiplet components of non-radial modes, i.e., $\langle \Gamma \rangle \gtrsim \nu_{\rm rot}$ (e.g., Ballot et al. 2006), we believe to be possible to impose loose constraints on the rotational splitting and stellar inclination for both stars. These constraints are based on a combined analysis involving correlation maps, $P_{\rm rot}(i)$ curves and estimates of $P_{\rm rot}$.

The results presented here point towards KIC 10273246 and KIC 10920273 being most likely evolved main-sequence stars. The global asteroseismic parameters reported for these stars, together with a detailed atmospheric analysis, should allow constraining their radius, mass and age with considerable precision (Creevey et al., in prep.). Further insight into the physics of these evolved solar-type stars – based on detailed modeling and inversion techniques – is now possible due to the high quality of the seismic parameters found.

Acknowledgements. Funding for this mission is provided by NASA's Science Mission Directorate. The authors wish to thank the entire *Kepler* team, without whom these results would not be possible. T.L.C. is supported by grant with reference number SFRH/BD/36240/2007 from FCT/MCTES, Portugal. This work was supported by the project PTDC/CTE-AST/098754/2008 funded by FCT/MCTES, Portugal.

Appendix A: Implementing Peirce's criterion

Peirce's criterion is an exact rule for the rejection of doubtful observations derived from the fundamental principles of probability theory. Quoting Peirce (1852): "The proposed observations should be rejected when the probability of the system of errors obtained by retaining them is less than that of the system of errors obtained by their rejection multiplied by the probability of making so many, and no more, abnormal observations".

Logic calls for an iterative assessment of the rejection when one or more observations are rejected. The iteration stops when no further improvement is possible. Based on the work of Gould (1855), we have implemented Peirce's criterion as follows:

1. compute the mean, $\bar{x}$, and the standard deviation, σ, for the observational sample $\{x_i\}$;
2. compute the rejection factor r from Gould (1855) assuming one doubtful observation;
3. reject observations satisfying $|x_i - \bar{x}| > r\sigma$;
4. if n observations are rejected then compute a new rejection factor r assuming $n+1$ doubtful observations;
5. repeat steps 3 to 4 until the number of rejected observations no longer increases.

References

Aigrain, S., Favata, F., & Gilmore, G. 2004, A&A, 414, 1139
Aizenman, M., Smeyers, P., & Weigert, A. 1977, A&A, 58, 41
Anderson, E. R., Duvall, Jr., T. L., & Jefferies, S. M. 1990, ApJ, 364, 699
Appourchaux, T. 2011, in Asteroseismology, Canary Islands Winter School of Astrophysics, Vol. XXII, ed. P. L. Pallé (CUP) [`arXiv:1103.5352v2`]
Appourchaux, T., Gizon, L., & Rabello-Soares, M. 1998, A&AS, 132, 107
Appourchaux, T., Michel, E., Auvergne, M., et al. 2008, A&A, 488, 705
Ballot, J. 2010, Astron. Nachr., 331, 933
Ballot, J., Turck-Chièze, S., & García, R. A. 2004, A&A, 423, 1051
Ballot, J., García, R. A., & Lambert, P. 2006, MNRAS, 369, 1281
Ballot, J., Appourchaux, T., Toutain, T., & Guittet, M. 2008, A&A, 486, 867
Ballot, J., Barban, C., & van't Veer-Menneret, C. 2011, A&A, 531, A124
Basu, S., Mazumdar, A., Antia, H. M., & Demarque, P. 2004, MNRAS, 350, 277
Batalha, N. M., Borucki, W. J., Koch, D. G., et al. 2010, ApJ, 713, L109
Baudin, F., Barban, C., Belkacem, K., et al. 2011, A&A, 529, A84
Bedding, T. R. 2011, in Asteroseismology, Canary Islands Winter School of Astrophysics, Vol. XXII, ed. P. L. Pallé (Cambridge University Press) [`arXiv:1107.1723v1`]
Bedding, T. R., Kjeldsen, H., Arentoft, T., et al. 2007, ApJ, 663, 1315
Bedding, T. R., Huber, D., Stello, D., et al. 2010a, ApJ, 713, L176
Bedding, T. R., Kjeldsen, H., Campante, T. L., et al. 2010b, ApJ, 713, 935
Benomar, O., Appourchaux, T., & Baudin, F. 2009a, A&A, 506, 15
Benomar, O., Baudin, F., Campante, T. L., et al. 2009b, A&A, 507, L13
Bonanno, A., Benatti, S., Claudi, R., et al. 2008, ApJ, 676, 1248
Borucki, W. J., Koch, D., Basri, G., et al. 2010, Science, 327, 977
Brown, T. M., & Gilliland, R. L. 1994, ARA&A, 32, 37
Brown, T. M., Gilliland, R. L., Noyes, R. W., & Ramsey, L. W. 1991, ApJ, 368, 599
Brown, T. M., Latham, D. W., Everett, M. E., & Esquerdo, G. A. 2011, AJ, 142, 112
Campante, T. L., Karoff, C., Chaplin, W. J., et al. 2010, MNRAS, 408, 542
Chaplin, W. J., Elsworth, Y., Isaak, G. R., et al. 2003, A&A, 398, 305
Chaplin, W. J., Houdek, G., Karoff, C., Elsworth, Y., & New, R. 2009, A&A, 500, L21
Chaplin, W. J., Appourchaux, T., Elsworth, Y., et al. 2010, ApJ, 713, L169
Chaplin, W. J., Kjeldsen, H., Bedding, T. R., et al. 2011a, ApJ, 732, 54
Chaplin, W. J., Kjeldsen, H., Christensen-Dalsgaard, J., et al. 2011b, Science, 332, 213
Christensen-Dalsgaard, J. 1993, in GONG 1992, Seismic Investigation of the Sun and Stars, ed. T. M. Brown, ASP Conf. Ser., 42, 347
Christensen-Dalsgaard, J. 2004, Sol. Phys., 220, 137
Christensen-Dalsgaard, J., Kjeldsen, H., Brown, T. M., et al. 2010, ApJ, 713, L164
Cunha, M. S., & Metcalfe, T. S. 2007, ApJ, 666, 413
Cunha, M. S., Aerts, C., Christensen-Dalsgaard, J., et al. 2007, A&ARv, 14, 217
Deheuvels, S., Bruntt, H., Michel, E., et al. 2010a, A&A, 515, A87
Deheuvels, S., Michel, E., Goupil, M. J., et al. 2010b, A&A, 514, A31
Dziembowski, W. 1977, Acta Astron., 27, 203
Dziembowski, W., & Goode, P. R. 1985, ApJ, 296, L27
García, R. A., Turck-Chièze, S., Boumier, P., et al. 2005, A&A, 442, 385
García, R. A., Mathur, S., Salabert, D., et al. 2010, Science, 329, 1032
García, R. A., Hekker, S., Stello, D., et al. 2011, MNRAS, 414, L6
Gaulme, P., Appourchaux, T., & Boumier, P. 2009, A&A, 506, 7
Gilliland, R. L., Brown, T. M., Christensen-Dalsgaard, J., et al. 2010a, PASP, 122, 131
Gilliland, R. L., Jenkins, J. M., Borucki, W. J., et al. 2010b, ApJ, 713, L160
Gizon, L., & Solanki, S. K. 2003, ApJ, 589, 1009
Gould, B. A. 1855, AJ, 4, 81
Grec, G., Fossat, E., & Pomerantz, M. A. 1983, Sol. Phys., 82, 55
Gruberbauer, M., Kallinger, T., Weiss, W. W., & Guenther, D. B. 2009, A&A, 506, 1043
Handberg, R., & Campante, T. L. 2011, A&A, 527, A56
Harvey, J. 1985, in Future Missions in Solar, Heliospheric & Space Plasma Physics, ed. E. Rolfe, & B. Battrick, ESA SP-235, 199
Hekker, S., Broomhall, A., Chaplin, W. J., et al. 2010, MNRAS, 402, 2049
Houdek, G., & Gough, D. O. 2007, MNRAS, 375, 861
Houdek, G., Balmforth, N. J., Christensen-Dalsgaard, J., & Gough, D. O. 1999, A&A, 351, 582
Huber, D., Stello, D., Bedding, T. R., et al. 2009, Comm. Asteroseismol., 160, 74
Jenkins, J. M., Caldwell, D. A., Chandrasekaran, H., et al. 2010, ApJ, 713, L87
Jiménez-Reyes, S. J., Chaplin, W. J., García, R. A., et al. 2008, MNRAS, 389, 1780
Kallinger, T., Mosser, B., Hekker, S., et al. 2010a, A&A, 522, A1
Kallinger, T., Weiss, W. W., Barban, C., et al. 2010b, A&A, 509, A77
Karoff, C., Metcalfe, T. S., Chaplin, W. J., et al. 2009, MNRAS, 399, 914
Karoff, C., Campante, T. L., & Chaplin, W. J. 2010, Astron. Nachr., in press [`arXiv:1003.4167v1`]
Kjeldsen, H., & Bedding, T. R. 1995, A&A, 293, 87
Kjeldsen, H., & Bedding, T. R. 2011, A&A, 529, L8
Kjeldsen, H., Bedding, T. R., Baldry, I. K., et al. 2003, AJ, 126, 1483
Koch, D. G., Borucki, W. J., Basri, G., et al. 2010, ApJ, 713, L79
Latham, D. W., Brown, T. M., Monet, D. G., et al. 2005, in BAAS, 37, 1340
Ledoux, P. 1951, ApJ, 114, 373
Libbrecht, K. G. 1992, ApJ, 387, 712
Liddle, A. R. 2009, Ann. Rev. Nucl. Part. Sci., 59, 95
Lomb, N. R. 1976, Ap&SS, 39, 447
Mathur, S., García, R. A., Catala, C., et al. 2010a, A&A, 518, A53
Mathur, S., García, R. A., Régulo, C., et al. 2010b, A&A, 511, A46
Mathur, S., Handberg, R., Campante, T. L., et al. 2011, ApJ, 733, 95
Metcalfe, T. S., Monteiro, M. J. P. F. G., Thompson, M. J., et al. 2010, ApJ, 723, 1583
Michel, E., Baglin, A., Auvergne, M., et al. 2008, Science, 322, 558
Michel, E., Samadi, R., Baudin, F., et al. 2009, A&A, 495, 979
Monteiro, M. J. P. F. G., Christensen-Dalsgaard, J., & Thompson, M. J. 2000, MNRAS, 316, 165
Mosser, B. 2010, Astron. Nachr., 331, 944
Mosser, B., & Appourchaux, T. 2009, A&A, 508, 877
Mosser, B., Belkacem, K., Goupil, M., et al. 2010, A&A, 517, A22
Osaki, Y. 1975, PASJ, 27, 237
Peirce, B. 1852, AJ, 2, 161
Press, W. H., & Rybicki, G. B. 1989, ApJ, 338, 277
Roxburgh, I. W. 2009, A&A, 506, 435
Roxburgh, I. W., & Vorontsov, S. V. 2006, MNRAS, 369, 1491
Samadi, R., Georgobiani, D., Trampedach, R., et al. 2007, A&A, 463, 297
Scargle, J. D. 1982, ApJ, 263, 835
Stahn, T., & Gizon, L. 2008, Sol. Phys., 251, 31
Stello, D., Bruntt, H., Kjeldsen, H., et al. 2007, MNRAS, 377, 584
Stello, D., Chaplin, W. J., Basu, S., Elsworth, Y., & Bedding, T. R. 2009a, MNRAS, 400, L80
Stello, D., Chaplin, W. J., Bruntt, H., et al. 2009b, ApJ, 700, 1589
Tassoul, M. 1980, ApJS, 43, 469
Toutain, T., & Appourchaux, T. 1994, A&A, 289, 649
Vandakurov, Y. V. 1967, AZh, 44, 786
Verner, G. A., Elsworth, Y., Chaplin, W. J., et al. 2011, MNRAS, 415, 3539
White, T. R., Brewer, B. J., Bedding, T. R., Stello, D., & Kjeldsen, H. 2010, Commun. Asteroseismol., 161, 39

Appendix D

A&A 527, A56 (2011)
DOI: 10.1051/0004-6361/201015451

Astronomy
&
Astrophysics

Bayesian peak-bagging of solar-like oscillators using MCMC: a comprehensive guide

R. Handberg[1] and T. L. Campante[1,2]

[1] Danish AsteroSeismology Centre, Department of Physics and Astronomy, Aarhus University, 8000 Aarhus C, Denmark
e-mail: `[rasmush;campante]@phys.au.dk`
[2] Centro de Astrofísica, DFA-Faculdade de Ciências, Universidade do Porto, Rua das Estrelas, 4150-762 Porto, Portugal

Received 22 July 2010 / Accepted 29 December 2010

ABSTRACT

Context. Asteroseismology has entered a new era with the advent of the NASA *Kepler* mission. Long and continuous photometric observations of unprecedented quality are now available which have stimulated the development of a number of suites of innovative analysis tools.

Aims. The power spectra of solar-like oscillations are an inexhaustible source of information on stellar structure and evolution. Robust methods are hence needed in order to infer both individual oscillation mode parameters and parameters describing non-resonant features, thus making a seismic interpretation possible.

Methods. We present a comprehensive guide to the implementation of a Bayesian peak-bagging tool that employs a Markov chain Monte Carlo (MCMC). Besides making it possible to incorporate relevant prior information through Bayes' theorem, this tool also allows one to obtain the marginal probability density function for each of the fitted parameters. We apply this tool to a couple of recent asteroseismic data sets, namely, to CoRoT observations of HD 49933 and to ground-based observations made during a campaign devoted to Procyon.

Results. The developed method performs remarkably well at constraining not only in the traditional case of extracting oscillation frequencies, but also when pushing the limit where traditional methods have difficulties. Moreover it provides an rigorous way of comparing competing models, such as the ridge identifications, against the asteroseismic data.

Key words. methods: data analysis – methods: statistical – stars: late-type – stars: oscillations

1. Introduction

Seismology of solar-like stars is a powerful tool that can be used to increase our understanding of stellar structure and evolution. Solar-like oscillations in main-sequence stars and subgiants have been measured thanks to data collected from ground-based high-precision spectroscopy (for a review e.g., Bedding & Kjeldsen 2008) and, more recently, to photometric space-based missions such as CoRoT (e.g., Michel et al. 2008). Red giants also exhibit solar-like oscillations, although at lower frequencies, and hence require longer time series in order to resolve them (e.g., De Ridder et al. 2009, and references therein). The launch of the NASA *Kepler* mission (Koch et al. 2010) definitely marked a milestone in the field of asteroseismology. *Kepler* will particularly lead to a revolution in the seismology of solar-like oscillators, since it will increase by more than two orders of magnitude the number of stars for which high-quality observations will be available, while allowing for long-term follow-ups of a selection of those targets. The large homogeneous sample of data made available by *Kepler* opens the possibility of conducting a seismic survey of the solar-like part of the colour-magnitude diagram, which researchers in the field already started naming as *ensemble asteroseismology*. As of the time of writing of this article, first results arising from the *Kepler* asteroseismic programme had already been made available (Bedding et al. 2010a; Chaplin et al. 2010; Gilliland et al. 2010; Hekker et al. 2010b; Stello et al. 2010; Christensen-Dalsgaard et al. 2010; Metcalfe et al. 2010).

The rich informational content of power spectra of solar-like oscillations allows fundamental stellar properties (e.g. mass, radius, and age) to be determined, and the internal structure to be constrained to unprecedented levels provided that individual oscillation mode parameters are measured (e.g., Christensen-Dalsgaard 2004). Furthermore, the measured stellar background signal provides us with valuable information on activity and convection. In the case of the highest signal-to-noise ratio (S/N) observations, for which it is possible to measure individual oscillation mode parameters, we expect asteroseismology to produce a major breakthrough on stellar structure and evolution, on topics as diverse as energy generation and transport, rotation and stellar cycles (e.g., Karoff et al. 2009).

For the past few years significant work has been invested in making preparations for the mode parameter analysis of *Kepler* data. This analysis involves the estimation of individual and average oscillation mode parameters, as well as estimation of parameters that describe non-resonant signatures of convection and activity. Examples include the work conducted in the framework of the AsteroFLAG consortium (Chaplin et al. 2008a) and the work undertaken by the CoRoT data analysis team (Appourchaux et al. 2006). This consequently paved the way for the development of suites of analysis tools for application to *Kepler* data (Hekker et al. 2010a; Huber et al. 2009; Karoff et al. 2010; Mathur et al. 2010; Mosser & Appourchaux 2009; Campante et al. 2010).

In the present study we give continuity to this work by presenting a comprehensive guide to the implementation of a

Bayesian peak-bagging[1] tool that employs a MCMC. These techniques derive from the tools traditionally used in helioseismology and are in many ways an extension of the maximum likelihood estimation (MLE) methods. This peak-bagging tool is to be applied to the power spectra of solar-like oscillators and used as a means to infer both individual oscillation mode parameters and parameters describing non-resonant features. Besides making it possible to incorporate relevant prior information through Bayes' theorem, this tool also allows one to obtain the marginal probability density function (PDF) for each of the model parameters (frequencies, mode heights, mode lifetimes, rotational splitting, inclination angle etc.). This is one of the main advantages of these MCMC techniques, as it not only performs well in low signal-to-noise conditions, but also provides reliable error bars on the parameters. Parameter space is sampled using a *Metropolis-Hastings* algorithm featuring a built-in *statistical control system* that allows to automatically set an appropriate instrumental law during the burn-in stage. Also included is *parallel tempering*, which increases the mixing properties of the Markov chain.

The outline of the paper is as follows: we start in Sect. 2 by providing an overview of the theory behind the power spectrum of solar-like oscillations, introducing the assumptions and the set of parameters needed to model the spectrum to the level of detail required by modern asteroseismic data. In Sect. 3 we describe the subjacent Bayesian statistical framework by highlighting the topics of parameter estimation and model selection. Section 4 is devoted to the modus operandi of advanced Markov chain Monte Carlo methods and their implementation. In Sect. 5 we present a couple of examples where this tool has been applied to recent asteroseismic data sets, evidencing some of its capabilities and illustrating its functioning. A summary and discussion are presented in Sect. 6.

2. The power spectrum of solar-like oscillations

Solar-like oscillations or p modes (pressure playing the role of the restoring force) are global standing acoustic waves. They are characterized by being intrinsically damped while simultaneously stochastically excited by near-surface convection. Therefore, all stars cool enough to harbor an outer convective envelope – whose locus in a H–R diagram approximately extends from the cool edge of the Cepheid instability strip up to the red giant branch – may be expected to exhibit solar-like oscillations.

Modes of oscillation are characterized by three wave numbers: n, ℓ and m. The radial order n characterizes the behaviour of the mode in the radial direction. The degree ℓ and the azimuthal order m determine the spherical harmonic describing the properties of the mode as a function of colatitude and longitude. In the case of stellar observations, the associated whole-disk light integration and consequent lack of spatial resolution strongly suppress the signal from all but the modes of the lowest degree (with $\ell \leq 3$). For a spherically symmetric star mode frequencies depend only on n and ℓ.

2.1. Statistics and likelihood function of the spectrum

Stellar p modes can be modelled as stochastically excited and intrinsically damped harmonic oscillators (Kumar et al. 1988). The frequency-power spectrum arising from such a system can in turn be modelled by a mean spectrum profile, $\mathscr{P}(\nu_j;\Theta)$, described by the set of parameters Θ which contain the desired physical information, multiplied by a random noise with a χ^2 probability distribution with 2 degrees of freedom (Woodard 1984; Duvall & Harvey 1986). This means that, at a fixed frequency bin j, the probability density, $f(P_j)$, that the observed power spectrum takes a particular value P_j, is related to the mean spectrum, $\mathscr{P}(\nu_j;\Theta)$, by:

$$f(P_j) = \frac{1}{\mathscr{P}(\nu_j;\Theta)} \exp\left[-\frac{P_j}{\mathscr{P}(\nu_j;\Theta)}\right]. \tag{1}$$

Very often when dealing with long time series, it is customary to divide the observational data set into several independent subsets, to compute their separate spectra and to average them. In doing so one aims at decreasing the variance in the power spectrum. The average power spectrum will then obey a χ^2 probability distribution with $2s$ degrees of freedom, χ^2_{2s}, s being the number of combined spectra (Appourchaux 2003a):

$$f(P_j) = \frac{s^{s-1}}{(s-1)!} \frac{P_j^{s-1}}{\mathscr{P}(\nu_j;\Theta)^s} \exp\left[-\frac{s\,P_j}{\mathscr{P}(\nu_j;\Theta)}\right]. \tag{2}$$

Equation (2) also holds when binning the power spectrum over s bins (Appourchaux 2004).

We would now like to specify the likelihood function, i.e., the joint PDF for the data sample $\{P_j\}$. Assuming that the frequency bins are uncorrelated, the joint PDF is simply given by the product of $f(P_j;\Theta)$ over some frequency interval of interest spanned by j:

$$L(\Theta) = \prod_j f(P_j;\Theta). \tag{3}$$

Notice that we have written $f(P_j;\Theta)$ to make the dependence on the parameters Θ explicit. In spite of the fact that Eq. (3) is valid for an uninterrupted data set, the same is not true when gaps are present in the time series. In that event, Stahn & Gizon (2008) have derived an expression for the joint PDF of solar-like oscillations in complex Fourier space, in agreement with the earlier work of Gabriel (1994). The latter PDF explicitly takes into account frequency correlations introduced by the convolution with the spectral window.

The basic idea when employing a Maximum Likelihood Estimator (MLE) is to determine estimates $\tilde{\Theta}$ so as to maximize the likelihood function (e.g., Toutain & Appourchaux 1994). Due to improved numerical stability, however, it is more convenient, in practice, to work with logarithmic probabilities:

$$\begin{aligned}\mathscr{L}(\Theta) &\equiv \ln L(\Theta)\\ &= -\sum_j \left\{\ln \mathscr{P}(\nu_j;\Theta) + \frac{P_j}{\mathscr{P}(\nu_j;\Theta)}\right\}. \end{aligned}\tag{4}$$

One therefore ends up maximizing the logarithm of the likelihood function instead:

$$\tilde{\Theta} = \arg\max_{\Theta} \{\mathscr{L}(\Theta)\}\,. \tag{5}$$

---

[1] The term "peak-bagging" has become the customary name for the examination of individual oscillation peaks in the field of asteroseismology. The origin of the name is explained in Appourchaux (2003b).

2.2. Modelling the power spectrum[2]

The power spectrum of a single mode of oscillation is distributed around a mean profile with an exponential probability distribution according to Eq. (1). As already mentioned, this mean profile contains the information on the physics of the mode. In the limit of taking the ensemble average of an infinite number of realisations of the power spectrum, it can be shown (Anderson et al. 1990) that the limit spectrum thus obtained follows in fact a standard Lorentzian profile near the resonance, i.e., for $|\nu - \nu_0| \ll \nu_0$. A Lorentzian profile is defined as:

$$\mathscr{M}(\nu; S, \nu_0, \Gamma) = \frac{S}{1 + \frac{4}{\Gamma^2}(\nu - \nu_0)^2}, \tag{6}$$

where S is the mode height and Γ is the mode linewidth. Γ is related to the mode lifetime, τ, through $\Gamma = (\pi\tau)^{-1}$. In the case of solar-type stars and for low angular degree ℓ, we can assume that Γ is a function of frequency alone, which is supported both by observations of the Sun and by theoretical models (e.g. Aerts et al. 2010; Dupret et al. 2009).

A power spectrum of solar-like oscillations will, of course, contain a myriad of modes spanning a broad range in frequency, superimposed on a background signal of both stellar and instrumental origin. The overall limit spectrum is then given by the sum of the separate limit spectra arising from the different sources, since interference effects from beating between the modes average out in the limit. Notice that we are assuming that a mode is uncorrelated with any other modes or with the background signal. In doing so, we neglect any eventual asymmetries of the Lorentzian profiles (Duvall et al. 1993; Abrams & Kumar 1996). Nevertheless, when dealing with long time series, such asymmetries should be included in order to avoid biases in mode frequency determination. Furthermore, the presence of gaps and the finite length of the time series lead to a degradation of the observed power spectrum, which then results from the convolution of the true spectrum (i.e., the one that would be obtained were there no gaps) with the power spectrum of the window function (i.e., the spectral window). However, this problem is overcome by convolving the final limit spectrum with the spectral window.

Ignoring any departure from spherical symmetry, non-radial modes differing only on the azimuthal number m are degenerate and their profiles will be combined into a single profile, that of the (n, ℓ) multiplet. Stellar rotation removes the $(2\ell + 1)$-fold degeneracy of the frequency of oscillation of non-radial modes, thus allowing for a direct measurement of the angular velocity of the star averaged over the region probed by these modes. When the angular velocity of the star, Ω, is small and in the case of rigid-body rotation, the frequency of a (n, ℓ, m) mode is given to first order by (Ledoux 1951):

$$\nu_{n\ell m} = \nu_{n\ell} + m\frac{\Omega}{2\pi}(1 - C_{n\ell}). \tag{7}$$

The kinematic splitting, $m\Omega/(2\pi)$, is corrected for the effect of the Coriolis force through the dimensionless quantity $C_{n\ell} > 0$. In the asymptotic regime, i.e., for high-order, low-degree p modes, rotational splitting is dominated by advection and the splitting between adjacent modes within a multiplet is $\nu_s \simeq \Omega/(2\pi)$. Second-order rotational effects are related to the distortion of the equilibrium structure of the star caused by centrifugal forces. Although negligible in the Sun, these effects are significant for faster solar-type rotators where these effects can cause non-negligible biases on frequency determinations (e.g., Ballot 2010). Large-scale magnetic fields may also introduce further corrections to the oscillation frequencies.

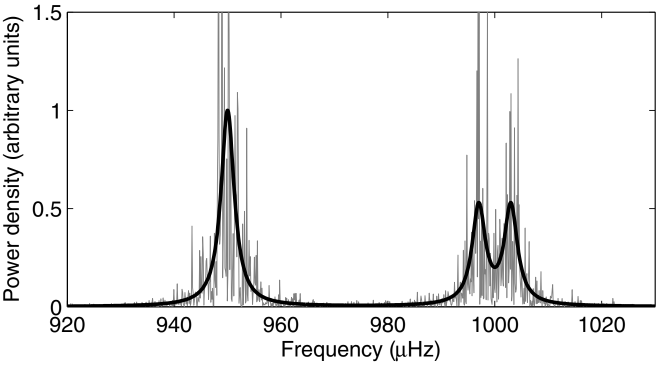

Fig. 1. Artificial power density spectrum of a $\ell = 0$ singlet and a $\ell = 1$ multiplet. One has $\nu_s = \Gamma = 3\,\mu$Hz. Notice how the $\ell = 1$ multiplet splits into its m components. The power spectrum (grey) is distributed around a mean spectrum (black) with an exponential probability distribution.

Assuming energy equipartition between the components of a multiplet, we define the following symmetric profile for a (n, ℓ) multiplet:

$$\mathscr{M}_{n\ell}(\nu; S_{n\ell}, \nu_{n\ell}, \Gamma_{n\ell}, \nu_s, i) = \sum_{m=-\ell}^{\ell} \mathscr{E}_{\ell m}(i)\, \mathscr{M}(\nu; S_{n\ell}, \nu_{n\ell}+m\nu_s, \Gamma_{n\ell}), \tag{8}$$

where $\mathscr{E}_{\ell m}(i)$ represents mode visibility within a multiplet and i is the inclination angle between the direction of the stellar rotation axis and the line of sight. The overall profile of a multiplet thus consists of the sum of $2\ell + 1$ Lorentzian profiles regularly spaced in frequency and scaled in height according to the $\mathscr{E}_{\ell m}(i)$ factors (see Fig. 1), which in turn are given by (Gizon & Solanki 2003):

$$\mathscr{E}_{\ell m}(i) = \frac{(\ell - |m|)!}{(\ell + |m|)!} \left[P_\ell^{|m|}(\cos i)^2\right], \tag{9}$$

where $P_\ell^m(x)$ are the associated Legendre functions. Notice that $\sum_m \mathscr{E}_{\ell m}(i) = 1$, meaning that $\mathscr{E}_{\ell m}(i)$ represents the relative power contained in a mode within a multiplet.

Since we are primarily interested in performing a so-called *global fit* (e.g., Appourchaux et al. 2008) to the observed power spectrum, whereby several radial orders are fitted simultaneously within a broad frequency range, we end up modelling the mean acoustic spectrum according to the following general relation:

$$\mathscr{P}(\nu; \Theta) = \sum_{n=n_0}^{n_{\max}} \sum_{\ell=0}^{\ell_{\max}} \sum_{m=-\ell}^{\ell} \frac{\mathscr{E}_{\ell m}(i)\, S_{n\ell}}{1 + \frac{4}{\Gamma_{n\ell}^2}(\nu - \nu_{n\ell} - m\nu_s)^2} + N(\nu), \tag{10}$$

where we have also included a profile describing the background signal, $N(\nu)$. Granulation, faculae and active regions might contribute to the stellar background signal, which is commonly modelled as a sum of power laws describing these physical phenomena (Harvey 1985; Aigrain et al. 2004):

$$N(\nu) = \sum_{k=1}^{k_{\max}} \frac{4A_k^2 B_k}{1 + (2\pi B_k \nu)^{C_k}} + N, \tag{11}$$

---

[2] To be precise, we will be modelling the power density spectrum and not the power spectrum. The former is independent of the window function and is obtained by multiplying the power spectrum by the effective length of the observational run, which can in turn be calculated as the reciprocal of the area integrated under the spectral window.

Table 1. Relative spatial response functions, V_ℓ/V_0, for a number of present and upcoming instruments/missions.

	Intensity			Velocity	
	VIRGO (862 nm)	CoRoT (660 nm)	*Kepler* (641 nm)^a	HARPS (535 nm)	SONG (550 nm)
V_0/V_0	1.00	1.00	1.00	1.00	1.00
V_1/V_0	1.20	1.22	1.22	1.35	1.35
V_2/V_0	0.67	0.70	0.71	1.02	1.01
V_3/V_0	0.10	0.14	0.14	0.48	0.47
V_4/V_0	–0.10	–0.09	–0.08	0.09	0.09

Notes. Notice the increased sensitivity to $\ell = 3, 4$ modes in velocity. Negative values of V_ℓ mean that the oscillations will appear to have reversed phases. $^{(a)}$ Calculated as the weighted mean over the spectral response function.

$\{A_k\}$ and $\{B_k\}$ being, respectively, the corresponding amplitudes and characteristic time-scales, whereas the $\{C_k\}$ are the slopes of each of the individual power laws. A flat component, N, is needed in order to model the photon shot noise. Equation (11) might just well incorporate any instrumental background signal. We refer to $S_{n\ell}/N(\nu_{n\ell})$ as the signal-to-noise ratio (in power) of the multiplet (n, ℓ).

Once again assuming energy equipartition between the different components of a multiplet, their heights can be expressed as:

$$S_{n\ell m} = \mathscr{E}_{\ell m}(i)\, S_{n\ell} = \mathscr{E}_{\ell m}(i)\, V_\ell^2\, \alpha_{n\ell}. \tag{12}$$

The quantity V_ℓ^2 is an estimate of the geometrical visibility of the total power in a multiplet (n, ℓ) as a function of ℓ, whereas $\alpha_{n\ell}$ depends mainly on the frequency and excitation mechanism, i.e., $\alpha_{n\ell} \simeq \alpha(\nu_{n\ell})$. Christensen-Dalsgaard (2003) concisely treats this issue of spatial filtering. Equation (12), however, is only strictly valid under one assumption: when the stellar flux is integrated over the full apparent disc, one must assume that the weighting function, W, which gives the contribution of a surface element to the integral, is a function of the distance to the disc centre alone, i.e., $W = W(\theta')$, where θ' is defined in an inertial frame with polar axis pointing toward the observer. In this case, the apparent mode amplitude can effectively be separated into two factors: $\mathscr{E}_{\ell m}(i)$ and V_ℓ^2. This assumption holds very well in the case of intensity measurements, since the weighting function is then mainly linked to the limb-darkening, whereas for velocity measurements departures might be observed due to asymmetries in the velocity field induced by rotation (see Ballot et al. 2006, 2008, and references therein). See Appendix A for how to compute $\mathscr{E}_{\ell m}(i)$ and V_ℓ.

The heights of non-radial modes are commonly defined based on the heights of radial modes according to Eq. (12), and taking into account the V_ℓ/V_0 ratios. Note that $\ell = 0$ modes constitute a sensible reference since they are not split by rotation. Table 1 displays the relative spatial response functions, V_ℓ/V_0, computed according to Bedding et al. (1996), for a number of present and upcoming instruments/missions used when measuring solar-like oscillations. Those performing intensity measurements are the red channel of the VIRGO SPM instrument on board the SOHO spacecraft (Fröhlich et al. 1995), as well as the CoRoT and *Kepler* space missions. On the other hand, velocity measurements are performed by the HARPS spectrograph (Mayor et al. 2003) and are the purpose of the forthcoming SONG network (Grundahl et al. 2007).

Finally, a possible set of parameters going into the model is given by:

$$\Theta = \{S_{n\ell}, \nu_{n\ell}, \Gamma_{n\ell}, \nu_{\rm s}, i, A_k, B_k, C_k, N\}\,. \tag{13}$$

We have described in detail how the modelling of a power spectrum of solar-like oscillations can be achieved. When actually fitting a model to an observed power spectrum, the set of parameters entering the model might differ from the one represented in Eq. (13). Moreover, it might be desirable to justifiably fix some of the parameters in order to reduce the dimension of parameter space.

3. Bayesian inference

Having set up the model of the power spectrum, we will now introduce the Bayesian statistical framework to be used for estimating the model parameters and for comparing competing models. Let us start by considering a set of competing hypotheses, $\{H_i\}$, not necessarily mutually exclusive. We should then be able to assign a probability, $p(H_i|D, I)$, to each hypothesis, taking into account the observed data, D, and available prior information, I, arising from theoretical considerations and/or previous observations. This is done through Bayes' theorem:

$$p(H_i|D, I) = \frac{p(H_i|I)p(D|H_i, I)}{p(D|I)}\cdot \tag{14}$$

The probability of the hypothesis H_i in the absence of D is called the *prior probability*, $p(H_i|I)$, whereas the probability including D is called the *posterior probability*, $p(H_i|D, I)$. The quantity $p(D|H_i, I)$ is called the *likelihood* of H_i, $p(D|I)$ being the *global likelihood* for the entire class of hypotheses. Bayesian inference thus encodes our current state of knowledge into a posterior probability concerning each member of the hypothesis space of interest. Moreover, the sum of the posterior probabilities over the hypothesis space of interest is unity, and thus

$$p(D|I) = \sum_i p(H_i|I)p(D|H_i, I). \tag{15}$$

3.1. Parameter estimation

Very often a particular hypothesis, i.e., a model of the power spectrum, is assumed to be true and the hypothesis space of interest then relates to the values taken by the model parameters Θ. These parameters are continuous, which means that the quantity of interest is a PDF. The global likelihood of model M, assumed true, is now given by the continuous counterpart of Eq. (15):

$$p(D|I) = \int p(\Theta|I)\, p(D|\Theta, I)\, {\rm d}\Theta. \tag{16}$$

Let us restate Bayes' theorem in order to account for this new formalism:

$$p(\Theta|D, I) = \frac{p(\Theta|I)p(D|\Theta, I)}{p(D|I)}, \tag{17}$$

where we have substituted the hypothesis, H_i, with the parameters of the model that is assumed true. The terms entering this equation have the same meaning as the corresponding terms entering Eq. (14). Use of Eq. (17) allows one to obtain the full joint posterior PDF, $p(\Theta|D, I)$, this being the Bayesian solution to the problem of parameter estimation in contrast to traditional point estimation methods (e.g. MLE). The procedure of *marginalisation* makes it possible to derive the marginal posterior PDF for a subset of parameters Θ_A, by integrating out the remaining parameters Θ_B, called *nuisance parameters*:

$$p(\Theta_\mathrm{A}|D,I) = \int p(\Theta_\mathrm{A},\Theta_\mathrm{B}|D,I)\,\mathrm{d}\Theta_\mathrm{B}. \tag{18}$$

Furthermore, assuming that the prior on Θ_A is independent of the prior on the remaining parameters, then by applying the product rule we have:

$$p(\Theta_\mathrm{A},\Theta_\mathrm{B}|I) = p(\Theta_\mathrm{A}|I)p(\Theta_\mathrm{B}|\Theta_\mathrm{A},I) = p(\Theta_\mathrm{A}|I)p(\Theta_\mathrm{B}|I). \tag{19}$$

We will be working, in practice, with logarithmic probabilities. The global likelihood of the model plays the role of a normalisation constant and we rewrite Eq. (17) as follows:

$$\ln p(\Theta|D,I) = \mathrm{const.} + \ln p(\Theta|I) + \mathscr{L}(\Theta). \tag{20}$$

3.2. Model comparison

We might also be facing a situation wherein several parametrized models are available to describe the same physical phenomenon. We then expect Bayes' theorem to allow for a statistical comparison between these competing models. In fact, Bayesian model comparison has a built-in *Occam's razor*, a principle also known as *lex parsimoniae*, by which a complex model is automatically penalised, unless the available data justifies its additional complexity. Notice that these might be intrinsically different models or similar models with varying number of parameters, or even the same model with different priors for its parameters.

Given two or more competing models, $\{M_i\}$, and our prior information, I, being in the current context that *one and only one of the models is true*, we can assign individual probabilities similarly to what has been done in Eq. (14), after substituting H_i with M_i:

$$p(M_i|D,I) = \frac{p(M_i|I)p(D|M_i,I)}{p(D|I)}, \tag{21}$$

where $p(D|M_i,I)$, also called the *evidence* of model M_i, is given by Eq. (16). The problem of model comparison is therefore analogous to the problem of parameter estimation as can be seen by comparing Eqs. (17) and (21).

Of particular interest to us will be calculating the ratio of the probabilities of two competing models,

$$O_{ij} \equiv \frac{p(M_i|D,I)}{p(M_j|D,I)} = \frac{p(M_i|I)p(D|M_i,I)}{p(M_j|I)p(D|M_j,I)} = \frac{p(M_i|I)}{p(M_j|I)}B_{ij}, \tag{22}$$

where O_{ij} is the *odds ratio* in favour of model M_i over model M_j, B_{ij} is the so-called *Bayes' factor* and the remaining factor is the *prior odds ratio*. We will always assume that we have no prior information impelling us to prefer one model over the other, and hence $p(M_i|I)/p(M_j|I) = 1$. One is now naturally in need of a scale by which to judge the ratio of the evidences of two competing models. The usual scale employed is the Jeffreys' scale (Jeffreys 1961), which we display in Table 2 for convenience.

Furthermore, the Bayesian framework makes it possible to extract parameter constraints even in the presence of model uncertainty, i.e., when the implementation of model selection has not been successful. This is done by simply combining the probability distribution of the parameters within each individual model, weighted by the model probability. This procedure, called *Bayesian model averaging* (see Liddle 2009, and references therein), is an analogue of the superposition of eigenstates of an observable in quantum mechanics.

Table 2. Jeffreys' scale.

$\ln O_{ij}$	Strength of evidence
<1	Not worth more than a bare mention
1–2.5	Significant
2.5–5	Strong to very strong
>5	Decisive

3.3. Ignorance priors

The main advantage of the Bayesian framework when compared to a frequentist approach is the ability to incorporate relevant prior information through Bayes' theorem and evaluate its effect on our conclusions. Assuming that the prior on each parameter is independent of the prior on any other parameter, then according to Eq. (19) we have:

$$p(\Theta|I) = \prod_k f_k(\Theta_k), \tag{23}$$

where $f_k(\Theta_k)$ is the prior PDF associated with the kth parameter entering the model. As our state of knowledge of a particular physical phenomenon evolves through continued study and experimentation, the set of priors relevant for the analysis of a new data set will change. In the early stages of research, however, we look for a set of priors that encode our rather limited state of knowledge, i.e., a set of *ignorance priors* (e.g., Gregory 2005a, and references therein).

When dealing with *location parameters*, e.g. $\{\nu_{n\ell}\}$ in Eq. (13), our choice of prior would at first be the *uniform prior*:

$$f_k(\Theta_k) = \begin{cases} \frac{1}{\Theta_k^\mathrm{max}-\Theta_k^\mathrm{min}} & \text{, for } \Theta_k^\mathrm{min} \leq \Theta_k \leq \Theta_k^\mathrm{max}, \\ 0, & \text{otherwise.} \end{cases} \tag{24}$$

If we are ignorant about the limits Θ_k^min and Θ_k^max, then we refer to $f_k(\Theta_k)$ as an improper prior, meaning that it is not normalised. An improper prior is not suitable for model comparison problems. On the other hand, when dealing with *scale parameters*, e.g. $\{S_{n\ell}\}$ in Eq. (13), our choice of prior might be that of a *Jeffreys' prior*:

$$f_k(\Theta_k) = \begin{cases} \frac{1}{\Theta_k \ln\left[\Theta_k^\mathrm{max}/\Theta_k^\mathrm{min}\right]} & \text{, for} \Theta_k^\mathrm{min} \leq \Theta_k \leq \Theta_k^\mathrm{max}, \\ 0, & \text{otherwise}\,. \end{cases} \tag{25}$$

By employing a Jeffreys' prior we are assigning equal probability per decade (scale invariance), mainly useful when the prior range spans several orders of magnitude. In case the prior lower limit includes zero, a *modified Jeffreys' prior* should be used instead to avoid the divergence at zero:

$$f_k(\Theta_k) = \begin{cases} \frac{1}{\Theta_k+\Theta_k^\mathrm{uni} \ln\left[\Theta_k^\mathrm{uni}+\Theta_k^\mathrm{max}/\Theta_k^\mathrm{uni}\right]} & \text{, for} 0 \leq \Theta_k \leq \Theta_k^\mathrm{max}, \\ 0, & \text{otherwise.} \end{cases} \tag{26}$$

For $\Theta_k \gg \Theta_k^\mathrm{uni}$, Eq. (26) behaves just like a Jeffreys' prior, whereas for $\Theta_k \ll \Theta_k^\mathrm{uni}$ it behaves like a uniform prior, thus not diverging at zero. Θ_k^uni marks the transition between the two regimes.

4. Markov chain Monte Carlo

After inspection of Eq. (18), the need for a mathematical tool that is able to efficiently evaluate the multi-dimensional integrals required in the computation of the marginal posteriors becomes clear. This constitutes the rationale behind the method known as Markov chain Monte Carlo, first introduced in the early 1950s by statistical physicists and nowadays widely used in all areas of science and economics.

4.1. Metropolis-Hastings algorithm

The aim is to draw samples from the *target distribution*, $p(\Theta|D,I)$, by constructing a pseudo-random walk in model parameter space such that the number of samples drawn from a particular region is proportional to its posterior density. Such a pseudo-random walk is achieved by generating a Markov chain, whereby a new sample, X_{t+1}, depends on the previous sample[3], X_t, in accordance with a time-independent quantity called the *transition kernel*, $p(X_{t+1}|X_t)$. After a burn-in phase, $p(X_{t+1}|X_t)$ is able to generate samples of Θ with a probability density converging on the target distribution. The Markov chain must fulfil three requirements in order to achieve this convergence: it must be *irreducible*, *aperiodic* and *positive recurrent* (Roberts 1996).

The algorithm that we employ in order to generate a Markov chain was initially proposed by Metropolis et al. (1953), and subsequently generalised by Hastings (1970), this latter version being commonly referred to as the Metropolis-Hastings algorithm. It works in the following way: Suppose the current sample, at some instant denoted by t, is represented by X_t. We would like to steer the Markov chain toward the next sampling state, X_{t+1}, by first proposing a new sample to be drawn, Y, from a *proposal distribution*, $q(Y|X_t)$, centred on X_t. Here we specifically treat $q(Y|X_t)$ as being a multivariate normal distribution with covariance matrix Σ. We employ independent Gaussian parameter proposal distributions and thus Σ is assumed diagonal. The proposed sample is then accepted with a probability given by:

$$\alpha(X_t, Y) = \min(1, r) = \min\left[1, \frac{p(Y|D,I)}{p(X_t|D,I)}\frac{q(X_t|Y)}{q(Y|X_t)}\right], \qquad (27)$$

where $\alpha(X_t, Y)$ is the *acceptance probability* and r is called the *Metropolis ratio*. In the present case of a symmetric proposal distribution, we have $q(X_t|Y) = q(Y|X_t)$. As a result, if the posterior density for the proposed sample is greater than or equal to that of the current sample, i.e., $p(Y|D,I) \geq p(X_t|D,I)$, then the proposal will always be accepted, otherwise it will be accepted with a probability given by the ratio of the posterior densities. If Y is not accepted, then the chain will keep the current sampling state, i.e., $X_{t+1} = X_t$. The procedure just described is repeated for a predefined number of iterations or, alternatively, for a number of iterations determined by a convergence test applied to the Markov chain (e.g., Gelman & Rubin 1992). The total number of iterations is denoted by $n_{\rm it}$.

Once a Markov chain has been created, the problem of marginalization becomes trivial, as the way to extract information on the individual parameters is simply to generate a histogram for each parameter and thus obtain its PDF. An appropriate number of bins in the histograms can be selected using for example Scott's criterion (Scott 1979). Usually the information in the PDF will be condensed using some summary statistics, like for example finding the median of the distribution and the 68% credible region around it.

4.2. Parallel tempering

The Metropolis-Hastings algorithm outlined above might become stuck in a local maximum of the target distribution, thus failing to fully explore all regions in parameter space containing significant probability. A way of overcoming this is to employ parallel tempering (e.g., Earl & Deem 2005), whereby a discrete set of progressively flatter versions of the target distribution are created by introducing a *temperature parameter*, $\mathscr{T}$. In practice, use is made of its reciprocal, $\beta = 1/\mathscr{T}$, referred to as the *tempering parameter*. By modifying Eq. (17), we generate the tempered distributions as follows:

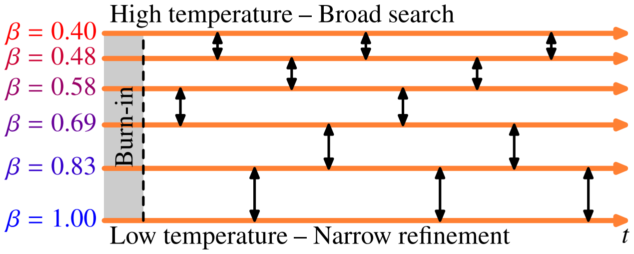

Fig. 2. Schematic representation of the functioning of the parallel tempering mechanism, whereby tempering chains are allowed to swap their parameter states (swaps are indicated by vertical arrows).

$$p(\Theta|D,\beta,I) \propto p(\Theta|I)\, p(D|\Theta,I)^{\beta}, \quad 0 < \beta \leq 1. \qquad (28)$$

For $\beta = 1$, we recover the target distribution, also called the *cold sampler*, whereas for $\beta < 1$ the hotter distributions are effectively flatter versions of the target distribution. Drawing samples from a hotter, i.e., flatter, version of the target distribution will allow, in principle, to visit regions of parameter space containing significant probability, otherwise not accessible to the basic algorithm. The problem of parameter estimation obviously continues to rely on samples drawn from the cold sampler. In Sect. 4.4 we describe how samples drawn from the remaining tempered distributions are useful in evaluating Bayes' factor.

Implementation of parallel tempering works in the following way: Several versions of the Metropolis-Hastings algorithm are launched in parallel (n_β in total), each being characterised by a different tempering parameter, β_i. At random intervals, comprehending a mean number ($n_{\rm swap}$) of iterations, a pair of adjacent chains, labelled with β_i and β_{i+1}, is randomly chosen and a proposal is made to swap their parameter states. The proposed swap is then accepted with a probability given by:

$$\begin{aligned}\alpha_{\rm swap} &= \min(1, r_{\rm swap})\\ &= \min\left[1, \frac{p(X_{t,i+1}|D,\beta_i,I)p(X_{t,i}|D,\beta_{i+1},I)}{p(X_{t,i}|D,\beta_i,I)p(X_{t,i+1}|D,\beta_{i+1},I)}\right], \qquad (29)\end{aligned}$$

where, at instant t, chain β_i is in state $X_{t,i}$ and chain β_{i+1} is in state $X_{t,i+1}$. By running such a set of cooperative chains, we effectively enable the algorithm to sample the target distribution in a way that allows for both the investigation of its overall features (low-β chains) and the examination of the fine details of a local maximum (high-β chains). A schematic representation of the functioning of the parallel tempering mechanism is shown in Fig. 2. In Fig. 3, a version of the Metropolis-Hastings algorithm is shown, written in pseudocode, and with the inclusion of the parallel tempering mechanism.

Concerning the values taken by the tempering parameter, $\{\beta_i\}$, optimal values are chosen in order to achieve a *swap acceptance rate* between adjacent levels of ∼50%. Heuristically, we can assert that by employing a geometric progression (cf. Benomar et al. 2009a),

$$\beta_i = \lambda^{1-i}, \qquad (30)$$

such a desideratum is reached by setting $\lambda \sim 1.2$. The number of chains, n_β, should be chosen such as to reach a desired balance between sampling efficiency and computational time. However,

---

[3] A remark on the notation: X_t may be thought of as a single vector in parameter space.

```
procedure ParallelTemperingMetropolis–Hastings
    $X_{0,i} = X_0\,,\ 1 \le i \le n_\beta$
    for $t = 0, 1, \ldots, n_{\mathrm{it}} - 1$ do
        for $i = 1, 2, \ldots, n_\beta$ do
            Propose a new sample to be drawn from a
              proposal distribution: $Y \sim N(X_{t,i}; \Sigma_i)$
            Compute the Metropolis ratio:
              $\ln r = \ln p(Y|D,\beta_i,I) - \ln p(X_{t,i}|D,\beta_i,I)$
            Sample a uniform random variable:
              $U_1 \sim \mathrm{Uniform}(0,1)$
            if $\ln U_1 \le \ln r$ then
                $X_{t+1,i} = Y$
            else
                $X_{t+1,i} = X_{t,i}$
            end if
        end for
        $U_2 \sim \mathrm{Uniform}(0,1)$
        if $U_2 \le 1/n_{\mathrm{swap}}$ then
            Select random chain:
              $i \sim \mathrm{UniformInt}(1, n_\beta - 1)$
            Compute $r_{\mathrm{swap}}$:
              $\ln r_{\mathrm{swap}} = \ln p(X_{t,i+1}|D,\beta_i,I) + \ln p(X_{t,i}|D,\beta_{i+1},I)$
                $- \ln p(X_{t,i}|D,\beta_i,I) - \ln p(X_{t,i+1}|D,\beta_{i+1},I)$
            $U_3 \sim \mathrm{Uniform}(0,1)$
            if $\ln U_3 \le \ln r_{\mathrm{swap}}$ then
                Swap parameter states of chains $i$ and $i+1$:
                  $X_{t,i} \leftrightarrow X_{t,i+1}$
            end if
        end if
    end for
    return $X_{t,i}\,,\ \forall t\,,\ i{:}\beta_i{=}1$
end procedure
```

Fig. 3. Version of the Metropolis-Hastings algorithm written in pseudocode and with the inclusion of parallel tempering.

when using the parallel tempering mechanism in model comparison problems, as we will get back to in Sect. 4.4, a large number of tempering chains are needed (typically $n_\beta \gtrsim 10$). The value of n_{swap} should be chosen inversely proportional to n_β (typically a few dozens).

4.3. Automated MCMC

So far we have not mentioned the need to adequately choose the set $\{\sigma\}$ of diagonal elements of the Σ matrix, indicating the width of the Gaussian proposal distribution for each parameter. The set of individual σ values specifies the direction and step size in parameter space when proposing a new sample to be drawn. The optimal choice of $\{\sigma\}$ is closely related to the average rate at which proposed state changes are accepted, the so-called *acceptance rate*. Accordingly, small σ values will lead to a large acceptance rate, with successive samples being highly correlated and ultimately requiring a large number of iterations in order to yield equilibrium distributions of model parameters. On the other hand, large σ values will lead to a low acceptance rate, meaning that proposed state changes will seldom be accepted. This is illustrated in Fig. 4, where the same simplified target distribution is sampled by three chains, each being characterised by a set of σ values differing on the respective magnitudes. Roberts et al. (1997) recommend, based on empirical studies, calibrating the acceptance rate to ~25% when dealing with a high-dimensional model as it is the case when performing a global peak-bagging.

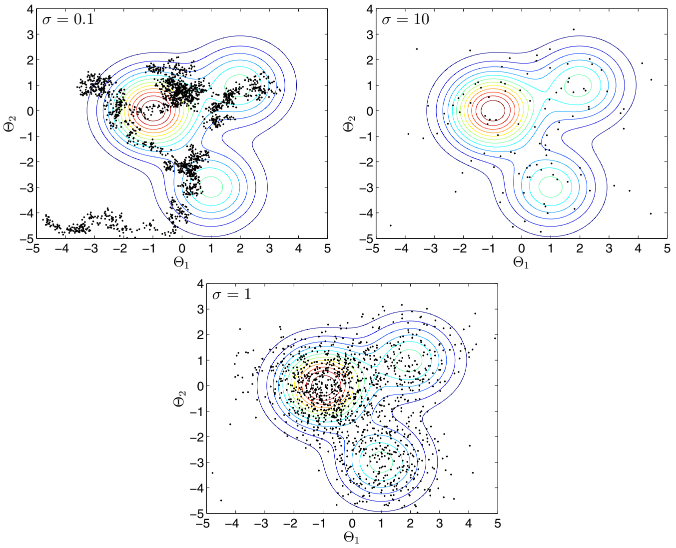

Fig. 4. The same target distribution sampled by three chains, each being characterised by a different set $\{\sigma\}$. The contours map the target distribution, which in turn depends only on the parameters Θ_1 and Θ_2. The starting point in each of the chains is $(\Theta_1, \Theta_2) = (-4.5, -4.5)$ and all contain 2000 iterations. Both parameters share a common σ-value whose optimal setting is $\sigma = 1$. It is important to note that given a sufficiently large number of iterations, all the chains would eventually map out the target distribution, however an optimal choice of the proposal distribution will result in significantly faster convergence.

One could, of course, employ a trial-and-error approach and manually calibrate the σ values. However, since we are dealing with a large number of parameters that, in addition, correspond to several different physical quantities, this would quickly become very time-consuming and impractical. We instead employ an automated process of calibration of the proposal σ values, which is based on a statistical control system similar to the one described in Gregory (2005b). The control system makes use of an error signal to steer the selection of the σ values during the burn-in stage of a single parallel tempering MCMC run, acting independently on each of the tempered chains. The error signal is proportional to the difference between the current acceptance rate and the target acceptance rate. As soon as the error signal for each of the tempered chains is less than a measure of the Poisson fluctuation expected for a zero mean error (computed as the square root of the target acceptance rate times the number of iterations between changes in the σ values), the control system is turned off and the algorithm switches to the standard parallel tempering MCMC. In practice this effectively marks the end of the burn-in stage.

The control system as briefly described here is also used in Gruberbauer et al. (2009), whereas Benomar et al. (2009a) employ a self-learning process that appropriately adapts the covariance matrix, assumed non-diagonal.

4.4. Model comparison using parallel tempering MCMC

We are now interested in computing the odds ratio, O_{ij}, in favour of model M_i over model M_j according to Eq. (22). When analysing solar-like oscillations, a recurrent difficulty is to correctly tag the modes of oscillation by angular degree ℓ. There are two possible ways of tagging the modes or, equivalently, two competing models. Computation of O_{ij} is thus a means of assessing which of the two identification scenarios is statistically more

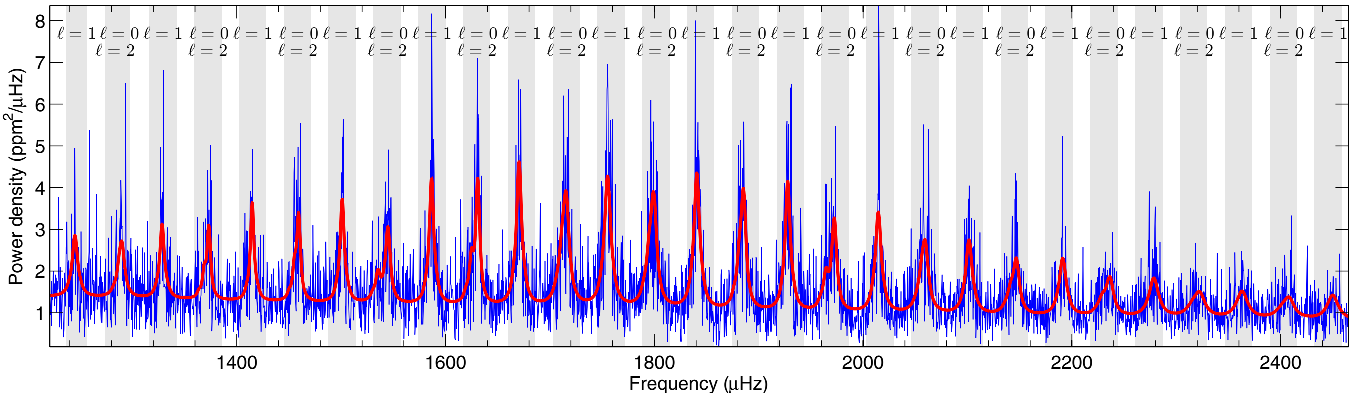

Fig. 5. Power density spectrum of HD 49933 with the best-fitting model (using prior set S2) overlaid. The shaded areas indicates the ranges of the uniform priors on the frequencies.

likely (although not necessarily physically more meaningful, as is often misinterpreted).

Samples drawn from the tempered distributions can, in principle, be used to compute the global likelihood, $p(D|M_i, I)$, of a given model M_i. Notice that Bayes' factor, B_{ij}, is defined as the ratio of the global likelihoods of two competing models:

$$B_{ij} \equiv \frac{p(D|M_i, I)}{p(D|M_j, I)} = \exp\left[\ln p(D|M_i, I) - \ln p(D|M_j, I)\right] \cdot \qquad (31)$$

It can be shown that the global likelihood of a model is given by (for a derivation see Gregory 2005b):

$$\ln p(D|M_i, I) = \int_0^1 \langle \ln p(D|M_i, X, I)\rangle_\beta \, \mathrm{d}\beta, \qquad (32)$$

where

$$\langle \ln p(D|M_i, X, I)\rangle_\beta = \frac{1}{n}\sum_t \ln p(D|M_i, X_{t,\beta}, I) \qquad (33)$$

is the expectation value of the natural logarithm of the likelihood for a particular tempered chain characterised by β. The set $\{X_{t,\beta}\}$ represents the corresponding samples drawn after the burn-in stage, while n is the number of samples in each set. A sufficient number ($\gtrsim$10) of parallel tempered chains is required if we are to estimate the integral in Eq. (32) by interpolating values of $\langle \ln p(D|M_i, X, I)\rangle_\beta$.

5. Examples

In the following we will pick a couple of examples where we have applied the described Automated Parallel Tempering MCMC formalism to recent measurements of solar-like oscillators.

5.1. HD 49933: the importance of priors

We have performed an analysis of the star HD 49933, based on 180 days of photometry from the CoRoT satellite arising from two runs: The initial 60-day run, IRa01, and 120 days from the longer second run, LRa01. The time series was split up into segments of 30 days and the power spectra of the individual segments were averaged to construct a mean power spectrum ($s = 6$ in Eq. (2)). The acoustic spectrum of this F5 main-sequence star has proven to be very difficult to interpret mainly due to the relatively large linewidths (see Fig. 5). We assume the ridge identification denoted as "Scenario B" in Benomar et al. (2009b).

Table 3. Prior input for the HD 49933 analysis.

Parameter	Prior
Frequencies	Uniform
Heights	Modified Jeffreys
Linewidths	Uniform
Inclination	Uniform (0°–90°)
Rotation	S1: Uniform on ν_s (0–10 μHz) S2: Gaussian on ν_s^* (1.65 ± 0.17 μHz)

The acoustic spectrum was fitted using the APT MCMC formalism, but using two different sets of priors (see Table 3). The first set (S1) was constructed using only ignorance priors, while the second set (S2) includes knowledge about the stellar rotation. From spectroscopic and asteroseismic studies of HD 49933, Bruntt (2009) was able to constrain the rotation of the star to $v\sin(i) = 10 \pm 1$ km s^{-1} and the radius to $R/R_\odot = 1.385 \pm 0.031$, which can be combined to impose a constraint on the projected rotational splitting, $\nu_\mathrm{s}^* = \nu_\mathrm{s}\sin(i)$, of 1.65 ± 0.17 μHz. In set S2 this knowledge is added as a gaussian prior on the projected splitting of the star. In both cases the fits were done using the following configuration:

- 15 orders were fitted with $\ell = 0, 1, 2$ modes in a fitting window spanning from 1220 to 2465 μHz (see Fig. 5);
- one linewidth and one height per order assigned to the $\ell = 0$ mode, and then linearly interpolated by frequency and scaled to the higher degree modes;
- rotation and inclination angle fitted with the two free parameters, ν_s^* and i;
- the background was parametrized as a sum of 3 Harvey-like models plus a white noise contribution;
- 800 000 samples were drawn from the target distribution, employing 10 parallel chains.

First of all, it is important to note that the results are consistent with the ones reported in Benomar et al. (2009b). For example the derived frequencies and linewidths are all well within the error bars. We will here focus on the results of the rotational splitting and inclination angle. The probability density functions for the fitted parameters when using ignorance priors (S1) are shown in Fig. 6a and, after applying the Gaussian prior on the projected splitting (S2), the results change to the ones shown in Fig. 6b.

What these results demonstrate is, first of all, that these techniques are extremely efficient at probing and constraining parameters which traditional methods would have considerable

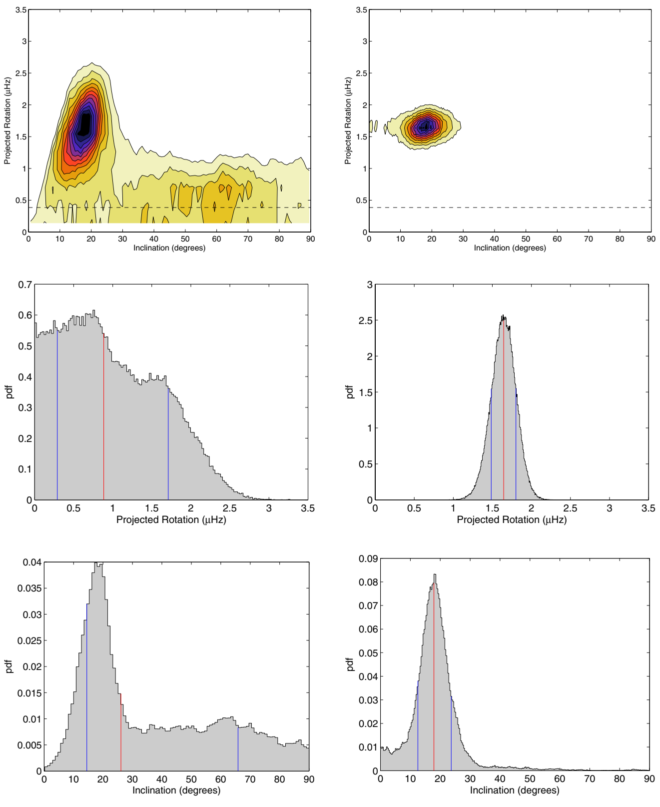

(a) (b)

Fig. 6. Results on the rotation and inclination angle of HD 49933. In both cases the prior on the inclination angle is uniform in the interval 0°–90°. **a)** We employ a uniform prior on rotation (S1). **b)** We employ a Gaussian prior on projected rotation (S2). The vertical lines in the histograms indicate the median and the boundaries of the 68% credible regions of the distributions. The dashed line in the top figures indicates the frequency resolution in the spectrum.

difficulty in constraining. In Benomar et al. (2009b), where similar techniques are employed, the derived inclination angle was $17^{\circ}{}^{+7^{\circ}}_{-9^{\circ}}$ and the rotational splitting placed in the range 3.5–6.0 μHz, with which our results are perfectly consistent with. Another point to be drawn from this example is the importance of the inclusion of prior knowledge. By incorporating our prior knowledge about the rotation of the star through the accurate measurements from a spectral analysis, we are able to yield a much cleaner constraint on the inclination angle, which in Fig. 6a has a considerable tail of probability towards large inclinations.

It is important to note that this prior on $\nu_{\rm s}^{*}$ is strong in the sense that it dominates the fit. This simply comes from the fact that the data do not provide any further information on this parameter and so our prior knowledge of the model is still providing the best constraint. In such cases one of course has to be careful that such a strong prior is not wrongfully restrictive. If other effects (in this case, for instance, differential rotation or second-order rotational effects) were present, this could introduce biases to the fitted results. This could of course be tested using the methodology described in Sects. 3.2 and 4.4, by constructing models that incorporate these effects and testing their significance.

5.2. Procyon: the problem of ridge identification

Here we address the issue of tagging the oscillation modes by angular degree in the case of the F5 star Procyon. We have thus reanalysed the data acquired during a multi-site campaign (Arentoft et al. 2008; Bedding et al. 2010b) carried to observe oscillations in this star. The data consist of high-precision velocity observations obtained over more than three weeks with eleven telescopes, representing the most extensive campaign organised so far on a solar-type oscillator.

The problem of ridge identification in F stars dates back to when CoRoT observations of HD 49933 were first analysed (Appourchaux et al. 2008), a problem that would be recently solved for this star only after a new longer time series was made available (Benomar et al. 2009b). Bedding et al. (2010b) address this same problematic in the case of Procyon by employing three distinct methodologies: (i) a collapsed power spectrum along several radial orders; (ii) a scaled échelle diagram (Bedding & Kjeldsen 2010); and (iii) Bayesian model comparison (as described in Sect. 4.4). The last-mentioned methodology statistically favours their Scenario A over their Scenario B identification, whereas the first and second methodologies suggest the contrary although without quantifying their preference for Scenario B in a statistical sense.

We performed a peak-bagging of the power spectrum of Procyon considering both identification scenarios while simultaneously testing for the presence of $\ell = 3$ modes. This gives a total of four competing models, i.e., $\{M_{\rm A}, M_{\rm A}^{\ell=3}, M_{\rm B}, M_{\rm B}^{\ell=3}\}$, the notation chosen to be unambiguous. The details of the peak-bagging as implemented here slightly differ from those presented in Bedding et al. (2010b), and especially concern the limits of the fitting window and the way in which the background was parametrized. The details are as follows:

- The peak-bagging was performed on the sidelobe-optimised power density spectrum whose intrinsic frequency resolution is 0.77 μHz. Peaks were described by symmetric Lorentzians centred on the mode frequencies. Three frequencies were fitted per overtone, each with a different angular degree ($\ell = 0, 1, 2$). Type of prior imposed at first: independent and uniform, centred (± 8 μHz) on the initial guesses. The mode frequencies were further constrained to lie close to the ridge centroids and to have only small jumps from one order to the next. Also, a Gaussian prior ($\mu = 4$ μHz, $\sigma = 5$ μHz) was imposed on the small frequency separation, $\delta\nu_{02}$, between adjacent modes with $\ell = 0$ and $\ell = 2$. The small separation was not itself a free parameter in the fit, but instead a derived quantity. Note that the last-mentioned constraint implies that the type of prior on the $\ell = 0, 2$ frequency parameters is ultimately not independent nor uniform. Optionally, modes with $\ell = 3$ could be included in the model with their frequencies fixed to

$$\nu_{n-1,3} = \nu_{n,1} - \tfrac{5}{3}(\nu_{n,0} - \nu_{n-1,2}), \qquad (34)$$

  according to the asymptotic relation (Tassoul 1980). A total of 14 overtones were considered and the fitting window runs from 500 to 1300 μHz. By employing this construction it is assumed that no mixed modes are present in the fitting window. The inclusion of $\ell = 3$ modes does not add any more free parameters, while adding however their features to the model spectrum which are derived from the fitted $\ell = 0, 1, 2$ frequencies.
- The linewidth was parametrized as a linear function of frequency, defined by two parameters Γ_{600} and Γ_{1200}, which are

Table 4. Model probabilities.

Model	ln $p(D\|\text{Model}, I)$	Probability
M_A	2789.723	39.25%
$M_\text{A}^{\ell=3}$	2790.046	54.23%
M_B	2785.806	0.78%
$M_\text{B}^{\ell=3}$	2787.801	5.74%

the values at 600 and 1200 μHz, respectively. Both parameters were fitted. Type of prior imposed: uniform in the range 0–10 μHz.

- The heights of radial modes in units of power density were fixed according to Chaplin et al. (2008b):

$$S_{n0} = \frac{2\,A^2\,T}{\pi T \Gamma_{n0} + 2}, \tag{35}$$

where A^2 is the total power of the mode as determined from the power envelope for radial modes (Kjeldsen et al. 2008), and T is the effective length of the observational run. The heights of non-radial modes were then defined based on the heights of radial modes according to Eq. (12), and taking into account the appropriate V_ℓ/V_0 ratios given in Table 1 of Kjeldsen et al. (2008).
- The background was parametrized as a linear function of frequency since it had previously been suppressed at low frequencies (high-pass cut at 280 μHz) to effectively remove slow variations.
- The inclination angle between the direction of the stellar rotation axis and the line of sight was fixed at 31.1°, which is the inclination of the binary orbit and is consistent with the rotational modulation of the velocity curve. The rotational splitting was fixed at 0.7 μHz, which was chosen to match the observed value of $v\sin(i) = 3.16$ km s^{-1} (Allende Prieto et al. 2002), given the known radius of the star of 2.05 $R_\odot$ (Kervella et al. 2004).
- We drew ~800 000 samples from the target distribution after a burn-in phase. We employed 12 parallel tempered chains.
- We thus have a total of 46 free parameters, namely, 42 frequencies, 2 parameters for the linewidth and 2 parameters for the background.

Table 4 summarises the model selection calculations assuming equal prior probabilities for the models belonging to our discrete model space. Individual probabilities are assigned to models according to Eq. (21). Similarly to Bedding et al. (2010b), Bayesian model comparison again statistically favours Scenario A over Scenario B. Furthermore, the presence of residual power due to $\ell = 3$ modes is suggested. Computing Bayes' factor in favour of model $M_\text{A}^{\ell=3}$ over model $M_\text{B}^{\ell=3}$ gives a factor of approximately 9:1 or, equivalently, a logarithmic factor of 2.2, which classifies as "significant" on Jeffreys' scale. Figure 7 displays the power density spectrum of Procyon in échelle format with the fitted frequencies for model $M_\text{A}^{\ell=3}$ overlaid.

6. Summary and discussion

In this paper, we have presented the basic theory and methods behind the extraction of parameters from the power spectra of solar-like stars. In order to handle the ever rising quality and complexity of modern asteroseismic data, we have developed a tool (APT MCMC) that enables us to constrain parameters associated with the subtlest features in the spectra. The algorithm has been extensively tested and performs extremely well, not only in the traditional case of extracting oscillation frequencies, but also when pushing the limit where traditional methods have difficulties, such as constraining linewidths, rotational splittings and stellar inclination angles. In this work we have focused on data in the signal-to-noise regime of current asteroseismic measurements. In the case of very high signal-to-noise ratios, other features in the power spectrum becomes important, such as mode asymmetries and rotational splittings dependent on ℓ, arising from differential rotation with radius. In future work these effects will be incorporated into the program and tested on solar data.

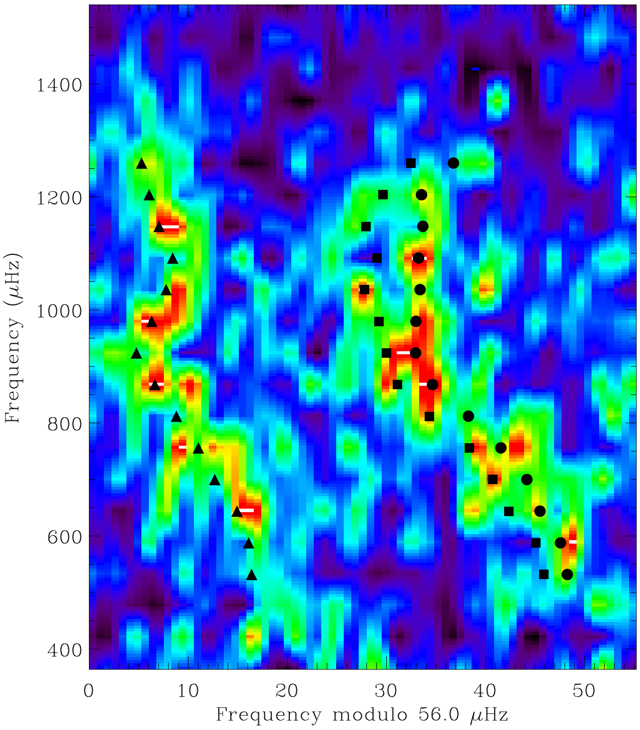

Fig. 7. Power density spectrum of Procyon (smoothed to 2 μHz) in échelle format. The fitted frequencies for model $M_\text{A}^{\ell=3}$ appear as overlaid filled symbols. Symbol shapes indicate mode degree: $\ell = 0$ (circles), $\ell = 1$ (triangles), $\ell = 2$ (squares).

One disadvantage of the method is that it can be quite computationally intensive, both to implement and run, when compared to traditional MLE fits. This is however balanced by the much added information outputted from the fits, specifically in the probability distributions of each parameter, making it easy to obtain accurate, reliable and realistic error bars on the results – a feature seriously missing from the traditional methods. The parameter estimation also benefits enormously from the possibilities the Bayesian formalism provides with inclusion of prior information. This not only allows control of the fit to, for example, not allow unphysical parameter combinations, but also include information into the fit that is better constrained by other measurements (as we saw in Sect. 5.1). Another powerful feature of the method lies in the parallel tempering, which not only keeps the fits from getting stuck in local maxima, but also provides an objective way of comparing different competing models, as it provides a way of calculating the global likelihood. This can for example be utilized in the familiar problem of ridge identification in solar-like stars (see Sect. 5.2).

A thing to keep in mind is also that the APT MCMC algorithm is completely general, in the sense that it could be applied to other problems without modification. MCMC methods are being used in various branches of astrophysics: cosmology (Liddle 2009), extra solar planets (Gregory 2005a) and stellar model fitting (Bazot et al. 2008), but in fact the methods would be applicable in any problem including parameter estimation. And as computational power continues to grow, the downsides are quickly becoming insignificant.

What could to some extent also be seen as a disadvantage of these methods is that they can never be fully automated, in the sense that they will not be able to handle a large number of stars without human interaction. The whole fundamental idea behind the Bayesian formalism is that it relies on "wise" human inputs on the priors and model setup that should not be done in an automated way. If nothing else, take this as a positive reassurance: You will, as an astrophysicist, never be obsolete to computers or monkeys with keyboards.

Acknowledgements. We would like to thank H. Kjeldsen, T. R. Bedding, C. Karoff, W. J. Chaplin, T. Appourchaux, R. A. García and O. Benomar for fruitful discussions and valuable comments. We also thank the anonymous referee for comments that helped improve the paper. T.L.C. is supported by grant with reference number SFRH/BD/36240/2007 from FCT/MCTES, Portugal. This work was supported by the project PTDC/CTE-AST/098754/2008 funded by FCT/MCTES, Portugal.

Appendix A: Computing $\mathscr{E}_{\ell m}(i)$ and V_ℓ

The $\mathscr{E}_{\ell m}(i)$ factors are given below for $\ell \in [0,4]$, having used Eq. (9):

$$\begin{aligned}
\mathscr{E}_{0,0}(i) &= 1\,, \\
\mathscr{E}_{1,0}(i) &= \cos^2 i\,, \\
\mathscr{E}_{1,\pm1}(i) &= \tfrac{1}{2}\sin^2 i\,, \\
\mathscr{E}_{2,0}(i) &= \tfrac{1}{4}(3\cos^2 i - 1)^2\,, \\
\mathscr{E}_{2,\pm1}(i) &= \tfrac{3}{8}\sin^2(2i)\,, \\
\mathscr{E}_{2,\pm2}(i) &= \tfrac{3}{8}\sin^4 i\,, \\
\mathscr{E}_{3,0}(i) &= \tfrac{1}{64}(5\cos(3i) + 3\cos i)^2\,, \\
\mathscr{E}_{3,\pm1}(i) &= \tfrac{3}{64}(5\cos(2i) + 3)^2\sin^2 i\,, \\
\mathscr{E}_{3,\pm2}(i) &= \tfrac{15}{8}\cos^2 i\sin^4 i\,, \\
\mathscr{E}_{3,\pm3}(i) &= \tfrac{5}{16}\sin^6 i\,, \\
\mathscr{E}_{4,0}(i) &= \tfrac{1}{64}(35\cos^4 i - 30\cos^2 i + 3)^2\,, \\
\mathscr{E}_{4,\pm1}(i) &= \tfrac{5}{256}(\tfrac{7}{2}\sin(4i) + \sin(2i))^2\,, \\
\mathscr{E}_{4,\pm2}(i) &= \tfrac{5}{128}(7\cos(2i) + 5)^2\sin^4 i\,, \\
\mathscr{E}_{4,\pm3}(i) &= \tfrac{35}{16}\cos^2 i\sin^6 i\,, \\
\mathscr{E}_{4,\pm4}(i) &= \tfrac{35}{128}\sin^8 i.
\end{aligned} \tag{A.1}$$

Notice that when the rotation axis is aligned with the line of sight ($i = 0°$), only the multiplet component with $m = 0$ is visible, thus making inviable an inference of rotation.

The spatial response function for each ℓ, V_ℓ, representing the ratio of the observed amplitude to the actual amplitude, is given here for the five lowest degree modes (Bedding et al. 1996):

$$\begin{pmatrix} V_0 \\ V_1 \\ V_2 \\ V_3 \\ V_4 \end{pmatrix} = \begin{pmatrix} 1 & \frac{2}{3} & \frac{1}{2} & \frac{2}{5} \\ \frac{2}{\sqrt{3}} & \frac{\sqrt{3}}{2} & \frac{2\sqrt{3}}{5} & \frac{1}{\sqrt{3}} \\ \frac{\sqrt{5}}{4} & \frac{4}{3\sqrt{5}} & \frac{\sqrt{5}}{4} & \frac{8}{7\sqrt{5}} \\ 0 & \frac{\sqrt{7}}{12} & \frac{4}{5\sqrt{7}} & \frac{\sqrt{7}}{8} \\ -\frac{1}{8} & 0 & \frac{3}{32} & \frac{16}{105} \end{pmatrix} \times \begin{pmatrix} 1-c & c-1 & c-1 \\ c & 1-2c & -c \\ 0 & c & 1-c \\ 0 & 0 & c \end{pmatrix} \times \begin{pmatrix} 1 \\ u_2 \\ v_2 \end{pmatrix}, \tag{A.2}$$

where u_2 and v_2 are wavelength-dependent classical limb-darkening coefficients (Allen 1973) and c is a parameter defining the observational method. This matrix product can be used for velocity measurements by setting $c = 1$ and for intensity measurements by setting $c = 0$.

References

Abrams, D., & Kumar, P. 1996, ApJ, 472, 882
Aerts, C., Christensen-Dalsgaard, J., & Kurtz, D. W. 2010, Asteroseismology, ed. C. Aerts, J. Christensen-Dalsgaard, & D. W. Kurtz (Springer)
Aigrain, S., Favata, F., & Gilmore, G. 2004, A&A, 414, 1139
Allen, C. W. 1973, Astrophysical quantities, 3rd edn., ed. C. W. Allen (Athlone Press)
Allende Prieto, C., Asplund, M., García López, R. J., & Lambert, D. L. 2002, ApJ, 567, 544
Anderson, E. R., Duvall, Jr., T. L., & Jefferies, S. M. 1990, ApJ, 364, 699
Appourchaux, T. 2003a, A&A, 412, 903
Appourchaux, T. 2003b, Ap&SS, 284, 109
Appourchaux, T. 2004, A&A, 428, 1039
Appourchaux, T., Berthomieu, G., Michel, E., et al. 2006, in ESA SP-10306, ed. M. Fridlund, A. Baglin, J. Lochard, & L. Conroy, 429
Appourchaux, T., Michel, E., Auvergne, M., et al. 2008, A&A, 488, 705
Arentoft, T., Kjeldsen, H., Bedding, T. R., et al. 2008, ApJ, 687, 1180
Ballot, J. 2010, Astron. Nachr., 331, 933
Ballot, J., García, R. A., & Lambert, P. 2006, MNRAS, 369, 1281
Ballot, J., Appourchaux, T., Toutain, T., & Guittet, M. 2008, A&A, 486, 867
Bazot, M., Bourguignon, S., & Christensen-Dalsgaard, J. 2008, Mem. Soc. Astron. Ital., 79, 660
Bedding, T. R., & Kjeldsen, H. 2008, in 14th Cambridge Workshop on Cool Stars, Stellar Systems, and the Sun, ed. G. van Belle, ASP Conf. Ser., 384, 21
Bedding, T. R., & Kjeldsen, H. 2010, Commun. Asteroseismol., 161, 3
Bedding, T. R., Kjeldsen, H., Reetz, J., & Barbuy, B. 1996, MNRAS, 280, 1155
Bedding, T. R., Huber, D., Stello, D., et al. 2010a, ApJ, 713, L176
Bedding, T. R., Kjeldsen, H., Campante, T. L., et al. 2010b, ApJ, 713, 935
Benomar, O., Appourchaux, T., & Baudin, F. 2009a, A&A, 506, 15
Benomar, O., Baudin, F., Campante, T. L., et al. 2009b, A&A, 507, L13
Bruntt, H. 2009, A&A, 506, 235
Campante, T. L., Karoff, C., Chaplin, W. J., et al. 2010, MNRAS, 408, 542
Chaplin, W. J., Appourchaux, T., Arentoft, T., et al. 2008a, Astron. Nachr., 329, 549
Chaplin, W. J., Houdek, G., Appourchaux, T., et al. 2008b, A&A, 485, 813
Chaplin, W. J., Appourchaux, T., Elsworth, Y., et al. 2010, ApJ, 713, L169
Christensen-Dalsgaard, J. 2003, Lecture Notes on Stellar Oscillations
Christensen-Dalsgaard, J. 2004, Sol. Phys., 220, 137
Christensen-Dalsgaard, J., Kjeldsen, H., Brown, T. M., et al. 2010, ApJ, 713, L164
De Ridder, J., Barban, C., Baudin, F., et al. 2009, Nature, 459, 398
Dupret, M., Belkacem, K., Samadi, R., et al. 2009, A&A, 506, 57
Duvall, Jr., T. L., & Harvey, J. W. 1986, in Seismology of the Sun and the Distant Stars, ed. D. O. Gough, NATO ASIC Proc. 169, 105
Duvall, Jr., T. L., Jefferies, S. M., Harvey, J. W., Osaki, Y., & Pomerantz, M. A. 1993, ApJ, 410, 829
Earl, D. J., & Deem, M. W. 2005, Phys. Chem. Chem. Phys. (Incorporating Faraday Transactions), 7, 3910
Fröhlich, C., Romero, J., Roth, H., et al. 1995, Sol. Phys., 162, 101
Gabriel, M. 1994, A&A, 287, 685
Gelman, A., & Rubin, D. 1992, Stat. Sci., 7, 457
Gilliland, R. L., Brown, T. M., Christensen-Dalsgaard, J., et al. 2010, PASP, 122, 131
Gizon, L., & Solanki, S. K. 2003, ApJ, 589, 1009
Gregory, P. C. 2005a, ApJ, 631, 1198

Gregory, P. C. 2005b, Bayesian Logical Data Analysis for the Physical Sciences: A Comparative Approach with “Mathematica” Support, ed. P. C. Gregory (Cambridge University Press)
Gruberbauer, M., Kallinger, T., Weiss, W. W., & Guenther, D. B. 2009, A&A, 506, 1043
Grundahl, F., Kjeldsen, H., Christensen-Dalsgaard, J., Arentoft, T., & Frandsen, S. 2007, Commun. Asteroseismol., 150, 300
Harvey, J. 1985, High-resolution helioseismology, Tech. Rep.
Hastings, W. K. 1970, Biometrika, 57, 97
Hekker, S., Broomhall, A., Chaplin, W. J., et al. 2010a, MNRAS, 402, 2049
Hekker, S., Debosscher, J., Huber, D., et al. 2010b, ApJ, 713, L187
Huber, D., Stello, D., Bedding, T. R., et al. 2009, Commun. Asteroseismol., 160, 74
Jeffreys, H. 1961, Theory of Probability, 3rd edn. (Oxford University Press)
Karoff, C., Metcalfe, T. S., Chaplin, W. J., et al. 2009, MNRAS, 399, 914
Karoff, C., Campante, T. L., & Chaplin, W. J. 2010, Astron. Nachr., in press `[arXiv:1003.4167v1]`
Kervella, P., Thévenin, F., Morel, P., et al. 2004, A&A, 413, 251
Kjeldsen, H., Bedding, T. R., Arentoft, T., et al. 2008, ApJ, 682, 1370
Koch, D. G., Borucki, W. J., Basri, G., et al. 2010, ApJ, 713, L79
Kumar, P., Franklin, J., & Goldreich, P. 1988, ApJ, 328, 879
Ledoux, P. 1951, ApJ, 114, 373
Liddle, A. R. 2009, Ann. Rev. Nucl. Part. Sci., 59, 95
Mathur, S., García, R. A., Régulo, C., et al. 2010, A&A, 511, A46
Mayor, M., Pepe, F., Queloz, D., et al. 2003, The Messenger, 114, 20
Metcalfe, T. S., Monteiro, M. J. P. F. G., Thompson, M. J., et al. 2010, ApJ, 723, 1583
Metropolis, N., Rosenbluth, A. W., Rosenbluth, M. N., Teller, A. H., & Teller, E. 1953, J. Chem. Phys., 21, 1087
Michel, E., Baglin, A., Auvergne, M., et al. 2008, Science, 322, 558
Mosser, B., & Appourchaux, T. 2009, A&A, 508, 877
Roberts, G. O. 1996, in Markov Chain Monte Carlo in Practice, (London: Chapman and Hall), 45
Roberts, G. O., Gelman, A., & Gilks, W. R. 1997, Ann. Appl. Prob., 7, 110
Scott, D. W. 1979, Biometrika, 66, 605
Stahn, T., & Gizon, L. 2008, Sol. Phys., 251, 31
Stello, D., Basu, S., Bruntt, H., et al. 2010, ApJ, 713, L182
Tassoul, M. 1980, ApJS, 43, 469
Toutain, T., & Appourchaux, T. 1994, A&A, 289, 649
Woodard, M. F. 1984, Ph.D. Thesis, AA (San Diego: University of California)

Appendix E

Monthly Notices
of the
ROYAL ASTRONOMICAL SOCIETY

Mon. Not. R. Astron. Soc. **408,** 542–550 (2010)   doi:10.1111/j.1365-2966.2010.17141.x

Modelling the autocovariance of the power spectrum of a solar-type oscillator

T. L. Campante,[1,2★] C. Karoff,[2,3] W. J. Chaplin,[3] Y. P. Elsworth,[3] R. Handberg[2] and S. Hekker[3]

[1] *Centro de Astrofísica, Faculdade de Ciências, Universidade do Porto, Rua das Estrelas, 4150-762 Porto, Portugal*
[2] *Danish AsteroSeismology Centre, Department of Physics and Astronomy, University of Aarhus, 8000 Aarhus C, Denmark*
[3] *School of Physics and Astronomy, University of Birmingham, Edgbaston, Birmingham B15 2TT*

Accepted 2010 June 4. Received 2010 June 4; in original form 2010 February 1

ABSTRACT

Asteroseismology is able to conduct studies on the interiors of solar-type stars from the analysis of stellar acoustic spectra. However, such an analysis process often has to rely upon subjective choices made throughout. A recurring problem is to determine whether a signal in the acoustic spectrum originates from a radial or a dipolar oscillation mode. In order to overcome this problem, we present a procedure for modelling and fitting the autocovariance of the power spectrum which can be used to obtain global seismic parameters of solar-type stars, doing so in an automated fashion without the need to make subjective choices. From the set of retrievable global seismic parameters we emphasize the mean small frequency separation and, depending on the intrinsic characteristics of the power spectrum, the mean rotational frequency splitting. Since this procedure is automated, it can serve as a useful tool in the analysis of the more than 1000 solar-type stars expected to be observed as part of the *Kepler* Asteroseismic Investigation (KAI). We apply the aforementioned procedure to simulations of the Sun. Assuming different apparent magnitudes, we address the issues of how accurately and how precisely we can retrieve the several global seismic parameters were the Sun to be observed as part of the KAI.

Key words: methods: data analysis – methods: statistical – stars: oscillations.

1 INTRODUCTION

Seismology of solar-type oscillators is a powerful tool that can be used to increase our understanding of stellar structure and evolution. Oscillations in main-sequence stars and subgiants have been measured, thanks to data collected from ground-based high-precision spectroscopy (for a review see e.g. Bedding & Kjeldsen 2008) and, more recently, to photometric space-based missions such as *CoRoT* (see e.g. Appourchaux et al. 2008; Michel et al. 2008). The *Kepler* mission (for a discussion on the expected results of the asteroseismic investigation see Christensen-Dalsgaard et al. 2008; Karoff et al. 2009) will lead to a revolution in the field of asteroseismology of solar-type oscillators, since it will increase by more than 2 orders of magnitude the number of stars for which high-quality observations will be available, while allowing for long-term follow-ups of a selection of these targets. As of the time of writing of this article, first results arising from the *Kepler* asteroseismic programme had already been made available (Bedding et al. 2010; Chaplin et al. 2010; Gilliland et al. 2010; Grigahcène et al. 2010; Hekker et al. 2010b; Kolenberg et al. 2010; Stello et al. 2010).

Due to the large number of stars observed with *Kepler*, automated and innovative analysis pipelines/tools are needed in order to cope with the plenitude of available data (see e.g. Huber et al. 2009; Mosser & Appourchaux 2009; Roxburgh 2009; Hekker et al. 2010a; Kallinger et al. 2010; Karoff, Campante & Chaplin 2010; Mathur et al. 2010). The automated pipelines dedicated to the analysis of acoustic spectra that have been developed so far aim mainly at measuring the frequency of maximum amplitude, $\nu_{\rm max}$, the maximum mode amplitude, $A_{\rm max}$, and the mean large frequency separation, $\Delta\nu$. In the present study, we give continuity to this work by presenting a tool capable of modelling and fitting the AutoCovariance of the Power Spectrum (ACPS)[1] of a solar-type oscillator. The current version of the tool accepts as free model parameters the mean small frequency separation parameter, D_0 (see Section 3.1.2 for the definition of this parameter), the mean rotational frequency splitting, $\nu_{\rm s}$, the mean linewidth, $\langle\Gamma\rangle$, and the stellar inclination angle, i. The output generated by this tool will hopefully contribute to further explore the diagnostic potential of solar-like oscillations, especially that of the large and small separations (see e.g. Christensen-Dalsgaard

---

★E-mail: campante@astro.up.pt; campante@phys.au.dk

[1] To be precise, we compute the autocovariance of the power density spectrum.

2004). These two quantities can in turn be used to provide estimates of the radii, masses and ages of solar-like stars with consistent uncertainties (Karoff et al. 2010).

We start in Section 2 by providing a logical basis that led us to the development of this particular analysis tool. This is followed by a thorough description of its implementation in Section 3. In Section 4 we apply the tool to simulated data, more specifically, to a solar analog as it would be seen by *Kepler*. A discussion and conclusions are presented in Section 5.

2 RATIONALE BEHIND THE ACPS-MODELLING PROCEDURE

Unlike a canonical *peak-bagging* procedure (see e.g. Anderson, Duvall & Jefferies 1990), in the framework of the ACPS-modelling procedure individual modes do not need to be tagged by angular degree, i.e. by wave number ℓ. This is required in peak-bagging to ensure the correct model is fitted to the observed modes. Instead we build a model that describes both the global and average properties of the most prominent modes, which are in turn encoded on a small set of free model parameters. This might be regarded as a major advantage, especially if we recall the ambiguity found in mode (angular degree) identification concerning the *CoRoT* target HD 49933, only recently solved after a new longer time-series was made available (Appourchaux et al. 2008; Benomar et al. 2009).

As it is currently implemented, the ACPS-modelling procedure assumes the small frequency separation to be constant and not a function of frequency. Especially for evolved stars, this was thought not to be a good approximation (Soriano & Vauclair 2008). However, in the light of the first *Kepler* results on red giants (Bedding et al. 2010), it is perfectly valid to assume – at least for low-luminosity red giants – a mean value of the small frequency separation between adjacent modes with $\ell = 0$ and 2, $\delta\nu_{02}$, it being in fact a nearly constant fraction of $\Delta\nu$. Therefore, the procedure presented herein can in principle also be employed in the case of evolved stars displaying solar-like oscillations. The ACPS-modelling procedure will however not provide sensible output when mixed modes (see e.g. Aizenman, Smeyers & Weigert 1977) are present. In any event, the presence of mixed modes will manifest clearly in the ACPS, either as a significant broadening of the peaks or by the appearance of extra peaks.

The way information is presented in the ACPS makes it very amenable for fitting. In fact, the ACPS of a solar-type oscillator will show prominent features at multiples of half the large frequency separation, a clear manifestation of the regular frequency structure of the acoustic spectrum. The shape of these features will depend upon the $\delta\nu_{02}$ and $\delta\nu_{01}$ spacings (see Section 3.1.2 for a definition of the latter), mode lifetime, rotation and stellar inclination. Fig. 1 displays an artificial acoustic spectrum of a solar analog (top panel) as it would be obtained from a 30-d long *Kepler*'s time-series together with a fit to its ACPS (bottom panel). Note the prominent features in the ACPS around 135 μHz and half that value. The latter feature is clearly split into two peaks which constitute a signature of $\delta\nu_{01}$. A signature of the $\delta\nu_{02}$ spacing is also present in the wings of the feature at $\Delta\nu$. The widths of either feature are generally a signature of the mode lifetime of the oscillations, whereas the presence of any fine structure is a signature of rotation and stellar inclination. The ACPS depicted in Fig. 1 does indeed provide us with information about the large and small frequency separations and mode lifetime. The question we address first is thus: *how do we extract this information from the autocovariance of the power spectrum?*

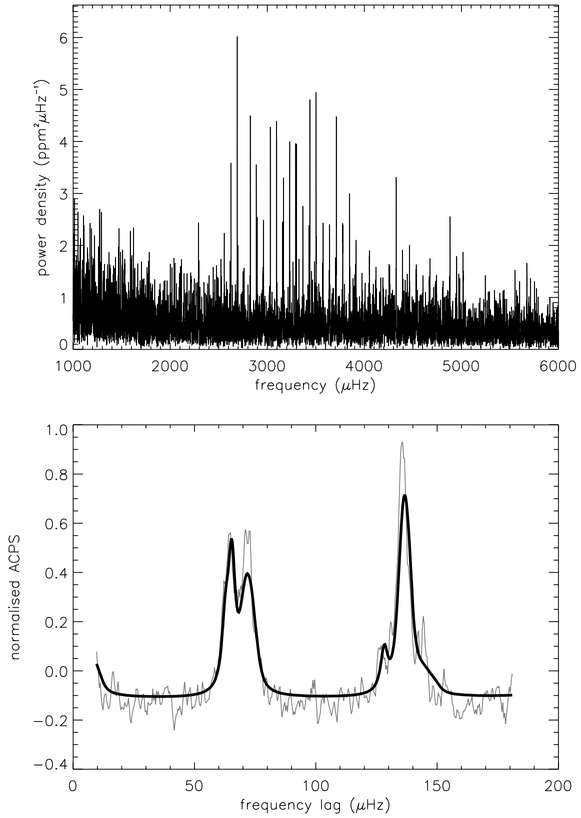

Figure 1. Top panel: artificial acoustic spectrum of a solar analog evidencing a regular frequency structure. Bottom panel: fit (black solid line) to the corresponding ACPS obtained using the MAP as our choice of summary statistic to represent the parameter posterior distributions. In order to enhance the visibility of the features in the ACPS, we have slightly smoothed it by running a boxcar average (this is done both to the observed and to the model ACPS). Note that the artificial star (Boris) has $\Delta\nu \simeq 135$ μHz (see discussion in Section 4).

3 THE ACPS-MODELLING PROCEDURE

We intend to fit the observed ACPS to an ACPS created from a model of the p-mode power density spectrum (PDS) that is described by a slightly modified asymptotic relation, which in turn depends only on a few free parameters (Section 3.1). Although we do not fully explore its potential, we opt for a Bayesian approach to the fitting problem for the simple reason that any prior information might be taken into account, particularly useful when constraining the parameter space (Section 3.2). Most importantly, we aim at obtaining a full joint posterior probability density function (PDF) concerning the set of model parameters, and hence we end up employing a Markov chain Monte Carlo (MCMC) sampler (Section 3.3).

3.1 Modelling the observed ACPS

The ACPS is computed as a function of the frequency lag, L, according to the following expression:

$$\mathrm{ACPS}(L) = \frac{1}{N}\sum_{j=0}^{N-L-1}(P_j - \overline{P})(P_{j+L} - \overline{P}), \tag{1}$$

where P_j is the particular value taken by the PDS at the fixed frequency bin j, $\overline{P}$ is the mean value of the sample population $\{P_j\}$, i.e. the mean value of the PDS within the frequency interval of interest and N is the total number of bins within this same frequency interval. The frequency interval of interest should be in accordance with the p-mode range. The lag L, which is expressed in terms of number of frequency bins, is allowed to vary between the corresponding frequency values of 10 μHz and $4/3\,\Delta\nu$. The reason why we constrain L to this range has to do with the fact that we are primarily interested in measuring the small frequency separation. The signature of the small frequency separation is in fact mainly conveyed by the features at $\Delta\nu/2$ and $\Delta\nu$. For L less than 10 μHz the ACPS is dominated by the signature of the window function, whereas for L greater than approximately $4/3\,\Delta\nu$ it reproduces the features seen below this value of the lag and thus becoming redundant. Finally, the ACPS is normalized after division by its maximum value.

As already stated, modelling the observed ACPS consists of two steps: (i) building a model of the subjacent p-mode PDS and (ii) computing its autocovariance as explained above. In what follows we provide the reader with the basic theory behind the power spectrum of solar-like oscillations and end up describing how the model p-mode spectrum is generated.

3.1.1 The model

Solar-like oscillations are global standing acoustic waves, also known as p modes, driven by near-surface turbulent convection (see e.g. Balmforth 1992a,b). Radial oscillation modes are characterized by the radial order n, whereas non-radial modes are additionally characterized by the non-radial wave numbers ℓ and m.

Ignoring any departure from spherical symmetry, non-radial modes differing only on the azimuthal wave number m are degenerate. Stellar rotation removes the $(2\ell + 1)$-fold degeneracy of the frequency of oscillation of non-radial modes. When the angular velocity of the star, Ω, is small and in the case of rigid-body rotation, the frequency of a (n, ℓ, m) mode is given to first order by (Ledoux 1951):

$$\nu_{n\ell m} = \nu_{n\ell} + m\frac{\Omega}{2\pi}(1 - C_{n\ell})\,. \tag{2}$$

The kinematic splitting, $m\Omega/(2\pi)$, is corrected for the effect of the Coriolis force through the dimensionless quantity $C_{n\ell} > 0$. In the asymptotic regime, i.e. for high-order, low-degree p modes, rotational splitting is dominated by advection and the splitting between adjacent modes within a multiplet is $\nu_{\rm s} \simeq \Omega/(2\pi)$. Typically, $\nu_{{\rm s}\odot} = 0.4$ μHz.

The PDS of a single mode of oscillation is distributed around a limit spectrum with an exponential probability distribution (Woodard 1984; Duvall & Harvey 1986). This limit spectrum contains the information on the physics of the mode and may be described as a standard Lorentzian profile near the resonance. It follows that the overall limit p-mode spectrum is given by (see e.g. Fletcher et al. 2006):

$$\mathcal{P}(\nu; S_{n\ell m}, \nu_{n\ell}, \nu_{\rm s}, \Gamma_{n\ell m}, N_\nu) = \sum_{n=n_0}^{n_{\max}}\sum_{\ell=0}^{\ell_{\max}}\sum_{m=-\ell}^{\ell} \frac{S_{n\ell m}}{1 + [2\,(\nu - \nu_{n\ell} - m\nu_{\rm s})/\Gamma_{n\ell m}]^2} + N_\nu(\nu)\,, \tag{3}$$

where $S_{n\ell m}$ is the mode height, $\nu_{n\ell}$ is the central frequency of the (n, ℓ) multiplet and $\Gamma_{n\ell m}$ is the mode linewidth. In the case of solar-type oscillators and for low angular degree ℓ, we can assume that Γ is a function of frequency alone. Γ is related to the mode lifetime, τ, through $\Gamma = (\pi\tau)^{-1}$. N_ν describes the background signal originating from both granulation and activity. Note we are assuming that a mode is uncorrelated with any other modes or with the background signal. The stellar background signal is commonly modelled as a sum of power laws describing these physical phenomena (Harvey 1985; Aigrain, Favata & Gilmore 2004):

$$N_\nu(\nu) = \sum_{k=1}^{k_{\max}} \frac{A_k^2 B_k}{1 + (2\pi B_k \nu)^{C_k}} + N\,, \tag{4}$$

$\{A_k\}$ and $\{B_k\}$ being, respectively, the corresponding amplitudes and characteristic time-scales, whereas the $\{C_k\}$ are the slopes of each of the individual power laws. A flat offset, N, is needed in order to model photon shot noise.

3.1.2 The mode frequencies

Before we start modelling the observed ACPS, we first need to select a suitable frequency interval for the purpose of our study. This interval should coincide with the frequency range in which p modes are located – i.e. from the frequency of the fundamental ($n = 0$) mode, $\nu_{\rm f}$, up to the atmospheric acoustic cut-off frequency, $\nu_{\rm ac}$.

We compute an estimate of the frequency of the fundamental mode by assuming that it scales with the mean stellar density and thus with the mean large frequency separation:

$$\nu_{\rm f} = \nu_{{\rm f}\odot}\,(\Delta\nu/\Delta\nu_\odot)\,, \tag{5}$$

where $\nu_{{\rm f}\odot} = 258$ μHz and $\Delta\nu_\odot = 135$ μHz.

An estimate of the atmospheric acoustic cut-off frequency is calculated by assuming that it scales with the frequency of maximum amplitude (Kjeldsen & Bedding 1995):

$$\nu_{\rm ac} = \nu_{{\rm ac}\odot}\,(\nu_{\max}/\nu_{\max\odot})\,. \tag{6}$$

For the Sun, one has $\nu_{{\rm ac}\odot} = 5300$ μHz and $\nu_{\max\odot} = 3100$ μHz.

We proceed with the assignment of frequency values to modes with degree $\ell = 0, 1, 2$ (see Section 3.1.3 for an explanation of this upper limit on ℓ) according to the asymptotic relation (Tassoul 1980):

$$\nu_{n\ell} = \Delta\nu\left(n + \frac{1}{2}\ell + \varepsilon\right) - \ell(\ell + 1)D_0\,, \tag{7}$$

where the quantity ε is sensitive to the surface layers and was taken to be 1.5. Moreover, D_0 is sensitive to the sound speed gradient near the core. If equation (7) holds exactly then it follows that[2] $\delta\nu_{02} = 6D_0, \delta\nu_{13} = 10D_0$ and $\delta\nu_{01} = 2D_0$.

The automated *Kepler* pipeline (Hekker et al. 2010a) used to supply input for the procedure described herein generates as output the smooth second-order change in the large frequency separation as a function of n, ${\rm d}\Delta\nu/{\rm d}n$. In cases where an estimate of ${\rm d}\Delta\nu/{\rm d}n$ is available we opt for a modified version of equation (7), which includes a second-order correction:

$$\nu_{n\ell} = \Delta\nu\left(n + \frac{1}{2}\ell + \varepsilon\right) - \ell(\ell + 1)D_0 + (n - n_{\max})^2\,\frac{{\rm d}\Delta\nu/{\rm d}n}{2}\,. \tag{8}$$

The overtone with the highest power, $n_{\max}$, is given by[3] round$[(\nu_{\max} - \nu_{\rm f})/\Delta\nu]$. For the sake of clarity, we should again stress that individual modes in the observed PDS do not need to be tagged by angular degree ℓ prior to the fit. Assignment of frequency

---

[2] $\delta\nu_{13}$ is the spacing between adjacent modes with $\ell = 1$ and 3, and $\delta\nu_{01}$ is the amount by which $\ell = 1$ modes are offset from the mid-point between the $\ell = 0$ modes on either side.

[3] The round[ ] function rounds the argument to its closest integer.

values to modes in the model of the PDS, according to either equation (7) or equation (8), is in fact done in complete ignorance of the correct mode tagging.

3.1.3 The mode heights

The height of a multiplet component can be expressed as

$$S_{n\ell m} = \mathcal{E}_{\ell m}(i)\, S_{n\ell} = \mathcal{E}_{\ell m}(i)\, V_\ell^2 \alpha_{n\ell}\,. \tag{9}$$

The $\mathcal{E}_{\ell m}(i)$ factor represents mode visibility within a multiplet and i is the inclination angle between the direction of the stellar rotation axis and the line of sight. This factor is given by (Gizon & Solanki 2003)

$$\mathcal{E}_{\ell m}(i) = \frac{(\ell - |m|)!}{(\ell + |m|)!} \left[P_\ell^{|m|}(\cos i) \right]^2 , \tag{10}$$

where $P_\ell^m(x)$ are the associated Legendre functions. The quantity V_ℓ^2 is an estimate of the geometrical visibility of the total power in a (n, ℓ) multiplet as a function of ℓ, whereas $\alpha_{n\ell}$ depends mainly on the frequency and excitation mechanism. Equation (9) is only strictly valid under one assumption: when the stellar flux is integrated over the full apparent disc, one must assume that the weighting function depends only on the distance to the disc centre. In this case, the apparent mode amplitude can effectively be separated into two factors: $\mathcal{E}_{\ell m}(i)$ and V_ℓ^2. This assumption holds very well in the case of intensity measurements, since the weighting function is then mainly linked to the limb darkening, whereas for velocity measurements, departures might be observed due to asymmetries in the velocity field induced by rotation (see Ballot, García & Lambert 2006; Ballot et al. 2008, and references therein). The heights of non-radial modes are commonly defined based on the heights of radial modes according to equation (9), and taking into account the V_ℓ/V_0 ratios (see e.g. Bedding et al. 1996). Note that $\ell = 0$ modes constitute a sensible reference since they are not split by rotation. In the present case of stellar observations or when observing the Sun-as-a-star, the associated whole-disc light integration strongly suppresses high-degree modes due to the lack of spatial resolution. Stellar observations are hence mostly sensitive to high-order acoustic eigenmodes with $\ell \leq 3$.

We compute the power envelope for radial modes as a function of frequency according to Kjeldsen et al. (2008). We start by subtracting a fit to the background signal from the observed PDS. The residual spectrum thus obtained is heavily smoothed over the range occupied by the p modes by convolving it with a Gaussian having a full width at half-maximum of $4\,\Delta\nu$. Finally, we multiply the smoothed, residual spectrum by $\Delta\nu/c$, where c is a factor that measures the effective number of modes per order and taken to be 3.03. The height, S_{n0}, of a radial mode in units of power density is then given by (Chaplin et al. 2008)

$$S_{n0} = \frac{2A^2 T}{\pi T \Gamma_{n0} + 2}\,, \tag{11}$$

where A^2 is the total power of the mode (as determined from the power envelope for radial modes) and T is the effective observational length.

3.1.4 Setting up the model

In order to generate the model p-mode spectrum, our modelling procedure requires the following input: The observed PDS sampled at the true resolution (i.e. computed over a grid of uncorrelated frequency bins), a fit to the background signal, $\nu_{\max}$ and $\Delta\nu$. The gradient of the large frequency separation with n, $\mathrm{d}\Delta\nu/\mathrm{d}n$, is optional. This input, with the exception of the observed PDS, might be obtained from the automated *Kepler* pipelines.

A common linewidth value is assigned to all the modes (a sensible assumption if the range in frequency of the spectrum being tested is not too wide). The fitted parameter $\langle\Gamma\rangle$ might then be interpreted as a mean linewidth.

The model p-mode spectrum (including the background signal) is finally assembled according to equation (3), taking into account the global seismic parameters fitted in our procedure, namely, D_0, ν_s, $\langle\Gamma\rangle$ and i. In case we would want to allow for the effect of the windowing and statistical weighting, then we should at this stage convolve the model p-mode spectrum with the spectral window.

3.2 Bayesian inference

3.2.1 Parameter estimation

In the framework of Bayesian parameter estimation, a particular model of the observed ACPS is assumed to be true and the hypothesis space of interest relates to the values taken by the model parameters, $\boldsymbol{\Theta} = \{D_0, \nu_s, \langle\Gamma\rangle, i\}$. These parameters are continuous, meaning that the quantity of interest is a PDF, in contrast to traditional point estimate methods. Let us state Bayes' theorem:

$$p(\boldsymbol{\Theta}|D, I) = \frac{p(\boldsymbol{\Theta}|I)\, p(D|\boldsymbol{\Theta}, I)}{p(D|I)}\,, \tag{12}$$

where D represents the available data and the prior information is represented by I. $p(\boldsymbol{\Theta}|I)$ is called the *prior probability*, whereas $p(\boldsymbol{\Theta}|D, I)$ is called the *posterior probability*. The *likelihood function* is represented by $p(D|\boldsymbol{\Theta}, I)$. $p(D|I)$, the *global likelihood*, simply plays the role of a normalization constant.

The procedure of *marginalization* makes it possible to derive the marginal posterior PDF for a subset of parameters $\boldsymbol{\Theta}_{\mathrm{A}}$, by integrating out the remaining parameters $\boldsymbol{\Theta}_{\mathrm{B}}$, the so-called *nuisance parameters*:

$$p(\boldsymbol{\Theta}_{\mathrm{A}}|D, I) = \int p(\boldsymbol{\Theta}_{\mathrm{A}}, \boldsymbol{\Theta}_{\mathrm{B}}|D, I)\, \mathrm{d}\boldsymbol{\Theta}_{\mathrm{B}}\,. \tag{13}$$

Furthermore, assuming that the prior on $\boldsymbol{\Theta}_{\mathrm{A}}$ is independent of the prior on the remaining parameters, then by applying the product rule we have

$$p(\boldsymbol{\Theta}_{\mathrm{A}}, \boldsymbol{\Theta}_{\mathrm{B}}|I) = p(\boldsymbol{\Theta}_{\mathrm{A}}|I) p(\boldsymbol{\Theta}_{\mathrm{B}}|\boldsymbol{\Theta}_{\mathrm{A}}, I) = p(\boldsymbol{\Theta}_{\mathrm{A}}|I) p(\boldsymbol{\Theta}_{\mathrm{B}}|I)\,. \tag{14}$$

The main advantage of the Bayesian framework when compared to a frequentist approach is the ability to incorporate relevant prior information through Bayes' theorem and to evaluate its effect on our analysis (see e.g. Brewer 2008, for possible applications of Bayesian probability theory in astrophysics).

3.2.2 The likelihood function

We would like to specify the likelihood function, i.e. the joint PDF for the data sample. We know that for a given frequency lag $L_i \in [L_{\min}, L_{\max}]$:

$$\mathrm{ACPS_o}(L_i) = \mathrm{ACPS_m}(L_i) + e_i\,, \tag{15}$$

where $\mathrm{ACPS_o}$ and $\mathrm{ACPS_m}$ are the observed and model ACPS, respectively. The error term e_i follows a Gaussian[4] distribution

---

[4] Each point in the ACPS is the sum of a large number of independent and identically distributed random variables. Therefore, the central limit theorem applies and the distribution of e_i should approach the normal distribution.

with zero mean and standard deviation σ_i. Hence, assuming that the model is deterministic, i.e. true, we can write

$$f\,[\text{ACPS}_{\text{o}}(L_i)] = \frac{1}{\sigma\sqrt{2\pi}} \exp\left\{-\frac{e_i^2}{2\sigma^2}\right\} = \frac{1}{\sigma\sqrt{2\pi}} \exp\left\{-\frac{[\text{ACPS}_{\text{o}}(L_i) - \text{ACPS}_{\text{m}}(L_i)]^2}{2\sigma^2}\right\}, \quad (16)$$

where $f\,[\text{ACPS}_{\text{o}}(L_i)]$ is the probability density that the observed ACPS takes a particular value $\text{ACPS}_{\text{o}}(L_i)$ at a frequency lag L_i. Note that we are assuming σ_i to be constant over the whole range spanned by L_i.

By ignoring the effect of correlation between points in the ACPS, we arrive at the following expression for the likelihood function:

$$\mathcal{L}(\mathbf{\Theta}) \equiv p(D|\mathbf{\Theta}, I) = \prod_i f\,[\text{ACPS}_{\text{o}}(L_i)]\;. \quad (17)$$

While the effect of correlation clearly must be present, the fact that we ignore it can be shown to only affect attempted error calculations and not the fitted values themselves (see Fletcher et al. 2006, and references therein). This does not constitute a problem in the present case, since we will be employing an MCMC sampler in order to obtain the marginal posteriors for each of the model parameters, from which we can estimate the uncertainties.

3.3 Markov chain Monte Carlo

After inspection of equation (13), the need for a mathematical tool that is able to efficiently evaluate the multidimensional integrals required in the computation of the marginal posteriors becomes clear. This constitutes the principal rationale behind the method known as MCMC, which aims at drawing samples from the *target distribution*, $p(\mathbf{\Theta}|D, I)$, by constructing a pseudo-random walk in model parameter space. Such a pseudo-random walk is achieved by generating a Markov chain, whereby a new sample, $\mathbf{\Theta}_{t+1}$, depends solely on the previous sample, $\mathbf{\Theta}_t$, in accordance with a time-independent quantity called the *transition kernel*, $p(\mathbf{\Theta}_{t+1}|\mathbf{\Theta}_t)$:

$$p(\mathbf{\Theta}_{t+1}|\mathbf{\Theta}_t) = q(\mathbf{\Theta}_{t+1}|\mathbf{\Theta}_t) \min\left[1, \frac{p(\mathbf{\Theta}_{t+1}|D, I)}{p(\mathbf{\Theta}_t|D, I)} \frac{q(\mathbf{\Theta}_t|\mathbf{\Theta}_{t+1})}{q(\mathbf{\Theta}_{t+1}|\mathbf{\Theta}_t)}\right], \quad (18)$$

where $q(\mathbf{\Theta}_{t+1}|\mathbf{\Theta}_t)$ is a *proposal distribution* centred on $\mathbf{\Theta}_t$. After a *burn-in* phase, $p(\mathbf{\Theta}_{t+1}|\mathbf{\Theta}_t)$ is able to generate samples of $\mathbf{\Theta}$ with a probability density converging on the target distribution. The algorithm that we employ in order to generate a Markov chain was initially proposed by Metropolis et al. (1953), and subsequently generalized by Hastings (1970), this latter version being commonly referred to as the *Metropolis–Hastings algorithm*.

The Metropolis–Hastings MCMC algorithm just outlined above runs the risk of becoming stuck in a local maximum of the target distribution, thus failing to fully explore all regions in parameter space containing significant probability. A way of overcoming this difficulty is to employ *parallel tempering* (see e.g. Earl & Deem 2005), whereby a discrete set of progressively flatter versions of the target distribution is created by introducing a *temperature parameter*, $\mathcal{T}$. In practice, use is made of its reciprocal, $\beta = 1/\mathcal{T}$, referred to as the *tempering parameter*. By modifying equation (12), we generate the tempered distributions as follows:

$$p(\mathbf{\Theta}|D, \beta, I) = C p(\mathbf{\Theta}|I)\, p(D|\mathbf{\Theta}, I)^{\beta}\,, \quad 0 < \beta \leq 1\,, \quad (19)$$

where C is a constant. For $\beta = 1$, we retrieve the target distribution, also called the *cold sampler*, whereas for $\beta < 1$, the hotter distributions are effectively flatter versions of the target distribution. By running such a set of cooperative chains in parallel and by further allowing for the swap of their respective parameter states, we enable the algorithm to sample the target distribution in a way that allows for both the investigation of its overall features (low-β chains) and the examination of the fine details of a local maximum (high-β chains). See Appendix A for the current version of the parallel tempering Metropolis–Hastings algorithm written in pseudo-code.

Moreover, based on a statistical *control system* (CS) similar to the one described in Gregory (2005), we automate the process of calibration of the Gaussian proposal σ_{CS} values, which specify the direction and step size in parameter space when proposing a new sample to be drawn. The optimal choice of $\{\sigma_{\text{CS}}\}$ is closely related to the average rate at which proposed state changes are accepted, the so-called *acceptance rate*. The control system makes use of an error signal to steer the selection of the σ_{CS} values during the burn-in stage of a single parallel tempering MCMC run, acting independently on each of the tempered chains. The error signal is proportional to the difference between the current acceptance rate and the target acceptance rate. As soon as the error signal for each of the tempered chains is less than a measure of the statistical fluctuation expected for a zero mean error, the control system is turned off and the algorithm switches to the standard parallel tempering MCMC.

4 APPLICATION TO SIMULATED DATA: THE SOLAR TWIN BORIS

We display the results obtained when applying the ACPS-modelling procedure to the particular case of Boris, an artificial main-sequence star created in the framework of the AsteroFLAG group for the purpose of conducting hare and hounds. Briefly, Boris is what we might call a solar analog ($L = 1.00\,\text{L}_{\odot}$; $T_{\text{eff}} = 5778$ K; $R = 1.00\,\text{R}_{\odot}$). We refer the reader to Chaplin et al. (2008) and Stello et al. (2009) for further insight into AsteroFLAG's activities.

4.1 Experimental setup

Boris was assumed to have an apparent visual magnitude of either $V = 8$ or 9 or 10 (these values correspond to the bright end of the nominal apparent magnitude target range for *Kepler*). In each case, 250 realizations of a PDS were generated. The goal was to assess both the accuracy and the precision of the several Bayesian summary statistics of the fitted parameters, namely, the maximum a posteriori (MAP), the median, the mean and the marginal posterior mode. These power density spectra were directly generated in Fourier space and include contributions arising from p modes, granulation, activity, photon shot noise and instrumental noise. They correspond to 30-d long time-series with a 60-second cadence, as it would be expected for *Kepler*'s high-cadence survey targets. The stellar inclination angle, i, entering the simulations was allowed to vary and was drawn from a probability distribution that assumes random orientations – sin(i). Reference values are given for the other model parameters by $D_0^{\text{ref}} = 1.43\,\mu\text{Hz}$, $\nu_{\text{s}}^{\text{ref}} = \nu_{\text{s}\odot} = 0.4\,\mu\text{Hz}$ and $\langle\Gamma\rangle^{\text{ref}} = 1.95\,\mu\text{Hz}$. All the remaining relevant quantities that enter the simulations were assigned 'solar' values.

A prototype of the Birmingham–Sheffield Hallam automated pipeline (Hekker et al. 2010a) was then run on the simulated power density spectra in order to retrieve useful input for the ACPS-modelling procedure, to be specific, a fit to the background signal, $\Delta\nu$ and $\mathrm{d}\Delta\nu/\mathrm{d}n$. The frequency interval of interest (for purposes of the computation of the ACPS) ranges from 2100 to 4500 μHz and $\nu_{\max}$ has been fixed at 3300 μHz.

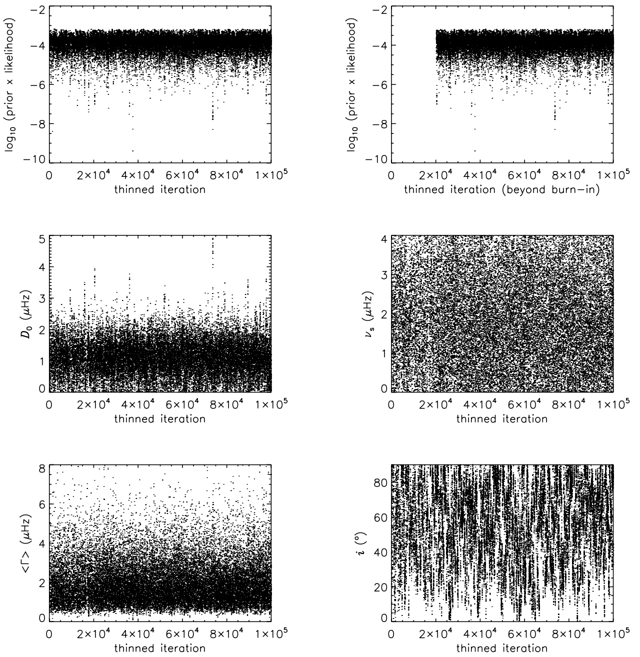

Figure 2. Sequence of 1×10^5 samples (at a thinning interval of 1) drawn from the target distribution ($\beta = 1$) by a Metropolis–Hastings MCMC. Top panels: behaviour of $\log_{10}[p(\mathbf{\Theta}|I)\,\mathcal{L}(\mathbf{\Theta})]$ as a function of the iteration number (a means of visually inspecting the convergence of the MCMC). Middle and bottom panels: behaviour of model parameter values as a function of the iteration number.

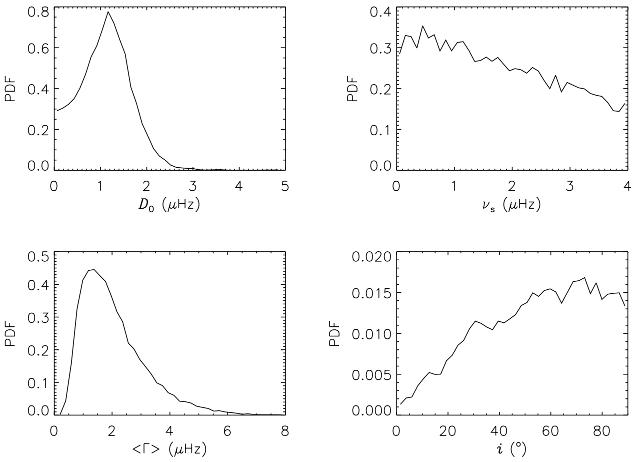

Figure 3. Binned marginal posterior PDFs of the model parameters. These are built after assembling the corresponding samples (beyond burn-in) depicted in the middle and bottom panels of Fig. 2. Based on these marginal posteriors, we may then evaluate the several Bayesian summary statistics for each of the model parameters.

Figs 1, 2 and 3 display the typical graphical output of the ACPS-modelling procedure resulting from the analysis of a single realization of the PDS of Boris (with $V = 8$ and a random orientation characterized by $i = 32\overset{\circ}{.}4$). Note that throughout the analysis of the full set of realizations of the power spectrum, uniform priors have been imposed on D_0, ν_s and $\langle\Gamma\rangle$, whereas $p(i|I) = \sin(i)$.

4.2 On retrieving D_0 and $\langle\Gamma\rangle$

Figs 4 and 5 result from the application of the ACPS-modelling procedure to the full set of realizations of the power spectrum

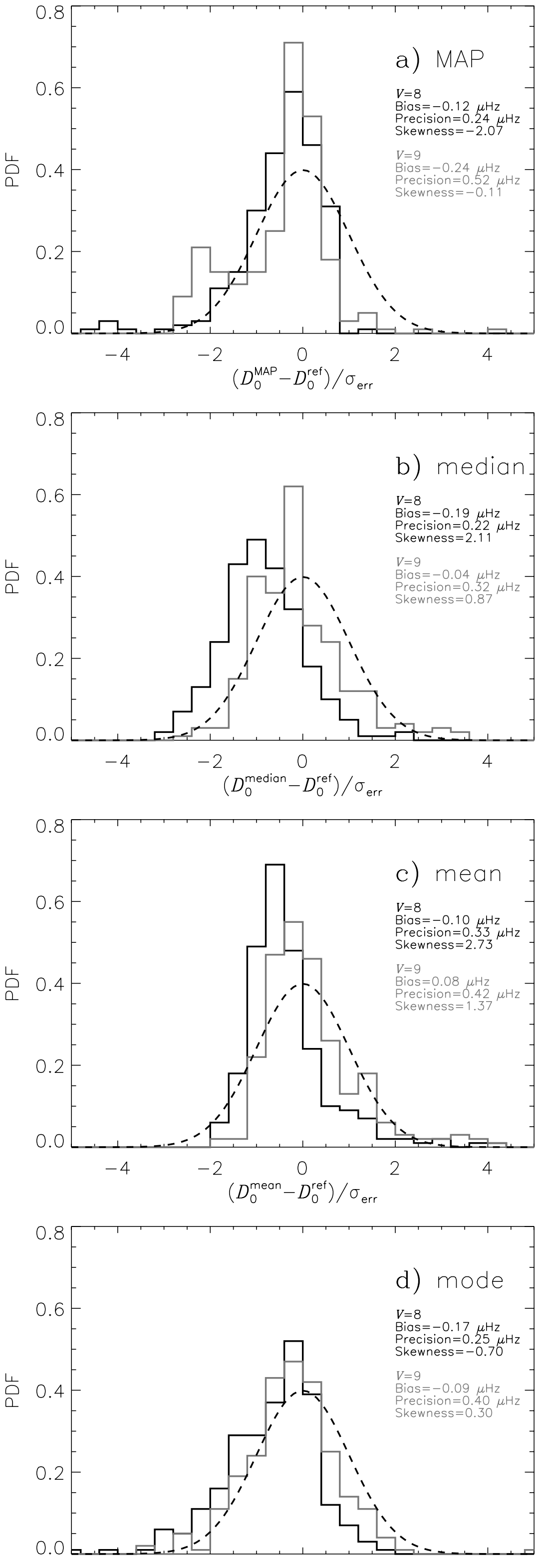

Figure 4. PDFs of the actual errors in the determination of D_0, which in turn have been normalized after division by their standard deviation, σ_err. Several Bayesian summary statistics have been considered: (a) the MAP, (b) the median, (c) the mean and (d) the mode. The solid black line corresponds to the set with $V = 8$, whilst the solid grey line corresponds to the set with $V = 9$. The dashed line represents the standard normal distribution.

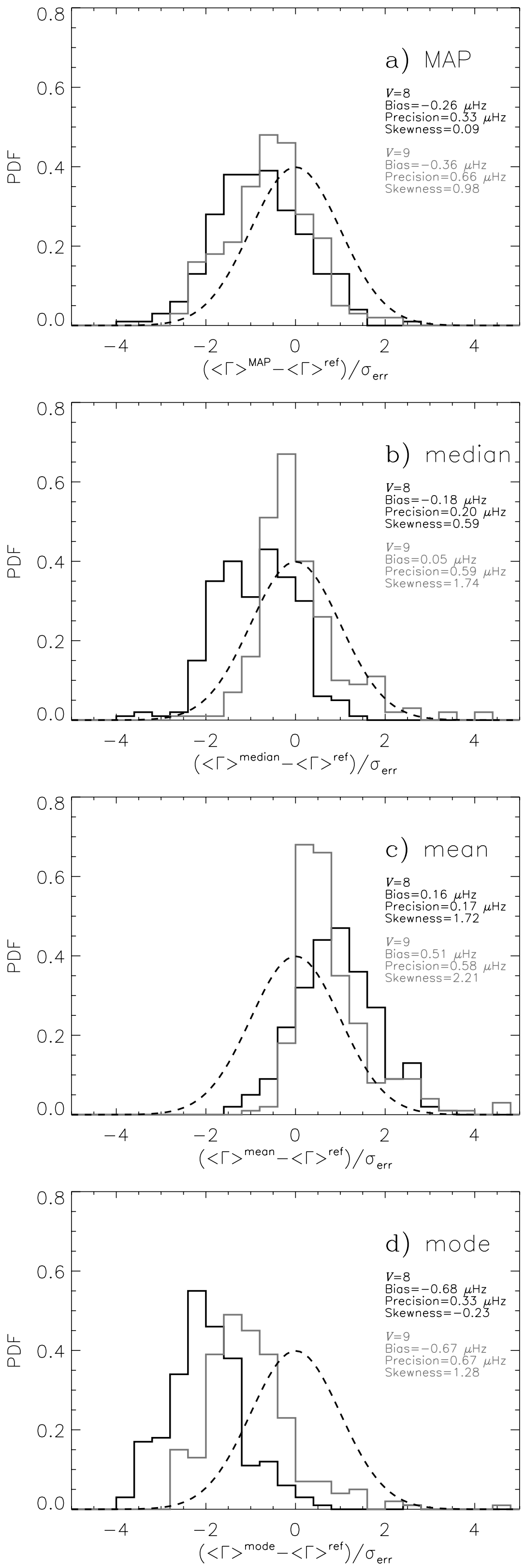

Figure 5. The same as in Fig. 4 but now regarding the estimation of $\langle\Gamma\rangle$.

(250 realizations for each value of V), allowing one to assess the potential biases of the Bayesian summary statistics of the fitted parameters D_0 and $\langle\Gamma\rangle$, respectively. The precision associated with these same estimators is also indicated in the plots.

When choosing a summary statistic to be used, we should make sure that it is representative of the marginal probability distribution of the parameter in question, a point that all the summary statistics considered seem to satisfy. The marginal posterior PDFs of D_0 and $\langle\Gamma\rangle$ are asymmetric (see Fig. 3) and well modelled by (Fierry Fraillon et al. 1998)

$$f(x) = K(x/s)^{\alpha}\exp[(x/s)^{\alpha+1}]\,, \tag{20}$$

where K is a normalization constant, s is an adjustable parameter describing the shape of the distribution and α defines the type of distribution ($\alpha = 0$ for a Boltzmann law and high values of α for a Gaussian law). Furthermore, the set of summary parameter values should provide a good fit to the data, the quality of which might be assessed by computing the rms of the residuals. This latter criterion led us to adopt the MAP as our choice of summary statistic.

It turns out from Figs 4 and 5 that the different estimators, although equally robust, present biases whose magnitude and sign vary with the estimator being considered, a direct consequence of the asymmetry of the marginal posterior PDFs of D_0 and $\langle\Gamma\rangle$. A way of overcoming these inherent biases would be to present these values normalized to the homologous values obtained after performing a similar analysis on Sun-as-a-star data covering an equivalent range in frequency (i.e. scaling by the ratio of the acoustic cut-off frequencies of the Sun and the target in question).

The MAP summary statistic allows one to determine D_0 with a relative error of 8 and 17 per cent for $V = 8$ and 9, respectively. On the other hand, determination of $\langle\Gamma\rangle$ is accomplished with a relative error of 13 and 18 per cent for $V = 8$ and 9, respectively.

A clear degradation of the precision associated with the estimators is seen when considering the set of fainter objects ($V = 9$). This is due to the fact that V is directly coupled to the photon shot noise level and hence to signal-to-noise ratio (S/N).

Note that no results have been plotted concerning the set characterized by $V = 10$ as no sensible output was generated by the ACPS-modelling procedure. We should mention that at this S/N, the automated pipeline is no longer capable of supplying an input value for $\mathrm{d}\Delta\nu/\mathrm{d}n$ and hence the model p-mode spectrum generated by the ACPS-modelling procedure assumes a constant large separation with n.

4.3 On retrieving *i* and ν_s

With the current experimental setup, we face a scenario where the linewidths of the individual modes present in the simulated power spectra are systematically larger than the rotational splitting, i.e. $\nu_s \lesssim \Gamma$. Consequently, multiplet components are blended together, which strongly correlates the inclination with the rotational splitting, making a successful retrieval of these global parameters not feasible. As a further matter, the spectral resolution is too low ($\delta\nu = 0.39\,\mu$Hz) and will only marginally allow the rotational splitting to be resolved. By again looking at the PDF of the inclination for a single realization of the power spectrum in Fig. 3, we realize that we are in fact retrieving the imposed prior since there is no enough evidence in the data to proceed otherwise. Fig. 6 corroborates this, if we bear in mind that $i^{\mathrm{mean}} \equiv \int_{0^\circ}^{90^\circ} i p(i|D,I)\,\mathrm{d}i \simeq \int_{0^\circ}^{90^\circ} i p(i|I)\,\mathrm{d}i = \int_{0^\circ}^{90^\circ} i\,\sin(i)\,\mathrm{d}i = 57^\circ$. Similarly, by looking at the PDF of the rotational splitting for a single realization of the power spectrum in Fig. 3, we notice that we are in fact retrieving the imposed uniform prior, although slightly biased towards low values of the splitting.

In order to demonstrate the full capability of this tool, we have applied it to a series of higher S/N realizations of the PDS of Boris (assumed to have $V = 8$), which now correspond to six-month

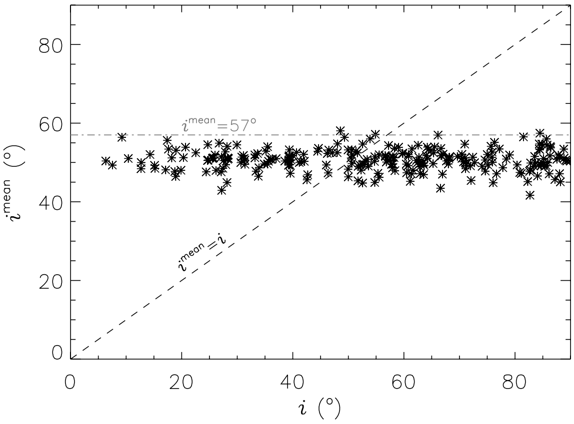

Figure 6. The posterior mean of the stellar inclination angle, $i^{\rm mean}$, versus the input inclination, i. This plot refers to the set of simulations with $V = 8$.

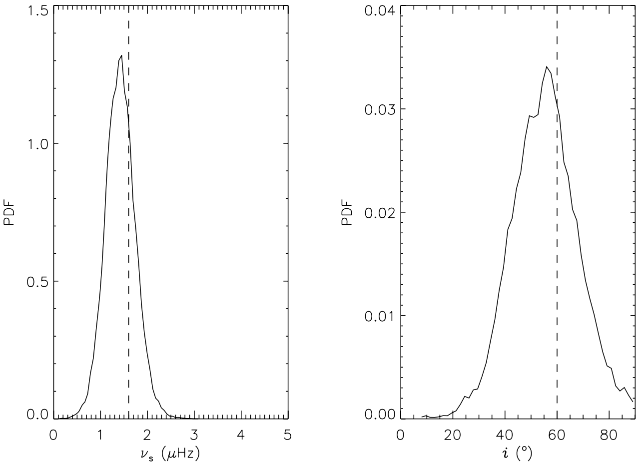

Figure 7. PDFs of $\nu_{\rm s}$ and i resulting from the application of the ACPS-modelling procedure to a single realization of the PDS of Boris. Reference values are given by $\nu_{\rm s}^{\rm ref} = 4\,\nu_{\rm s\odot} = 1.6$ μHz and $i^{\rm ref} = 60°$, and are represented by dashed vertical lines. MAP estimates are in turn given by $\nu_{\rm s}^{\rm MAP} = 1.44^{+0.26}_{-0.36}$ μHz and $i^{\rm MAP} = 55.9°{}^{+11.8°}_{-13.2°}$, therefore being within uncertainties of the reference values.

long time-series ($\delta\nu = 0.06$ μHz). Since we wish to avoid a scenario where $\nu_{\rm s} \lesssim \Gamma$ and enter a more favourable regime where instead $\Gamma < \nu_{\rm s} \lesssim \delta\nu_{02}$, we (i) increased the reference value for the mean rotational splitting, $\nu_{\rm s}^{\rm ref} \in \{2\,\nu_{\rm s\odot}, 4\,\nu_{\rm s\odot}, 6\,\nu_{\rm s\odot}\}$, while (ii) simultaneously adopting a narrower frequency interval of interest, ranging from 2100 to 3300 μHz, at the low-frequency end of the acoustic spectrum. This latter step will effectively decrease the reference value for the mean linewidth, $\langle\Gamma\rangle^{\rm ref}$, since we use solar-mode linewidths when generating the artificial power density spectra, which are known to increase towards higher frequencies. Finally, we adopted $i^{\rm ref} = 60°$ and imposed uniform priors on all the model parameters. Fig. 7 illustrates a case where the inclination and the rotational splitting have been successfully retrieved, after applying the ACPS-modelling procedure to a single realization of the PDS of Boris.

5 SUMMARY AND DISCUSSION

(i) We have developed a new data analysis tool based on modelling and fitting the autocovariance of the acoustic PDS of a solar-type oscillator. Its main advantage when compared to a canonical peak-bagging procedure relies on the fact that there is no need to carry out mode (angular degree ℓ) identification prior to performing the fit. This procedure is in principle also suitable for being employed in the case of evolved stars displaying solar-like oscillations.

(ii) The implementation of the ACPS-modelling procedure has been thoroughly described. Furthermore, its automated character makes this procedure appropriate for the analysis of a large number of data sets (e.g. arising from the *Kepler* mission).

(iii) The ACPS conveys information on the large and small frequency separations, mode lifetime and rotation. The current version of the ACPS-modelling procedure accepts $D_0, \nu_{\rm s}, \langle\Gamma\rangle$ and i as free parameters. The prospective inclusion of $\Delta\nu$ and $\mathrm{d}\Delta\nu/\mathrm{d}n$ as additional free parameters is envisaged.

(iv) The tool has been applied to simulated data mimicking what would have been expected for a solar analog observed at high cadence during *Kepler*'s survey phase. We assessed the potential biases as well as the precision associated with the several Bayesian summary statistics of the fitted parameters D_0 and $\langle\Gamma\rangle$, having been able to decide on a preferred summary statistic, namely, the MAP. We addressed a way of overcoming the inherent biases. These biases would not in any case underpin the usefulness of this procedure, since the preferred summary statistic is given together with robust estimates of the uncertainties; an MCMC sampler is employed in order to obtain the marginal posteriors for each of the model parameters, from which we can estimate the uncertainties. For instance, using the SEEK routine (Quirion et al., in preparation), in order to estimate stellar parameters and basing it on a set of asteroseismic parameters returned by this procedure, would lead to the estimation of a set of stellar parameters possessing robust uncertainties (see discussion in Karoff et al. 2010).

(v) No sensible output has been generated by the ACPS-modelling procedure for the set with $V = 10$. We could argue, of course, that by increasing the effective observational length of the simulated data, the method could successfully reach a lower S/N since realization noise is expected to scale as $1/\sqrt{T}$.

(vi) Furthermore, retrieval of both i and $\nu_{\rm s}$ could not be achieved with the current experimental setup and a reason for that was given based on the intrinsic characteristics of the simulated spectra. An example has however been included whereby the full capability of this tool is demonstrated.

ACKNOWLEDGMENTS

TLC is supported by grant with reference number SFRH/BD/36240/2007 from FCT/MCTES, Portugal. CK acknowledges financial support from the Danish Natural Sciences Research Council. WJC, YPE and SH acknowledge the support of the Science and Technology Facilities Council (STFC), UK. We wish to thank the anonymous referee for valuable comments.

REFERENCES

Aigrain S., Favata F., Gilmore G., 2004, A&A, 414, 1139
Aizenman M., Smeyers P., Weigert A., 1977, A&A, 58, 41
Anderson E. R., Duvall T. L., Jr, Jefferies S. M., 1990, ApJ, 364, 699
Appourchaux T. et al., 2008, A&A, 488, 705
Ballot J., García R. A., Lambert P., 2006, MNRAS, 369, 1281
Ballot J., Appourchaux T., Toutain T., Guittet M., 2008, A&A, 486, 867
Balmforth N. J., 1992a, MNRAS, 255, 639
Balmforth N. J., 1992b, MNRAS, 255, 603

Bedding T. R., Kjeldsen H., 2008, in van Belle G., ed., ASP Conf. Ser. Vol. 384, 14th Cambridge Workshop on Cool Stars, Stellar Systems, and the Sun. Astron. Soc. Pac., San Francisco, p. 21

Bedding T. R., Kjeldsen H., Reetz J., Barbuy B., 1996, MNRAS, 280, 1155

Bedding T. R. et al., 2010, ApJ, 713, L176

Benomar O. et al., 2009, A&A, 507, L13

Brewer B. J., 2008, preprint (arXiv e-prints)

Chaplin W. J. et al., 2008, Astron. Nachr., 329, 549

Chaplin W. J., Houdek G., Appourchaux T., Elsworth Y., New R., Toutain T., 2008, A&A, 485, 813

Chaplin W. J. et al., 2010, ApJ, 713, L169

Christensen-Dalsgaard J., 2004, Sol. Phys., 220, 137

Christensen-Dalsgaard J., Arentoft T., Brown T. M., Gilliland R. L., Kjeldsen H., Borucki W. J., Koch D., 2008, J. Phys. Conf. Ser., 118, 012039

Duvall T. L., Jr, Harvey J. W., 1986, in Gough D. O., ed., NATO ASIC Proc. 169, Seismology of the Sun and the Distant Stars Solar Doppler Shifts: Sources of Continuous Spectra. Reidel, Dordrecht, p. 105

Earl D. J., Deem M. W., 2005, Phys. Chemistry Chemical Phys. (Incorporating Faraday Transactions), 7, 3910

Fierry Fraillon D., Gelly B., Schmider F. X., Hill F., Fossat E., Pantel A., 1998, A&A, 333, 362

Fletcher S. T., Chaplin W. J., Elsworth Y., Schou J., Buzasi D., 2006, MNRAS, 371, 935

Gilliland R. L. et al., 2010, PASP, 122, 131

Gizon L., Solanki S. K., 2003, ApJ, 589, 1009

Gregory P. C., 2005, Bayesian Logical Data Analysis for the Physical Sciences: A Comparative Approach with ‘Mathematica’ Support. Cambridge Univ. Press, Cambridge

Grigahcène A. et al., 2010, ApJ, 713, L192

Harvey J., 1985, in Rolfe E., Battrick B., eds, Future Missions in Solar, Heliospheric and Space Plasma Physics. ESA, Noordwijk, p. 199

Hastings W. K., 1970, Biometrika, 57, 97

Hekker S. et al., 2010a, MNRAS, 402, 2049

Hekker S. et al., 2010b, ApJ, 713, L187

Huber D., Stello D., Bedding T. R., Chaplin W. J., Arentoft T., Quirion P., Kjeldsen H., 2009, Comm. Asteroseismol., 160, 74

Kallinger T. et al., 2010, A&A, 509, A77

Karoff C., Metcalfe T. S., Chaplin W. J., Elsworth Y., Kjeldsen H., Arentoft T., Buzasi D., 2009, MNRAS, 399, 914

Karoff C., Campante T. L., Chaplin W. J., 2010, preprint (arXiv e-prints)

Kjeldsen H., Bedding T. R., 1995, A&A, 293, 87

Kjeldsen H. et al., 2008, ApJ, 682, 1370

Kolenberg K. et al., 2010, ApJ, 713, L198

Ledoux P., 1951, ApJ, 114, 373

Mathur S. et al., 2010, A&A, 511, A46

Metropolis N., Rosenbluth A. W., Rosenbluth M. N., Teller A. H., Teller E., 1953, J. Chem. Phys., 21, 1087

Michel E. et al., 2008, Sci, 322, 558

Mosser B., Appourchaux T., 2009, A&A, 508, 877

Roxburgh I. W., 2009, A&A, 506, 435

Soriano M., Vauclair S., 2008, A&A, 488, 975

Stello D. et al., 2009, ApJ, 700, 1589

Stello D. et al., 2010, ApJ, 713, L182

Tassoul M., 1980, ApJS, 43, 469

Woodard M. F., 1984, PhD thesis, Univ. California, San Diego

APPENDIX A: PARALLEL TEMPERING METROPOLIS–HASTINGS

```
procedure PT METROPOLIS–HASTINGS
    $\mathbf{\Theta}_{0,i} = \mathbf{\Theta}_0\ ,\ 1 \leqslant i \leqslant n_\beta$
    for $t = 0, 1, \ldots, n_{\mathrm{it}} - 1$ do
        for $i = 1, 2, \ldots, n_\beta$ do
            Propose a new sample to be drawn from a proposal distribution: $\mathbf{\Lambda} \sim N(\mathbf{\Theta}_{t,i}; \mathbf{C}_i)$
            Compute the Metropolis ratio:
                $r = \frac{p(\mathbf{\Lambda}|D,\beta_i,I)}{p(\mathbf{\Theta}_{t,i}|D,\beta_i,I)} \frac{q(\mathbf{\Theta}_{t,i}|\mathbf{\Lambda})}{q(\mathbf{\Lambda}|\mathbf{\Theta}_{t,i})}$
            Sample a uniform random variable:
                $U_1 \sim \mathrm{Uniform}(0,1)$
            if $r \geqslant U_1$ then
                $\mathbf{\Theta}_{t+1,i} = \mathbf{\Lambda}$
            else
                $\mathbf{\Theta}_{t+1,i} = \mathbf{\Theta}_{t,i}$
            end if
        end for
        $U_2 \sim \mathrm{Uniform}(0,1)$
        if $1/n_{\mathrm{swap}} \geqslant U_2$ then
            Select random chain:
                $i \sim \mathrm{UniformInt}(1, n_\beta - 1)$
            $j = i + 1$
            Compute $r_{\mathrm{swap}}$:
                $r_{\mathrm{swap}} = \frac{p(\mathbf{\Theta}_{t,j}|D,\beta_i,I)p(\mathbf{\Theta}_{t,i}|D,\beta_j,I)}{p(\mathbf{\Theta}_{t,i}|D,\beta_i,I)p(\mathbf{\Theta}_{t,j}|D,\beta_j,I)}$
            $U_3 \sim \mathrm{Uniform}(0,1)$
            if $r_{\mathrm{swap}} \geqslant U_3$ then
                Swap parameter states of chains $i$ and $j$:
                    $\mathbf{\Theta}_{t,i} \leftrightarrow \mathbf{\Theta}_{t,j}$
            end if
        end if
    end for
    return $\mathbf{\Theta}_{t,i}\ ,\ \forall t\ ,\ i\!:\!\beta_i\!=\!1$
end procedure
```

Figure A1. Pseudo-code-written version of the parallel tempering Metropolis–Hastings algorithm. n_β is the total number of tempered chains, n_{it} is the number of iterations when running the MCMC, $q(\mathbf{\Lambda}|\mathbf{\Theta}_{t,i}) = N(\mathbf{\Theta}_{t,i}; \mathbf{C}_i)$ is a multivariate Gaussian distribution centred on $\mathbf{\Theta}_{t,i}$ and with diagonal covariance matrix, $\mathbf{C}_i$, and n_{swap} is the mean number of iterations between successive proposals to swap the parameter states of two adjacent chains.